The Design and Analysis of a DC SQUID for a SQUID Microscope

by

Willem Adriaan Burger

Thesis presented in partial fulfilment of the requirements for the degree of
Master of Science in Electronic Engineering

at Stellenbosch University

Department of Electronical Engineering

Supervisor: Prof W.J. Perold

December 2008

Declaration

By submitting this thesis electronically, I declare that the entirety of the work contained therein is my own, original work, that I am the owner of the copyright thereof (unless to the extent explicitly otherwise stated) and that I have not previously in its entirety or in part submitted it for obtaining any qualification.

Date: December 2008

Abstract

The Design and Analysis of a DC SQUID for a SQUID Microscope

W.A. Burger

Department of Electronical Engineering
University of Stellenbosch
Private Bag X1, 7602 Matieland, South Africa

Thesis: MscEng

March 2008

This thesis relates to the analysis and design of a SQUID microscope. Superconductor theory is discussed in depth to provide a thorough understanding of Josephson junctions and of dc SQUID magnetometers. The behaviour and suitability of different types of single-layer dc SQUIDs are looked at. The quality of the superconducting material patterned onto a substrate and the Josephson junction design used affect the behaviour of a practical dc SQUID. Noise and cooling play an integral part in the design and operation of a dc SQUID. The source of noise is looked at in an effort to minimize its effect. Cryocooling is essential to real world operation so different cooling strategies and their consequences are analyzed. This thesis focuses on modeling the behaviour of the dc SQUID to creating a practical system for use inside a SQUID microscope. Operating the dc SQUID with the appropriate electronics will linearize the device, reduce the effect of noise, and create a device with wide bandwidth. Each step in creating a practical system is discussed in detail. Simulations are used to create models predicting the behaviour of the dc SQUID and the electronics. They are then used to design and create practical electronic systems. Measurements are performed on Josephson junctions and dc SQUID magnetometers using the designed electronics. The Josephson junctions behave as predicted and were successfully tested. The dc SQUIDs did not behave as predicted and were not successfully tested. The SQUIDs were damaged, either by a malfunction in the cryocooler or through age related deterioration. A full test of the flux-locked loop was not possible and the dc SQUID was not linearized.

Uittreksel

Die Ontwerp en Analise van 'n GS SQUID vir 'n SQUID Mikroskoop

("The Design and Analysis of a DC SQUID for a SQUID Microscope")

W.A. Burger

Departement Elektroniese Ingenieurswese
Universiteit van Stellenbosch
Privaatsak X1, 7602 Matieland, Suid Afrika

Tesis: MscIng

Maart 2008

Hierdie tesis handel oor die ontwerp en die analise van 'n SQUID mikroskoop. Die supergeleier teorie word in diepte bespreek om 'n deeglike grondkennis van die Josephson-vlak en die dc SQUID magneetsensors te dokumenteer. Daar word na verskillende tipes enkelvlak gs SQUID modelle gekyk om hulle gedrag en toepaslikheid te bestudeer. Die supergeleidende materiaal se kwaliteit en die tipe Josephson-vlak wat benut word om 'n gs SQUID to konstrueer, speel 'n groot rol in die gedrag van die stelsel. Drywing van 'n praktiese gs SQUID word sterk beïnvloed deur beide ruis en die toerusting wat gebruik word vir verkoeling. Die vorming van ruis word bestudeer om die invloed daarvan op die stelsel te probeer verminder. Tans benodig supergeleiers goeie verkoeling om te funksioneer, omdat hulle net by lae temperture kan werk. Verskillende strategieë vir verkoeling word geanaliseer, en hulle invloed op die werking van 'n gs SQUID word bespreek. 'n Groot gedeelte van hierdie tesis word gebruik om 'n model van 'n praktiese gs SQUID te skep. Hierdie model moet gebruik kan word om 'n SQUID mikroskoop te produseer. Met die regte elektronika sal 'n gs SQUID verander word in 'n lineêre stelsel met lae ruis en hoë bandwydte. Elke stap om 'n praktiese stelsel te bou word in diepte bespreek. Simulasies word gebruik om te bepaal hoe 'n praktiese gs SQUID en sy elektronika sal funksioneer. Simulasies kan dus gebruik word om die elektronika vir 'n praktiese stelsel te ontwerp. Josephson-vlakke en gs SQUID magneetsensors word getoets met die ontwerpte elektronika. Die Josephson-vlakke is gemeet en het die verwagte resultate gegee. Die gs SQUIDs is ook gemeet, maar hulle het nie funksioneer soos verwag nie. Terwyl die vlakke suksessvol gemeet is, was die meting van die dc SQUIDS nie suksesvol nie. Die SQUID elemente was beskadig, óf deur foutiewe toerusting, óf deur veroudering. 'n Volledige toets van die geslote lus terugvoer stelsel was onmoontlik, en die gs SQUID kon nie lineêr aangedryf word nie.

Acknowledgements

I would like to express my sincere gratitude to the following people and organisations who have contributed to making this work possible:

- The NRF for financial support on this project,
- Ulrich Büttner for his technical help on using laboratory equipment, counseling on the practical aspects of using superconductors, and for providing the devices used for testing,
- Akram Elkaseh for producing the superconductive films used to create the test devices,
- Ashley Cupido for manufacturing the printed circuit boards,
- Wessel Croukamp for providing components and equipment,
- Prof W.J. Perold of the University of Stellenbosch in his role as my study leader.

Contents

List of Figures

List of Tables

Chapter 1

Introduction to High-Temperature Superconductors

1.1 Introduction

The discovery of the first high-temperature superconductor led to an era of intense research, paving the way for a multitude of new devices and applications. A large portion of the research was conducted to understand the fundamentals of the high-T_c superconductors. One commonly used device is the Superconducting Quantum Interference Device (SQUID), capable of detecting magnetic fields with unprecedented sensitivity.

1.2 Motivation for the Understanding and Development of Superconducting Devices

Superconductors have yielded some niche devices that can not be manufactured using other materials available to mankind. The Meissner effect of magnetic flux expulsion in superconductors is used in Maglev trains for electromagnetic suspension, and powerful superconducting magnets are used to levitate the mass of the train above the track. Other devices for which there is an analog available, the superconductor usually yields better performance, higher accuracy and a lower noise floor. Some of these devices include Rapid Single Flux Quantum (RSFQ) logic, similar to digital logic at multiple gigahertz; SQUID magnetometers, similar to Hall probes but with far higher sensitivity; RF notch filters with a lower noise floor; high power electromagnets and permanent magnets; accurate oscillators; and precise voltage measurement devices. The only drawback to superconductors is that they require active cooling. The power expended on cooling can usually be negated by the increased performance of the device and by a great reduction in size and weight. Thin-film notch filters and digital logic circuits built by HYPRES are being used by the US Navy due to superior performance to their analog and digital equivalents. The same material used in constructing ultra sensitive magnetic flux detectors can also create immensely powerful permanent electromagnets in the multiple Tesla range [6]. Recent research into cheaper and safer magnetic resonance imaging (MRI) scanners requires SQUID sensors capable of detecting fields smaller than 30 millitesla, about 1000 times the Earth's magnetic field. This field is a far less powerful and safer than that required by a typical MRI scanner, which is about 3 Tesla, and permits examination of patients with metallic implants and pacemakers.

1.3 Superconductors: A Brief History

The first superconductors were discovered during the advent of the 20th century by Heike Kamerlingh Onnes [7] (1853-1926) during research into cryogenics. From 1882 to 1923 Onnes was a professor of experimental physics at the University of Leiden. A large part of his research, from 1895 to 1906, was to verify Van der Waal's law of corresponding states [8] over a range of temperatures. The law was tested by studying the general thermodynamic properties of liquids, gases and metals over a wide range of temperatures and pressures. In order to subject materials to very low temperatures, the cryogenic experimental techniques had to perfect. In 1904 Onnes founded a large cryogenics laboratory and by 1906 he had improved the hydrogen-liquefaction machine (cryostat). The liquefaction machine made use of the Joule-Thomson effect, where a gas is compressed and cooled below the inversion temperature and is then allowed to expand, resulting in some of the gas undergoing liquefaction. Onnes was the first person to successfully liquefy helium in 1908 at the University of Leiden [9] by using the improved cryostat. His aim of creating a solid helium state was only realized after his death by his student, Willem Hendrik Keesom (1876-1956), and Wander Johannes de Haas (1878-1960) in 1926.

Some researchers such as William Thomson (1824-1907), better known as Lord Kelvin, thought that when the temperature of a conductor approaches near absolute zero the flow of electrons would come to a complete stop. Other researchers, including Onnes, believed that the resistance would linearly decrease and ultimately drop to nil. Liquid helium boils at 4.22 K at standard atmospheric pressure, and the cryostat managed to further decrease the temperature to 0.9 K. Using these low temperatures, Onnes discovered in 1911 that pure mercury suddenly loses all measurable resistance when its temperature reached the boiling point of liquid helium [10, 11]. Initially he called this phenomenon "supraconductivity", but later renamed it to "superconductivity". Mercury was the first of many materials discovered to show superconductivity, with lead and tin following.

The fundamental theory of conventional superconductivity to explain the characteristics of these low-temperature superconductors (LTS) was developed in 1957 by John **B**ardeen (1908-1991), Leon **C**ooper (1930-), and Robert **S**chrieffer (1931-), now called the BCS theory [12] in honor of its creators. Until 1986 it was thought that all superconductors are limited by their *critical temperature*, T_C, to extremely low temperatures. The upper thermal limit of $T_C = 23.2$ K for Nb_3Ge (Niobium-Germanium) was the highest temperature obtainable by LTS. Running these low-T_C devices requires either an expensive cryogenic cooler or liquid helium as a coolant.

The discovery a of high-temperature superconductor (HTS) copper oxide (cuprate) perovskite changed the whole outlook on superconductors. In September of 1986 Johannes Georg Bednorz (1950-) working with K. Alexander Muller (1927-) discovered the first HTS $La_{1.85}$-$Ba_{0.15}$-Cu-O_4 (Lanthanum-Barium-Copper-Oxide, LBCO) that had a T_c of 30 K. The higher the temperature at which a superconductor can operate, the less expensive it is to run, especially if liquid helium is not required. This discovery led to increased effort in researching new materials that become superconductive at higher temperatures. Chu increased the temperature by replacing Lanthanum (La) with Yttrium (Y), creating $Y_{1,2}$-$Ba_{0,8}$-Cu-$O_{4-\delta}$ with a T_C of 92 K. This was later replaced by the discovery of Y-Ba_2-Cu_3-$O_{7-\delta}$ (Yttrium-Barium-Copper-Oxide, YBCO) with a T_c of 90 K. Most of the newer materials have a T_C far above the 77.35 K boiling point of liquid nitrogen, a relatively inexpensive and readily available coolant, simplifying the design of a device and significantly reducing the running costs.

The BCS theory does not describe the workings of HTS and it is believed that other effects are responsible for their superconductivity. These effects may, in fact, be the reason LTS work as well. Research into Bose-Einstein condensates, with temperatures billionth of a degree above absolute zero, could lead to a better understanding of how superconductors work and hopefully lead to room temperature devices.

Chapter 2

Superconductivity

2.1 Introduction

The best known property of a superconductor is its ability to conduct dc current without any measurable resistance. This lack of resistance must not be misinterpreted to imply that superconductors are perfect conductors. On a quantum level the superconductors have additional properties to consider, especially the high-temperature superconductor's asymmetrical crystal lattice leading to anisotropy of the super-current. The most notable properties include capacitance, inductance, critical parameters that destroy the superconductivity, the Josephson effect and magnetic flux expulsion.

In an effort to understand how these materials work, their unique magnetic properties, as well as the macroscopic function of the electrons at a quantum level, must be examined. The following sections discuss two models used for superconducting research and manufacturing [13]. Each model has advantages and disadvantages, where the simpler classical model is used to describe the simpler superconducting structures, and the more complex Macroscopic Quantum Model (MQM) is used to describe complex functions such as the Josephson effect. Each subsequent classical model builds up from the preceding model to include effects not yet described, thus refining the superconducting theory into a usable and practical form that encompasses all the phenomena attributed to superconductors. The MQM treats electrons as wave-particles and is used to describe the function of flux quantization and the Josephson junction.

2.2 Classical Electromechanical Model

The classical model of superconductors describes a material with zero resistance and perfect diamagnetism [13]. This model does not try to explain why the material works, but only how it works. This is a phenomenological approach to understanding superconductors, ignoring the true mechanics behind it. Unfortunately this approach does not work for SQUID systems as some of the characteristics that make it function can not be explained except by using macroscopic quantum effects. The advantage of the classical model is that it can be used to describe bulk superconductors, such as the superconducting wires, with relative ease.

Using magnetoquasistatic (MQS, $\nabla \times \mathbf{H} \approx \mathbf{J}$) or electroquasistatic (EQS, $\nabla \times \mathbf{E} \approx 0$) systems with the resistance approaching nil ($R \to 0$, $\sigma_0 \to \infty$) might seem like good approximations to make, as it converts a good conductor into a perfect conductor. An inductor with no resistance will develop a potential across itself if the driving frequency of the current is not zero. As was stated earlier, superconductors must not be confused with perfect conductors. The behaviour of a superconductor inside a uniform magnetic field must be analyzed to help understand why the perfect conductor can not be used for a model.

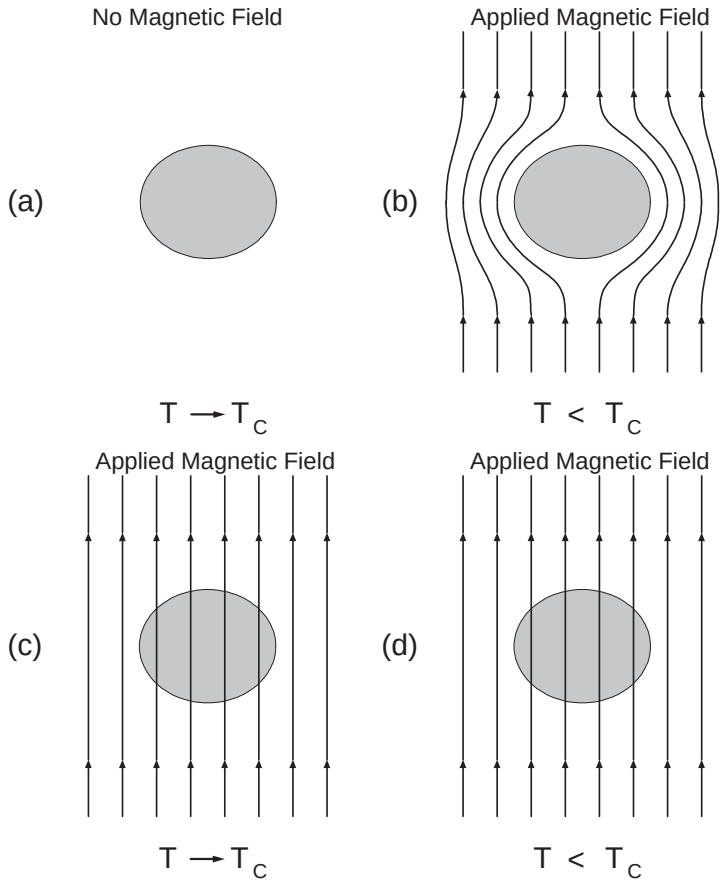

Figure 2.1: Effect of a uniform magnetic field on a perfect conductor.

Assuming that the conductor becomes a perfect conductor for temperatures below T_c, Figure 2.1 can be used to theoretically examines the effect of a uniform magnetic field on a perfect conductor. In Figure 2.1 (a) the material is cooled into a perfect conducting state without any externally applied magnetic fields. A uniform magnetic field is then applied, Figure 2.1 (b), and as a result the perfect conductor prevents any magnetic flux from penetrating. If however the conductor is cooled in the presence of the magnetic field, Figure 2.1 (c), the contained flux will remain inside the perfect conductor, Figure 2.1 (d). Experimental results show that the magnetic flux is expelled from the superconductor when it is cooled in the presence of a magnetic field. This flux expulsion is called the Meissner effect. The inductive nature of the superconductor is modeled, but penetration into the material is a problem as it will become infinitely small as the material becomes perfectly conductive, which is physically impossible.

The MQS and EQS equations can not be refined enough to include flux expulsion or penetration depth, so a conductor with the resistance approaching nil can not be used.

2.3 London Equations

One of the first real attempts to understand superconducting materials was made by the London brothers [13]. The London equations describe the function of simplistic (bulk) superconducting materials by adapting electron movement to all of the observable of the phenomena of the superconductor.

The first London equation is derived from classical Newtonian motion, electrodynamics and the Drude's model for ohmic conductors. This equation describes the movement of electrons in a perfect conductor at a microscopic level. It was found that direct interaction between the electrons must be expressly ignored to yield results, whereas in the MQM model (Section 2.6) the interaction of electrons

is what results in superconductivity. The resulting equation is a modification of Ohm's law and is known as the first London equation, where the electric field intensity, $\mathbf{E}$, is

$$\mathbf{E} = \frac{\partial}{\partial t}\left(\Lambda \mathbf{J}\right), \tag{2.3.1}$$

where $\mathbf{J}$ is the current density and Λ represents the inertia of the electrons. Λ describes the same function as an inductor, L. With a star (*) indicating superelectron quantity, Λ becomes

$$\Lambda = \frac{m^*}{n^*(q^*)^2}, \tag{2.3.2}$$

where m^*, n^* and q^* are the superelectron mass, the superelectron number density and the negative superelectronic charge, respectively. Inside a uniform, nondispersive material the magnetic field, $\mathbf{H}$, is represented by

$$\left(\frac{\mu_0}{\Lambda} - \nabla^2\right)\frac{\partial}{\partial t}\mathbf{H} = 0, \tag{2.3.3}$$

with a penetration depth, λ, independent of frequency

$$\lambda = \sqrt{\frac{\Lambda}{\mu_0}}. \tag{2.3.4}$$

The behaviour of a perfect conductor using these equations can be examined by placing it inside a uniform magnetic field, assuming that the conductor becomes a perfect conductor for temperatures below T_c. In Figure 2.1 (a) the material is cooled into a perfect conducting state without any externally applied magnetic fields. A uniform magnetic field is then applied, Figure 2.1 (b), and as a result the conductor prevents any magnetic flux from penetrating. If however the conductor is cooled in the presence of the magnetic field, Figure 2.1 (c), the contained flux will remain, Figure 2.1 (d). The results are the same as with the theoretical model in Section 2.2. The main difference in this model is the inclusion of penetration depth while the inductive nature of the superconductor is maintained. Fortunately this model can be improved to include a very important (bulk) effect, the expulsion of magnetic flux from a superconductor, also known as the Meissner effect..

To improve the London model, the penetration depth, λ, of the first London equation is combined with the Meissner effect observed in superconductors. The second London equation

$$\nabla \times (\Lambda \mathbf{J}) = -\mathbf{B} = -\mu_0 \mathbf{H}, \tag{2.3.5}$$

is combined with London I (2.3.1) to form

$$\nabla \times \frac{\partial}{\partial t}\left(\Lambda \mathbf{J}\right) = -\frac{\partial \mathbf{B}}{\partial t} = -\mu_0 \frac{\partial \mathbf{H}}{\partial t}, \tag{2.3.6}$$

where $\mathbf{B}$ is the magnetic flux density.

The behaviour of a perfect conductor with flux expulsion using these equations can be examined by theoretically placing it inside a uniform magnetic field. It is assumed that the conductor becomes a perfect conductor for temperatures below T_c. In Figure 2.2 (a) the material is cooled into a perfect conducting state without any externally applied magnetic fields. A uniform magnetic field is then applied, Figure 2.1 (b), and as a result the conductor prevents any magnetic flux from penetrating. If the conductor is cooled in the presence of the magnetic field, Figure 2.2 (c), the contained flux is expelled, Figure 2.2 (c), as in 2.1 (b). This model includes the inductive nature of the superconductor, penetration depth and flux expulsion.

The London model is a good approximation of what is known to happen to superconductors when

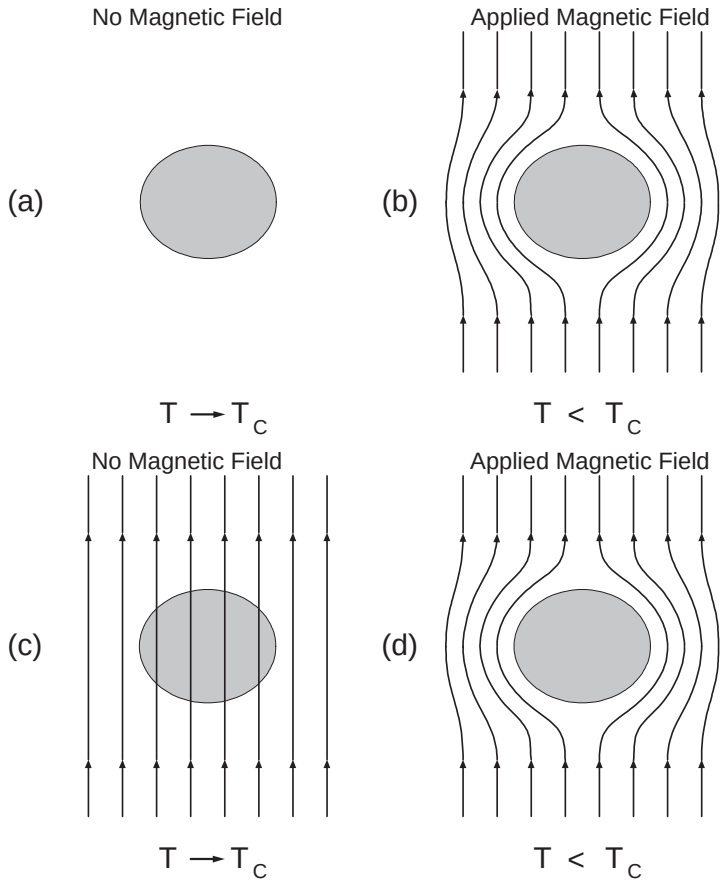

Figure 2.2: Effect of a uniform magnetic field on a superconductor.

they are cooled below T_c. This model does not describe the Josephson quantum effects, but for simpler devices such as transformers, inductors and wires this model is adequate and relatively easy to use. The influence of temperature, current and large applied magnetic fields on superconductivity must also be examined. For the effect of current and temperature on superconductors the two-fluid model in Section 2.4 can be used. Section 2.5 examines the critical magnetic field, describing the effect of a large magnetic field on a superconductor. The superconductor is either of type I or type II, depending on how the material will transition from a superconductor into a normal conductor with the application of a large magnetic field. A type I superconductor will transition sharply into normal conductivity, while a type II will first transition into an intermediate state before transitioning into normal conductivity.

2.4 Two-Fluid Model

Superconductors exhibit their unique properties only when cooled below a certain temperature, known as the critical temperature, T_c. The various theories state that a supercurrent forms due to electrons pairing up into superelectrons, forming Cooper-pairs that flow without experiencing any resistance. When the temperature drops below T_c all of the electrons do not suddenly transform into Cooper pairs, but follow a nonlinear curve defined by the ambient temperature (T).

The ability of electrons to pair up into Cooper pairs probably occurs when the thermal vibration inside a lattice falls below a certain threshold at T_c, causing the electrons not to disperse but to pair up, effectively flowing without resistance along the lattice. As the temperature drops below T_c the atomic vibration is further reduced, resulting in more Cooper pairs being able to form. If electrons truly pair, or if there is an unknown interaction between some of the material's atoms and electrons is open to

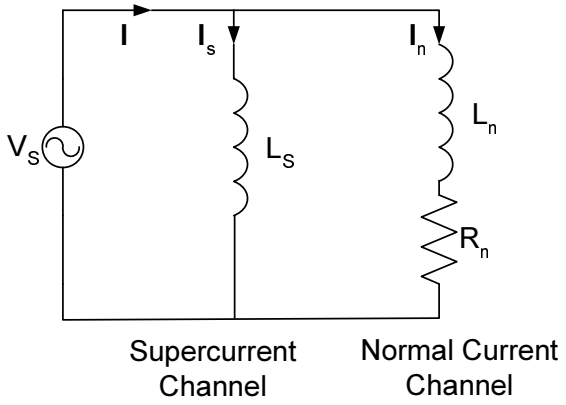

Figure 2.3: Separated current channels in a superconductor.

interpretation, but the Cooper pair formation hypothesis works adequately.

The two-fluid model works by mathematically separating the superelectrons from the normal electrons inside the superconductor, and assigning each to a distinctly separate conductive channel as shown in Figure 2.3 [13]. The superelectrons form the supercurrent in the superconductive channel, and can be modeled by using an inductor indicating the inertia, L_s. The normal (unpaired) electrons form a normal current in the normal channel, and can be modeled by using an inductor indicating the inertia, L_n, coupled with a series resistor indicating dispersion, R_n. As these two channels operate inside the same conductor, the normal channel is shunted to the superconducting channel and the total current density, $\mathbf{J}$, becomes

$$\mathbf{J} = \mathbf{J}_s + \mathbf{J}_n, \tag{2.4.1}$$

where $\mathbf{J}_s$ represent the supercurrent density and $\mathbf{J}_n$ the normal current density inside a superconductor. To find a correlation between temperature and the critical current density, the penetration depth, λ, in (2.3.4) is transformed into a function of temperature

$$\lambda(T) = \frac{\lambda_0}{\sqrt{1 - \left(\frac{T}{T_c}\right)^4}} \quad \text{for} \quad T \leq T_c, \tag{2.4.2}$$

where T is the absolute temperature, T_c is the critical temperature and λ_0 is the penetration depth at 0 K. The penetration depth (2.3.4) for type II superconductors can be rewritten as

$$\lambda_0 = \sqrt{\frac{\Phi_0}{H_{cl,0}}}, \tag{2.4.3}$$

where $H_{cl,0}$ is the lower critical magnetic field at 0 K and Φ_0 is a single magnetic flux quantum. If penetration depth of mercury at 0 K is defined an arbitrary value of unity, $\lambda_0 = 1$, then the temperature dependent penetration depth is given by the solid line in Figure 2.4(a). As the temperature rises above 0 K the penetration depth increases exponentially, implying that the material is becoming less superconductive. The resistance of mercury is shown in Figure 2.4(b), with a sudden drop in resistance at 4.22 K indicating the transition from a normal conductor into superconductor.

Maximum Cooper pair density, and thus the critical current density, J_c, is a function of temperature. Cooper pairing only occurs below the critical temperature, and as the temperature drops below T_c the maximum Cooper pair density rises. Modifying the London I (2.3.1) to include temperature dependence results in

$$\mathbf{E} = \frac{\partial}{\partial t}\left(\Lambda(T)\mathbf{J_s}\right) \quad \text{for} \quad T \leq T_c, \tag{2.4.4}$$

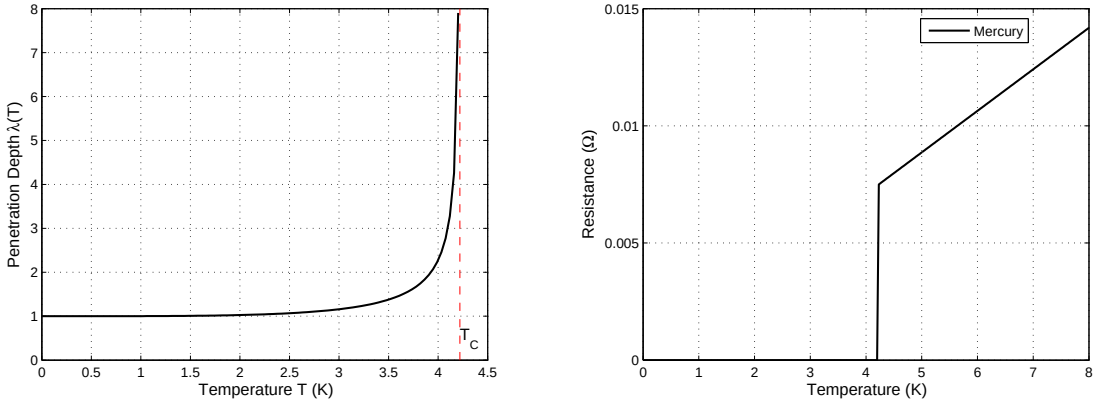

(a) (b)

Figure 2.4: (a) $\lambda(T)$ penetration depth of mercury with a T_c of 4.22 K and (b) the transition from a normal conductor into a superconductor.

where $\Lambda(T)$ represents the temperature dependence

$$\Lambda(T) = \frac{m^*}{n_0^*(q^*)^2}\left(\frac{1}{1-\left(\frac{T}{T_c}\right)^4}\right) = \frac{m}{n_{tot}e^2}\left(\frac{1}{1-\left(\frac{T}{T_c}\right)^4}\right) \quad \text{for} \quad T \leq T_c, \tag{2.4.5}$$

where m^* is the superelectron mass, n^* is the superelectron number density, q^* is the negative superelectronic charge, m is the electron mass, n is the electron number density and e is the negative electronic charge. To explain the temperature dependence of the Cooper pair density in (2.4.5), the distribution of electrons inside the material must be considered. If the maximum amount of electrons in a medium is n_{tot}, and the absolute maximum amount of Cooper pairs (superelectrons) is n_0^*, it is a given that the absolute maximum number of superelectrons at 0 K is

$$n_0^* = \frac{n_{tot}}{2}, \tag{2.4.6}$$

as there are two electrons per Cooper pair and there are no unpaired electrons left. The ratio of electrons to superelectrons is given by

$$n_{tot} = 2n^*(T) + n(T). \tag{2.4.7}$$

The amount of superelectrons for temperatures below T_C can be calculated by using

$$n^*(T) = \frac{n_{tot}}{2}\left(1-\left(\frac{T}{T_c}\right)^4\right) \quad \text{for} \quad T \leq T_c. \tag{2.4.8}$$

The temperature dependent normal current density is

$$\mathbf{J_n} = \frac{\tilde{\sigma}_0(T)}{1+j\omega\tau_{tr}}\mathbf{E} \quad \text{for} \quad T \leq T_c, \tag{2.4.9}$$

where τ_{tr} is the characteristic time of the material (scattering time), and $\tilde{\sigma}_0(T)$ is the temperature dependent frequency independent conductivity quantity

$$\tilde{\sigma}_0(T) = \frac{n_{tot}e^2\tau_{tr}}{m}\left(\frac{T}{T_c}\right)^4 \quad \text{for} \quad T \leq T_c, \tag{2.4.10}$$

showing that the dc conductivity of the normal channel is temperature dependent for $T<T_c$. The electrons not forming part of the normal conductive channel become part of the superconductive channel, resulting in the expression (2.4.5). The temperature dependent supercurrent density (2.4.4) can be expressed in a more convenient form

$$\mathbf{J_s} = \frac{1}{j\omega\mu_0 \left(\lambda(T)\right)^2}\mathbf{E} \quad \text{for} \quad T \leq T_c. \tag{2.4.11}$$

The superconductor can be divided into two distinct conducting channels, the superconducting channel and the normal conducting channel. When the current in the superconducting channel exceeds the critical current, overloading the available superelectrons, the remaining current will start to flow through the normal channel. The RCSJ and RSJ models (Section 2.8.2 and 2.8.4) use this two-fluid model to help explain the operation of Josephson junctions.

2.5 Critical Magnetic Field

In the Two-Fluid model the effect of temperature on the transition into superconductivity and the supercurrent was discussed. In this section the effect of a magnetic field is taken into account as it can affect the superconductivity and temperature where the transition occurs. The critical temperature and the magnetic field both contribute to the thermal level below which materials exhibit superconductivity.

There is a critical magnetic field strength above which the superconductor saturates and returns to the normal conductive state [13, 1, 14]. For type I superconductors the transition from a superconductive to a normal state occurs suddenly when the increasing magnetic field rises above the critical magnetic field, H_c. There are two distinct states that the material can be in. The first state is the superconductive state where all the magnetic flux is expelled. The second state is the normal conductive state where the magnetic flux permeates the material and the superconductivity is destroyed. Type I materials are usually pure metals such as Niobium (Nb) or Mercury (Hg) and exhibit isotropic behaviour.

For type II superconductors there are three distinct states, two superconductive and one normal state. The first state is the superconductive state where all the magnetic flux is expelled. This occurs for magnetic fields less than the lower critical magnetic field, H_{cl}. The second state occurs above the lower critical magnetic field, H_{cl}, and below the upper critical magnetic field, H_{cu}. Additional flux penetrates the superconductor, causing vortices to form in the material. As the magnetic field rises above H_{cl}, the amount of vortices increase until the material saturates at the upper critical magnetic field, H_{cu}. The material then transitions into the third state, normal conductivity.

While the transition from the first to the second superconductive state involves small field strengths, the transition into normal conductive state requires significantly larger magnetic fields. For YBCO the upper critical magnetic field is estimated to be above 100 T in the c-axis and above 600 T in the $Cu - O_2$ planes. The difference is due to the anisotropic nature of high-T_c superconductors described in Section 4.2.

Most superconducting devices operate within relatively small magnetic fields, or have shielding to isolate them from external magnetic fields. SQUID magnetometers have sensitivities in the nano-Tesla range, nT, and are usually not subjected to fields large enough to destroy superconductivity. Gradiometers used in MRI devices that operate with large magnetic fields are exceptions, but they will not be discussed in this thesis. For the scope of this thesis the superconducting material that the SQUID is composed of is only subjected to magnetic fields far below the upper critical magnetic field, $H_{applied} << H_{cu}$.

2.6 Macroscopic Quantum Model

The microscopic quantum model theory, describing why classical low-temperature superconductors work, was created by John Bardeen, Leon Cooper and Robert Schrieffer, and is called the BCS theory [12]

in honor of its creators. The macroscopic quantum model (MQM) theory is based on the macroscopic effect of the microscopic quantum probability of matter. The BCS theory combines to form the London equations in addition to macroscopic quantum effects that can not be explained using the classical models.

The MQM is based on probability theory where the position of a single electron, defined a a quantum particle, is fundamentally unknown and is considered a random variable. Probability theorem states that the positional error is reduced when the probability set increases to including more electrons. While the position of a single electron is theoretically impossible to pin down, the collective effect of all the electrons in a large structure can be predicted, so the net movement of the current can be predicted. On a quantum level an electron can be modeled as a particle, and at a macroscopic scale the electrons collectively can be modeled as waves. This duality is called the wave-particle duality, giving rise to the Josephson Tunneling effect. Flux expulsion is the only macroscopically visible proof that the quantum model works.

To convert the classical equations into wave-particle equations, the *Einstein-de Broglie Relations*, Dirac's version of Planck's constant is first defined as

$$\hbar = \frac{h}{2\pi}, \tag{2.6.1}$$

where $h = 6.6262 \times 10^{-34}$ J-sec is Planck's constant. The total energy of the quantum particle, ε, is

$$\varepsilon = \hbar\omega, \tag{2.6.2}$$

where ω is the frequency of oscillation. The momentum of the quantum particle, $\mathbf{p}$, is a 'quantum-mechanical momentum' that can be used in the Hamiltonian function, and is defined as

$$\mathbf{p} = \hbar\mathbf{k}, \tag{2.6.3}$$

where $\mathbf{k}$ is the wavevector and is related to the wavelength, λ, by

$$|\mathbf{k}| = \frac{2\pi}{\lambda}. \tag{2.6.4}$$

The probability, $\wp$, of a particle being at a certain place, $\mathbf{r}$, at a certain time, t, is

$$\wp(\mathbf{r}, t) \equiv |\psi(\mathbf{r}, t)|^2 \equiv \psi^*(\mathbf{r}, t)\,\psi(\mathbf{r}, t), \tag{2.6.5}$$

where ψ is the uniform plane wave. Since the particle exists, the probability of that particle being somewhere inside infinite space is guaranteed. Integrating the uniform plane wave, ψ, gives the probability of a single quantum particle existing in infinite space

$$\|\psi(\mathbf{r}, t)\| = \int \wp(\mathbf{r}, t)\, dv = \int \psi(\mathbf{r}, t)\,\psi^*(\mathbf{r}, t)\, dv = 1. \tag{2.6.6}$$

The uniform plane wave, ψ, is the key for combining quantum functions with wavevectors and is defined as

$$\psi = \widehat{\psi} e^{i(\mathbf{k}\cdot r - \omega t)}, \tag{2.6.7}$$

where $\mathbf{k}$ is the wavevector and i is represents imaginary number $\sqrt{-1}$.

The quantum Hamiltonian, $\mathcal{H}$, is used to convert classical equations into quantum mechanical equations and represents the total energy in a system [15]. Using a single Newtonian particle with mass m

under the influence of an external potential energy vector, $\mathbf{V}(\mathbf{r},t)$, the Hamiltonian is given by

$$\mathcal{H} = \frac{\hbar^2}{2m}\nabla^2 + \mathbf{V}(\mathbf{r},t). \tag{2.6.8}$$

Schrödinger's equation for a free particle is obtained by applying the uniform plane wave to both sides of the Hamiltonian equation. Adding the wavevector to the quantum particle results in

$$\mathcal{H}\psi = i\hbar\frac{\partial\psi}{\partial t} = -\frac{\hbar^2}{2m}\nabla^2\psi + \mathbf{V}(\mathbf{r},t)\,\psi, \tag{2.6.9}$$

describing the evolution of a wave-particle in space and time. The potential vector applied onto the particle is defined as $\mathbf{V}(\mathbf{r},t)$. The *probability current*, $\mathbf{J}_\wp$, of a quantum particle at a certain point and time under the influence of an applied magnetic field becomes

$$\mathbf{J}_\wp = \mathrm{Re}\left\{\psi^*\left(\frac{\hbar}{im}\nabla - \frac{q}{m}\mathbf{A}(\mathbf{r},t)\right)\psi\right\}, \tag{2.6.10}$$

where $\mathbf{A}(\mathbf{r},t)$ is a vector potential of the applied magnetic field, representing the external potential energy function $\mathbf{V}(\mathbf{r},t)$.

Moving up from single quantum probability to a macroscopic quantum probability encompassing multiple particles, the uniform plane wave, ψ, in (2.6.5) becomes the collective wavefunction Ψ, where

$$\Psi^*(\mathbf{r},t)\,\Psi(\mathbf{r},t) = n^*(\mathbf{r},t), \tag{2.6.11}$$

with n^* describing density of superelectrons in a localized area. Integrating the collective wavefunction over infinite space gives the total amount of superelectrons

$$\int \Psi^*(\mathbf{r},t)\,\Psi(\mathbf{r},t)\,dv = n^*_{tot}. \tag{2.6.12}$$

The collective wavefunction is defined as

$$\Psi(\mathbf{r},t) = \sqrt{n^*(\mathbf{r},t)}e^{i\theta(\mathbf{r},t)}, \tag{2.6.13}$$

where θ is the phase of the complex number $i = \sqrt{-1}$. The macroscopic form of the probability current of a quantum particle, $\mathbf{J}_\wp$, becomes the supercurrent density

$$\mathbf{J}_s = q^*\mathrm{Re}\left\{\Psi^*\left(\frac{\hbar}{im^*}\nabla - \frac{q^*}{m^*}\mathbf{A}(\mathbf{r},t)\right)\Psi\right\}. \tag{2.6.14}$$

The supercurrent density reduces to a more useable function by combining (2.6.14) with (2.6.13) into

$$\mathbf{J}_s = q^*n^*(\mathbf{r},t)\left(\frac{\hbar}{m^*}\nabla\theta(\mathbf{r},t) - \frac{q^*}{m^*}\mathbf{A}(\mathbf{r},t)\right) \tag{2.6.15}$$

$$\Lambda\mathbf{J}_s = -\left(\mathbf{A}(\mathbf{r},t) - \frac{\hbar}{q^*}\nabla\theta(\mathbf{r},t)\right). \tag{2.6.16}$$

The curl of (2.6.16) results in the same equation given by London II 2.3.5

$$\nabla\times(\Lambda\mathbf{J_s}) = -\mathbf{B}. \tag{2.6.17}$$

Similarly, the London I can also be obtained by using the MQM. Thus there is a correlation between the more classical approach and the quantum approach to superconductivity.

There are now two fundamentally different approaches to modeling superconductors, with each model resulting in the same fundamental equations.

2.7 Energy Gap

In weakly coupled superconductors there is a low-energy excitation gap. An external energy source of greater than twice the energy gap, 2Δ, is required for creating an electron-hole pairing at the Fermi surface [1]. The external energy can be thermal or electric. The Cooper pair electrons are bound together with the binding energy given by 2Δ, and each electron requires an energy of at least Δ to separate. As a consequence the normal electrons in a superconductor contain at least Δ more energy than their equivalent in a normal conductor. This energy gap at 0 K for YBCO is given by

$$\Delta(0) \equiv \Delta_0 = 3.52\frac{k_B T_c}{2} \approx k_B T, \tag{2.7.1}$$

where k_b is the Boltzman constant and T_c the transition temperature of the material. The energy gap-to-transition temperature ratio, $2\Delta(0)/k_B T_c$, is higher in high-T_c superconductors than in low-T_c superconductors. This ratio is subject to anisotropy in type II low-T_c superconductors.

When the current flowing through the energy gap of a junction is slightly greater than I_c at 0 K, then a steady-state voltage will develop

$$V = \frac{2\Delta_0}{e}, \tag{2.7.2}$$

where Δ_0 is the energy gap for the junction at 0 K and e is the charge of an electron.

2.8 Josephson Junction

2.8.1 Basic Josephson Junction

The Josephson junction (JJ) is one of the two elements used to convert flux into voltage. The junction usually consists of a superconductor-normal-superconductor (SNS) interface or a superconductor-insulator-superconductor (SIS) interface, two weakly coupled superconducting electrodes. Through the effect of Cooper-pairing as described by quantum theory, electrons will pair up and tunnel through the junction's barrier. If the current flowing through the barrier remains below a critical current I_c, then all of the electrons will pair up into Cooper-pairs and tunnel through the barrier as a supercurrent. A dc supercurrent will experience no resistance as it traverses the material, flowing through what is known as the superconducting channel and comprising solely out of Cooper-pairs. The junction will sustain this superconducting behaviour until the critical current I_c is exceeded. When the current through the junction rises above the critical current, the current exceeding I_c is forced to flow through the barrier using other conductive channels. The superconducting channel becomes saturated and the additional electrons are forced to flow through a normal channel, similar to the Two-Fluid model (Section 2.4). This causes a potential to develop across the barrier, giving rise to the unique behaviour of the Josephson junction. In this model the normal conductor is considered to be an insulator, so the SNS interface is used throughout.

The superconducting channel can only be described using the Macroscopic Quantum Model (MQM). When taking the SNS junction, as seen in Figure 2.5, (2.6.15) is used to describe the supercurrent through the junction. At the boundary interface ($\pm a$) with no external magnetic field applied, the supercurrent reduces to

$$\mathbf{J}_s(\pm a, t) = \mathbf{J}_0, \tag{2.8.1}$$

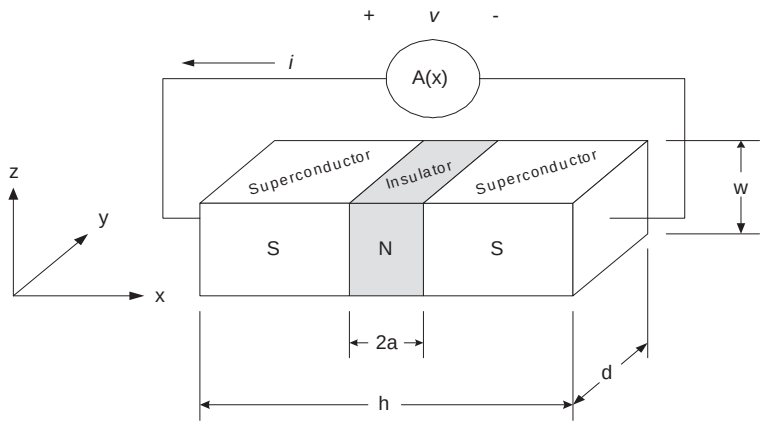

Figure 2.5: Superconductor-Normal-Superconductor (SNS) Josephson junction.

and the phase of the wavevector is

$$\frac{\partial}{\partial t}\theta\left(\pm a,t\right)=-\frac{\mathcal{E}_0}{\hbar}, \tag{2.8.2}$$

where $\mathcal{E}_0 = m^* v_s^2/2$ is the constant kinetic energy of a superelectron with mass m^* and velocity v_s. Inside the insulator the supercurrent reduces to

$$\mathbf{J}_s = \mathbf{J}_c \sin\left(\theta_1 - \theta_2\right) \tag{2.8.3}$$

when the applied potential exceeds the kinetic energy, $\mathbf{V}(x) > \mathcal{E}_0$. $\mathbf{J}_c$ The phases θ_1 and θ_2 are the phases at the respective interfaces, defining the wavefunctions (2.6.13) at the boundaries as

$$\Psi(-a) = \sqrt{n_1^*}e^{i\theta_1} \tag{2.8.4}$$

$$\Psi(+a) = \sqrt{n_2^*}e^{i\theta_2}, \tag{2.8.5}$$

where $\sqrt{n_x^*}$ is the magnitude of the wavefunction, n^* is the density of the superelectrons in a localized area and $i = \sqrt{-1}$ is the complex number of the exponent e. The critical current density of the junction, $\mathbf{J}_c$, has a magnitude defined as

$$\mathrm{J}_c = \frac{q^*\hbar}{m^*\zeta}\frac{\sqrt{n_1^* n_2^*}}{2\sinh\left(\frac{a}{\zeta}\right)\cosh\left(\frac{a}{\zeta}\right)} = \frac{e\hbar\sqrt{n_1 n_2}}{2m\zeta\sinh\left(\frac{2a}{\zeta}\right)}. \tag{2.8.6}$$

When a magnetic vector potential $\mathbf{A}\left(\mathbf{r},t\right)$ is applied to the junction, a phase difference will start to develop between the respective phases of the wavevectors across the junction. This is called the *gauge-invariant phase difference*, φ, where

$$\varphi\left(y,z,t\right) = \theta_1\left(y,z,t\right) - \theta_2\left(y,z,t\right) - \frac{2\pi}{\Phi_0}\int_1^2 \mathbf{A}\left(\mathbf{r},t\right)\cdot d\mathbf{l}. \tag{2.8.7}$$

When the junction is generalized into a one-dimensional, time variant system, the current through the junction, i, simplifies into

$$i = I_c \sin\varphi, \tag{2.8.8}$$

where the time differential gauge-invariant phase difference, φ, is

$$\frac{d\varphi}{dt} = \frac{2e}{\hbar}v = \frac{2\pi}{\Phi_0}v, \tag{2.8.9}$$

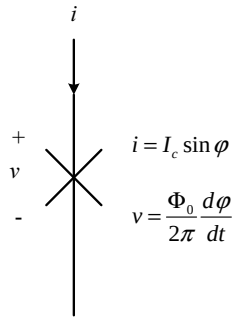

Figure 2.6: Schematic representation of a basic Josephson junction.

where Φ_0 is a single magnetic flux quantum and v is the potential across the junction. If the phase φ remains between $\pm\pi/2$ then only the supercurrent will flow through the junction and no potential is generated across the junction. This only occurs while the current is restricted to $|i| \leq I_c$. If the current exceeds I_c then the phase slips, with φ evolving with time t according to

$$v = \frac{\Phi_0}{2\pi}\frac{d\varphi}{dt}, \tag{2.8.10}$$

generating a potential, v, across the junction. A schematic representation of a basic Josephson junction is shown in Figure 2.6. The initial potential will be a steady-state $2\Delta_0/e$ (2.7.2) when the current is slightly higher than I_c at 0 K. The phase slips at a rate that is proportional to the voltage.

If a potential, $v(t)$, is applied across the junction, then the gauge-invariant phase difference will evolve with time according to (2.8.9). For a constant (dc) applied voltage, V_0, (2.8.9) is integrated over time to give the time-variant gauge-invariant phase difference,

$$\varphi(t) = \varphi(0) + \frac{2\pi}{\Phi_0}V_0 t, \tag{2.8.11}$$

where the initial phase is $\varphi(0)$. There is a linear relationship between φ and the applied voltage. The current-phase relationship (2.8.8) for a dc potential is

$$i = I_c \sin\left(\frac{2\pi}{\Phi_0}V_0 t + \varphi(0)\right) = I_c \sin\left(2\pi f_J t + \varphi(0)\right), \tag{2.8.12}$$

and is known as the *ac Josephson effect*. The frequency of the Josephson junction, the Josephson frequency f_J, is

$$f_J = \frac{V_0}{\Phi_0} = \frac{2e}{\hbar}V = 483.60 \times 10^{12} V_0 \quad \text{(Hz)}, \tag{2.8.13}$$

and is a function of the phase slip (2.8.10). It is apparent that the current through a Josephson junction will oscillate at exactly 483.60 MHz per μV_{DC} applied, irrespective of the critical current or any other junction parameter. The Josephson frequency is used to define the voltage standard, since measuring the current's frequency is more accurate than other available technique.

The energy in a junction, W_J, is the integral of the current and potential over time,

$$W_J = \int_0^{t_0} ivdt \tag{2.8.14}$$

$$= W_{J_0} - \frac{\Phi_0 I_c}{2\pi}\cos\varphi, \tag{2.8.15}$$

where the initial energy in the junction is the constant W_{J_0} and is given by

$$W_{J_0} = \frac{\Phi_0 I_c}{2\pi}. \tag{2.8.16}$$

With no applied current, the Josephson coupling energy for the two electrodes is $E_J = W_{J_0} = \Phi_0 I_c/2\pi$.

The basic junction only describes the Josephson tunneling effect, ignoring secondary junction effects such as capacitance and shunt resistance. These secondary effects alter the behaviour of an actual junction so significantly that the basic Josephson junction alone is not suitable for simulations or additional theoretical work.

2.8.2 RCSJ Model

The standard junction model used in simulation to describe the effect of the Josephson junction is the resistively- and capacitively-shunted junction (RCSJ). This model uses the superconducting channel in conjunction with a resistive channel, R_n, and a capacitive channel, C. The *Stewart-McCumber parameter* (2.8.28) describes the damping of the junction and the hysteresis of the junction. When using low-T_c multilayer junctions, there is usually a significant amount of intrinsic capacitance and the RCSJ model is applicable, and these junctions must be analyzed. The high-T_c single layer junctions made with step-edge or grain boundaries have negligible small capacitance and are considered to be resistively-shunted junctions, RSJ.

The basic junction only describes the current (2.8.8) and phase (2.8.9) of the junction due to the Josephson tunneling effect, ignoring secondary junction effects such as capacitance and shunt resistance. These secondary effects alter the behaviour of an actual junction so significantly that the basic Josephson junction alone is not suitable for simulations or additional theoretical work. The two-fluid model (2.4.1) indicates that a superconductor can contain both a superconducting channel and a normal channel, with their respective currents flowing in parallel. For the Josephson junction the two-fluid model is modified to include a third channel, the capacitive channel. The model uses the superconducting channel to describe the supercurrent through a basic junction, while the normal channel is split into a resistive channel and a capacitive channel.

The conductance through the normal channel, σ_n, can be derived from (2.4.9) and (2.4.10) as

$$\sigma_n(\omega) = \frac{ne^2}{m}\left(\frac{\tau_{tr}}{j\omega\tau_{tr}+1}\right). \tag{2.8.17}$$

At steady-state (dc) the conductance reduces to

$$\sigma_n(\omega = 0) = \frac{ne^2\tau_{tr}}{m}, \tag{2.8.18}$$

depicting the conductance of the junction's normal shunt resistance. The normal conductance for the entire junction, G_n, is thus

$$G_n(\omega = 0) = \frac{1}{R_n} = \frac{2\pi I_c \tau_i}{\Phi_0}, \tag{2.8.19}$$

where R_n is the normal shunt resistance of the junction. The relation of the critical current, I_c, to the normal shunt resistance, R_n, at 0 K is

$$V_c \equiv I_c R_n = \frac{\Phi_0}{2\pi\tau_i}, \tag{2.8.20}$$

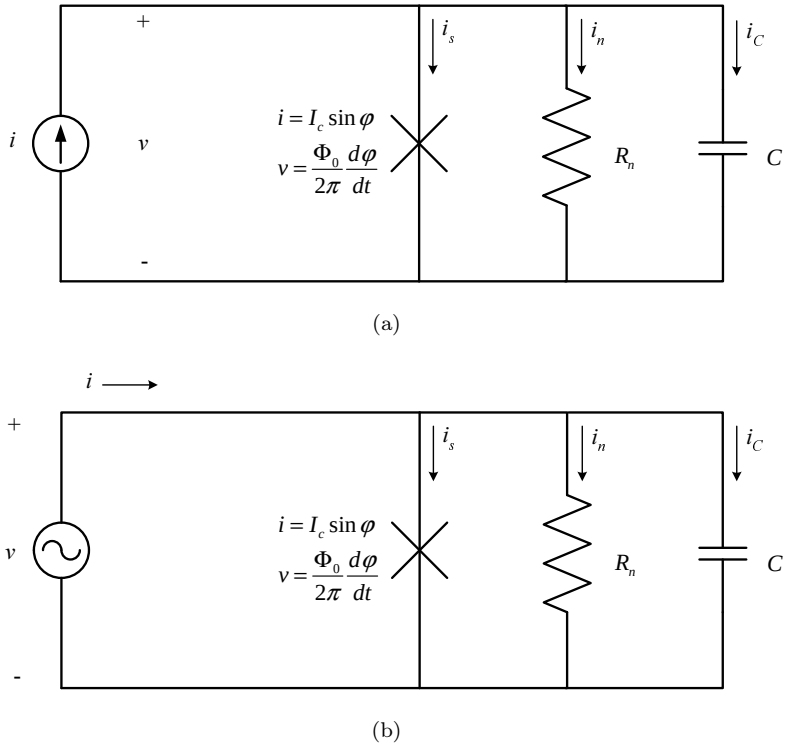

Figure 2.7: Schematic representation of a resistively- and capacitively-shunted Josephson junction for (a) a current input source i with a voltage response v, and (b) a voltage input source v with a current response i.

where τ_i is the characteristic drag time for the junction,

$$\tau_i = \frac{\hbar}{\pi\Delta_0}, \tag{2.8.21}$$

and where Δ_0 is the energy gap (2.7.1). The critical current, I_c, and the normal shunt resistance, R_n, are inversely proportionate to each other at 0 K. The characteristic voltage $V_c \equiv I_c R_n$ plays an important role in evaluating the performance of various junctions and SQUIDs.

The capacitive channel is due to the parallel plate capacitor effect. When the junction is composed of two structurally large plates separated by an insulator, as in Figure 2.5, the resulting capacitance is

$$C = \frac{\epsilon A}{2a}, \tag{2.8.22}$$

where $A = \text{wd}$ is the area of the superconducting plates at the interface of the SNS junction, $2a$ is the thickness of the junction or insulating layer, and ϵ is the dielectric constant.

The revised model for the Josephson junction is known as the *resistively- and capacitively-shunted junction* (RCSJ), incorporating the basic Josephson junction with a shunt resistor and a shunt capacitor (Figure 2.7). In the revised model the superconductive channel flows alongside the normal conductive and the capacitive channels inside the same material, resulting in a more realistic representation of a practical JJ. For the RCSJ the total current through the junction, i, is

$$i = I_c \sin\varphi + vG_n(v) + C\frac{dv}{dt}, \tag{2.8.23}$$

which can be combined with the voltage-phase relation (2.8.9) to give

$$i = I_c \sin\varphi + \frac{d\varphi}{dt}\frac{\Phi_0}{2\pi}G_n(v) + \frac{d^2\varphi}{dt^2}\frac{\Phi_0}{2\pi}C \tag{2.8.24}$$

$$= I_c \sin\varphi + \frac{d\varphi}{dt}\frac{\Phi_0}{2\pi}\frac{1}{R_n} + \frac{d^2\varphi}{dt^2}\frac{\Phi_0}{2\pi}C. \tag{2.8.25}$$

There are two time-constants that can be extracted from this equation. The first is the RC time-constant,

$$\tau_{RC} = R_n C, \tag{2.8.26}$$

and the second is the junction time-constant,

$$\tau_J = \frac{1}{2\pi f_J} = \frac{\Phi_0}{2\pi}\frac{1}{I_c R_n}, \tag{2.8.27}$$

where f_J is the frequency of the Josephson junction (2.8.13). The ratio between these constants is known as the *Stewart-McCumber parameter*, where

$$\beta_c = \frac{\tau_{RC}}{\tau_J} \tag{2.8.28}$$

$$= \frac{2\pi}{\Phi_0}\left(I_c R_n^2 C\right), \tag{2.8.29}$$

describing the damping on the junction and indicating the possibility of hysteresis occurring.

In SQUID designs the effect of the hysteresis can cause the working point of the system to be undefinable, as it could reside anywhere on the junction's rising of falling edge in Figure 2.11 and 2.12, making it difficult to to design and operate such a system. The effect of hysteresis on the sensor is examined in [16], showing how it adversely affects system performance.

The damping parameter usually causes the junction to be in one of three configurations, as a strongly overdamped system with $\beta_c << 1$, as a critically-damped system with $\beta_c \approx 1$, or as a strongly underdamped system with $\beta_c >> 1$. Damping affects the current-voltage relation (I-V) of the junction.

2.8.3 Overdamped Josephson Junction (RSJ)

A strongly overdamped Josephson junction occurs when the *Stewart-McCumber parameter* is very small, given as $\beta_c << 1$. This could occur when either the shunt resistance, R_n, or capacitance, C, of the junction is zero, but in an actual junction there must always be a finite shunt resistance. The strongly overdamped Josephson is also known as the resistively-shunted junction (RSJ) with a schematic representation shown in Figure 2.8. In (2.8.21) it is shown that even close to 0 K the junction has a shunt resistance, so in the overdamped system the capacitance is considered to be so small that it is removed from (2.8.24), resulting in

$$i = I_c \sin\varphi + \frac{d\varphi}{dt}\frac{\Phi_0}{2\pi}\frac{1}{R_n}. \tag{2.8.30}$$

The dynamic voltage response to a dc current, I, can be expressed in terms of the characteristic voltage, $V_c \equiv I_c R_n$, as

$$v(t) = 0 \quad \text{for} \quad I \le I_C \tag{2.8.31}$$

$$= I_c R_n \frac{\left(\frac{I}{I_c}\right)^2 - 1}{\left(\frac{I}{I_c}\right) + \cos\omega t} \quad \text{for} \quad I > I_C \tag{2.8.32}$$

$$= V_c \frac{i^2 - 1}{i + \cos\omega t} \quad \text{normalized for} \quad I > I_C, \tag{2.8.33}$$

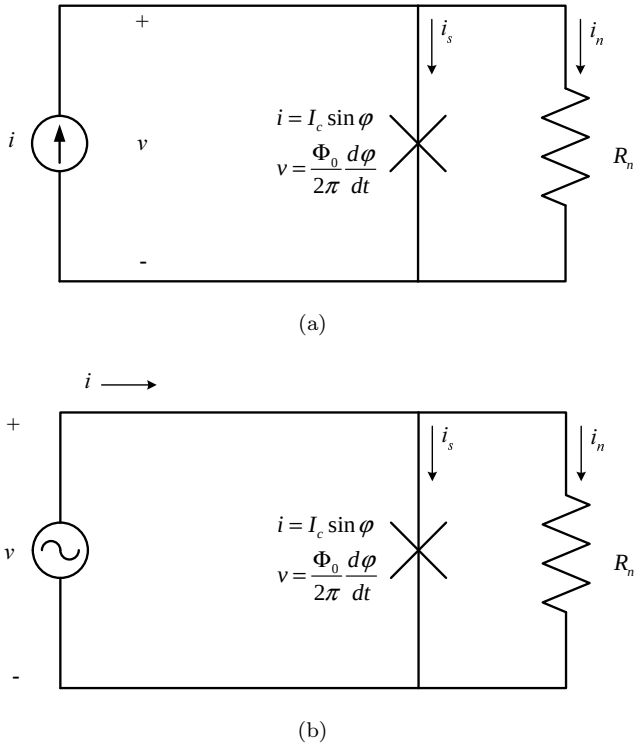

Figure 2.8: Schematic representation of a resistively-shunted Josephson junction for (a) a current input source i with a voltage response v, and (b) a voltage input source v with a current response i.

where $i = I/I_c$ is the normalized current. The voltage, v, oscillates with the frequency

$$\omega = \frac{\left(\frac{I}{I_c}\right)^2 - 1}{\tau_J} = \frac{i^2 - 1}{\tau_J}. \tag{2.8.34}$$

The frequency of the voltage oscillation will increase linearly as the dc current increases, while the peak value stays at the characteristic voltage V_c and the DC voltage increases. The time-average voltage response to a dc current can also be expressed in terms of the characteristic voltage, $V_c \equiv I_c R_n$, as

$$\langle v(t)\rangle = 0 \quad \text{for} \quad I \leq I_C \tag{2.8.35}$$

$$= I_c R_n \sqrt{\left(\frac{I}{I_c}\right)^2 - 1} \quad \text{for} \quad I > I_C \tag{2.8.36}$$

$$= V_c \sqrt{i^2 - 1} \quad \text{normalized for} \quad I > I_C, \tag{2.8.37}$$

shown in Figure 2.9. While $I \leq I_C$ the gauge-invariant phase difference φ evolves, remaining between $\pm\pi/2$, but the potential across the junction remains zero (2.8.35). All of the current will flow through the superconductive channel as shown in (2.4.1, 2.4.11), while no current will flow through the resistive channel. When the current through the junction exceeds the critical current (2.8.36), $I > I_C$, the supercurrent saturates and the remaining current is forced to flow through the resistive channel (2.4.1, 2.4.11, 2.4.9), creating a potential across the junction. The initial potential will be a steady-state $2\Delta_0/e$ (2.7.2) when the current is slightly higher than I_c at 0 K.

The frequency of the voltage across the junction is

$$f = \frac{\langle v(t)\rangle}{\Phi_0}, \tag{2.8.38}$$

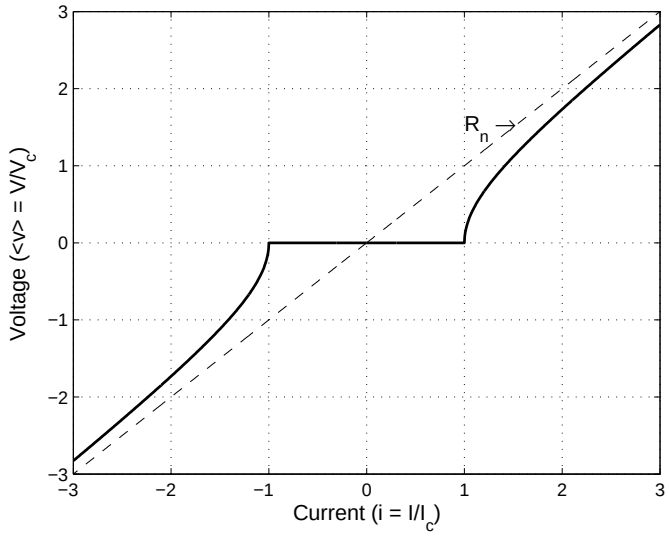

Figure 2.9: Voltage-current characteristic of a overdamped Josephson junction.

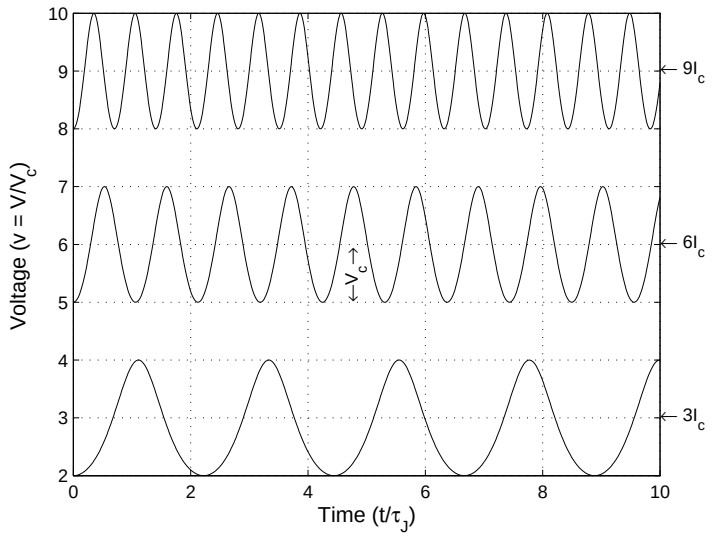

Figure 2.10: Dynamic voltage-current characteristic of a overdamped Josephson junction. The voltage offset and oscillation frequency are proportional to the applied current while the peak-to-peak amplitude is a constant $2V_c$.

with a peak-to-peak amplitude of $V_{ac} = 2V_c = 2I_cR_n$ and an offset voltage $V_0 = V_cI/I_c$, as can be seen in Figure 2.10. As the current through the junction rises above I_c, the majority of the current will be forced to flow through the resistive channel and create an ever increasing dc potential across the junction. This potential causes part of the supercurrent in the superconductive channel to oscillate at the Josephson frequency (2.8.13), reducing the maximum dc supercurrent through the junction. As the maximum dc supercurrent is reduced, more current will be forced to flow through the normal channel, causing the junction to behave increasingly like a resistive component for currents $I > I_c$. When the current is large, $I >> I_C$, most of the current will flow through the resistive channel, resulting in a nearly dc potential across the junction.

In the overdamped system the voltage response of the rising current coincides with that of the falling current, indicating that there is no I-V hysteresis present in the junction. Systems with no hysteresis are preferred in complex SQUID circuits as they generally simplify design and are easy to create using

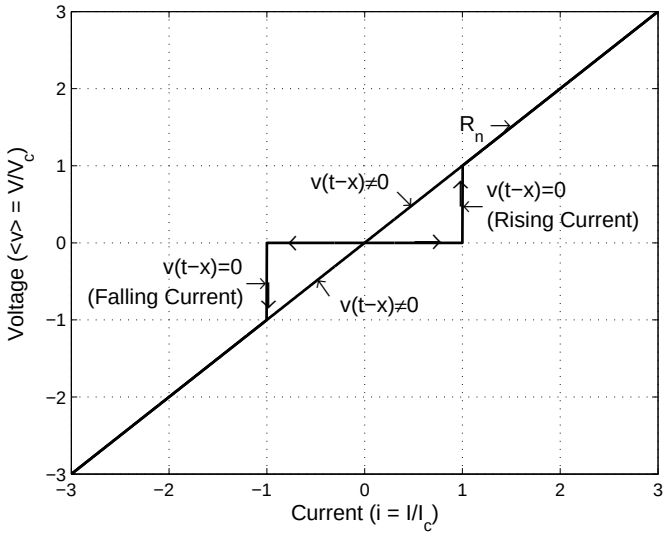

Figure 2.11: Voltage-current characteristic of a underdamped Josephson junction.

high-T_C superconductors. Most high-T_c junctions are intrinsically overdamped, $\beta_c << 1$, as shown in Sections 4.7 to 4.9.

When a constant voltage is applied across the junction, the current through the junction oscillates at 483.60 MHz per μV_{DC} (2.8.13). This oscillation frequency is irrespective of the shunt resistance, shunt capacitance or critical current. The time average current through the junction is simply the voltage divided by the resistance, and the V-I response is a straight line with a slope given by the shunt resistance. There is no V-I hysteresis for any voltage biased junction.

2.8.4 Underdamped Josephson Junction

A strongly underdamped Josephson junction occurs when the *Stewart-McCumber parameter* is very large, given as $\beta_c >> 1$. This occurs when the junction has a larger shunt capacitance, C, and can found in multi-layered devices that have capacitive junction designs. The parallel RC circuit predominates the system, determining the dynamic of the junction. and when a finite current flows through the resistor and causes a potential across the junction, the circuit has a linear DC voltage response for currents smaller than I_c.

In Figure 2.7(a) the dc component of the junction's voltage response to a dc current, I, can now be expressed in terms of the characteristic voltage, $V_c \equiv I_c R_n$, as

$$\langle v(t)\rangle = 0 \quad \text{for} \quad I \leq I_C; \quad \lim_{x\to 0} \langle v(t-x)\rangle = 0 \tag{2.8.39}$$

$$= IR_n \quad \text{for} \quad I > I_C; \quad \lim_{x\to 0} \langle v(t-x)\rangle \neq 0. \tag{2.8.40}$$

From Figure 2.11, with no current flowing through the shunt resistor, the time-average voltage across the junction will remain zero, $\langle v\rangle = 0$, while the current flowing through the junction remains below the critical current $I < I_c$. When the current rises above I_c, a potential develops across the junction, initially switching to $2\Delta/e$ (2.7.2). The system transitions into a linear dc response (2.8.40), only returning to a zero potential when there is no more current flowing through the junction and the RC circuit has dissipated all of its energy. The underdamped junction has a hysteretic response as the current-voltage (I-V) relation depends on the previous state the junction was in.

When a constant voltage is applied across the junction (Figure 2.7(b)), the current through the junction oscillates at 483.60 MHz per μV_{DC} (2.8.13). This oscillation frequency is irrespective of the

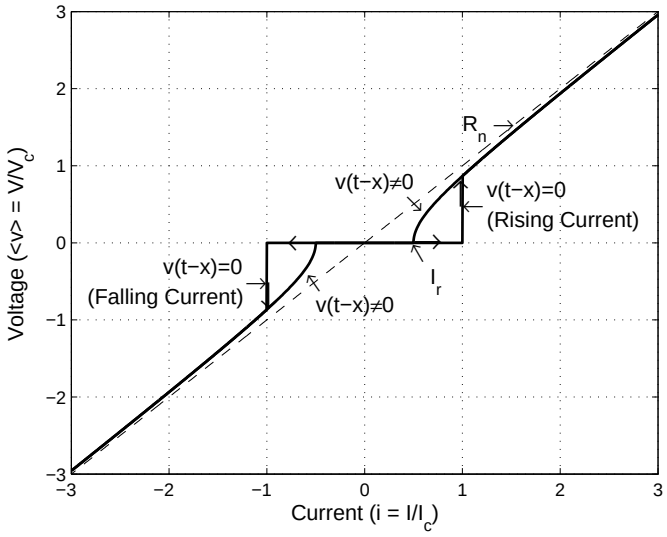

Figure 2.12: Voltage-current characteristic of a damped Josephson junction.

shunt resistance, shunt capacitance or critical current. The time average current through the junction is simply the voltage divided by the resistance, and the V-I response is a straight line with a slope given by the shunt resistance. There is no V-I hysteresis for any voltage biased junction.

2.8.5 General Damped Josephson Junction

A general damped Josephson junction consists of a superconducting channel with a shunt RC circuit, and has a damping constant given by $0 > \beta_c > 1$. The RC circuit sets the return current, I_r, and thus determines the hysteresis of the system. The dc component of the junction's voltage response to a dc current (Figure 2.7(a)) can now be expressed in terms of the characteristic voltage, $V_c \equiv I_c R_n$, as

$$\langle v(t)\rangle = 0 \quad \text{for} \quad I \leq I_C; \quad \lim_{x\to 0}\langle v(t-x)\rangle = 0 \tag{2.8.41}$$

$$= I_c R_n \sqrt{\left(\frac{I}{I_r}\right)^2 - 1} \quad \text{for} \quad I > Ir; \quad \lim_{x\to 0}\langle v(t-x)\rangle \neq 0 \tag{2.8.42}$$

$$= 0 \quad \text{for} \quad I < Ir; \quad \lim_{x\to 0}\langle v(t-x)\rangle \neq 0. \tag{2.8.43}$$

From Figure 2.12, with no current flowing through the shunt resistor, the time-average voltage across the junction will remain zero, $\langle v\rangle = 0$, while the current flowing through the junction remains below the critical current $I < I_c$. When the current rises above I_c, a potential develops across the junction, initially switching to $2\Delta/e$ (2.7.2). The system transitions into a nonlinear dc response (2.8.40), only returning to a zero potential when the current flowing through the junction drops below the minimum return current threshold, $I < I_r$, and the RC circuit has dissipated all of its energy. For certain values of β_c the damped junction will exhibit a hysteretic I-V behaviour. As β_c increases from 0 the return current I_r will decrease from I_c down to 0, resulting in an ever larger hysteresis response (Figure 2.13). An approximation of β_c is

$$\beta_c = 2\left(\frac{I_c}{I_r}\right)^2 + (2-\pi)\frac{I_c}{I_r}. \tag{2.8.44}$$

In multilayered devices it is possible to convert overdamped junctions exhibiting hysteretic behaviour into underdamped non-hysteretic junctions. The addition of an appropriately valued secondary shunt resistor will reduce β_c below 1.

When a constant voltage is applied across the junction (Figure 2.7(b)), the current through the

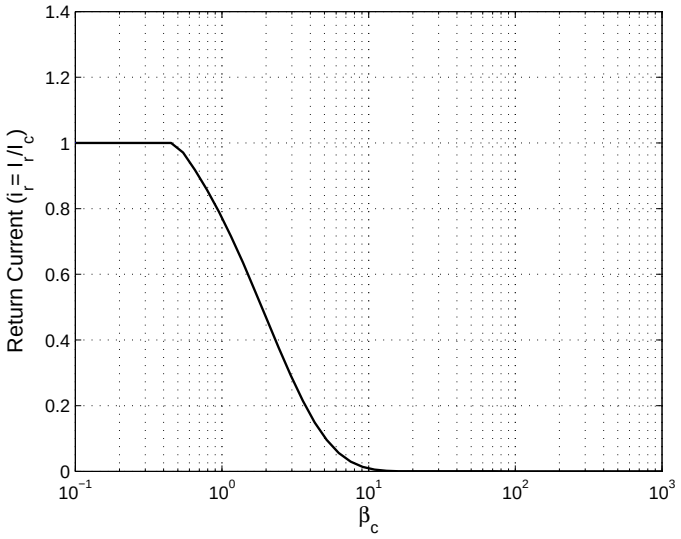

Figure 2.13: Return current of a damped Josephson junction due to the damping constant β_c.

junction oscillates at 483.60 MHz per μV_{DC} (2.8.13). This oscillation frequency is irrespective of the shunt resistance, shunt capacitance or critical current. The time average current through the junction is simply the voltage divided by the resistance, and the V-I response is a straight line with a slope given by the shunt resistance. There is no V-I hysteresis for any voltage biased junction.

2.8.6 RSJ Response to AC Signals

The signal response of the RSJ model must be analyzed with respect to dynamic voltage and current sources. For the dynamic current response, $i(t)$, the voltage applied to the resistively-shunted junction (RSJ) is defined as

$$v(t) = V_0 + V_s \cos(\omega_s t), \tag{2.8.45}$$

where V_0 is the dc voltage component and V_s is the alternating voltage component with frequency ω_s [13]. For (2.8.30) with the voltage $v(t)$ applied (2.8.45), the junction's current response becomes

$$i(t) = \frac{V_0}{R} + \frac{V_s}{R}\cos(\omega_s t) + I_c \sum_{n=-\infty}^{+\infty} (-1)^n J_n\left(\frac{2\pi V_s}{\Phi_0 \omega_s}\right) \sin\left[(2\pi f_J - n\omega_s)\, t + \varphi(0)\right], \tag{2.8.46}$$

where $f_J = \frac{V_0}{\Phi_0}$ is the Josephson frequency (2.8.38), φ_0 is the initial phase of the junction and n is an integer. The time-average of a sinusoidal signal $\cos(\omega_s t)$ developing over time is zero, so for the time-average current of (2.8.46) this term can simply be removed. The time-average of the sinusoidal signal $\sin\left[(2\pi f_J - n\omega_s)\, t\right]$ will also be zero at certain frequencies, so for the time-average current of (2.8.46) this sinusoidal signal can be represented by

$$\langle \sin\left[(2\pi f_J - n\omega_s)\, t\right] \rangle = \delta_{2\pi f_J, n\omega_s} = \begin{cases} 1 & \text{if} \quad 2\pi f_J = n\omega_s \\ 0 & \text{if} \quad 2\pi f_J \neq n\omega_s. \end{cases} \tag{2.8.47}$$

Consequently the time-average current becomes

$$\langle i \rangle = \frac{V_0}{R} + I_c \sum_{n=-\infty}^{+\infty} (-1)^n J_n\left(\frac{2\pi V_s}{\Phi_0 \omega_s}\right) \sin\left[\varphi(0)\delta_{2\pi f_J, n\omega_s}\right], \tag{2.8.48}$$

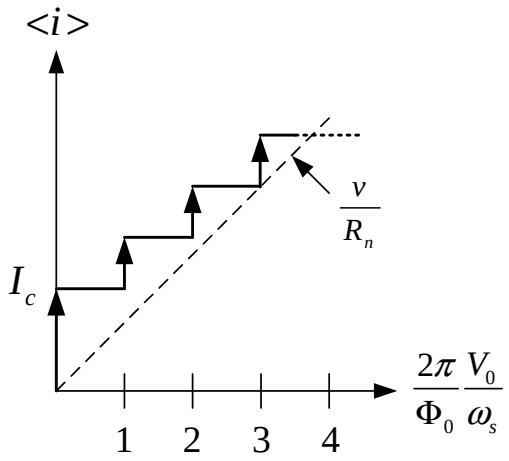

Figure 2.14: Shapiro steps represent the voltage-current response of Josephson junction with an applied microwave frequency.

representing a straight line with a slope of $\langle i \rangle = \frac{V_0}{R}$ and containing discontinuities when $\delta_{2\pi f_J, n\omega_s} = 1$. These discontinuities are due to the basic Josephson junction, resulting in a potential

$$V_0 = n\left(\frac{\Phi_0}{2\pi}\right)\omega_s \tag{2.8.49}$$

$$= n\frac{h}{2e}f_s, \tag{2.8.50}$$

forming when $\delta_{2\pi f_J, n\omega_s} = 1$, where n is an integer, h is Planck's constant, e the electron's charge and $\omega_s = 2\pi f_s$ the applied microwave frequency. The dynamic voltage response only occurs when the series resistance of the voltage source is small enough so that it can be modeled as an ideal voltage source. If the resistance is large enough, then the alternating voltage will act as an alternating current.

For the dynamic voltage response, $v(t)$, the current applied to the RSJ is defined as

$$i(t) = I_0 + I_s \cos(\omega_s t), \tag{2.8.51}$$

where I_0 is the dc current component and I_s is the alternating current component with frequency ω_s. For (2.8.30) with the current $i(t)$ applied (2.8.51), the junction's voltage response becomes $V_0 = n(\Phi_0/2\pi)\omega_s$. This response is also known as Shapiro steps (Figure 2.14), where the induced high-frequency current interferes with the Josephson frequency [13, 17]. The time-average output voltage is a staircase function with relation to the input frequency and dc current. When the Josephson frequency is equal to an integer multiple of the applied frequency, the output voltage increases by another step. The voltages at which the steps occur are determined by the driving frequency ω_s and the Josephson characteristics.

For small ac currents driving the RSJ the current can be rewritten as the sum of the current through the resistor and the junction,

$$i(t) = I_c \sin\varphi(t) + \frac{v(t)}{R} \tag{2.8.52}$$

where v(t) is the voltage across the resistor and thus the junction. From this the equivalent Josephson inductance is described as

$$L_J = \frac{\Phi_0}{2\pi I_c \cos\varphi(t)} \tag{2.8.53}$$

$$= \frac{\Phi_0}{2\pi I_c \sqrt{1 - \left(\frac{I_0}{I_c}\right)^2}} \tag{2.8.54}$$

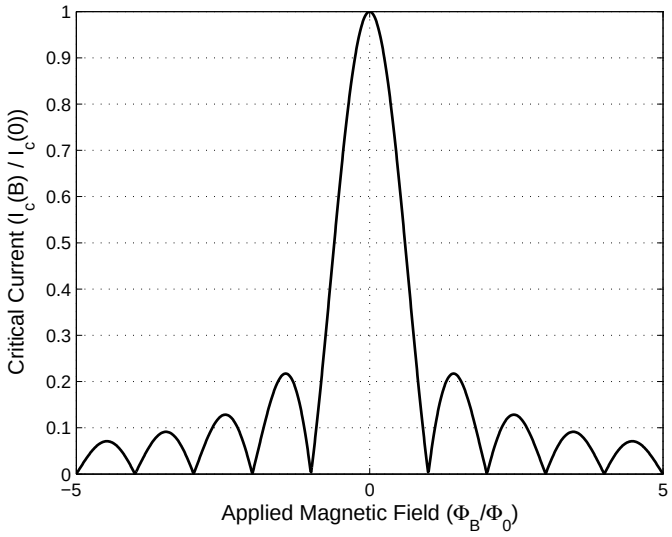

Figure 2.15: Magnetic field dependence of the critical current for a Josephson junction.

where (2.8.53) is restricted by the maximum instantaneous current through the RSJ always being smaller than the critical current, $I_s + I_0 < I_c$, and the ac current being smaller than the DC current, $I_s << I_0$.

2.8.7 Magnetic Field Effect

A unique feature of the SIS Josephson junction is that it has a dc critical current that is dependent on the applied magnetic field [14, 13, 17]. If a magnetic flux density B is applied perpendicular to the junction, the magnetic field dependence of the dc critical current, $I_c(B)$, is given by

$$I_c(B) = I_c(0) \left| \frac{\sin\left[\pi\left(\frac{\Phi_B}{\Phi_0}\right)\right]}{\pi\left(\frac{\Phi_B}{\Phi_0}\right)} \right| \tag{2.8.55}$$

where $I_c(0)$ is the dc critical current with no externally applied flux (Figure 2.15). For a junction with length L, width W and a film thickness t, the critical current is given by $I_c(0) = J_0WL$ and the penetrating magnetic flux is given by $\Phi_B = BLt$. J_0 is the critical current density with no externally applied flux. The junction exhibits a critical current that has a Frauenhoff pattern, becoming zero for $\Phi_B = n\Phi_0$ $(n = \pm 1, 2, 3, 4, ...)$.

2.9 Flux Quantisation

The SQUID sensor has a pickup loop broken by one or more Josephson junctions (JJ), depending on the SQUID configuration used. The loop is used to transform the perpendicular vector of any applied magnetic field into a circulating supercurrent. Using only a superconducting loop by itself is not enough to measure the applied magnetic flux, as the supercurrent can not be directly measured by any standard devices. The JJs are used to transform the supercurrent into a measurable voltage, but this section will only discuss the theory for the loop.

The critical current I_c in a superconducting loop will change under the influence of magnetic fields and high temperatures. Since the JJ's critical current, $I_c \approx 100\mu A$, is very small compared to that of the superconducting loop, $J_c \approx 100 A/\text{cm}^2$, changes in the loop's I_c will not be noticeable as the current circulating inside the loop will not be high enough. While a large enough magnetic field can destroy the superconductivity in the loop, the field will cause any JJ to stop functioning long before the

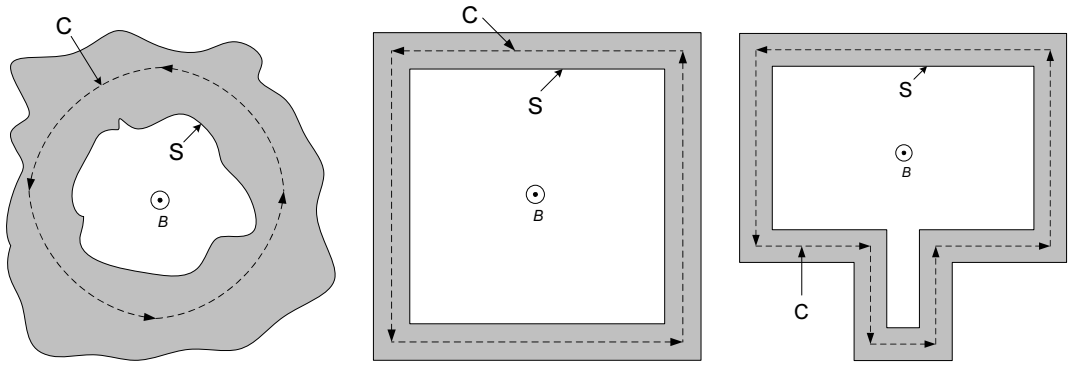

(a) (b) (c)

Figure 2.16: Superconducting loop with an internal surface area S and closed integration contour C for (a) a generic hole, (b) a square, and (c) a typical SQUID pickup loop (not to scale).

critical field strength is reached. Extreme magnetic fields in a magnetometer will cause it to overload and stop functioning long before the loop loses superconductivity. The loop is thus considered to be superconductive while the temperature remains below the critical temperature, T_c.

Applying Stoke's theorem, where the circular integration of the vector potential of the applied field is the same as the surface integral of the magnetic flux intensity,

$$\oint_C \mathbf{A} \cdot d\mathbf{l} = \int_S \mathbf{B} \cdot d\mathbf{s}, \tag{2.9.1}$$

to the supercurrent (2.6.16) will result in

$$\oint_C (\Lambda \mathbf{J}_s) \cdot d\mathbf{l} = -\oint_C \mathbf{A} \cdot d\mathbf{l} + \oint_C \frac{\hbar}{q^*} \nabla\theta \cdot d\mathbf{l} \tag{2.9.2}$$

$$\Rightarrow \oint_C (\Lambda \mathbf{J}_s) \cdot d\mathbf{l} = -\int_S \mathbf{B} \cdot d\mathbf{s} + \frac{\hbar}{q^*} \oint_C \nabla\theta \cdot d\mathbf{l}. \tag{2.9.3}$$

Using the relation where the circular integration of the phase is

$$\oint_C \nabla\theta \cdot d\mathbf{l} = 2\pi n, \tag{2.9.4}$$

(2.9.3) becomes

$$\oint_C (\Lambda \mathbf{J}_s) \cdot d\mathbf{l} + \int_S \mathbf{B} \cdot d\mathbf{s} = n\Phi_0 \tag{2.9.5}$$

$$\Phi = n\Phi_0, \tag{2.9.6}$$

where Φ_0 is a single magnetic flux quantum. (2.9.5) and (2.9.6) describe the flux quantisation effect of superconducting loops. The flux through an arbitrary hole in a type II superconductor (Figure 2.16) will always be an integer multiple of Φ_0.

If there was no preexisting supercurrent flowing in the loop and a magnetic field is applied across the hole, then the superconductor will induce a supercurrent so that the total flux through the surface S will remain zero, or integer multiples of Φ_0 if flux manages to penetrate. This is the flux expulsion described by (2.3.5). If a preexisting flux permeates the superconductor's hole, a supercurrent will start to flow to ensure that the penetrating flux will always be at the nearest integer multiple of Φ_0, irrespective of the amount of flux applied before the device became superconductive. If the magnetic field is removed, a non-dissipating supercurrent will ensure that the flux through the hole will be maintained.

2.10 Conclusion

The fundamentals of superconductivity describe the underlying effects of superconductors and are applied to create a model for Josephson junctions. The Josephson junction forms a critical part of the SQUID, and its properties are discussed in depth. The basic junction determines the I-V behaviour unique to superconductors and is evolved to include aspects of a practical junction such as resistance and capacitance, resulting in the RCSJ and RSJ models that describe their real world equivalent. High-temperature superconductors are most accurately described by the RSJ model, having the advantage of not requiring additional shunt resistance to prevent I-V hysteresis. Large magnetic fields and ac sources tend to change the characteristics of junctions, resulting in lower critical current, changing the I-V responce or resulting in Shapiro steps. Another property of superconductors discussed is the effect of flux quantization inside a superconducting loop. Combining a Josephson junctions with a superconducting loop gives rise to the SQUID. It is important to first comprehend the basics behind the elements constituting the SQUID.

Chapter 3

SQUID Theory

3.1 Introduction

The **S**uperconducting **QU**antum **I**nterference **D**evice (SQUID) microscope comprises of a SQUID sensor, control electronics and a cooling unit. A SQUID sensor in itself is basically a flux-to-voltage converter, and is as such the most sensitive magnetic flux detector known. This chapter will examine some of the theory behind the dc SQUID sensor, which is basically a superconducting loop with two Josephson junctions (JJ) in parallel. The dc SQUID has a lower intrinsic flux noise than the rf SQUID and is more suitable for the SQUID microscope. For this project the direct current (dc) SQUID configuration will be used and the theory behind the radio frequency (rf) SQUID configuration will not be discussed.

To work properly the SQUID needs to be cooled to working temperatures and the flux-to-voltage converter's output must be linearized. The theory behind the control electronics and cooling of the SQUID will be discussed in subsequent chapters.

3.2 DC SQUID

3.2.1 Introduction

The Superconducting QUantum Interference Device (SQUID) sensor is the principal device used by the SQUID microscope. It translates the magnetic flux passing through a superconducting pickup loop into a measurable voltage or current, combining the processes of flux quantization with Josephson tunneling.

The sensor consists of a superconducting pickup loop broken by one or more Josephson Junctions (JJ). The pickup loop converts the contained flux into a current which is then converted by the junctions into a measurable voltage. When a SQUID consists of a superconducting loop with two parallel Josephson junctions, and is biased using a dc current, it is known as a dc SQUID. A typical dc SQUID is shown in Figure 3.1.

3.2.2 Basic Superconducting Quantum Interference

To help describe the operation of the sensor, the ideal JJ is initially used, with (2.8.6) and (2.8.7) describing the critical current and gauge-invariant phase difference, respectively. Unless specified, both junctions are considered to have the same parameters such as the critical current, I_c, shunt resistance, R_n, and shunt capacitance, C. The junctions are also considered to be small, having a homogeneous critical current density throughout the cross-section of the junction. The shunt resistance and the junction capacitance are to be disregarded at first, and their influence will be discussed later in the chapter.

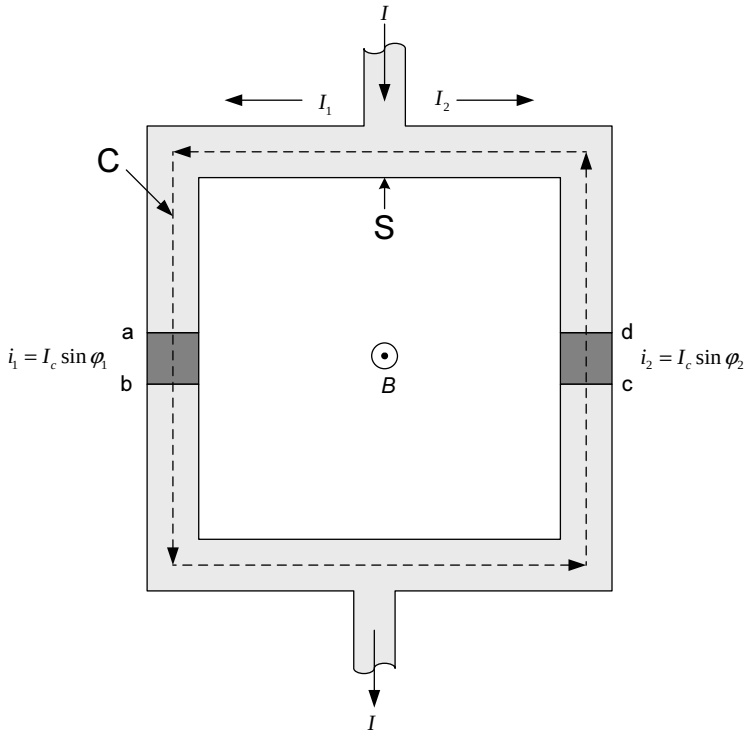

Figure 3.1: Superconducting loop with two parallel Josephson junctions forming a dc SQUID. The loop has an internal surface area S and closed integration contour C.

In Figures 3.1 and 3.2(a) the total current flowing through the sensor , i, is the sum of the current through each junction, in this case i_1 and i_2, and is given by

$$\begin{aligned} i &= i_1 + i_2 && (3.2.1)\\ &= I_c \sin\varphi_1 + I_c \sin\varphi_2 && (3.2.2)\\ &= 2I_c \cos\left(\frac{\varphi_1 - \varphi_2}{2}\right) \sin\left(\frac{\varphi_1 + \varphi_2}{2}\right), && (3.2.3) \end{aligned}$$

where I_c is the critical current of a single junction, and φ_1 and φ_2 are the gauge-invariant phase differences of the respective junctions [13]. Both junctions are considered to be small junctions, having a homogeneous critical current density

$$j_c = \frac{I_c}{A_J}, \tag{3.2.4}$$

throughout the entire junction cross-section of area, A_J. The circulating current induced by the magnetic flux through the superconducting loop is given by (2.9.4). The integration of the phases can be rewritten to include the junctions, resulting in

$$\oint_C \nabla\theta \cdot d\mathbf{l} = 2\pi n = (\theta_a - \theta_d) + (\theta_d - \theta_c) + (\theta_c - \theta_b) + (\theta_b - \theta_a), \tag{3.2.5}$$

with the phases of the junctions defined by (2.8.7). Rewriting the gauge-invariant phase difference for the junctions results in

$$\begin{aligned} \theta_b - \theta_a &= -\varphi_1 - \frac{2\pi}{\Phi_0}\int_a^b \mathbf{A}\cdot dl && (3.2.6)\\ \theta_d - \theta_c &= \varphi_2 - \frac{2\pi}{\Phi_0}\int_c^d \mathbf{A}\cdot dl, && (3.2.7) \end{aligned}$$

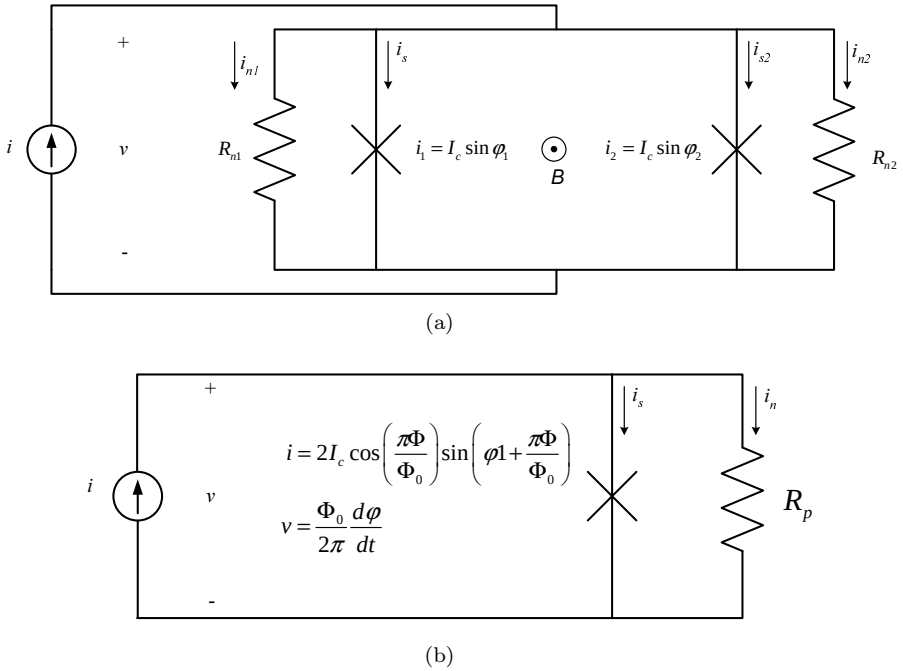

Figure 3.2: Schematic representation of a RSJ dc SQUID for a current input source i with a voltage response v (a), and the simplified model (b). The effect of loop inductance is ignored.

where Φ_0 is a single magnetic flux quantum. If the junction length, $2a$, is considered to be small enough so that the integration path of the superconductor is continuous, (3.2.5) can be rewritten as

$$2\pi n = \varphi_2 - \varphi_1 - \frac{2\pi}{\Phi_0}\oint_C \mathbf{A}\cdot dl - \frac{2\pi}{\Phi_0}\int_C \Lambda\mathbf{J}\cdot dl, \tag{3.2.8}$$

further reducing to

$$\varphi_2 - \varphi_1 = 2\pi n + \frac{2\pi\Phi}{\Phi_0}, \tag{3.2.9}$$

showing that there is a relation between the phase differences and the total flux. Combining (3.2.9) with (3.2.3), the total current becomes

$$i = 2I_c \cos\left(\frac{\pi\Phi}{\Phi_0}\right)\sin\left(\varphi_1 + \frac{\pi\Phi}{\Phi_0}\right), \tag{3.2.10}$$

which is similar to a single basic Josephson junction (2.8.1) with the critical current and phase a function of flux. The basic dc SQUID experiences oscillation of the total current i dependent on the flux Φ, due to the interference of the two supercurrents flowing through Josephson junctions. The potential developing across the junction due to phase slip (2.8.10) is used to measure magnetic fields.

3.2.3 Loop Inductance

A practical dc SQUID has a intrinsic pickup loop of area A_{SQ} for the surface S in Figure 3.1 with a loop inductance L_{SQ} [13]. If the pickup loop has a very small area then the SQUID will have a very small loop inductance, resulting in low sensitivity. The SQUID is chosen for its high sensitivity, so the the area of the pickup loop will result in a small but definitive loop inductance as shown in Figure 3.3. The effect of loop inductance in a SQUID must be examined.

To see the effect of external flux on a SQUID with finite loop inductance, the current through each

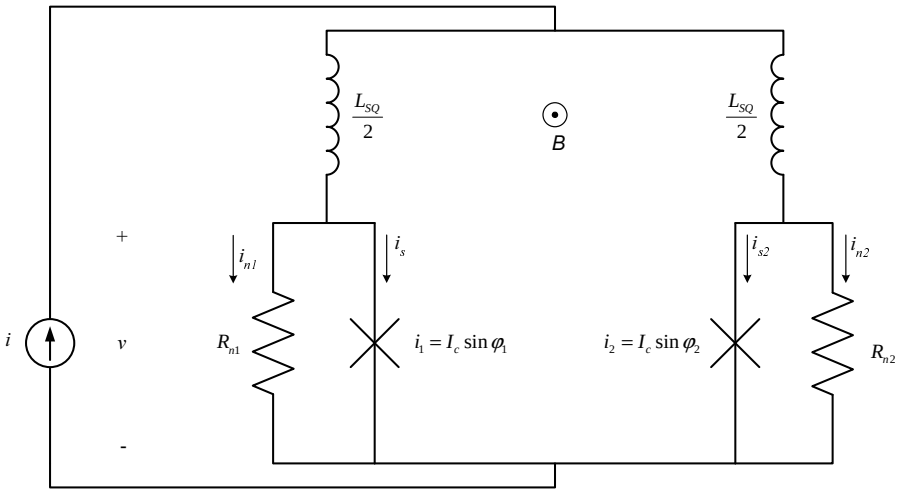

Figure 3.3: Schematic representation of a RSJ dc SQUID with loop inductance L_{SQ} for a current input source i with a voltage response v. The loop inductance is split to represent the branching of the input current in Figure 3.1.

junction is reexamined, resulting in

$$i_1 = \frac{I_B}{2} + I_{cir} \tag{3.2.11}$$

$$i_2 = \frac{I_B}{2} - I_{cir}, \tag{3.2.12}$$

where I_B and I_{cir} are the biasing current and the circulating current, respectively. Since the biasing current generates no flux through the device, the circulating current reduces to

$$I_{cir} = \frac{i_1 - i_2}{2} = \frac{I_c \sin\varphi_1 - I_c \sin\varphi_2}{2}. \tag{3.2.13}$$

The total flux through the device, Φ, is the sum of the external flux, Φ_{ext}, and the flux generated by the current flowing in the loop. Combining (3.2.1) and (3.2.13) with (3.2.11) and (3.2.12), the flux through the loop becomes

$$\Phi = \Phi_{\mathrm{ext}} + L_{SQ} I_{cir} \tag{3.2.14}$$

$$= \Phi_{\mathrm{ext}} + L_{SQ}\left(\frac{I_c \sin\varphi_1 - I_c \sin\varphi_2}{2}\right) \tag{3.2.15}$$

$$= \Phi_{\mathrm{ext}} + L_{SQ} I_c \sin\left(\frac{\pi\Phi}{\Phi_0}\right)\cos\left(\varphi_1 + \frac{\pi\Phi}{\Phi_0}\right), \tag{3.2.16}$$

where L_{SQ} is the loop inductance. From flux quantization it is known that the flux through the SQUID loop must always be a multiple of Φ_0, so (3.2.14) can be written as

$$\Phi = \Phi_{\mathrm{ext}} + L_{SQ} I_{cir} = n\Phi_0, \tag{3.2.17}$$

where n is the integer closest to the value of $\Phi_{\mathrm{ext}}/\Phi_0$, whereas in the normal superconducting loop n is kept at the current integer until the next integer is reached. This is caused by the junctions minimizing their energy (2.8.15) by reducing the circulating current in the superconducting loop. (3.2.17) is only valid for significantly large SQUID loop inductances. The circulating current is given as

$$I_{cir} = \frac{n\Phi_0 - \Phi_{\mathrm{ext}}}{L_{SQ}}. \tag{3.2.18}$$

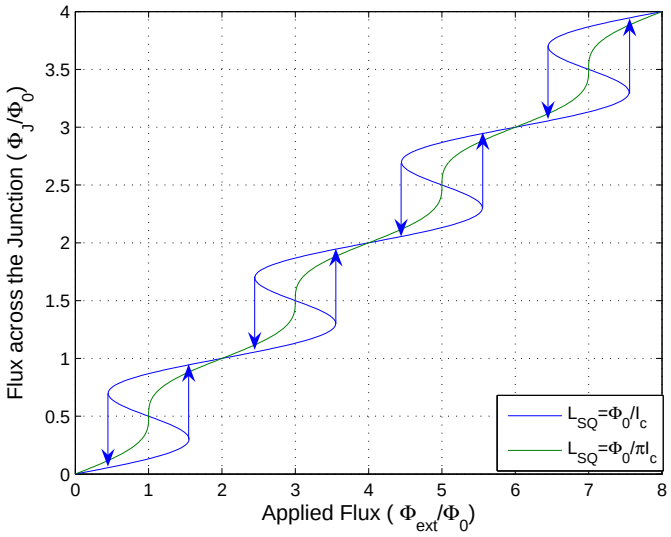

Figure 3.4: The flux across the junction Φ_J vs. the applied flux Φ_{ext} showing the hysteretic effect of the loop inductance L_{SQ} for a dc SQUID.

The maximum bias current that the device can sustain while maintaining superconductivity is

$$i_{\max} = 2I_c - \frac{2\left|\Phi_{\text{ext}} - n\Phi_0\right|}{L_{SQ}}. \tag{3.2.19}$$

Looking at a single junction, as the external flux increases the maximum bias current must decrease accordingly. The maximum bias current through the junction can be given as

$$i_{1,\max} = I_c - \frac{2\Phi_{\text{ext}}}{L_{SQ}}, \tag{3.2.20}$$

where the critical current couples with the circulating and biasing current. The total current for a SQUID (3.2.10) with a significant inductance is

$$i = i_{\max}\sin\left(\varphi_1 + \frac{\pi\Phi}{\Phi_0}\right) \tag{3.2.21}$$

$$= \left[2I_c - \frac{2\left|\Phi_{\text{ext}} - n\Phi_0\right|}{L_{SQ}}\right]\sin\left(\varphi_1 + \frac{\pi\Phi}{\Phi_0}\right), \tag{3.2.22}$$

where n is the integer closest to the value of Φ_{ext}/Φ_0, due to the junctions minimizing their energy by reducing the circulating current in the superconducting loop. With a substantial loop inductance the SQUID will exhibit hysteresis. This hysteresis is evident when comparing the applied flux, Φ_{ext}, to the flux across a junction, Φ_{J}:

$$\Phi_{\text{ext}} = 2\Phi_{\text{J}} + L_{SQ}I_c\sin\left(\frac{2\pi\Phi_{\text{J}}}{\Phi_0}\right). \tag{3.2.23}$$

Figure 3.4 shows that if the loop inductance is small enough then the hysteresis described in (3.2.23) will not occur [18]. The largest possible loop inductance for a SQUID with no hysteresis is when

$$L_{SQ} << \frac{\Phi_0}{I_c}, \tag{3.2.24}$$

where L_{SQ} is small enough for the current circulating in the loop to have no effect on the external flux.

The maximum bias current for the SQUID with (3.2.24) is

$$i_{\max} = 2I_c \left|\cos\left(\frac{\pi\Phi_{\text{ext}}}{\Phi_0}\right)\right|, \tag{3.2.25}$$

since the loop induction is now considered small enough to be neglected. The total current for a SQUID (3.2.10) with an insignificant inductance is

$$i = 2I_c \left|\cos\left(\frac{\pi\Phi_{\text{ext}}}{\Phi_0}\right)\right| \sin\left(\varphi_1 + \frac{\pi\Phi}{\Phi_0}\right). \tag{3.2.26}$$

For junctions with different critical currents, the maximum biasing current can be given as

$$i_{\max} = \sqrt{I_{c1}^2 + I_{c2}^2 + 2I_{c1}I_{c2}\cos\frac{2\pi\Phi}{\Phi_0}}, \tag{3.2.27}$$

which is a vector magnitude of the two different junctions.

3.2.4 Flux-to-Voltage Conversion

Section 2.8.2 shows that the basic Josephson junction does not represent an actual junction, thus introducing both the RCSJ and RSJ models. The RSJ model adds the shunt resistance intrinsic to all high-T_c junctions, yielding a more realistic model with a defined I-V response. For a more realistic dc SQUID model the two parallel basic junctions are replaced by resistively-shunted junctions (RSJ), creating what is known as a magnetometer. The dc SQUID magnetometer converts flux into a measurable voltage output [13, 1, 19].

Combining (3.2.1) with (2.8.30), total current flowing through the sensor, i, is given by

$$\begin{aligned} i &= i_1 + i_2 + i_{R_1} + i_{R_2} && (3.2.28)\\ &= I_c\sin\varphi_1 + I_c\sin\varphi_2 + \frac{v}{R_1} + \frac{v}{R_2} && (3.2.29)\\ &= 2I_c\cos\left(\frac{\varphi_1-\varphi_2}{2}\right)\sin\left(\frac{\varphi_1+\varphi_2}{2}\right) + v\left(\frac{1}{R_1}+\frac{1}{R_2}\right), && (3.2.30)\end{aligned}$$

where the critical current I_c is the same for both junctions and $\beta_c = 0$ for the RSJ. Similar to (3.2.10), when (3.2.9) is combined with (3.2.30), the total current becomes

$$i = 2I_c\cos\left(\frac{\pi\Phi_{\text{ext}}}{\Phi_0}\right)\sin\left(\varphi_1 + \frac{\pi\Phi_{\text{ext}}}{\Phi_0}\right) + v\left(\frac{1}{R_1}+\frac{1}{R_2}\right). \tag{3.2.31}$$

To help define the voltage developing across the SQUID, an equivalent RSJ circuit is modeled from (3.2.31). The phase of the equivalent circuit is

$$\varphi = \varphi_1 + \frac{\pi\Phi_{\text{ext}}}{\Phi_0}, \tag{3.2.32}$$

and for a SQUID with $L_{SQ} << \Phi_0/I_c$ the critical current is given by (3.2.25),

$$i_{\max} = 2I_c\left|\cos\left(\frac{\pi\Phi_{\text{ext}}}{\Phi_0}\right)\right|. \tag{3.2.33}$$

If the external applied flux is constant, then the voltage phase relation is

$$\frac{d\varphi}{dt} = \frac{d\varphi_1}{dt} = \frac{2\pi}{\Phi_0}v. \tag{3.2.34}$$

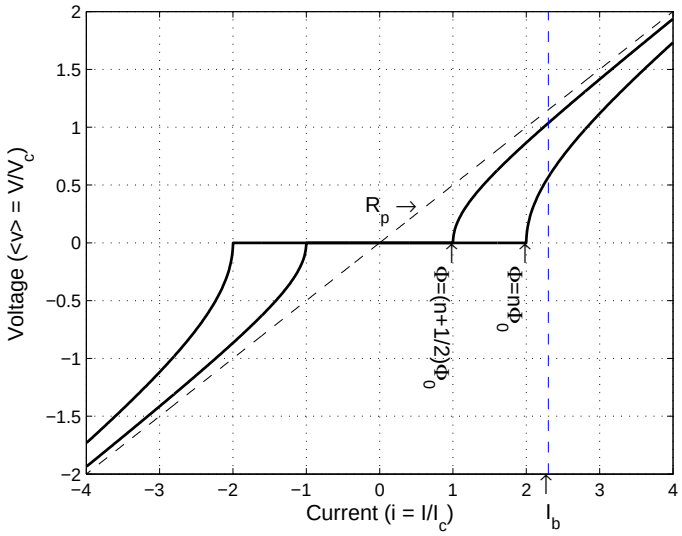

Figure 3.5: Voltage-current response of a dc SQUID with $\beta_L = 1$ and $\beta_c = 0$. The applied flux is at integer $n\Phi_0$ and half-integer $(n + 1/2)\Phi_0$ values.

The parallel resistors combine to form

$$\frac{1}{R_p} = \frac{1}{R_1} + \frac{1}{R_2}. \tag{3.2.35}$$

The equivalent RSJ circuit can be written as

$$i = i_{\max} \sin\varphi + \frac{1}{R_p}\frac{\Phi_0}{2\pi}\frac{d\varphi}{dt}. \tag{3.2.36}$$

The time-average voltage across a junction is given by (2.8.35) and for the dc SQUID equivalent circuit the dc component becomes

$$\langle v(t)\rangle = IR_p\sqrt{1 - \left(\frac{2I_c}{I}\cos\left(\frac{\pi\Phi_{\text{ext}}}{\Phi_0}\right)\right)^2} \quad \text{for} \quad I > i_{\max} \tag{3.2.37}$$

$$= i_{\max}R_p\sqrt{\left(\frac{I}{i_{\max}}\right)^2 - 1} \quad \text{for} \quad I > i_{\max}, \tag{3.2.38}$$

where I is the the dc bias current. The voltage-current characteristic of a dc SQUID with $\beta_L = 1$ and $\beta_c = 0$ can be seen in Figure 3.5 while the voltage-flux response can be seen in Figure 3.6 for various biasing currents.

The maximum bias current that the SQUID can sustain with the junctions maintaining superconductivity is dependent on the applied external flux. As the flux increases or decreases the maximum bias current follows a sinusoidal pattern with a period of two fluxons. Similarly the V-I response (3.2.37) follows a rectified sinusoidal pattern with a period of one fluxon. If the bias current is kept constant at $I = 2I_c$ and the external flux changes, the DC voltage output will undergo a single period change for each applied fluxon. By keeping count of each of the changes, the amount of fluxons and thus the magnetic field difference can be measured. Unfortunately the rectification in (3.2.37) removes any information on the direction of change of the magnetic field. The resolution on this type of measurement is also limited to one fluxon, reducing the sensitivity and accuracy of the SQUID. If the bias current I is greater than $2I_c$ when there is no flux applied to the SQUID, then the voltage response to applied flux will be sinusoidal. A sinusoidal signal can be linearized.

For a bias current of about $I_b = I_c$, an applied flux of $\Phi_0/2$, and $\beta_L \leq 1$, the I-V has a constant

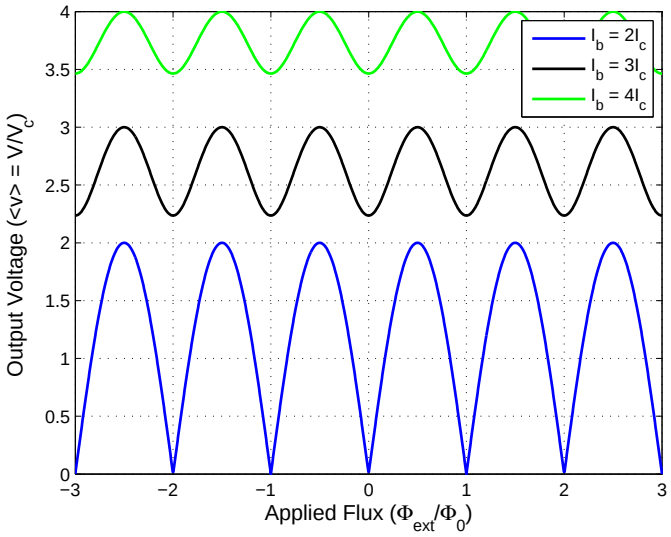

Figure 3.6: Voltage-flux response of a dc SQUID for various biasing currents I_b with $\beta_L = 1$ and $\beta_c = 0$.

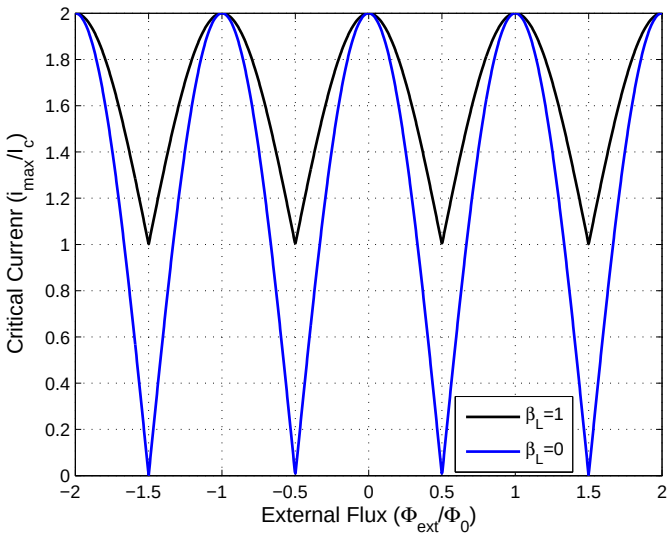

Figure 3.7: Maximum bias current vs. flux Φ_{ext}/Φ_0 for the screening parameters $\beta_L = 1$ and $\beta_L = 0$.

dynamic resistance

$$R_{\text{dyn}} = \frac{dV}{dI} = \frac{R_n}{2}. \tag{3.2.39}$$

3.2.5 Screening Parameter

Using the RCSJ model for identical junctions in a SQUID, the screening parameter β_L is introduced [1, 16, 20], where

$$\beta_L = \frac{2L_{SQ}I_c}{\Phi_0} \tag{3.2.40}$$

creates a relationship between the SQUID's loop inductance, L_{SQ}, and the critical current, I_c, of a single junction. The optimal relationship is when $\beta_L = 1$ [21], as this is where the critical current at $\Phi_{\text{ext}} = (\Phi_0/2 + n\Phi_0)$ is approximately half of that at $\Phi_{\text{ext}} = n\Phi_0$. The effect of the screening parameter on the maximum bias current is shown in Figure 3.7.

While a $\beta_L = 1$ would be ideal for a dc SQUID, it is important to note here the restrictions placed

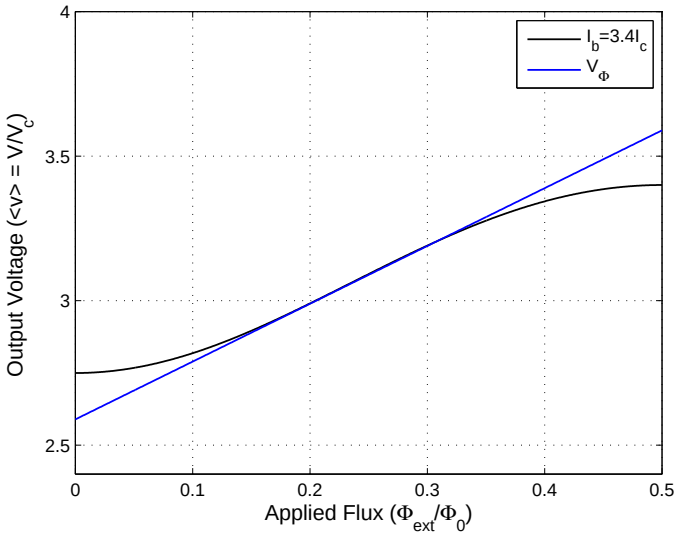

Figure 3.8: Voltage sensitivity V_Φ of a RSJ SQUID biased at $3.4I_c$. The slope for the optimal screening parameter β_L=0 is $2V_\Phi/\Phi_0$, as indicated by the blue line.

on the SQUID by noise: The upper limit of the inductor size is set by the thermal constraint (5.5.13), $L_{SQ} << \Phi_0^2/4k_BT$, and by the hysteresis constraint (3.2.24), $L_{SQ} << \Phi_0/I_c$. The lower current limit is constrained due to thermal noise (5.5.5), $\Gamma << 1$.

3.2.6 Sensitivity

SQUID magnetometers are the most sensitive magnetic field sensors available. The performance of a sensor is given in terms of its sensitivity, the magnetic field sensitivity and the magnetic flux resolution [13, 1, 19]. The magnetic field resolution, B_N, is a function of thermal noise and is always less than one flux quantum. Thermal noise is discussed in Section 5.5.

The magnetic field sensitivity, $\delta B/\delta\Phi$, is equivalent to the field-to-flux conversion coefficient. For a SQUID with a pickup loop of area A_{SQ}, the flux coupling into the SQUID is

$$\Phi_{SQ} = B_a A_{SQ}, \tag{3.2.41}$$

where B_a is the applied magnetic flux density perpendicular to the pickup loop. The SQUID is designed to have a small loop induction to reduce thermal noise (5.5.13), resulting a pickup loop with a small area A_{SQ}. Increasing the area of the SQUID pickup loop will increase the magnetic field sensitivity, but will simultaneously increase the loop inductance. There are two design possibilities for increasing the effective area of the SQUID, A_{eff}, without affecting the loop inductance, L_{SQ}, in a single-layer SQUID. The large-area washer SQUID uses a larger film width to focus the magnetic field and the directly-coupled SQUID has a secondary, larger pickup loop.

The voltage sensitivity of the SQUID is given by

$$V_\Phi = \frac{\delta\langle v\rangle}{\delta\Phi_\mathrm{ext}} \approx \frac{R_p\delta i}{\frac{1}{2}\Phi_0} = \frac{2R_p}{L_{SQ}}, \tag{3.2.42}$$

where R_p is the junction resistance at the optimum bias current and L the loop inductance. For a SQUID that has parallel junctions with identical shunt resistances, R_n, the voltage sensitivity can be simplified to

$$V_\Phi \approx \frac{R_n}{L_{SQ}} \approx \frac{1}{\sqrt{\pi L_{SQ}C}}. \tag{3.2.43}$$

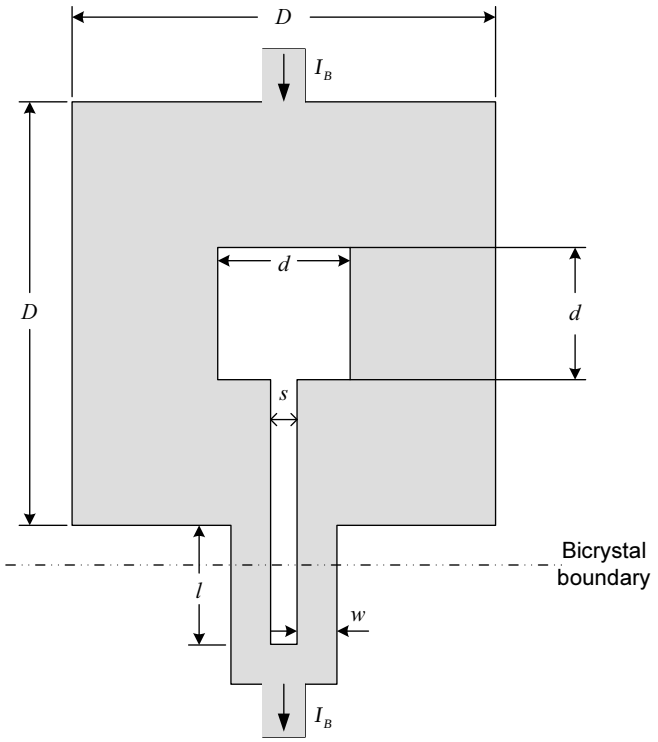

Figure 3.9: Layout of a large-area washer dc SQUID. The bicrystal boundary for the junctions is indicated by the dashed line.

The maximum response for a small flux change, $\delta\langle v\rangle/\delta\Phi_{\text{ext}}$, occurs in a SQUID with $\beta_L = 1$ when the applied flux stays at $\Phi_{\text{ext}} \approx (\Phi_0/4 + n\Phi_0/2)$. Using electronic feedback control, the SQUID should be biased with the working point at $\Phi_0/4$. If the SQUID is designed for $\beta_L = 2L_{SQ}I_c/\Phi_0 = 1$ and $\beta_c = 0$, then (3.2.43) can be further reduced to

$$V_\Phi \approx \frac{R_n}{L_{SQ}} = \frac{2V_c}{\Phi_0}, \tag{3.2.44}$$

where $V_c = I_cR_n$ was introduced by (2.8.20), and V_Φ is in volts per flux quantum. Simulations indicate that the optimum bias current is between $3.3 < I_b/I_c < 3.5$, as shown in Figure 3.8. The slope at the optimal screening parameter is $2V_\Phi$ per Φ_0 as indicated by the blue line.

3.3 Large-Area Washer DC SQUID

The large-area washer dc SQUID is designed to focus the applied magnetic field through the SQUID loop [1, 22]. The advantage of this layout is that the SQUID can be manufactured on a bicrystal or biepitaxial substrate using a single layer process.

The large-area washer dc SQUID uses a larger film width for the SUQID loop to act as a flux focuser, increasing the effective area of the SQUID . In a type II superconductor flux is expelled from the bulk material. So for a wide superconducting film the magnetic field will be deflected to either side, compressing the field outside the edge of the film. If this film forms a superconductive loop with a small center hole as shown in Figure 3.9, then a significant portion of the magnetic field applied directly to the film will be deflected through the hole. The effective area of the SQUID becomes

$$A_{eff} = dD, \tag{3.3.1}$$

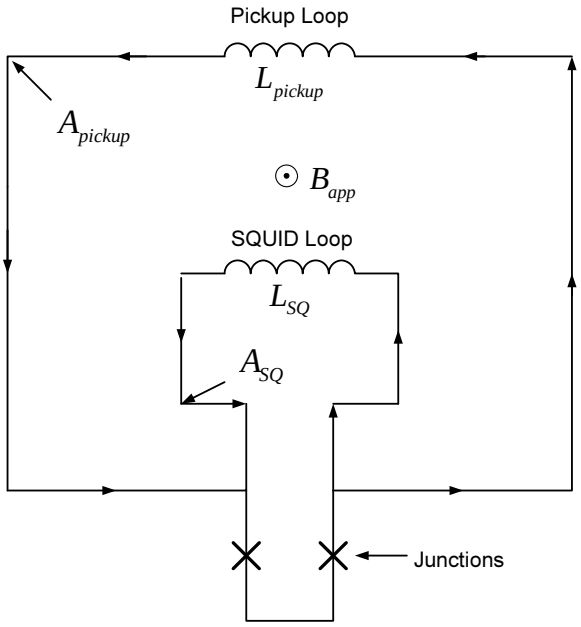

Figure 3.10: Layout of a directly-coupled dc SQUID (not to scale).

where A_{eff} is the effective area of the SQUID, d is the inner dimensions of the SQUID and D is the outer dimensions.

If a large-area washer dc SQUID is cooled in a static magnetic field it will tend to show in a significant increase in noise (Section 5.6), decreasing the sensor's performance. Flux vortices hop randomly among pinning sites creating flux noise, and the amount of vortices in a film is proportional to the width and quality of the superconductive film. The relation of line width to the noise threshold flux density is given by (5.5.21), showing that the effect of flux trapping will becomes worse as the film width increases. The washer can be designed to incorporate slots and holes to trap vortices during cooling, and the quality of the material can be improved to reduce pinning sites.

For single layered devices the directly-coupled dc SQUID is preferred as it has has a higher sensitivity for similar dimensions.

3.4 Directly-Coupled DC SQUID

The directly-coupled dc SQUID shown in Figure 3.10 is a single layer SQUID that can be manufactured on a bicrystal or biepitaxial substrate using a single layer process [23, 1, 18]. A secondary, larger pickup loop is directly connected to the SQUID loop. Flux applied to the secondary loop will create a circulating current (2.9.6), and since the SQUID loop forms part of the secondary loop, the circulating current is injected directly into the SQUID loop. It is important to note that the circulating current from the pick loop is not inductively coupled with the SQUID loop as it is with flux transformers, but uses direct injection. The effective area of the SQUID becomes

$$A_{eff} = A_{SQ} + \alpha A_{pickup}\left(\frac{L_{SQ}}{L_{pickup}}\right) \tag{3.4.1}$$

$$\Phi_{eff} = B_{app}A_{SQ} + B_{app}\alpha A_{pickup}\left(\frac{L_{SQ}}{L_{pickup}}\right), \tag{3.4.2}$$

where A_{eff} is the effective area of the SQUID, A_{SQ} the area of the SQUID, A_{pickup} the area of the pickup loop, L_{SQ} the inductance of the SQUID loop, L_{pickup} the inductance of the pickup loop, α the coupling

constant and B_{app} is the applied magnetic flux density. The fraction of the SQUID loop that forms part of the pickup loop defines the coupling constant, α, and when α is at unity the current through the pickup loop induces the maximum possible flux through the SQUID loop. For practical SQUIDS the coupling constant is typically $\alpha > 0.8$ [24]. The area of the pickup loop is always much larger than for the SQUID loop, $A_{pickup} >> A_{SQ}$, and as a consequence the induction for the pickup loop is much larger than for the SQUID loop, $L_{pickup} >> L_{SQ}$, resulting in a significantly improved effective area.

The magnetic field sensitivity, $\delta B/\delta\Phi$, the voltage sensitivity, $V_\Phi = \delta\langle v\rangle/\delta\Phi_{\text{ext}}$ (3.2.43), and the magnetic field noise, B_n (5.5.19), are enhanced since the apparent flux of the SQUID, Φ_{eff}, has increased without increasing the SQUID loop inductance, L_{SQ}.

If a directly-coupled dc SQUID is cooled in a static magnetic field it will tend to show an increase in l/f noise (Section 5.5.7), decreasing the sensor's performance. The thermal noise of the SQUID loop can be improved by incorporating slots and holes to trap the flux during cooling, or by using thinner SQUID loop line widths.

3.5 Room-Temperature Sample Measurement

The field and spatial resolution rapidly diminishes as the distance between the SQUID sensor and the sample is increased [25], so it is important to keep this distance as small as possible. If the sample to be measured is at room-temperature, then insulating material is required to thermally separate the sample from the sensor held at cryogenic temperatures. The insulator must be effective enough to prevent external heat from producing additional thermal noise in the SQUID, but thin enough to allow the sensor to be as close to the sample as possible.

The magnetic field sensitivity of a dc SQUID is $B_a = \Phi_{SQ}/A_{eff}$ from (3.2.41) for (3.3.1) and (3.4.1), while the fall-off rate for the magnetic source depends on its type. At a distance r from the source the magnetic field will scale at $1/r$ for a simple wire and $1/r^3$ for a dipole. The optimal distance between the sample and the source requires that $r^2{=}A_{eff}$, as given by [25]. This sensor-to-sample distance is a trade-off between the field sensitivity and the spatial resolution. To achieve the best possible spatial resolution for SQUID-based microscopy, a small SQUID is scanned as close as possible to the sample [26].

3.6 Conclusion

The basic dc SQUID describes how the quantum interference between two parallel Josephson junctions results in a flux to voltage conversion. Improving on the basic model by using RSJ junctions and including loop inductance, a practical SQUID is modeled. Performance factors such as sensitivity, loop inductance, loop area and screening are introduced. The loop inductor must be small enough not to cause hysteresis, but must have a large enough area to be sensitive to magnetic fields. Two designs are shown that enhance the magnetic field sensitivity of the SQUID, either by focusing flux into the SQUID loop or by direct coupling from larger pickup loop.

Chapter 4

High-Temperature Superconductor Material Properties

4.1 Introduction

The manufacturing techniques used to produce a high-T_c superconducting play an important part in creating and characterising a dc SQUID magnetometer. Superconductors are a result of the unique properties of certain materials that behave in a specific way when cooled to low temperatures. In order to characterize superconducting device properly it is crucial to have a basic understanding of the material.

High-T_c materials have a highly anisotropic nature, producing weak links when the crystal lattice is misorientated. This anisotropic effect can be used to produce Josephson junctions in controlled situations, and prevented when not desired during YBCO deposition. The source of anisotropy and weak links in thin-film high-T_c will be discussed, as well as how these films can be deposited onto substrates.

The type of junction used has a large impact on the performance of a SQUID. There are five commonly used junctions, sorted into ramp-edge, grain-boundary and step-edge junctions. The merits for each type is discussed.

4.2 Anisotropy

Most of the high-T_c superconductors have perovskite crystal structures, forming CuO_2 planes that contribute to superconductivity [1]. The CuO_2 planes are based on Cu atoms surrounded by four oxygen

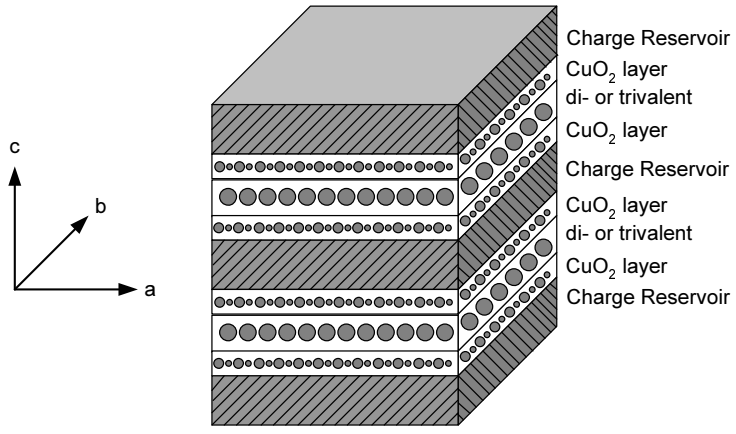

Figure 4.1: Generic structure of the superconducting cuprate. The CuO_2 layers are separated by charge reservoir blocks [1].

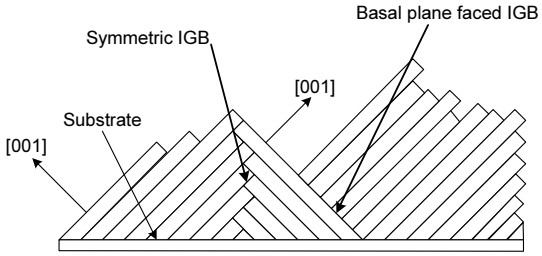

Figure 4.2: Schematic representation of YBCO forming a symmetric intrinsic grain-boundary (SGB) and a basal-plane-faced (BPF) intrinsic grain-boundary.

atoms, alternating with non-copper planes, as shown in Figure 4.1. These CuO_2 sheets are considered to be 2-dimensional in cuprate superconductors. For YBCO superconductors the non-copper planes are formed by alternating Ba-Y-Ba in the c-axis. These alternating non-copper planes draw electrons away from the oxygen sites in the copper planes, creating holes used to conduct Cooper-pairs.

This layered crystal structure results in anisotropic conductivity for high-T_c materials, with a higher current along the CuO_2 plane than perpendicular (c-axis) to it. The energy gap (2.7.1),Δ, penetration depth (2.4.3), λ, and coherence length are also anisotropic. The growth rate of YBCO during deposition is also anisotropic, with a higher growth rate along the CuO_2 planes than along th c-axis. Anisotropy is a important property for manufacturing single layer devices, especially when creating Josephson junctions.

4.3 Weak Links

In thin-film high-T_c superconductors the critical current through a strip of film is directly proportional to the width of the film. For a certain critical current density, J_c, the critical current, I_c, decreases as the width of the film is reduced. If the film suddenly constricts from a few μm to a few nm the I_c is dramatically reduced at the constriction point, leading to a weak link in the material. With the proper layout the constriction point is Josephson coupled and exhibits most of the Josephson junction properties. Constriction junctions can be use to create Josephson Junctions for thin-film devices. Whether these types of junctions are magnetically linked is still under investigation.

Grain-boundaries occur due to the anisotropic nature of high-T_c superconductors, with a symmetric intrinsic grain-boundary (SGB) and a basal-plane-faced (BPF) intrinsic grain-boundary shown in Figure 4.2. Lattice mismatches cause the critical current density to differ at each side of the boundary, leading to a discontinuity in the film as describe in Section (4.2). In improperly prepared films these boundaries occur randomly, severely degrading the performance by limiting the current density ($10 - 100\text{A/cm}^2$). Properly prepared films have a current density of about 10^6A/cm^2 at 77 K [1]. These grain-boundaries cause a reduction of the critical current density, J_c, and are Josephson weak links [27]. The critical current is a function of the degree of orientation between the two crystals. The Josephson effect occurs in the c-axis, and is an intrinsic behaviour of high-T_c superconductors. Grain-boundary junctions are used to manufacturing single layer devices, instead of using the multilayer approach required by the low-T_c devices.

Most of the high-T_c superconductors devices sold use grain-boundary junctions produced by using bicrystal substrates.

4.4 HTS Substrates

To form a reliable superconducting film, YBCO must be deposited onto a suitable substrate [1]. The most widely used substrates are MgO, AlO_2, $SrTiO_3$ [21], $LaAlO_3$ and $NdGaO_3$. Substrates must be

chemically and structurally compatible with the superconducting film that is to be deposited. During thermal cycling the substrates and films are cooled from room temperature to as low as 5 K. Deposition of YBCO can occur at temperatures above $800°C$ and the substrate should be stable at such high temperatures. The substrates must be capable of handling repeated thermal cycling without crumbling or cracking, otherwise the devices would have an unacceptably short life expectancy. The films and substrates must have identical thermal expansion coefficients to prevent the film from mechanical shearing during cooling. For deposition the crystal lattice of the deposited film and substrate must match for the film to grow epitaxially, with the correct orientation. The orientation (001) is optimal for YBCO to grow in the c-axis on the substrate. On (100) orientated perovskite substrates it is possible to grow (100) or (001) orientated YBCO films, where, on (110) orientated substrates, it is possible to grow (110) or (103) orientated films. The orientation is dependent on the substrate's temperature and pressure during deposition.

On MgO, with (100) and (110) orientation, YBCO will tend to grow along the c-axis, irrespective of deposition temperature or pressure. MgO has a significant lattice mismatch when used with perovskite crystals, but it is relatively inexpensive and has a thermally independent dielectric constant, $\epsilon = 10$. AlO_2 has a high chemical reactivity. For an in-depth study of substrates selection for high-T_c superconducting thin films, please refer to [28].

4.5 HTS Deposition Techniques

High-temperature superconductors can be manufactured in bulk form or as thin films on a substrate. The material in bulk form can be used to create high current superconducting wires and other applications that specifically avoid the Josephson effect for maximum current density. The thin film devices are of more interest as they are used to create superconducting electronics. In Sections (4.2) and (4.3) the behaviour of anisotropic superconductors is discussed. When creating thin film devices, the film must only exhibit the Josephson effect where desired. Random weak links can lead to lower device performance, lower critical current or result in a malfunctioning device [27]. To produce suitable films for manufacturing SQUIDs, the composition of the YBCO film must be kept within tight constraints during deposition. Any impurities or contamination usually result in unstable and unusable devices. Depositing thin YBCO films on a substrate requires both skill, care and a good understanding of the growth characteristics of perovskite crystal structures.

There are various techniques to produce thin film devices. The current techniques employed are pulsed-laser deposition and inverse cylindrical dc magnetron sputtering. These processes are called in-situ techniques, where the basic crystalline structure and phase are formed during deposition. To improve the chance of achieving superconductivity, these substrates are annealed after deposition to ensure that the YBCO has the correct oxidization and phase. In-situ deposition usually results in smoother film surfaces than those obtained using ex-situ techniques.

The in-situ deposition techniques require that the substrate be heated to high temperatures. Even substrate heating can only be achieved by bonding the substrate to the heater by using silver paste, allowing only single sided devices to be the manufactured.

After the film has been deposited, it is of the utmost importance to prevent moisture in the air from damaging the YBCO film. The film must be transported inside a tightly sealed container with a drying agent (desiccant), preferably with an inert gas replacing the air and providing an inert environment. A vacuum chamber containing a desiccant is suitable for long-term storage, with the vacuum preventing environmental contamination and the desiccant absorbing any moisture in the event of a breach. When YBCO is exposed to the atmosphere, the moisture in the air causes a surface reaction layer to form [29].

The surface reaction between moisture and YBCO causes a reduction in the Cu concentration inside film, ultimately preventing the film from becoming superconductive.

The effect of exposure to air was observed in thin film YBCO superconductors with embedded Josephson junctions. Initially the film had a dark-gray colour and the RSJ voltage-current characteristic shown in Figure 2.9 was prominent. After the sample was exposed to the atmosphere for a day, the colour had turned to a lighter shade of gray and the voltage-current characteristic had all but disappeared. After an additional week of atmospheric exposure, the film had nearly turned translucent and no superconductivity could be detected. Figure E.6 on p.156 shows how dark the the YBCO film should be after deposition and before environmental damage can occur. The YBCO film in Figure E.5 on p.156 was not properly stored and became semitransparent due to atmospheric exposure.

4.5.1 Pulsed-Laser Deposition

In pulsed-laser deposition (PLD) a target of YBCO or other material is ablated with the use of a high power laser [1, 18, 30]. The resulting vapor is deposited on a substrate, usually a heated square of MgO.

The YBCO target is placed inside the PLD chamber on a rotating spool, preventing the laser from pitting the material. This allows for both a longer operational lifetime for the bulk YBCO source and a more uniform plume. The high power laser is focused onto a small spot on the edge of the rotating target and a high vacuum is pulled. External gases, usually oxygen, are injected into the chamber to provide a reactive agent for the plume.

If the energy of the laser is high enough and the pulse short enough, the YBCO will separate (ablate) from the surface of the source with no significant heating to the bulk material. The ablated material is ejected perpendicularly from the surface and forms a plume that encompasses the heated substrate. This plume reacts to any external gases added to the chamber, changing the chemical composition. The plume can then condense onto the substrate and the YBCO is grown along the substrate's crystalline structure. This deposition is relatively slow, typically in the order of $100\,\text{Å}/\text{s}$. Ideally this plume consists of ions or angstrom sized particles to ensure a smooth surface film. If the energy of the laser is too small there is the possibility of larger particles of YBCO ablating and depositing onto the substrate. This causes a greater surface roughness and polycrystalline islands to form in the film. If the laser energy is too large the resulting ions will have too much energy. These energetic ions bombard the target and damage the growing film. There is thus an optimum laser energy where the ablation forms ions energetic enough to react to the applied gases, but not energetic enough to damage the film.

By nature the plume has an irregular shape and inconsistent distribution. When this plume is deposited on the substrate, the irregularity in plume density leads to different growth rates and film thicknesses. This can be avoided by rotating both the sample and target, averaging out the difference.

The PLD has been superseded by inverse cylindrical dc magnetron sputtering. The magnetron sputtering deposition results in higher deposition rates, lower surface roughness and higher T_c.

PLD takes place in a near vacuum with relatively low oxygen content, creating YBCO films with the incorrect crystalline phase. After YBCO deposition the substrates are usually annealed to oxidize the film. Annealing at the correct temperature and pressure in a pure oxygen environment causes oxygen to diffuse throughout the YBCO film, resulting in the correct material phase and a higher T_c.

4.5.2 Magnetron Sputtering

Magnetron sputtering is similar to PLD with an ion plasma replacing the laser source [1]. Sputter deposition uses chemically inert argon ions, energizes the argon to form a plasma. These ions are accelerated by a dc magnetron and bombard a cylindrical YBCO target, tearing out the atoms. These atoms form a plume that deposit onto the heated substrate.

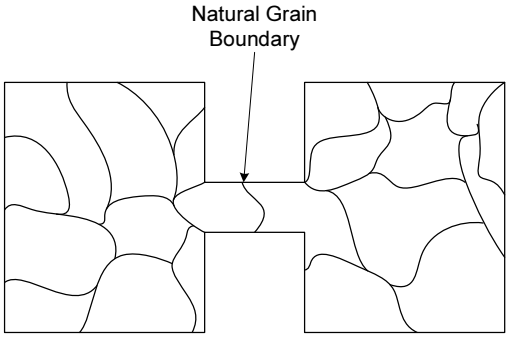

Figure 4.3: Natural grain boundary Josephson junction.

Magnetron sputtering takes place in a near vacuum with relatively low oxygen content, creating YBCO films with the incorrect crystalline phase. After YBCO deposition the substrates are usually annealed to oxidize the film. Annealing at the correct temperature and pressure in a pure oxygen environment causes oxygen to diffuse throughout the YBCO film, resulting in the correct material phase and a higher T_c.

4.6 HTS Natural Grain-Boundary Josephson Junctions

In polycrystalline YBCO films there are randomly distributed weak links throughout the film, and the material only exhibits a high current density for wide films, as discussed in Section (4.3) [27]. Figure 4.3 shows how natural grain-boundary junctions are created by using polycrystalline YBCO and constricting the film at a specific point. This isolates a few weak links in the film and the constriction functions as a Josephson junction. The inherent randomness of the grain-boundaries results in varying parameters for the junctions. It is thus impossible to characterize these junctions for design purposes, and their use is restricted to rf SQUIDS. The random natural grain-boundary junctions are avoided when creating dc SQUIDs.

4.7 HTS Ramp-Edge Multilayer Josephson Junctions

The high-temperature superconductor ramp-edge multilayer Josephson junctions (JJ) in Figure 4.4 are structurally similar to those used by low-temperature multilayer junctions [1, 31]. Both designs use the superconductor-normal-superconductor (SNS) or superconductor-insulator-superconductor (SIS) interface as described in Section 2.8. To form the ramp-edge multilayer JJ, two YBCO layers are separated by insulating material. A metal layer acts as a barrier between the two YBCO layers and one of the substrate materials described in Section 4.4 is used as an insulator. This type of junction is defined as an extrinsic interface, as the Josephson effect is created extrinsically to the YBCO.

With low-temperature multilayer junctions there are usually a significant capacitance between the parallel superconducting plates. This results in the resistively- and capacitively-shunted junction (RCSJ) (Section 2.8.2) where an additional external shunt resistance is required to reduce hysteresis. High-temperature multilayer junctions do not exhibit this behaviour and the capacitance tends to be insignificantly smaller. These junctions are considered to be a resistively-shunted junction (RSJ) (Section 2.8.4) and exhibit the voltage response to a dc current given by (2.8.20). RSJ's are ideal for manufacturing SQUID magnetometers as they tend to have a large I_cR_n product and no hysteretic behaviour. Moeckly *et al* found a critical current spread of 10% for YBCO ramp-edge junctions [32].

The advantage of this type of junction is that it can be placed virtually anywhere on the substrate, greatly simplifying the design of a SQUID. The disadvantage is that production of multilayer devices requires several deposition and etching steps, increasing the complexity of production. Deposition of the

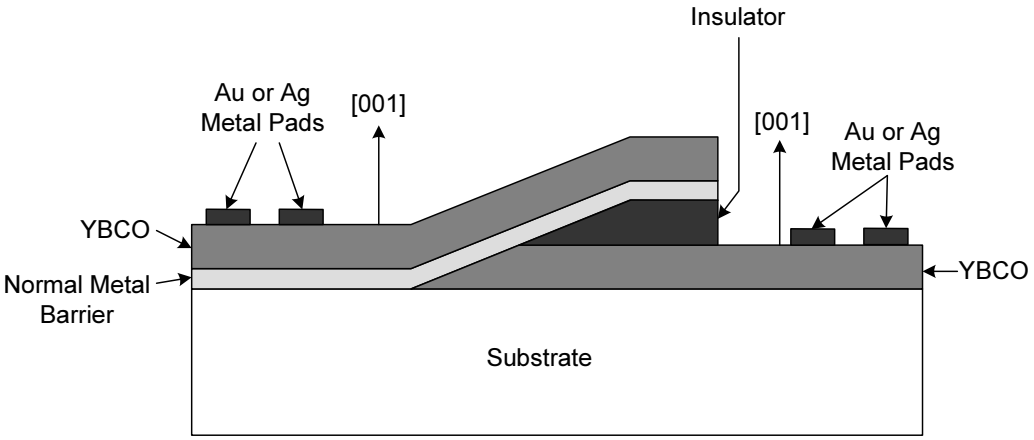

Figure 4.4: Cross-section of a ramp-edge SNS junction. The metal sandwiched between top and bottom YBCO layers on the ramp forms the actual SNS junction.

metal layers can damage the YBCO layers already present and ion argon milling can damage the ramp edge and any other exposed materials. This process is not currently viable as it is extremely complex and material intensive. Each layer requires a unique photolithographic mask that has to be aligned with high precision. Using the Atomic Force Microscope (AFM) in place of photolithographic masks to pattern the photoresist before etching should greatly simplify this process.

4.8 HTS Grain-Boundary Josephson Junctions

During film deposition YBCO crystals will grow on top of a (100) MgO substrate in a c-axis orientation. On a single uniform substrate the YBCO film will have a uniform phase and highly orientated crystal structure, resulting in a high-T_c film with a uniform high critical current density and no unwanted weak links. By varying the substrate's orientation or chemical composition the YBCO film can be grown along a different orientation.

Bicrystal junctions are formed on bicrystal substrates in Figure 4.5(a). To manufacture bicrystal substrates a uniform substrate is physically cut and rejoined at an angle. After the substrate has been cut and rejoined, there will be a different substrate orientation on both sides of the joint. When YBCO is deposited onto the substrate, it will grow along the substrate's orientation, resulting in an orientation mismatch in the YBCO crystal lattice at the joint. If the angle between the substrates is large enough, the orientation mismatch can lead to a Josephson coupled weak link known as a grain-boundary junction. The Josephson coupling occurs due to the anisotropic behaviour of high-T_c superconductors (Section 4.2) and is known as an intrinsic interface, since the weak links and grain-boundaries are intrinsic effects in YBCO. The Josephson effect occurs in the c-axis and the grain-boundary must be designed to orientate the lattice mismatch accordingly. For a comprehensive study on the orientation dependence of the critical current density J_c in YBCO grain-boundaries, please refer to [27] and [17].

Biepitaxial junctions are formed on biepitaxial substrates in Figure 4.5(b) [33]. To manufacture biepitaxial substrates a thin layer, known as the seed layer, is deposited onto the substrate to change the orientation of the substrate. This layer is placed at points where the designer wants to create junctions. A buffer layer is deposited on top of both the seed layer and the rest of the substrate, creating a suitable substrate to grow YBCO, as well as reducing the slope at the interface. The buffer layer orientates itself along the layer that it covers, resulting in a different substrate orientation on both sides of the interface. When YBCO is deposited onto the substrate, it will grow along the substrate's orientation, resulting in an orientation mismatch in the YBCO crystal lattice at the interface of the seed layer. This interface may

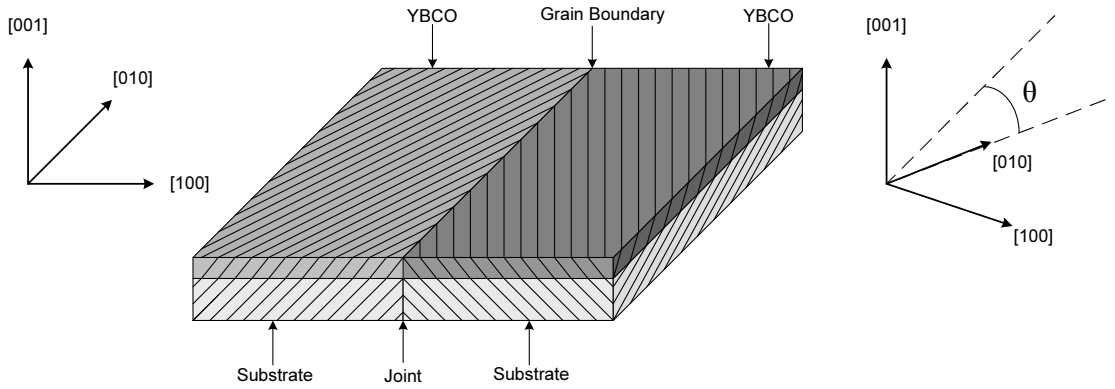

(a)

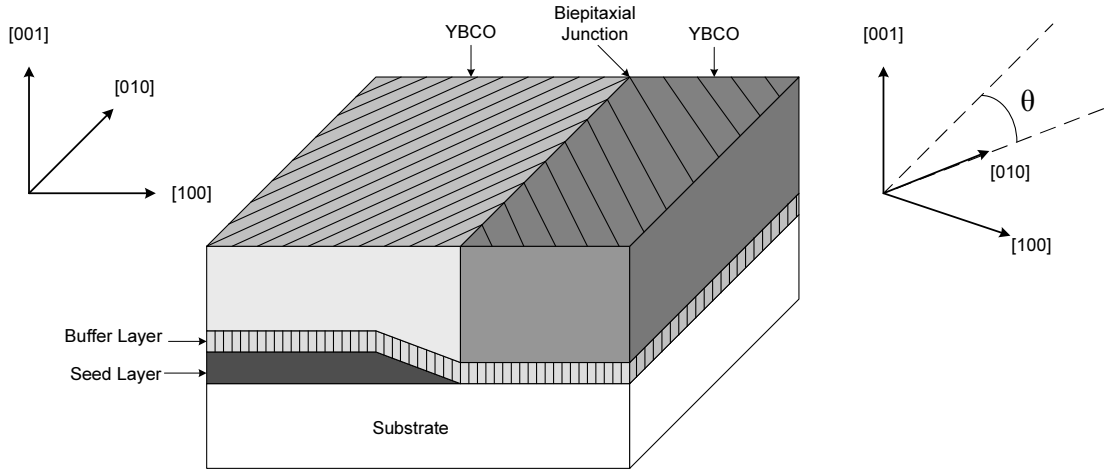

(b)

Figure 4.5: Cross-section of YBCO deposited onto (a) a bicrystal substrate, and (b) a biepitaxial substrate. The grain boundary forms at the respective interfaces with a lattice mismatch angle Θ.

look like a step-edge, but the step height is smaller than the YBCO's film thickness. If the angle between the substrates is large enough, the orientation mismatch can lead to a Josephson coupled weak link known as a grain-boundary junction. The Josephson effect occurs in the c-axis and the grain-boundary must be designed to orientate the lattice mismatch accordingly.

The critical current density of a grain-boundary junctions is dependent on the grain-boundary's orientation mismatch angle. These grain-boundaries have been measured and are known to exhibit the properties of Josephson Junctions. The critical current is also extremely sensitive to small magnetic fields [27].

Biepitaxial substrates require multiple depositions in order to achieve the desired substrate layout before YBCO deposition They are more versatile for the design of SQUIDs and other superconducting electronic devices and can be manufactured by the same processes used for in-situ YBCO deposition. Bicrystal substrates require equipment capable of joining cut substrates, limiting the designs possibilities, but do not require multiple depositions

SQUIDs that utilize bicrystal grain-boundary junctions are relatively easy to create, especially with commercially available pre-manufactured substrates. These substrates are relatively expensive and can only be used for a single SQUID with a pickup loop. They are also one-shot so that if a defective YBCO layer is deposited it is nearly impossible to reuse the substrate successfully. The bicrystal Josephson junctions for YBCO have been well defined, can be precisely manufactured, are reproducible and exhibit no intrinsic capacitance across the boundary. YBCO bicrystal junctions are resistively-shunted junction

(RSJ) (Section 2.8.4) with a critical current and shunt resistivity defined by the dimensions of the junction [34].

The fixed bicrystal grain-boundary line complicates the layout of SQUID sensors. Josephson junctions can only be created across this bicrystal line, so the SQUID's layout must be designed with this in mind. The layout of the bicrystal grain-boundary also limit the freedom of the position and size of the pickup loop when creating superconducting film with no weak links. This is usually achieved by using wider film widths.

4.9 HTS Step-Edge Josephson Junctions

Step-edge junctions are similar to grain-boundary junctions, with a change in the vertical height replacing the grain-boundary [1]. These junctions mostly behave like RSJ junctions [35]. There are a few different techniques used to manufacture step edges.

The first type of step-edge is when a layer is deposited on top of the substrate and the excess it milled away one one side. The deposition layer is preferably composed of the same or similar material to the substrate and along the same orientation. In this example MgO with (100) orientation is used. After milling there will be two layers left over at different heights, separated by a ramp with a slope angle α. For this example the angle of the slope is defined as $\alpha = 45°$. If the thickness of the superconducting film is less than the height of the step, the minimum angle to create weak links is $\alpha > 10°$ When YBCO is deposited onto the milled substrate, it will grow along a (100) c-axis orientation parallel to the c-axis of both the top and bottom layer. At the edges of the steps the YBCO will orientate itself at 90° (010) to the YBCO layer and then again at 90° (100) in a step-wise fashion until both edges have been joined.

Each (100) to (010) and (010) to (100) crystal reorientation will produce a distinct weak link junction. There is a minimum of two distinct weak link junctions for any step-edge, one at each end of the slope. These junctions do not always have exactly the same characteristics such as the critical current density or shunt resistance. The top and bottom grain-boundaries have been shown not to have the same characteristics, leading to the multiple weak links in series expressing their Josephson effects at distinctly different currents. The step-edge junction does not display the same current-voltage relation as with the RSJ (2.8.36). While step-edge junctions tend to behave similarly to RSJ at higher temperatures, at low temperatures they start to behave more like underdamped RCSJ with $\beta_c >> 1$.

Another type of step-edge is created by cutting a trench into the substrate. This trench can be either milled or laser cut to the desired shape at virtually any place on the substrate. The cross section of the trench defines its behaviour, with narrow trenches with steep edges behaving differently trenches with shallower edges or a flat section in the middle. The advantage of trenching is that the junctions can be placed virtually anywhere on the substrate, simplifying the design of superconducting devices. The disadvantage is the amount of series weak links produced, usually with two weak links per edge resulting in four weak links per trench. Reproducing the parameters of a junction is also difficult, with a larger uncertainty of junction parameters when compared to bicrystal junctions. Luine *et al* found a critical current spread of 30%-50% for YBCO step-edge junctions [35].

Step-edge junctions have the advantage of being placed anywhere on the substrate and thus simplify the design. They can be manufactured on a variety of substrates, as opposed to bicrystal substrates that are expensive or difficult to manufacture.

4.10 Conclusion

Before manufacturing or purchasing a dc SQUID magnetometer, it is important to understand the properties of the underlying materials. The techniques used to create the SQUID junctions and pickup loops

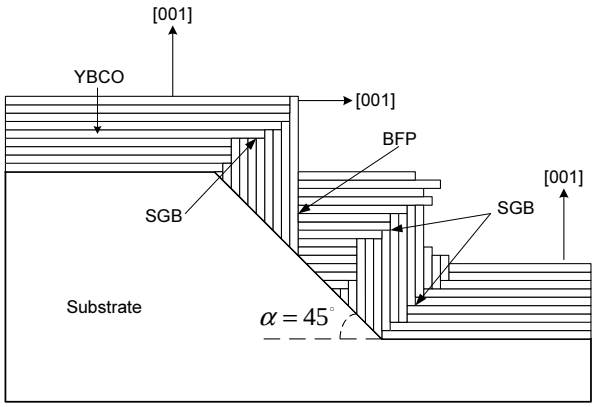

(a)

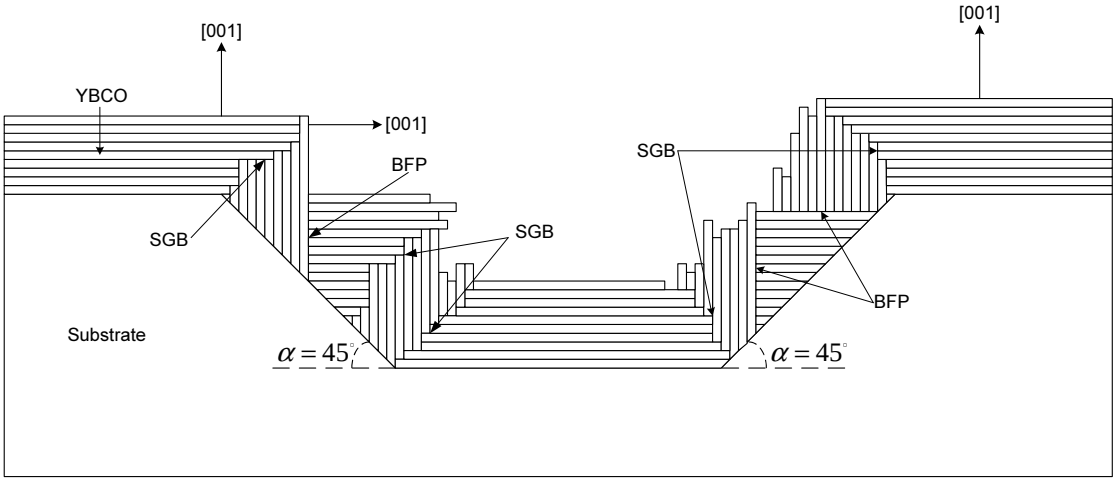

(b)

Figure 4.6: Schematic representation of YBCO deposited onto (a) a step-edge, and (b) a trench. A weak link is formed by the symmetric intrinsic grain-boundary (SGB) and by the basal-plane-faced (BPF) intrinsic grain-boundary.

can result in sensitive magnetometers with low intrinsic noise, or in films that create excessive noise and unbalanced, capacitive junctions with hysteretic response. The quality of the YBCO film and the type of junction used is thus directly related to the performance of a high-T_c dc SQUID magnetometer, where the critical current and shunt resistance dictates the performance (3.2.44).

The two deposition techniques described are currently in use at the University of Stellenbosch. It is important to produce very high quality YBCO films in order to reduce pinning sites and increase the critical current throughout the material. Producing a homogeneous crystal structure will also prevent unwanted weak links inside the material that can reduce the performance and increase noise. There is an ongoing study to improve these films and produce high quality junctions and SQUID devices.

The substrate used for deposition will dictate how the crystal will grow, orientate itself along the lattice and ideally forming a homogeneous crystal structure. For grain-boundary junctions a bicrystal or biepitaxial substrate can be used, making use of the anisotropic nature of YBCO. Both substrates result in definable junctions with the critical current and shunt resistance are related to the width of the junction. The grain-boundary junctions have no intrinsic capacitance and are ideal for magnetometers.

The type of junction used has a significant effect on a SQUID. The ramp-edge multilayer junction requires multiple depositions and increasing the difficulty and cost to produce junctions. Step-edge junctions are difficult to characterize and reproduce accurately, and should be avoided.

Chapter 5

Noise

5.1 Introduction

Superconductors have excellent noise characteristics when compared to semiconductors, but they are not noiseless. Both the intrinsic noise of the sensor and the extrinsic noise of the control system can severely limit the performance of dc SQUID magnetometers. The origin of noise in dc SQUID magnetometer must be explored in order to design a SQUID microscope with the highest possible sensitivity.

The various noise sources are discussed in this chapter. Only by understanding the origin of noise can its effect on the device be predicted and minimized or even eliminated. Each noise source places a unique constraint onto the SQUID, and either increasing noise, forcing a design compromise or reducing the sensitivity of the SQUID. The design and implementation of a SQUID is therefore highly dependent on its noise characteristics, and novel techniques have been developed to increase the magnetic field resolution without increasing noise. Even with a highly sensitive magnetometer the overall performance of the SQUID will ultimately depend on the SQUID electronics, discussed in Chapter 7, and the cooling system, discussed in Chapter 6

There are two general types of noise in a dc SQUID, white noise and 1/f noise. White noise has a constant power spectrum from very low to very high frequencies and plays a significant role on the performance and design of a dc SQUID. 1/f noise is a frequency dependent power spectrum, reducing as the frequency increases, and is thus only important at low frequencies.

5.2 Telegraph Noise

Telegraph noise (telegraphing) sometimes occurs in superconductors [1], consisting of random pulses of variable length and equal height. Telegraphing is different to shot noise. Shot noise behaves like white noise and results in minor voltages developing across the junction. When a SQUID experiences telegraphing it will suddenly generate a relatively larger potential for an undeterminable time, causing SQUID electronics to require resetting. The time between appearances as well as the pulse length of the potential is unknown, but the magnitude of the potential is always the same. Telegraphing is due to some manufacturing error, and there is no known way to remove this type of noise short of replacing the dc SQUID. The appearance of telegraphing marks the demise of a practical SQUID.

5.3 White Noise Definition

White noise is a result of random processes such as the flow of charges or thermal vibrations in a component at a temperature above 0 K. It can be generated inside a device (intrinsic) or be the result of noise coupling from an external source (extrinsic). The noise level present in a system sets the lower

limit for an output signal strength that can be measured. The white noise intrinsic to a SQUID is either shot noise or thermal noise. Both shot and thermal noise are well understood and are defined in terms of their noise power spectral density. Voltage noise spectral density is given in terms of voltage, S_v in units of V^2/Hz, which is interchangeable with current, $S_i = S_v/R^2$ in units of I^2/Hz, using $V = RI$. For white noise the power spectrum density is constant with frequency, resulting in a flat spectrum from very low to very high frequencies [1, 36]. The mean value of noise is assumed to be zero unless otherwise specified. The rms value is non-zero and is given by

$$x_{\text{rms}} = S_x^{1/2}\sqrt{B}, \tag{5.3.1}$$

in units of $\text{X}/\sqrt{\text{Hz}}$, where B is the bandwidth of the device. White noise sources can be treated as Gaussian distributed random variables, and their powers are additive. The peak-to-peak noise for Gaussian-distributed noise can be approximated as about 6 times the rms noise, so

$$x_{\text{peak}} \approx 6S_x^{1/2}\sqrt{(B)}. \tag{5.3.2}$$

5.4 Josephson Junction Shot Noise

Shot noise is produced when current flows through a potential barrier (2.7.1), and was originally found to occur in diodes and transistors. Shot noise is also known as quantum noise, and is generated by zero-point energy fluctuations inside the shunt resistance of the junction [1]. The shot noise constant spectral density, S_i, is given by

$$S_i\,(f) = 2eI_{DC} \tag{5.4.1}$$

where e is the electron's charge and I_{DC} is the average current. The shot noise has a constant noise spectral density that is independent of frequency, and is considered to be white noise.

5.5 Thermal Noise

5.5.1 Introduction

Thermal noise plays a significant role in all high-T_c types of SQUID sensors [37]. At 77 K thermal noise is substantial enough to restrict the design possibilities of both the Josephson junction and the SQUID. For the RCSJ model thermal noise can lead to rounding of the I-V characteristics or even cause the junction to decouple. A properly designed SQUID must have the lowest possible noise, so it is important to specify the effect of thermal noise on the total noise in the system. The SQUID loop is highly susceptible to thermal noise, with excessive thermal noise from the SQUID loop causing the quantum interference to become unobservable. Thermal fluctuation from cooling the superconductor can also be picked up by the SQUID, causing significant measurements errors. The cooling systems and their effect on the SQUID will be discussed in Chapter 6.

5.5.2 Josephson Junction Thermal Noise

Thermal noise in a Josephson junction occurs due to Brownian motion of the charge carriers, and is known as Josephson or Nyquist noise. The shunt resistance of a RCSJ is used to define the voltage noise power density, S_v, so that

$$S_v\,(f) = \frac{4hfR}{e^{hf/k_BT} - 1} \tag{5.5.1}$$

$$= 4k_BTR_n, \tag{5.5.2}$$

where $h = 6.626 \times 10^{-34}(\mathrm{J} - \mathrm{sec})$ is Planck's constant, $k_B = 1.38 \times 10^{-23}(\mathrm{J/K})$ is Boltzmann's constant, f is the center frequency of the bandwidth in Hz, T is the absolute temperature, and $R = R_n$ is the shunt resistance of the junction [36]. The voltage noise spectral density is independent of frequency [1]. The rms noise voltage for a junction is

$$v_{\mathrm{rms}} = \sqrt{4k_B T R_n B}, \tag{5.5.3}$$

where B is the bandwidth of the system in Hz. Another way of examining thermal noise in a junction is to consider the current noise spectral density, S_I, so that

$$S_I(f) = \frac{4k_B T}{R_n}, \tag{5.5.4}$$

using the same parameters as (5.5.2). At low biasing currents the noise current rounds out the I-V curve and reduces the apparent critical current.

The design of a Josephson junction is restricted by thermal noise affecting critical junction parameters. The thermal noise for the junction energy gap is given by (2.7.1) and can be approximated as $k_B T$, whereas the maximum coupling energy of the junction is given by (2.8.16) [38, 16, 1]. For a reasonable Josephson coupling the coupling energy must be larger than the thermal noise, $I_c \Phi_0 >> k_B T$. The relation between the energy gap and junction energy is given by

$$\Gamma = \frac{\Delta(0)}{W_{J_0}} = \frac{2\pi k_B T}{I_c \Phi_0}. \tag{5.5.5}$$

To reduce the thermal noise of a junction or a SQUID and ensure a reasonable Josephson coupling, Γ should be restricted to $\Gamma << 1$. This is known as the small-fluctuation limit since thermal noise will only causes minor fluctuations in the junction.

5.5.3 SQUID Voltage Noise

Thermal (white) noise of a dc SQUID is different to that of a single Josephson junction [1, 25, 19, 13]. The SQUID has two parallel junctions inductively coupled to form the SQUID loop. For a dc SQUID the voltage noise spectral density is approximately four times its operating temperature:

$$S_v(f) = 16 k_B T R_n. \tag{5.5.6}$$

If the thermal noise due to the SQUID loop inductance becomes significantly large, then the SQUID will have a significantly reduced sensitivity. A properly designed SQUID must have the lowest possible noise while still maintaining a high sensitivity, so the effect of thermal noise and the design limits it places on the SQUID loop must be considered. The magnetic energy stored in a superconducting loop with a single fluxon trapped is approximately

$$W_s \approx \frac{1}{2}\frac{\Phi_0^2}{L_{SQ}}, \tag{5.5.7}$$

where L_{SQ} is the SQUID loop inductance. The thermal energy, ε_T, at temperature T is

$$\varepsilon_T = \frac{1}{2} k_B T, \tag{5.5.8}$$

while for an inductor the mean energy per Hz is

$$\varepsilon_L = \frac{1}{2} L_{SQ} I_n^2, \tag{5.5.9}$$

where I_n is the average current through the loop's inductor. In this case I_n will represent the noise current flowing through the inductor. To understand the effect of thermal energy on the noise current, the thermal energy ε_T is directly compared to energy of the inductor ε_L,

$$\varepsilon_T = \varepsilon_L \tag{5.5.10}$$

$$\Rightarrow I_n^2 = \frac{k_B T}{L_{SQ}}. \tag{5.5.11}$$

The Φ-I coupling of a superconducting loop's inductance is given by $\Phi = LI$, so for the noise current in (5.5.11) the equivalent flux noise is

$$\Phi_n^2 = (L_{SQ} I_n)^2 = L_{SQ} k_B T. \tag{5.5.12}$$

The SQUID's periodic V-Φ function is given by (3.2.37) and limits the equivalent flux noise to $|\Phi_n| \leq \Phi_0/2$ for normal operation. To keep the thermal noise below the sensitivity of the SQUID, the thermal energy (5.5.8) must be significantly less than the magnetic energy (5.5.7), so the loop inductance is limited to

$$L_{SQ} << \frac{\Phi_0^2}{4 k_B T}. \tag{5.5.13}$$

If the constraint set by (5.5.13) is not maintained, then the quantum interference will be unobservable. The loop inductance of a SQUID operating at a temperature of $T = 77$ K must be kept below $L_{SQ} < 1$ nH to restrict thermal noise. Consequently, the maximum pickup area of the SQUID, A_{SQ}, will also be constrained. It is important to keep the noise of the system as low as possible to improve the sensitivity of the SQUID. This is best done by increasing the effective area, A_{eff}, of the SQUID without increasing the inductance.

5.5.4 SQUID Flux Noise

Thermal flux noise is produced by the uncorrelated hopping of flux vortices amongst pinning sites in the films [39, 40, 19]. Flux noise is a white voltage noise across the SQUID, where $S_\Phi^{1/2}(f)$ is frequency independent down to a frequency of about 1 Hz, below which it tends to scale at 1/f. For the scope of this thesis flux noise will be treated as white noise only, with $S_\Phi(f) = S_v(f)/V_\Phi^2$ due to $\Phi = Li$. A SQUID with an optimal screening parameter, $\beta_L = 1$, has a thermal flux noise spectral density:

$$S_\Phi = \frac{16 k_B T L_{SQ}^2}{R_n}, \tag{5.5.14}$$

where k_B is Boltzmann's constant, T is the absolute temperature, and R_n is the junction shunt resistance.

With a properly manufactured SQUID the flux noise can be greatly reduced. One way to reduce the thermal flux noise of a SQUID is to increase the value of the shunt resistance, R_n. Using an RSJ junction will remove the need for the secondary shunt required by the RCSJ junction to maintain $\beta_c << 1$, resulting in a higher shunt resistance and lower flux noise. Another way to improve thermal flux noise is to create a higher quality superconducting film, thereby reducing the density of pinning sites.

5.5.5 SQUID Energy Resolution

The energy resolution of the SQUID, $\varepsilon(f)$, is used to compare the performance of different dc SQUIDs [1, 19]. Energy resolution, also known as the noise energy, is given by

$$\varepsilon(f) = \frac{S_\Phi(f)}{2L_{SQ}} \tag{5.5.15}$$

$$= \frac{8k_BTL_{SQ}}{R_n} \tag{5.5.16}$$

$$\approx 16k_BT\sqrt{L_{SQ}C}. \tag{5.5.17}$$

The energy resolution can be improved by reducing the temperature, T, reducing the SQUID loop, L_{SQ}, or increasing the shunt resistance, R_n. If the SQUID is designed for $\beta_L = 2L_{SQ}I_c/\Phi_0 = 1$ and $\beta_c = 0$, then (5.5.15) can be further reduced to

$$\varepsilon(f) \approx \frac{4k_BT\Phi_0}{V_c}, \tag{5.5.18}$$

where $V_c = I_cR_n$ is introduced by (2.8.20).

5.5.6 SQUID Magnetic Field Noise

The rms magnetic field noise, B_N, also called the magnetic field resolution, is an important figure of merit for dc SQUID magnetometers [1, 19]. Magnetometers are used in applications where the magnetic field noise of a bare SQUID is too high, especially in cases when high spatial resolution is required. SQUID magnetometers are designed to have a large pickup loop while maintaining the thermal flux noise spectral density of a small SQUID loop. B_N forms a basis to compare different magnetometers, where the rms magnetic field noise is given by

$$B_N(f) \equiv \sqrt{S_B(f)} \tag{5.5.19}$$

$$= \frac{\sqrt{S_\Phi(f)}}{A_{eff}}, \tag{5.5.20}$$

where A_{eff} is the effective area of the SQUID.

By including an additional pickup loop, A_{pickup}, or increasing the outer dimensions of the SQUID washer, D, the apparent noise is reduced by a few orders of magnitude. Large-area washer and direct-coupled SQUIDs increase the effective area of their pickup loop (3.4.1) and (3.3.1), A_{eff}, while maintaining the magnetic field noise of only the SQUID pickup loop, which is S_Φ for a SQUID loop with area A_{SQ}. Multilayer devices tend to have the lowest magnetic field noise, but are costly and more difficult to manufacture than single layer devices.

5.5.7 Flux Trapping

A SQUID microscope must work in an unshielded environment, and in any unshielded environment there is always the presence of external magnetic flux that can disrupt the operation of the SQUID sensor. The magnetic flux can be from the earth's dc magnetic field or from larger ac or dc magnetic sources such as electric motors, PC power supplies or CRT monitors. When cooling the SQUID in an unshielded environment, the presence of a dc magnetic field will increase the low frequency $1/f$ noise, with even a few microtesla making a noticeable difference in noise. It has been found that as the film width of the

SQUID loop is reduced, the static magnetic field can rise without affecting the $1/f$ noise, with

$$B_T = \frac{\pi \Phi_0}{4w^2}, \tag{5.5.21}$$

where B_T is the threshold flux density, w the line width and Φ_0 a flux quantum.

The addition of slots and holes inside thicker line widths can also help to eliminate the additional $1/f$ noise and raise the threshold [41]. The applied flux will penetrate these artificial voids rather than couple with pinning sites in the film, reducing the amount of extra vortices created at pinning sites. With a properly manufactured SQUID the flux noise due to flux trapping can be greatly reduced. Improving the quality of the superconducting film will also reduce the density of pinning sites and improves the flux noise.

5.6 1/f Noise

For a dc SQUID that operates at very low frequencies the spectral density of the flux noise, S_Φ, tends to scale by $1/f$ below a certain frequency, usually around 1 Hz [39, 40, 1]. This noise spectral density varies inversely with frequency,

$$|f|^{-\alpha}, \tag{5.6.1}$$

where α is usually $(1.2 > \alpha > 0.8)$. For homogeneous materials the $1/f$ noise is represented by

$$\frac{S_i(f)}{\left(\bar{I}\right)^2} = \frac{S_v(f)}{\left(\bar{V}\right)^2} = \frac{\alpha_H}{f\bar{N}}, \tag{5.6.2}$$

where S_i is the shot noise, $\bar{I}$ is the mean current, S_v is the voltage noise spectral density, $\bar{V}$ is the mean voltage, α_H is Hooge's parameter which varies with material, and $\bar{N}$ is the total number of charge carriers in the material. The frequency where the white noise overlaps with the $1/f$ noise is called the corner frequency, f_c. There are two sources of $1/f$ noise, the thermal motion of vortices and critical current fluctuations. Other terms for $1/f$ noise are llf noise, flicker noise and excess noise.

5.6.1 Thermal Motion of Vortices

The first type of $1/f$ noise to be discussed is the flux noise described in Section 5.5.4 [40, 39, 1, 19]. Flux noise is white voltage noise generated by the dc SQUID, where $S_\Phi^{1/2}(f)$ is frequency independent down to the corner frequency, f_c, which is usually between about 1 Hz and 10 Hz, depending on the design and film quality. For frequencies below f_c the flux noise tends to scale at 1/f. Thermal flux noise is produced by the uncorrelated hopping of flux vortices amongst pinning sites in the films, occurring due to thermal activation [42]. These pinning sites occur naturally in the high-T_c superconducting films as defects in the crystal structure. A vortex can be trapped in this defect and then tends to hop to or between other pinning site if the thermal energy is sufficient. If the crystal is not c-orientated at random spots on the YBCO film due to improper deposition, then a pinning site will have formed. When a polycrystalline film with a high density of pinning sites is cooled in the presence of a magnetic field, there will be a higher number of vortices forming, resulting in higher noise. Cooling a high-T_c dc SQUID in the presence of the earth's magnetic field can result in a factor 50 $1/f$ flux noise power increase [19]. When the SQUID cooled in fields above a few μT, the $1/f$ flux noise spectral density, $S_\Phi^{1/2}(f)$, increases linearly with the applied field B_0 [43]. While low-T_c SQUIDs tend not experience this phenomenon at 4.2 K, a high-T_c SQUID operating at 77 K will exhibit significant performance degradation.

With proper manufacturing techniques the $1/f$ flux noise can be greatly reduced in a high-T_c dc SQUID operating at 77 K. Creating a higher quality epitaxial YBCO film will significantly reduce the

density of pinning sites when compared to polycrystalline film. Another technique used to reduce thermal noise is to incorporate slots and holes to expressly trap the flux during cooling, creating strong pinning sites and preventing vortices from hopping. Section 5.5.7 shows how the threshold flux density increases exponentially as the line width is reduced. By using a thinner line width the SQUID loop will exhibit a better noise performance. Flux dams have also successfully been used to lower the $1/f$ noise, and work by using a weak link inside the pickup loop to limit the circulating current [44, 19].

5.6.2 Critical Current Fluctuations

The second type of $1/f$ noise to be discussed, known as the llf noise, is the result of a junction with a fluctuating critical current and normal resistance [40, 39, 1, 19]. The normalized fluctuation of the shunt resistance R_n and the critical current I_c in grain-boundary Josephson junctions were found to be almost independent of the temperature and misorientation angle [45], and no correlation was found between the fluctuations of R_n and I_c. For the two parallel junctions in a dc SQUID the critical current can fluctuate concurrently (in phase) and produce a potential across the SQUID, or fluctuate out of phase causing a circulating current to flow in the SQUID loop. The spectral density of the flux noise is

$$S_{\Phi,in-phase} \cdot f \approx \left(\frac{R_n}{V_\Phi}\right)^2 S_I f \tag{5.6.3}$$

$$S_{\Phi,out-of-phase} \cdot f \approx \frac{\Phi_0^2}{8}\frac{\beta_L}{I_c} S_I f. \tag{5.6.4}$$

Both the in-phase and out-of-phase S_Φ scale linearly with $1/f$. The in-phase noise offset will cause the output voltage to shift as shown in Figure 5.1(a), increasing or decreasing the offset of the V-Φ output. The out-of-phase noise offset will cause a shift in the apparent flux as shown in Figure 5.1(b).

Current bias reversal and flux modulation are used to reduce this llf noise for low frequency applications [41, 40]. If the current bias is reversed above the corner frequency at f_c there will be a dramatic reduction in the $1/f$ noise. For each SQUID the optimal bias reversal frequency is obtained by trial and error. A reduction of about 100 times was achieved by [40] by using bias reversal.

5.7 Other Sources of Noise

Radio frequencies (RF) coupling with the Josephson junctions result in Shapiro steps, while coupling with the SQUID and pickup loop results in rounding of the V-Φ curve [19]. By changing the V-Φ relation the voltage sensitivity V_Φ is affected, resulting in reduced sensitivity. Current bias reversal and the flux modulation caused by operating a SQUID in a flux-locked loop can be used to reduce most of the RF interference. The rf noise can also be reduced by shielding the SQUID with mu-metals, but movement in the earth's magnetic field will cause eddy currents to form inside the shield. If a cryocooler imparts force on the SQUID and shield in the form of vibration, then the effect of eddy currents in the shielding will be significant.

Temperature fluctuations and drift can cause a substantial change in the output of a dc SQUID, resulting in noise or imprecise readings. The temperature change can be caused by the oscillating coolant in a regenerative cycle cryocooler (Section 6.4), or by a change in ambient pressure in a cryostat changing the cryogen's temperature (Section 6.3). The critical current of a junction is temperature dependent, causing it to oscillate with temperature. Bias current reversal is used to remove this effect.

The largest problem with temperature fluctuations is that it affects the effective area of the SQUID, A_{eff} [19, 46]. The temperature dependence of the London penetration depth $\lambda(T)$ (2.4.2) causes A_{eff} (3.3.1 and 3.4.2) to vary with temperature. If the SQUID is operating in an unshielded environment, especially with a SQUID microscope, then by changing the effective area in an ambient magnetic field

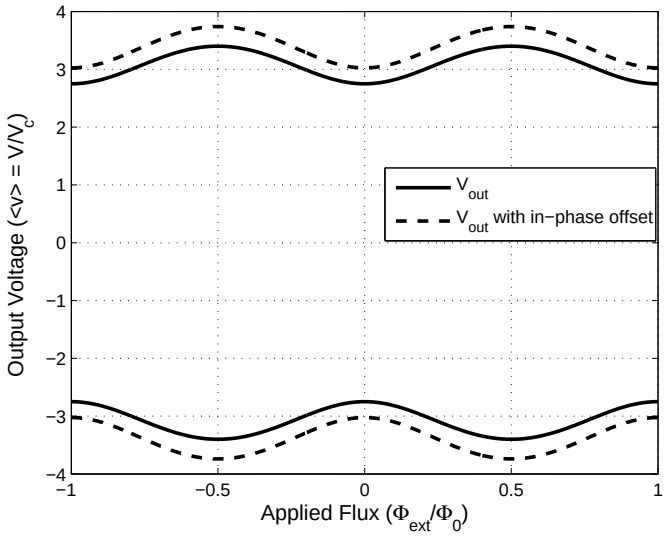

(a)

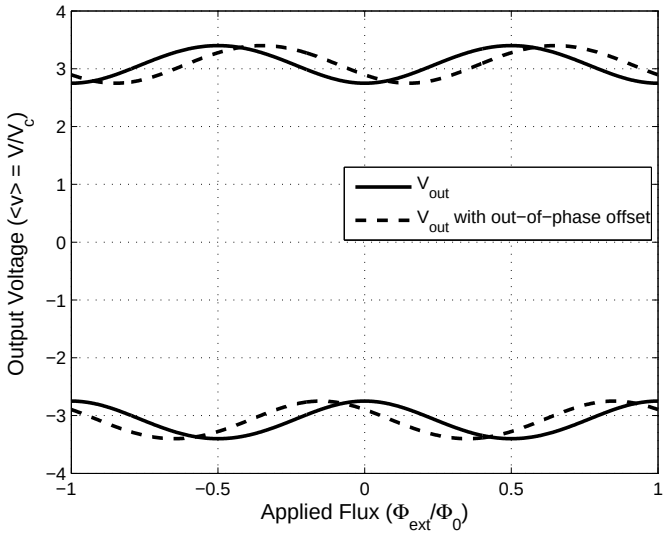

(b)

Figure 5.1: Effect of fluctuations in the critical current I_c and shunt resistance R_n. For (a) in-phase fluctuations a voltage offset will develop and for (b) out-of-phase fluctuations a shift in flux will occur.

will cause the SQUID to register a flux change, $\Delta\Phi$, where

$$\Delta\Phi = \frac{\delta\Phi}{\delta T} \cdot \Delta T = B \cdot \frac{\delta A_{eff}}{\delta T}, \tag{5.7.1}$$

where ΔT is the temperature change, $\delta\Phi/\delta T$ is the coefficient of temperature change to flux change, and B is the ambient magnetic field. For a typical device the change in flux can be as high as $\delta\Phi/\delta T = 0.5\ \Phi_0/\mathrm{K}$. The temperature drift must be kept below twice the noise performance of the SQUID, so for a noise level of about $200\mu\Phi_0/Hz^{1/2}$ the cryocooler can operate with a maximum $\Delta T = 400\mu K$. The appropriate cooling system must be chosen to keep the effect of temperature fluctuation below the SQUID noise threshold. The use of a high-pass filter can also dramatically improve the noise for measuring frequencies above 1 Hz or so.

5.8 Conclusion

Noise is an always present companion in electronic system. For a dc SQUID, which is an extremely sensitive magnetometer, the effect of noise can greatly reduce sensitivity and can even cause the device to stop functioning altogether. Understanding the origins of noise and how it affects the dc SQUID is therefore vitally important for designing, manufacturing or purchasing, and operating a practical SQUID with the lowest possible noise.

There are many sources of noise, but by far the largest source is the thermal environment in which a SQUID operates. Thermal noise for low-T_c devices is relatively insignificant, but with high-T_c devices operating at 77 K the noise will set severe restrictions on design and operation. This chapter mainly covers the origins and effects of the thermal noise on a SQUID and presents a list of parameters to quantify the performance of different designs. Voltage noise $S_v(f)$, current noise $S_i(f)$, flux noise $V_\Phi(f)$, energy resolution $\varepsilon(f)$, and magnetic field noise B_N define the performance of a SQUID, and with each noise source a recommendation is given on minimizing its effect. The most prominent limitation imposed by thermal noise is on the maximum size of the SQUID loop. The sensitivity of a SQUID can be improved by either reducing the noise of a system or by increasing the magnetic field coupling into the device.

The effect of excessive noise when measuring at very low frequencies is also discussed. Excessive noise increases inversely with frequency and severely limits the sensitivity of a SQUID operating below 1 Hz.

Chapter 6

Cryocooling

6.1 Introduction

Superconductors only exhibit their unique properties when they are cooled to low temperatures. Research is being conducted to increase the transition temperature to above room temperature, but the current generation of superconductors only function below about 130 K. YBCO has a transition temperature of about 95 K and is strongly dependent on the quality of the superconductor. Superconductors are reliant on cryogenic cooling, and thus the design and implementation of the cooling unit must be examined.

There are two unique ways to cool a superconductor to the desired operating temperature. The first and simplest way to cool the superconductor is to immerse it in a cryogenic liquid. The cryogenic liquid can also be contained in a cryostat, where thermal energy transfer is used to cool down a superconducting sample outside the liquid. This is a more passive system and the energy required for cooling comes from the evaporation of the liquid. Liquid nitrogen is relatively inexpensive and easy to use, but must be readily available and the cryostat needs to be refilled as the liquid boils away. One of the main advantages of liquid cooling is that cooling system is independent of an external power supply, preventing power failures from disrupting the coolant. There is also very little electromagnetic interference (EMI) originating from the cooler, mostly from eddy currents forming in metals near the SQUID. Unfortunately the temperature of the liquid, usually its boiling point, is fixed at a certain pressure.

The second type of cryogenic cooling utilizes a mechanical refrigeration unit. Energy, usually electrical energy from the power grid, is used to extract thermal energy (absorb heat) from the superconductor and cool it to operating temperatures. The refrigeration units produce significant EMI and thermal fluctuations, but have variable operating temperatures.

Manufacturing and electronically operating a high-T_c dc SQUID magnetometer is more difficult than it is with a low-T_c magnetometer, but the power requirements for cooling increase linearly as the operating temperature is lowered. Cooling high-T_C devices is far simpler, less expensive, and the coolers tend to be lighter and smaller due to less thermal insulation (isolation). This more than makes up for the shortcomings of the high-T_c magnetometer.

Any type of cryocooler has numerous problems associated with it and these are discussed in this chapter. Ideally the cooling unit must have variable thermal output, high efficiency, reliability, compactness, low vibration, low thermal fluctuation and produce low EMI. The SQUID sensors have very little thermal energy output and are considered to be small cooling loads. They are extremely sensitive to magnetic fields and vibration in the earth's magnetic field. The main consideration for the cooling SQUID systems is thermal stability, vibration and EMI. The aim is to reduce the noise generated by the cooler to levels below the noise of the magnetometer.

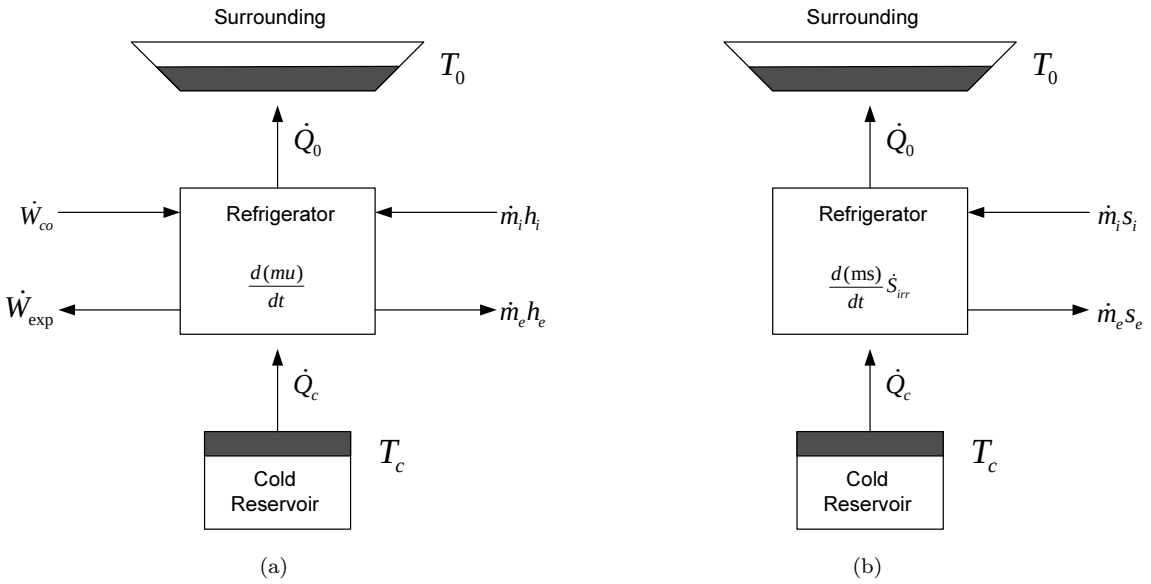

Figure 6.1: Graphical representation of the (a) first and (b) second laws of thermodynamics.

6.2 Thermodynamics

Thermodynamics play a large role in cryocooling. The flow of heat to and from the SQUID sensor, thermal fluctuation and average temperature are critical to the performance of a SQUID system. For mechanical cryocoolers the efficiency of the refrigeration units relates to the performance, and thermodynamics help to evaluate the performance of various units.

The first law of thermodynamics, the law of energy balance in Figure 6.1(a) [47, 48], is given by

$$\left(\dot{Q}_c - \dot{Q}_0\right) + (\dot{m}_i h_i - \dot{m}_e h_e) = \left(\dot{W}_{\text{exp}} - \dot{W}_{\text{co}}\right) + \frac{d(mu)}{dt}, \tag{6.2.1}$$

where $\dot{Q}_c$ is the absorbed heat by the refrigerant at temperature T_c, $\dot{Q}_0$ is the heat emitted by the surrounding environment at temperature T_0, $\dot{m}_i$ and $\dot{m}_e$ are the flow rates of mass entering and exiting the system, respectively, h_i and h_e are the enthalpies of the fluids entering and exiting the system, respectively, $\dot{W}_{\text{exp}}$ is the power produced from any expansion process in the system, $\dot{W}_{\text{co}}$ is the power delivered to the system from the compressor, and mu is the internal energy of the system. Enthalpy is the amount of energy in a system capable of doing mechanical work. The second law of thermodynamics, the law of entropy balance in Figure 6.1(b), is given by

$$\frac{d(ms)}{dt} = \left(\frac{\dot{Q}_c}{T_c} - \frac{\dot{Q}_0}{T_0}\right) + (\dot{m}_i s_i - \dot{m}_e s_e) + \dot{S}_{\text{irr}}, \tag{6.2.2}$$

where ms is the entropy of the refrigerator, s_i and s_e are the specific entropies of the of the fluids entering and exiting the system, respectively, and $\dot{S}_{\text{irr}}$ is the entropy production rate inside the system associated with irreversible processes. For a complete, closed refrigeration system $\dot{W}_{\text{exp}}$ is considered to be zero, and the flow rates of mass entering and exiting the system are zero. The entropy production rate is zero if all processes are reversible, so $\dot{S}_{\text{irr}} = 0$. The ratio of the desired power to the actual power driving the system is known as the coefficient of performance (COP), and is given by

$$\text{COP}_{\text{Carnot}} = \frac{\dot{Q}_c}{\dot{W}_{\text{co}}} = \frac{T_c}{T_0 - T_c}, \tag{6.2.3}$$

Property	He^4	H_2	Ne	N_2	Ar
Normal boiling point [K]	4.222	20.39	27.10	77.36	87.30
Heat of vaporisation at NBP [J/g]	20.72	445.6	85.75	199.18	161.14
Heat of vaporisation per volume of liquid at NBP [J/cm^2]	2.588	31.55	103.5	160.6	244.8
Triple-Point temperature [K]	2.177	13.96	24.56	63.15	83.81
Triple-Point pressure [kPa]	5.042	7.20	43.38	12.46	68.91
Cost	Very high	High	Prohibitive	Low	High

Table 6.1: Properties of Cryogenic Fluids

for an ideal refrigeration system. COP represents the refrigeration power in watt per watt of input power into the system. The Carnot value indicates the cooling power of an ideal refrigerator. Specific power is simply the inverse of the COP, denoting the input power in watt required for a desired refrigeration in watt. A practical refrigeration system will have a COP that is less than ideal. The relative COP of an actual refrigerator, the efficiency, is given by

$$\eta = \frac{\text{COP}_{\text{actual}}}{\text{COP}_{\text{Carnot}}}, \tag{6.2.4}$$

representing the efficiency of the refrigerator compared to the Carnot value's ideal cooling power, and not the absolute efficiency of the refrigerator. For a comprehensive analysis of thermodynamics and COP for cryocoolers, please refer to [47].

6.3 Open Cryogenic Systems

Open cryogenic systems use liquids that boil away at cryogenic temperatures. These systems are open circuits, where the venting gas is released into the environment and acts as a coolant. This evaporation constantly reduces the volume of the cryogenic liquid and the cryogen needs to be replaced at regular intervals for continuous use. Liquefaction usually occurs outside the laboratory environment and availability is important when using cryogenic liquids. The name usually associated with an open cryogenic systems is cryostat, or more specifically a dewar. A dewar is defined as vacuum flask that holds liquid air or helium for scientific experiments.

6.3.1 Cryogenic Liquids

There is a selection of gases that can be liquefied into cryogenic liquids and used at superconducting temperatures. Each type of gas has a unique boiling point. Since the temperature at which a liquid boils depends on the surrounding gas pressure, the temperature of the liquid can be tweaked by varying the pressure inside the container. It is possible to use a simple pressure valve to maintain a higher gas pressure inside a container, with the gas released from evaporation causing the pressure to build up. Higher pressure will result in higher cryogenic temperatures, but care must be taken not to cause the container to explode due to overpressurization. A container that is built for high gas pressures is usually based on a metal, making the design of a SQUID system more difficult and raising the manufacturing cost. By using a vacuum source to lower the ambient pressure of the container it is possible to lower the temperature of the liquid. The container has to be sealed to prevent atmosphere from leaking in and a

pressure control valve is required to maintain a constant gas pressure inside the container. A roughing pump can be used to evacuate gases from the container, but this requires the use of an electric motor, creating magnetic noise that can picked up by the SQUID. External vacuum sources would be preferred if at all possible. A simple vacuum chamber will not have enough volume to handle expanding gases for prolonged periods. It is also important to stay above the triple-point temperature and pressure or the liquid will start to solidify.

The price, heat capacity, availability and boiling temperature of a cryogenic liquid plays a large role when choosing the appropriate liquid for the SQUID. For low-T_c superconductors the choice of coolant is limited to liquid helium with a normal boiling point (NBP) of 4.22 K. This is an expensive liquid compared to liquid nitrogen and absorbs little heat during vaporisation, about 20.72 J/g heat of vaporisation at NBP or 2.588 J/cm^2 heat of vaporisation per volume of liquid at NBP. Transportation and storage is difficult as any hard impact on a container filled with liquid helium can start a chain reaction where the energy released by gas forming causes the surrounding liquid to vaporise. A significant portion of the coolant is lost before this reaction abates. Helium is also a rare gas and is only available in certain places on earth such as oil wells. The gas is usually liquefied on-site and must be transported by truck. Transportation causes mechanical energy to evaporate the gas during transport, increasing the cost per volume even further. The wide spread use of low-T_c superconductors has caused the price of helium to double from 2002 to 2007 [49]. With increased sales of MRI machines, the demand on helium to cool the superconducting coils has increased since 2003 by 25%, while helium production has only increased by about 12.5%. According to a 2000 National Academy of Science report, the total U.S. resources of helium, including the 170000 metric tons of military and technological stockpile, will be exhausted before 2035. This will give rise to helium shortages, drastically increasing the price of the gas and reducing availability. Helium is a nonrenewable gas that can escape the earth's atmosphere and must be recycled. Recycling helium requires either a large storage tank to compress the gas after vaporisation, or a liquefaction plant to recycle the cryogen. Both options do not allow for small or compact low-T_c cryostat designs, so high-T_c superconductors are preferred. Liquid hydrogen should be avoided when using high-T_c devices as there are better, more cost effective options at higher temperatures.

Most YBCO based high-T_c devices can use any coolant that has a boiling point below 80 K. The electrical parameters of the SQUID, such as critical current and thermal noise, improve as the temperature is lowered. Cost and availability must be weighed when choosing the appropriate coolant for the cryostat. Nitrogen is abundant in the atmosphere and liquefiers for liquid nitrogen are more abundant than for other cryogenic gases. There is thus a higher availability of liquid nitrogen, which also has the advantage of bringing down the cost per volume of coolant. Liquid nitrogen has a NBP of 77.36 K which is adequate for high quality YBCO films used in SQUID sensors. It is an inexpensive liquid compared to liquid hydrogen and absorbs a lot of heat during vaporisation, about 199.18 J/g heat of vaporisation at NBP or 160.6 J/cm^2 heat of vaporisation per volume of liquid at NBP. For YBCO based high-T_c SQUIDs the cryogen of choice is liquid nitrogen due to price and thermal performance. Cryogenic liquids are compared in Table 6.1.

6.3.2 Open System Cryostat

The cryogenic liquid must be stored inside a thermally insulating flask, a cryostat, to reduce the thermal energy entering the system. The superconductor's application dictates the type of dewar required.

A simple dewar will suffice for testing a SQUID that is not directly exposed to an external stimulus kept at room temperature. The sensor is simply immersed inside the cryogenic liquid and quickly cools down to the temperature of the liquid. Liquid immersion limits the temperature range of the sensor to the NBP, with pressurization allowing higher temperatures. Without any electrically powered compressors

to cool down the sensor or adjust gas pressure, the cryostat itself will produce no EMI to interfere with the SQUID.

The cryostat can be thermally isolated by either using vacuum insulation or foam insulation. Vacuum insulation has a lower liquid vaporisation rate than foam insulation, but a foam insulated dewar is easier to construct. The material used in a cryostat with vacuum insulation must be strong enough to withstand atmospheric pressure, with special emphasis placed on reinforcing any flat plates at either end. Most low-T_c cryostats use aluminized Mylar (commercially available as *space blankets*) to reduce thermal radiation into the container, but this material must be avoided due to external magnetic fields causing eddy currents in the aluminium that interfere with the magnetometer.

The sensor is placed through the neck of the dewar with the electronic cables trailing to the outside. The neck must be large enough to allow the sensor and connecting cables to pass, as well as allow the liquid to be refilled regularly without removing the sensor. Using thermally resistant yet strong material for the neck and sealing it with a gas permeable foam plug will reduce heat entering from the environment. The foam plug prevents the gas in the neck from forming a thermal convection, and the escaping gas cools down both the foam and the neck to further reduce heat entering through the neck.

The choice of construction material is not very constrictive for simple dewars, and a fully stainless steel or aluminium dewar can be fabricated. To prevent the eddy currents forming in the cryostat's metal from interfering with the SQUID sensor, as well as reducing any external magnetic interference, the sensor can be surrounded by a layer of mu-metal. Another option is to use glass-fiber and epoxy to construct the dewar, thereby removing most of the metal from the construction and removing the problem of eddy currents.

For a more comprehensive SQUID cryostat that allows external samples to be measured, such as for the SQUID microscope, the design is far more complex. The sensor must be suspended inside a vacuum in thermal contact with the liquid reservoir. Ideally the sensor is electrically isolated from the cryostat, and is far enough from metallic components to avoid eddy currents. The sensor must also be as close as possible to the device under test (DUT), with a nonmagnetic separator shielding it from the environment and maintaining a vacuum. The distance between the magnetometer and the DUT should be in the order of 0.1 mm.

6.4 Closed Cryogenic Systems

Closed cryogenic systems differ from open cryogenic systems in that the mass of the system is constant and cooling is achieved through the compression and expansion of gases. The gases are usually mechanically compressed and the generated heat removed, thereby converting electrical power into cooling power. The compressor is the source of the cooling power, but is also the source of electromagnetic interference (EMI), electrostatic discharge (ESD), mechanical vibration and thermal fluctuations. Gas flowing from the compressor into the cold finger must be free from impurities, so any oil contamination from the compressor must be removed after compression. This filter requires regular maintenance. There are two main types of commercially available cryocoolers, namely the recuperative cryocoolers and the regenerative cryocoolers.

Cryocoolers that use counterflow heat exchangers to recuperate cooling energy from returning gases are called recuperative cryocoolers. Recuperative cryocoolers circulate the coolant at a steady flow rate. The coolant from the heat exchanger is compressed at a steady pressure and forced back into the heat exchanger, causing the gas to heat up. Most of the heat created by the compression is released into the environment before the gas enters the heat exchanger. The preferred method of cooling the gas is to use a water cooling system, mainly due to its high thermal capacity, efficiency and availability. As the compressed gas passes through the heat exchanger, more heat is absorbed by the gas returning from the cold finger. From the heat exchanger the cooled compressed gas is forced through an arbitrary length of

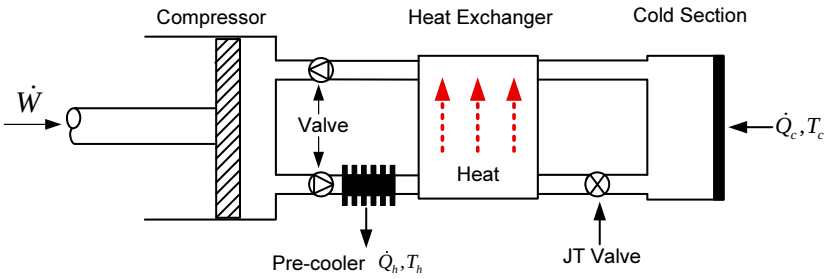

Figure 6.2: Schematic of a Joule-Thomson cryocooler.

insulated piping toward the cold finger. A longer pipe allows the compressor to be placed at a distance from the cold finger to reduce EMI from the compressor motor. At the cold finger the gas is allowed to expand. As the gas expands it cools down, absorbing surrounding thermal energy in the process and cooling down the cold finger. This gas is then pulled back into the heat exchanger to restart the cycle.

Cryocoolers that use regenerators to transfer cooling energy from the compressor into the cold finger are called regenerative cryocoolers. Regenerative cryocoolers use compressors to pulse their gases. The compressor can be a simple valveless pressure oscillator, or a continuous pressure compressor with switching valves to regulate the pressure oscillation. In the high-pressure half-cycle the gas is pressurized and passes through the cold regenerator into the cold section. Most of the heat created by the compression is released into the environment before the gas enters the regenerator. The preferred method of cooling the gas is to use a water cooling system, mainly due to its high thermal capacity, efficiency and availability. As the compressed gas flows through the cold regenerator a matrix absorbs the heat and cools the gas down even further, known as precooling. The matrix must have a large surface area for optimal heat transfer and a large heat capacitance for higher efficiency. During the low-pressure half-cycle the gas is depressurized and flows from the cold section back into the main compressor, passing through the heated regenerator. The decompression allows the gas in the cold finger to expand and absorb the surrounding thermal energy, thereby cooling down the cold finger. Decompression causes the gas to cool down, and as this cooled gas flows back through the heated regenerator it reabsorbs the heat deposited during the high-pressure half-cycle. The matrix inside the regenerator releases the stored heat into the gas and returns to a cold state. By oscillating the gas, the cooling power oscillates and the temperature of the cold section will oscillate slightly at the operating frequency. Thermal damping will help reduce the amplitude of this oscillation, but using a metal heatsink can cause eddy currents to form and interfere with the SQUID sensor.

The advantages and disadvantages each type of cryocooler will be discussed in this section. A good rule of thumb is that any cryocoolers using valves to modulate the gas flow will have a lower efficiency. Cryocoolers are prohibitively expensive, with the price increasing as the size decreases. The compressors also have a limited mean time between failures (MTBF), limiting the use of the cryocooler.

6.4.1 Joule-Thomson Cryocooler - Recuperative Cycle

Joule-Thomson cryocoolers are based on the recuperative cycle, generating cooled high-pressure gas for use in the cold finger in Figure 6.2 [1, 47, 48]. A nozzle, valve or similar device is used to inject the high-pressure gas into the low-pressure cold section. Cooling power is produced when the gas expands inside the cold section. The low-pressure gas tries to normalize to the surrounding temperature, absorbing surrounding thermal energy in the process. Any liquid formed inside the cold stage due to gas liquefaction does not pose a problem, since the liquid readily absorbs surrounding thermal energy and evaporates. As the temperature is lowered the amount of cooling increases for a given pressure change. It is important for the cooling process that the coolant is below the inversion point after expansion. The normalized

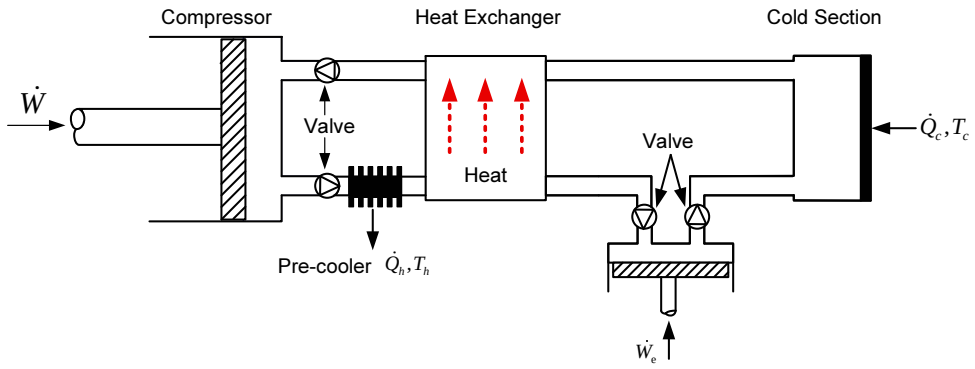

Figure 6.3: Schematic of a Brayton cryocooler.

gas is then evacuated by the compressor. Any impurity in the gas that reaches the cold stage has the potential to block the injection nozzle or freeze up any small opening, reduce efficiency or preventing the cooler from function.

The construction of a small cryocooler allow for rapid cooling of the cold stage, with some units reaching operating temperatures of 80 K in a matter of seconds. The Joule-Thomson cryocoolers have no moving parts or electromechanical motors in the cold section, reducing EMI and mechanical vibration. This simplifies the design of the cold stage and reduces the construction cost. The compressor can be placed a distance from the cold section and the gases piped over a distance, further reducing EMI from the compressor's motor.

Joule-Thomson cryocoolers have a small relative COP [1], $\eta \approx 5\%$ at 80 K, and require a secondary compressor for temperatures below 70 K. For a sensible COP the high-pressure gas must compressed to about 200 bar, reducing the life expectancy of the compressor. Open cycle Joule-Thomson coolers may also be constructed, but they tend to use a large amount of gas for a relatively short time. For an open cycle unit a standard nitrogen gas cylinder can result in 0.25 W of cooling power at 70 K for about 50 hours.

6.4.2 Brayton Cryocooler - Recuperative Cycle

Brayton cryocoolers, often referred to as the reverse-Brayton cycle, are based on the recuperative cycle, generating cooled high-pressure gas for use in the cold finger in Figure 6.3 [50, 48]. They are similar to Joule-Thomson cryocoolers, but with an entry end exit valve controlling the gas flow through a secondary compressor into the cold section. The entry valve opens to allow high-pressure gas to enter the expansion engine when it is at minimum volume, and closes when enough gas has entered the chamber. As the expansion engine cycles the pressure inside the chamber is reduced, allowing the gas to expand and cool down. The exit valve opens and the expanded gas is forced into the cold section by the cycling engine. When the compressor reaches minimal volume the exit valve closes and the entry valve opens again. The low-pressure gas tries to normalize to the surrounding temperature inside the cold section, absorbing surrounding thermal energy in the process. Any liquid formed inside the cold stage due to gas liquefaction does not pose a problem, since the liquid readily absorbs surrounding thermal energy and evaporates. As the temperature is lowered the amount of cooling increases for a given pressure change. It is important for the cooling process that the coolant is below the inversion point after expansion. The normalized gas is then evacuated by the compressor. Any impurity in the gas that reaches the cold stage has the potential to block any small opening, reduce efficiency or preventing the cooler to function correctly. The expansion engine can be replaced by an expansion turbine supported on gas bearings, allowing for smaller designs and higher reliability.

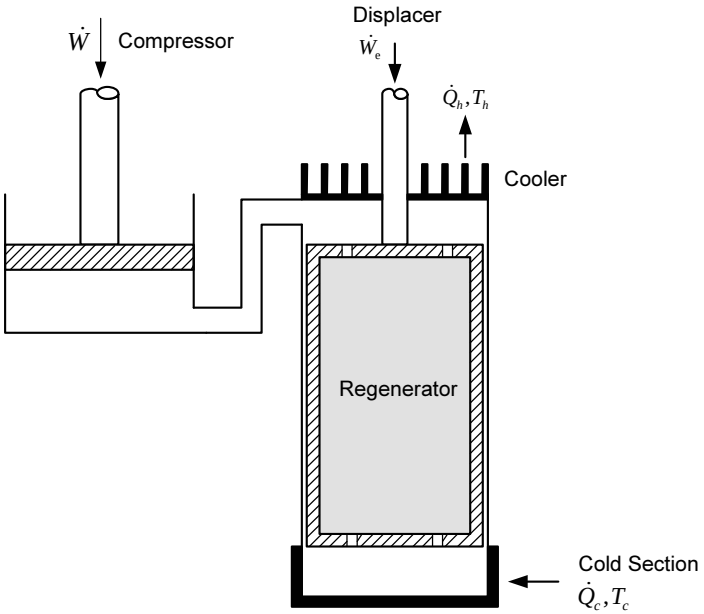

Figure 6.4: Schematic of a Stirling cryocooler with a regenerator inside the displacer.

Brayton cryocoolers are efficient coolers for temperatures between 6 K and 70 K and require lower pressure for the high-pressure gas. Lower compression results in a longer life expectancy for the compressor. The space industry, aeronautics industry and military is conducting research into increasing efficiency and reducing the size of these coolers. The relative COP can reach as high as $\eta = 20\%$ at 80 K using micro-fabrication technology, but is usually between $\eta = 4\%$ to $\eta = 5\%$ for standard Brayton cryocoolers [47].

6.4.3 Stirling Cryocooler - Regenerative Cycle

Stirling cryocoolers in Figure 6.4 are based on the regenerative cycle, where oscillation of the gas pressure is modulated to produce cooling [1, 48]. Oscillating gas pressure from the compression piston through the regenerator is not enough to create a cooling effect, and a secondary piston or displacer is required. The displacer is used to isolate the cooling and heating effect of the compressing gas, and must create a phase balance between the flow of the gas and the pressure oscillations. There must be a small pressure difference across the displacer, with very little pressure drop occurring due to gas moving through the regenerator.

When the displacer moves toward the cold section, the volume of the cold section is reduced and gas is forced through the regenerator toward the warm section. As the gas flows past the regenerator the cooling power is released by the gas into the regenerator, with the end facing the cold section retaining the most cooling power. The flow of gas must create a large thermal gradient across the regenerator with the cold section far colder than the warm section. With a larger thermal gradient the cryocooler will become more efficient. The compression piston compresses the gas and heat is produced. In the warm section this heat is released by heat exchange into the ambient environment. The displacer moves toward the warm section and increases the volume of the cold section, forcing the gas through the regenerator toward the cold section. As the gas flows through the regenerator the cooling power is reabsorbed, precooling the gas, with the maximum cooling occurring at the end facing the cold section. The compression piston expands the gas, allowing the gas to cool down. During the decompression stage the bulk of the gas resides in the cold section, allowing for maximum cooling. The cooling gas absorbs the ambient thermal energy and cools down the cold section. The displacer then moves toward the cold section, restarting the

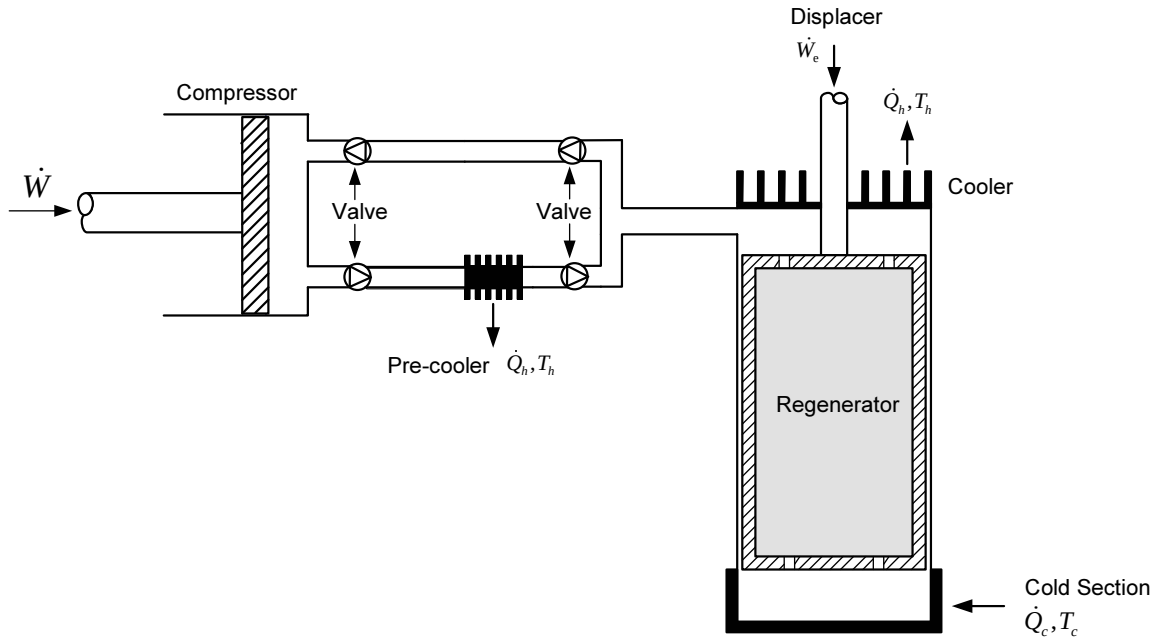

Figure 6.5: Schematic of a Gifford-McMahon cryocooler.

process.

If the compression piston and displacer are powered by a motor then they tend to have sinusoidal movement. It is important that the compression piston and the displacer operate at the same frequency, w, but are out of phase for refrigeration to occur. The decompression of the gas has to lag behind the displacer moving toward the warm section by 90°. This allows the gas to flow through the regenerator in phase with the pressure. Practical Stirling cryocoolers use a displacer that incorporates the regenerator, allowing for simplified designs with the cold end of the cylinder providing a convenient cold finger. The displacer typically operates at high rates of between 30 Hz and 60 Hz, keeping the system compact but reducing the reliability and longevity (MTBF) of the displacer.

The Stirling cycle has an efficiency between $\eta = 5\%$ and $\eta = 45\%$ at 80 K according to [47], and a practical efficiency between $\eta = 1\%$ and $\eta = 25\%$ at 80 K according to [48]. The Stirling cycle is known for its high efficiency, but has a low reliability with an average MTBF of about 5000 hours. The electric motors powering the compression piston and displacer cause vibration and create large EMI. Since the displacer has to be as close as possible to the end of the cold section for optimal cooling, it is not possible to separate the displacer motor and reduce EMI. A metal displacer moving through a magnetic field will cause magnetic noise that could potentially interfere with the SQUID sensor, especially if the displacer containing a metallic regenerator.

6.4.4 Gifford-McMahon Cryocooler - Regenerative Cycle

Gifford-McMahon (GM) cryocoolers (Figure 6.5) are based on the regenerative cycle, where oscillation of the gas pressure is modulated to produce cooling [1].

The compressor can be a valved piston compressor or a scroll compressor, both available as conventional oil-lubricated compressors. It is important to remove any contaminant from the gas flowing into the cold head, so the high-pressure stage must flow through an oil separator. To keep the system compact and reduce the cost of the cryocooler, the compressor's electric motor operates between 50 Hz and 60 Hz. The gas inside the thermal exchanger is kept constant, with an intake and exhaust valve on the compressor regulating the gas flow. Heat from the compressed gas is released by the thermal exchanger

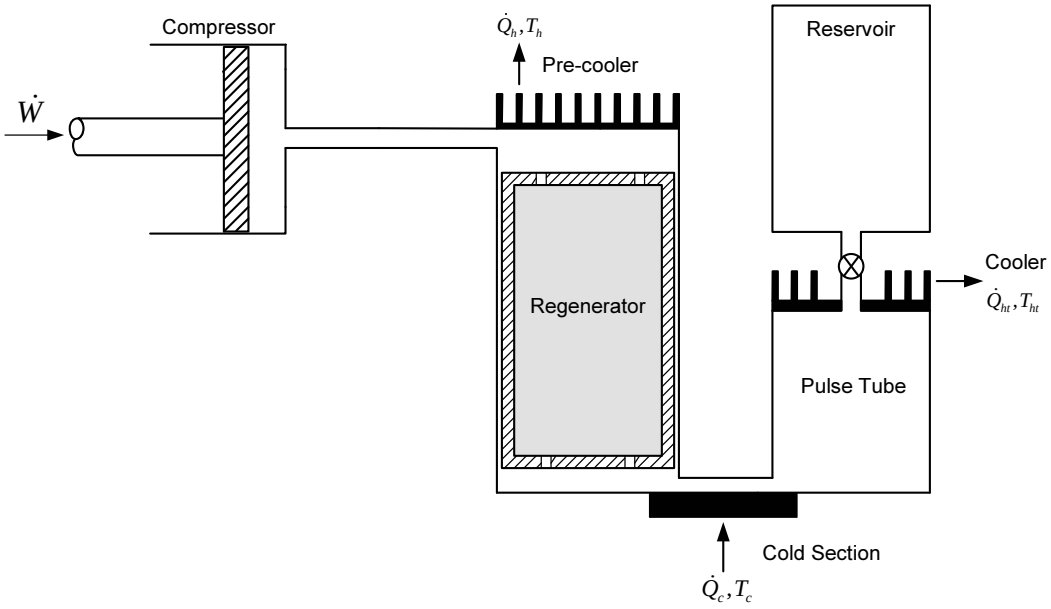

Figure 6.6: Schematic of a pulse-tube cryocooler.

into the surrounding environment. A second pair of valves control the movement of gas into and out of the cold section, creating the oscillating gas pressure required by the regenerative cycle. The second pair of valves is located at the warm end of the cold section, and switching between high and low pressure must be regulated to be in phase with the displacer.

The cold section of the GM cryocooler is essentially the same as for the Stirling cryocooler, where a displacer and regenerator are used to isolate the cooling and heating effect of the compressing gas. For details on how the Stirling cycle's cold section works, please refer to Section 6.4.3. The GM and Sterling cycle vary in that the Sterling's displacer operates at high rates of between 30 Hz and 60 Hz, while the GM's displacer operates at low rates of between 1 Hz and 2 Hz. This results in a displacer with a higher longevity (MTBF) and reliability, but at the cost of a less compact system.

The displacer can also be pneumatically driven by using the oscillating gas from the compressor. This removes the EMI crated by a motor inside the cold section, but the metal displacer moving through a magnetic field will still cause magnetic noise that could potentially interfere with the SQUID sensor. One advantage of the GM cycle is that the main compressor can be located farther from the cold section, reducing EMI and vibration from the electric motor. Typical units range from 10 W to 300 W refrigeration power at 80 K [1]. Even with this large amount of cooling power, the GM cryocoolers are known for low efficiency, mostly due to the two sets of valves. The single-stage GM cycle has an efficiency between $\eta = 4\%$ and $\eta = 8\%$ at 80 K, and can reach temperatures down to 30 K. Using two-stages allows for even lower temperatures.

6.4.5 Pulse Tube Cryocooler - Regenerative Cycle

The pulse tube cryocoolers (Figure 6.6) are based on the regenerative cycle, where oscillation of the gas pressure is modulated to produce cooling [1, 48]. The oscillating gas pressure can be created by either using a compression piston or a compressor with pressure control valves. If the valveless compression piston technique is used to create gas oscillation for the cryocooler, the unit is referred to as a Stirling-type pulse tube (Section 6.4.3). For a compact cryocooler the piston in a Sterling-type pulse tube usually operates between 20 Hz and 60 Hz, sacrificing reliability and MTBF for compactness. If the gas oscillations are the result of a set of valves controlling the flow of a compressor, the unit is referred to

as a Gifford-McMahon-type (GM-type) pulse tube (Section 6.4.4). The compressors in a GM-type pulse tube typically operate operate between 1 Hz and 2 Hz, ensuring higher reliability and a longer MTBF.

The pulse tube cycle is unique in that it releases heat between the compression chamber and regenerator section, as well as at the warm end of the pulse tube. A large reservoir is connected to the warm section of the pulse tube, using an orifice to control gas flow. The reservoir must be large enough to store additional gas during the compression phase without any noticeable change in ambient pressure. The orifice coupled with the reservoir functions similarly to the displacer in the Stirling cycle, separating the heating and cooling phases and creating the cooling effect. Ideally the compression and expansion of gas inside the pulse tube is adiabatic, occurring without loss or gain of heat, limiting the minimum diameter for a pulse tube at a given frequency. Additionally, gas flowing through the regenerator must not cause a pressure differential to develop.

The compressor increases the pressure of the gas, forcing it to flow through the regenerator and into the pulse tube. Adiabatic compression causes the gas to heat up, so the gas is cooled by a heat exchanger before reaching the regenerator. As the gas flows through the regenerator the stored cooling power is absorbed, precooling the gas, with the maximum cooling occurring at the end facing the cold section. The gas flowing through the regenerator causes the gas at the warm end of the pulse tube to compress, increasing its pressure and thereby heat up. A heat exchanger at the warm end of the pulse tube cools this compressed gas. There is now a high pressure inside the pulse tube, forcing the gas to flow through the orifice into the reservoir until the pressure equalizes. The gas nearest to the cold section of the pulse tube was precooled by the regenerator and never reaches the warm section or mixes with the warm gas.

The compressor depressurizes the gas, forcing it to flow from the pulse tube back through the regenerator and into the compressor. Adiabatic decompression causes the gas to cool down, allowing it to absorb surrounding thermal energy and cool down the cold section. As the gas flows past the regenerator the cooling power is released by the gas into the regenerator, with the end facing the cold section retaining the most cooling power. Since the pulse tube is now at a lower pressure than the reservoir, the gas inside the reservoir is forced to flow through the orifice back into the pulse tube until pressure equalizes. The gas from the reservoir forces the cold, low-pressure gas through the cold end and regenerator, further cooling them down. The warm gas from the reservoir never reaches the cold section of the pulse tube.

The cold end of the pulse tube is isolated from the warm end by a layer of gas in the center that never leaves the tube. This layer forms a thermal gradient, similar to that of the regenerator, isolating the sections. The main advantage of the pulse tube cycle is that there are no moving parts in the cold section. Lacking both the moving displacer and driving motor used by the Stirling or GM cycle, the pulse tube creates very little vibration, has a higher reliability and longer MTBF. This also reduces the EMI and magnetic noise that could potentially interfere with the SQUID sensor.

Single-stage pulse tube cryocoolers can reach temperatures of about 20 K and dual-stage cryocoolers can reach temperatures of about 2 K [48]. Pulse tube cryocoolers using coaxial geometry are used by NASA as oxygen liquefiers, with a typical efficiency of $\eta = 17\%$. Practical pulse tube refrigerators typically have efficiencies less than $\eta = 20\%$.

6.4.6 Cryocooler Comparison

The various types of cryocoolers are compared in Table 6.2. Parameters affecting the choice of cryocooler are operating temperature, cooling power, efficiency, size, mechanical and thermal vibration, electromagnetic interference (EMI), reliability and cost.

The high-T_c SQUID sensor itself requires only a small amount of cooling power, typically between 0.5 W and 2 W for temperatures between 60 K and 80 K. With any environmental heat radiating into the system should be minuscule. Environmental heating can be reduced with proper thermal insulation,

Property	Joule-Thomson	Brayton	Stirling	Gifford-McMahon	Pulse Tube
Temperature Range [K]	67-91	6-70	80	4.2 (2-Stage) 30 (1-Stage)	2 (2-Stage) 20 (1-Stage)
Refrigeration Power [W]	0.25 (80 K)	7 (70 K)	0.15-1.75 (67 K) 7.5 (77 K)	10-300 (80 K)	2 (77 K) 7-15 (77 K)
Efficiency (η @ 80 K)	5%	4-5% 20% (Space)	1-10% (Old) 15-25% (New)	4-8%	$< 20\%$ 24% (Space)
EMI Source		Compressor	Displacer Regenerator	Displacer Regenerator	Regenerator
Life Expectancy	Depends on Compressor	10 Years (Space)	5000 h 10 Years (Space)	5 Years	Depends on Compressor
Size (smallest)	Handheld Open Cycle	Handheld Space App	Handheld Space App	Large Cold Section	Handheld Space App

Table 6.2: Properties of Cryocoolers

reducing the thermal load on the cooler. All of the cryocoolers described in this chapter have sufficient cooling power and operate at temperatures suitable for SQUID systems.

Efficiency of the cooler is a factor of the cooler's type, cost and size. The size of the cryocooler is proportional to efficiency, with the pulse tube cycle having the highest average efficiency. Cost also plays a large role, as the most expensive cryocoolers designed for space applications have the highest efficiency, smallest size and highest longevity. In a laboratory environment there is usually ample space and sufficient available power, so size and efficiency is not important. For laboratory use the Gifford-McMahon (GM) and pulse tube cryocoolers have the best prices and longevity.

EMI and vibration can interfere with sensitive superconductors, degrading their performance. SQUIDs are extremely sensitive to magnetic fields and vibration in the earth's magnetic field. The electric motors powering the compression pistons and displacers cause vibration and create large EMI. The close proximity of the displacer's motor to the SQUID sensor causes the most significant EMI. Additional magnetic noise interfering with the SQUID sensor can occur due to the metal displacer moving through a magnetic field, especially if the displacer contains a metallic regenerator. The Brayton, Stirling and GM cycles use displacers and should be avoided when designing SQUID systems. GM cryocoolers have the largest amount of vibration, caused by the displacer oscillating at 1 Hz. Lacking both the moving displacer and driving motor used by the Stirling or GM cycle, the pulse tube Joule-Thomson cycles create very little vibration and EMI.

For a laboratory environment a pulse tube cryocooler is the optimum choice between cost and performance. The size of the compressor and cold stage depends entirely on the application. For SQUID systems the design of the cryocooler poses the problem of keeping the system noise below the sensor's threshold.

6.5 Reducing Cryocooling Interference

Cryocoolers are the source of three noises, namely vibration, thermal fluctuation and EMI. The vibration mainly occurs due to movement of the displacer, but can also be the result of moving valves. The movement of the metallic displacer in a magnetic field and the stray magnetic fields from the motors for the compressors and displacers cause EMI. Since most of the cryocooler is manufactured using metal, the problem of eddy currents is also a problem as it is with . Thermal fluctuations occur due to the oscillating cooling in the regenerative cycle, with the cold section The pulse tube cryocoolers and the Joule-Thomson cryocoolers produce very little mechanical vibration, making them a better choice for magnetometers working in unshielded environments. The vibration experienced by these coolers originates from the

main compressor and is transmitted through the gas piping. By adding damping to the piping the transmitted vibration can be greatly reduced, and by using non-metallic materials to construct the cold sections the problem of eddy currents can be solved.

While it can be speculated that switching off a cryocooler after reaching operating temperatures will reduce all of these problems, in practice it is not so simple. The first problem is that the cold section will slowly heat up, causing thermal drift and affecting the magnetometer. This can be solved by a thermal buffer, but using a metal such as copper will result in the generation of more eddy currents. If a liquid such as nitrogen is used as the buffer, then the cryocooler must have a evacuation port for the evaporating gases to sustain the vacuum environment. The second problem is that the main compressor for the cryocooler must be allowed to cool down for a few minutes before resuming operation, or the repeated cycling will severely reduce the reliability and lifetime of the compressor. The thermal buffer must be sufficiently large to maintain a constant temperature while the compressor is off. For high-T_c magnetometers a cryostat will be far easier to use and less expensive. The third and largest problem, especially with older cryocoolers, is that when the cryocooler is switched off a electrostatic discharge (ESD) occurs. Gases moving through the cryocooler pick up static electricity and the thermal insulators work efficiently as electrical insulators, causing the cold section of the cryocooler to build up a static electricity. The breakdown voltage for N_2 is reduced in a near vacuum to about 210 V [51], so a low static potential will result in a spark forming between the cold section and superconducting wires in the magnetometer. When the magnetometer is connected the electronics a static discharge will occur, damaging the Josephson junctions and destroying the SQUID. The cold section must be properly grounded and each grounding wire is a good conductor of heat, resulting in lower efficiency. When the electrical motors for the displacer and compressor are switched off they can cause a transient potential across the entire cryocooler, and with the low breakdown voltage can cause a discharge through the magnetometer. The motors must be sealed and well grounded if the cryocooler is to be cycled.

The piping used to transfer the gas from the compressor to the cold section is usually covered by a braided metal to enhance mechanical strength. This braid is important for the longevity and reliability of the cryocooler, but the large area encompassed the piping in respect to electromagnetic interference results in a significant ground loop. This ground loop causes excessive additional noise for any measurement inside the cryocooler, and the only cure is to break the conducting loop. By using special ceramic or plastic connectors, shown in Figure E.11(c) on p.160, the piping connected to the cold section can be electrically insulated from the compressor without affecting the efficiency. These connectors are expensive and unavailable for older cryocoolers, but are invaluable for low-noise systems.

Thermal fluctuations can be reduced by including a thermal capacitor to act as damper, also known as a passive thermal filter. The material must conduct heat efficiently from the magnetometer to the cold section while damping any thermal oscillation above (5.7.1). Good thermal capacitors have a high volumetric heat capacity as space is usually restricted inside the coolers.

Distancing the magnetometer from the cooler will result in lower EMI from the displacer and lower the effect of eddy currents. For cryostats with non-metallic outer covers the magnetometer can be separated a short distance from the coolant by using a non-magnetic and thermally conductive material such as sapphire. The cooling power of the cryocoolers can also be transported a distance from the cold section to the magnetometer. For short distances a non-magnetic and thermally conductive material can also be used. Longer distances require either a heat pipe or forced gas circulation [19]. Heat pipes are mainly used in space applications. Inside the pipe the working gas is liquefied at the cold section and will move along the pipe toward the warm section through capillary action along embedded grooves. At the cold section the liquid will absorb heat through evaporation, and the expanding gas will force itself to move back toward the cold section. Heat pipes are extensively used in the cooling of modern PC CPU's and are able to transfer large amounts of thermal power, over 40 W of thermal power per pipe, over long

distances with minimal temperature drop. If the heat pipe is constructed of a metal then there will still be the problem of eddy currents. Forced gas circulation will transport the cooling power from the cold section through a closed loop to the magnetometer, using a centrifuge or diaphragm pump. The gas is cooled at the cold section and releases the cooling power at the magnetometer.

6.6 Material Properties

Each part of the cryostat and cryocooler is created using either metal, crystal, rubber, foam or composite materials. The choice of material depends on the mechanical strength, thermal capacity and conductivity, thermal expansion, and electric and magnetic characteristics for each part.

Differences in the thermal expansion between the construction materials can cause them to separate or crack at the interface. Cycling between hot and cold will exacerbate this problem, causing the material to fatigue and allow atmosphere to enter the the vacuum and destroy the insulation. The materials must either have similar coefficients, or the interface must be designed to handle the small movement by using a gasket. The linear thermal expansion for a material is

$$\frac{\Delta L}{L_0} = \alpha \Delta T, \tag{6.6.1}$$

where ΔL is the change in length, L_0 is the original length, α is the linear expansion coefficient, and ΔT is the change in temperature. the expansion of $\Delta L/L_0$ is usually given as a percentage. The volumetric thermal expansion for a material is

$$\frac{\Delta V}{V_0} = 3\alpha \Delta T, \tag{6.6.2}$$

since the expansion coefficient for an isotropic material is three times the linear expansion coefficient, where ΔV is the change in volume and V_0 is the original volume. Volumetric expansion is important to consider when designing a SQUID microscope. The outer shell will maintain its shape at ambient temperature, but the inner container and thermal conductors will shrink when the liquid nitrogen is added. This causes the magnetometer to retract, increasing the distance to the aperture and the device under test. If the cryostat is allowed to reheat and the magnetometer is too close to the aperture, then thermal expansion will cause damage to the magnetometer and the cryostat.

The outer shell of the cooler is either metal or epoxy reinforced fibreglass. The most important properties when choosing the material for the outer shell are mechanical strength and stress resistance. If the cooler is thermally insulated by using a vacuum then the casing must be able to withstand the atmospheric pressure. The amount of compression the material can undergo before buckling is known as the stiffness of the material, known as Young's modulus. Young's modulus represents the ratio of a material's tensile stress to its tensile strain,

$$E \equiv \frac{\sigma}{\epsilon}, \tag{6.6.3}$$

where σ represents the tensile stress and ϵ represents the tensile strain. Yield strength is the amount of stress a material can undergo before physically deforming, σ, representing the maximum load that can be applied to the material.

Important properties to consider when choosing the materials for the inner container, the neck of the dewar and the thermal interface between the cold section and the magnetometer are specific heat, thermal conductivity, electrical conductivity and magnetic characteristics. Connecting the cold section to the magnetometer requires a material with high volumetric heat capacity, high thermal conductivity, low electric conductivity and no effect on magnetic fields. The neck of the dewar must have a low thermal conductivity and a high tensile strength. Thermal conductivity is the ability of a material to conduct

heat across a thermal gradient. The thermal conductivity of a material is given by

$$k = \frac{\Delta Q}{\Delta t}\frac{L}{A\Delta T}, \tag{6.6.4}$$

where $\Delta Q/\Delta t$ is the heat flow rate, L is the distance, A is the area of the material, and ΔT is the thermal gradient. Specific heat (capacity), C_{p}, specifies the the amount of heat required to increase a certain mass of material by 1 K under constant pressure. More important is the volumetric heat capacity, which is the specific heat capacity for a certain volume of material, or simply put the ability of a volume of material to store heat without undergoing a phase change.

Highly thermal conductive metals are always good electrical conductors and will cause eddy current that interfere with the magnetometer. Certain non-metals such as sapphire and diamond have excellent thermal conductivity but are non-magnetic and electrically insulating. Sapphire must be a single crystalline Al_2O_3 for optimum heat transfer, but polycrystalline diamond exhibit the same high thermal conductivity. This raises the possibility of using manufactured polycrystalline diamond in a SQUID microscope as it has the ideal properties for use with a magnetometer.

The high modulus of sapphire allows it to be used as a window between the magnetometer and the sample [25, 26]. A 1 mm thick sapphire window with an outer-dimension of 25 mm and an inner-dimension of 1.5 mm is strong enough to be used at atmospheric pressure. The inner 1.5 mm window can be reduced to a thickness of 25 μm for specialized magnetometers that need to be close to the sample.

6.7 Conclusion

The merits of the various cooling techniques are discussed with emphasis on their use with dc SQUID magnetometer for a SQUID microscope. A cryostat is relatively easy and inexpensive to construct and the running costs for high-T_c devices is low. The cryostat is limited by the need to regularly replenish the coolant and usually only operates at the temperature of the coolant. Liquid nitrogen is easy to acquire in a university environment and is one of the least expensive coolants, but for field use availability becomes the limiting factor. The problem associated with production of the coolant remains obscure to the user as it is simply available on demand.

The cryocoolers operate with the simplicity of an on switch, but their manufacturing costs are far higher and they have a limited life expectancy. The price increases as the size of the cryocooler decreases, but if mobility is important they are unsurpassed. The various types of cryocoolers are discussed, and it quickly becomes apparent that using them with a magnetometer requires novel approaches to reduce the noise they produce. Pulse-tube coolers prove to be the most promising as they produce the least amount of noise, can be compact, and the cold section can be produced entirely out of composite materials. Cryocoolers generate cooling power by consuming relatively large amounts of power from the power grid and are susceptible to power outages. There is also the danger of a electrostatic discharge destroying the magnetometer.

Various techniques are given how for reducing the noise produced by both the cooling systems. Reducing the metal content by using composites and crystals close to the magnetometer reduces the formation of eddy currents and EMI. Distancing the magnetometer from EMI sources such as the moving displacer and electric compressor motors will result in lower noise and unwanted signals. The relevant material properties used for the noise reduction are explained.

Chapter 7

SQUID Electronics

7.1 Introduction

An electronic interface is needed in order to determine the amount of magnetic flux applied perpendicularly to the dc SQUID. The dc SQUID is biased with a current and the potential developing due to the magnetic flux is measured. To accurately display the amount of flux with the highest possible sensitivity, the SQUID must be properly set up. Detail regarding the dc SQUID is given in Section 3.2, indicating its non-linear, non-hysteretic and periodic flux-to-voltage conversion. The output oscillation period is one magnetic flux quantum, Φ_0, while the potential generated is typically in the μV range. A feedback scheme is used to optimize the voltage sensitivity and linearize the flux-to-voltage conversion by locking the dc SQUID in a flux-locked loop. Low frequency noise can be reduced by modulating the bias current at a frequency above the corner frequency.

The electronic read-out schemes are designed to either operate at room temperature or inside the cooled environment. The addition of a matching circuit allows for a room temperature preamplifier to match the output of the SQUID.

7.2 Flux-locked Loop

7.2.1 Small Signal SQUID Response

The flux-locked loop (FLL) is designed to linearize the V-Φ transfer function of the dc SQUID and maintain the maximum voltage sensitivity [1, 19]. Biasing the dc SQUID at a certain work point, W, results in a voltage sensitivity, V_Φ=$\delta v/\delta\Phi_{\text{ext}}$ (3.2.42), with $V_\Phi \approx R_n/L_{SQ}$ at the optimum working point. The optimum work point occurs at the steepest sections of the V-Φ sinusoidal output, located at $\Phi_{\text{a}} \approx (\Phi_0/4 + n\Phi_0/2)$ for $\beta_L = 1$ and $\beta_c = 0$, where n is an integer. It must be noted that the working point is at an offset voltage, V_{offset}. V_Φ has a nearly linear output at W for small input signals, with the applied peak-to-peak flux amplitude smaller than $\delta\Phi_{\text{a,max,pp}}$, but will have a non-linear response for larger signals, so

$$\Phi_{\text{lin,pp}} = \delta\Phi_{\text{a,max,pp}} \leq \frac{\Phi_0}{\pi}, \tag{7.2.1}$$

where $\Phi_{lin,pp}$ is the (nearly) linear flux range as shown in Figure 7.1. The peak-to-peak linear output voltage developing across the SQUID due to $\Phi_{\text{lin,pp}}$ is

$$V_{\text{lin,pp}} = \Phi_{\text{lin,pp}} V_\Phi. \tag{7.2.2}$$

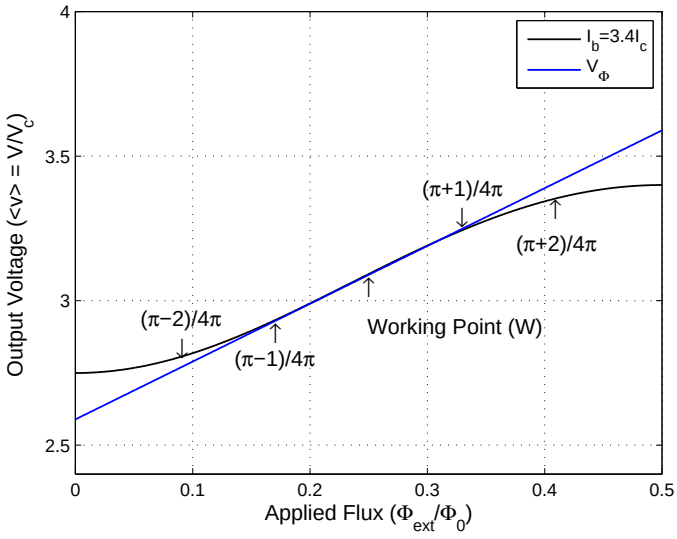

Figure 7.1: Voltage sensitivity V_Φ of a RSJ SQUID biased at $3.4I_c$; the working point W is indicated as well as the linear range $\Phi_{\mathrm{lin,pp}}$ and the minimized non-linear error range $\delta\Phi_{\mathrm{pp}}$.

As the applied flux approaches Φ_0/π, there will be a slight voltage difference between the straight line approximation V_Φ and the actual output, resulting in the non-linearity error flux

$$\Phi_{\mathrm{nl}} \approx \pm\frac{\delta\Phi_{\mathrm{pp}}^3}{48\Phi_{\mathrm{lin}}^2}. \tag{7.2.3}$$

To minimize the non-linear error, the input signal flux range is minimized to

$$\delta\Phi_{\mathrm{pp}} = \frac{\Phi_{\mathrm{lin,pp}}}{2} \leq \frac{\Phi_0}{2\pi}, \tag{7.2.4}$$

resulting in a very linear V-Φ for only a small input range $\delta\Phi_{\mathrm{pp}}$. The voltage response to small flux input signals is shown in Figure 7.2. Since the environmental magnetic flux noise from nearby transformers and electric motors tends to always be larger than this small signal for sensitive SQUID magnetometers, using just the working point biasing will not suffice. It is possible to constrain the maximum input signal by reducing the SQUID loop, but this will result in low sensitivity.

7.2.2 Basic Flux-locked Loop

By using a flux-locked loop the maximum input signal is greatly increased, usually to hundreds of fluxons, and is limited mainly by the feedback electronics [1, 19]. For the FLL the SQUID in Figure 7.3 is again biased at the working point W to ensure the optimum voltage sensitivity, V_Φ. The bias voltage of the preamplifier, V_{b}, is set to correspond to that of the working point, resulting in a zero voltage output at the working point. When an external magnetic flux is applied the output voltage of the SQUID will change, causing the preamplifier to change its output accordingly. This voltage change is amplified, integrated, and fed back to the SQUID with a feedback coil. The feedback coil is coupled with the SQUID loop by mutual inductance, M_{f}, and the current through the coil is set by the feedback resistor, R_{f}. Choosing the appropriate resistance and inductance will result in the impedance of the coil being negligible. The coil creates a magnetic field that is dependent on the integrator's voltage coupled with the feedback resistor, $I_{\mathrm{f}} = V_{int}/R_{\mathrm{f}}$. Through mutual coupling the magnetic field from the coil will counteract the external applied magnetic flux, causing the potential across the SQUID to return to the bias point and the apparent flux to return to the working point W, at $\Phi_0/4$. Since the bias point and the offset voltage

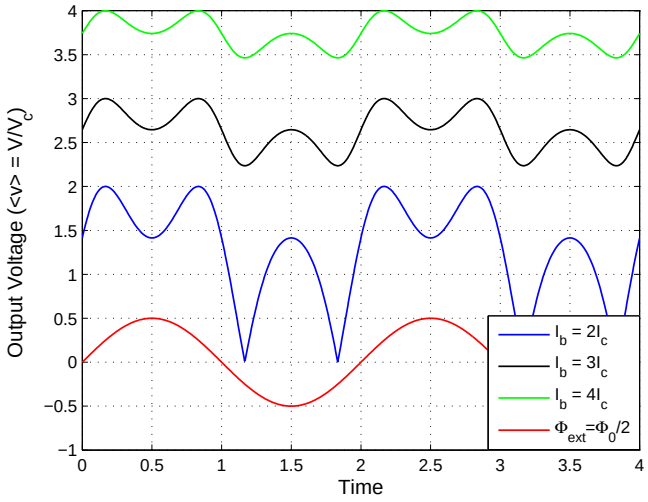

(a)

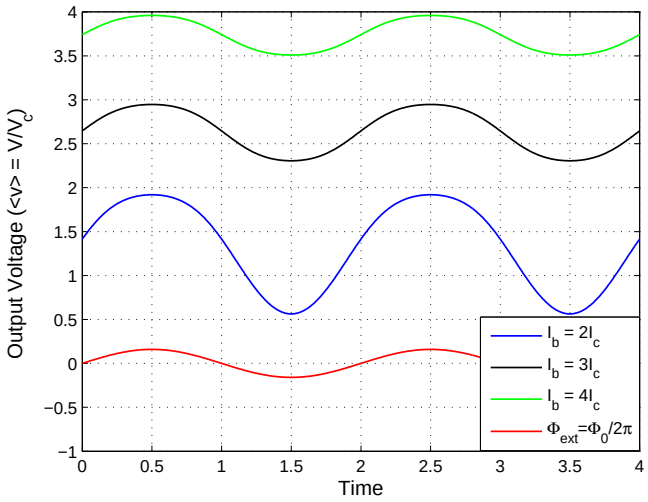

(b)

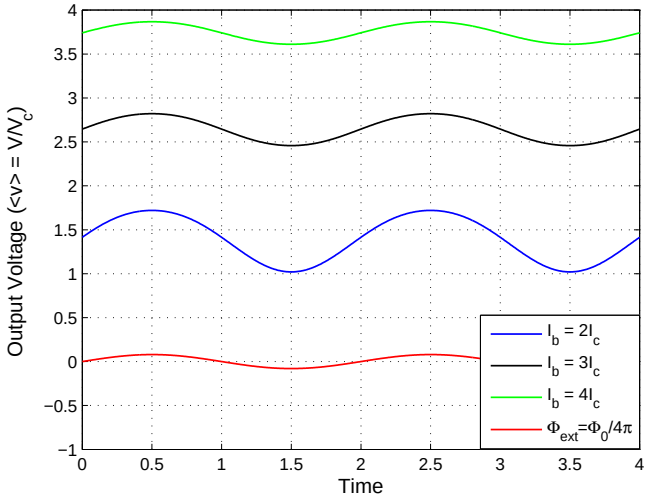

(c)

Figure 7.2: Voltage response of a RSJ SQUID biased at various currents for a flux input signal of (a) $\Phi_{\text{ext}} = \Phi_0$, (b) $\Phi_{\text{ext}} = \Phi_0/2\pi$ and (c) $\Phi_{\text{ext}} = \Phi_0/4\pi$ with an additional biasing flux $\Phi_b = \Phi_0/4$ to simulate the working point.

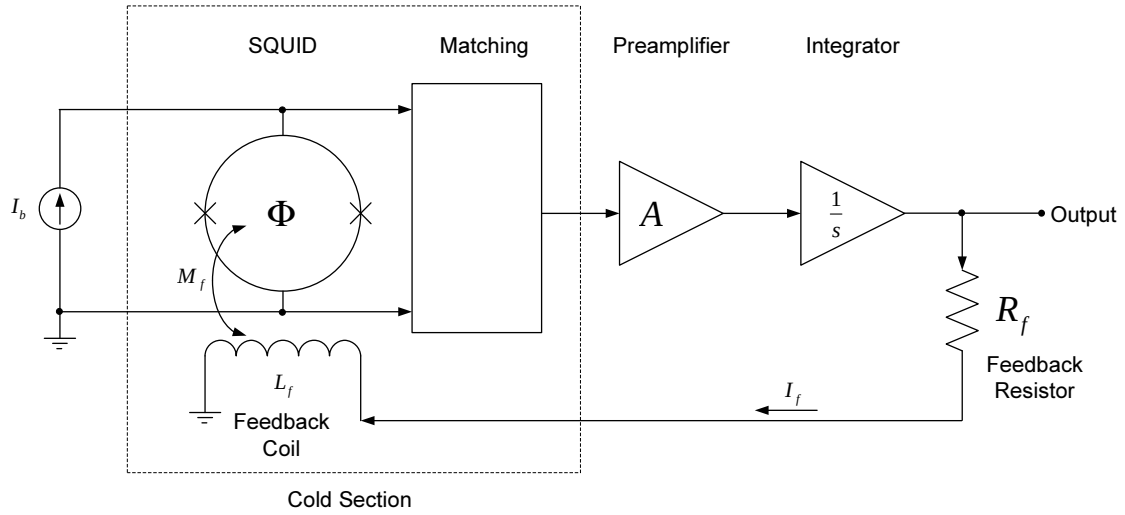

Figure 7.3: Generic schematic for a basic current biased flux-locked loop. The components located in the cold section are surrounded by the dashed line.

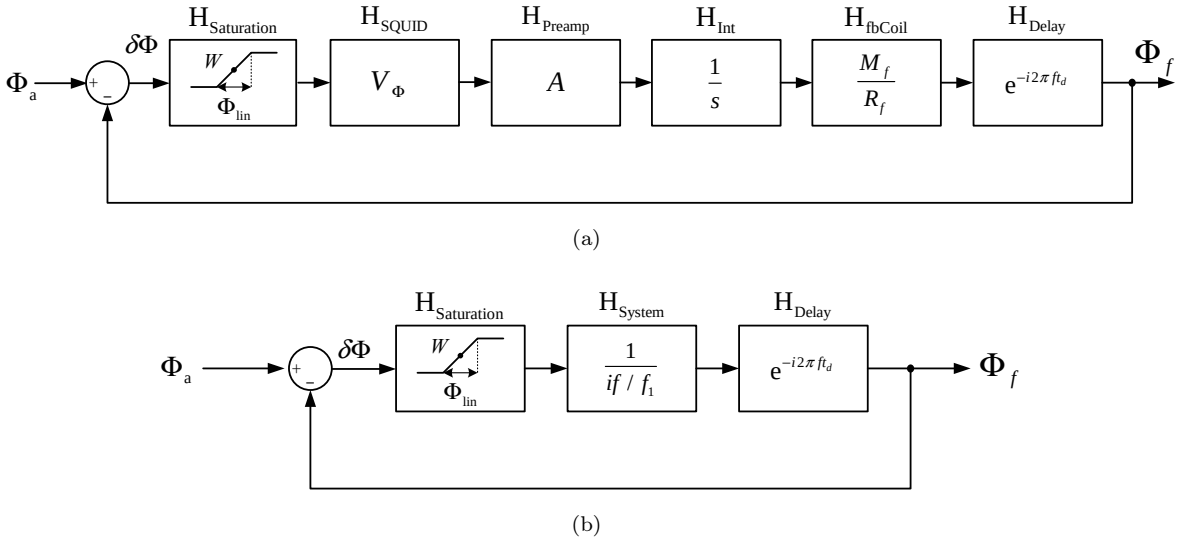

Figure 7.4: Compound block diagram for (a) the complete closed-loop dc SQUID transfer function, and (b) the simplified closed-loop transfer function.

are the same again, the preamplifier will have a zero voltage output again. The integrator will retain its output voltage until the external flux is changed, maintaining the feedback field. The voltage output of the integrator is a linear representation of the applied magnetic field.

7.2.3 Flux-locked Loop Design

The FLL is a negative feedback circuit designed to keep the magnetic flux applied to the SQUID at $\Phi_a \approx \Phi_0/4$ when biased at the working point, W, with a maximum magnetic flux deviation of $\delta\Phi \leq \Phi_0/4$ (7.2.4). The output from the integrator is linear to the applied flux, and the SQUID will exhibit this linearity until the output of integrator reaches the supply voltage rails.

The transfer-function (TF) of the FLL in Figure 7.4(a) is used to calculate the values for the feedback system [19]. The open-loop FLL TF can be split into sections,

$$\mathrm{H_{FLL,ol}} = \mathrm{H_{Saturation}} \cdot \mathrm{H_{Squid}} \cdot \mathrm{H_{Preamp}} \cdot \mathrm{H_{Int}} \cdot \mathrm{H_{fbCoil}} \cdot \mathrm{H_{Delay}}. \tag{7.2.5}$$

The arrangement of the open-loop TF sections is unimportant for the outcome of a closed system [52], so it is possible to move the mutual feedback coil ahead of the SQUID as long as it does not precede the saturation or the position of the feedback does not change. To help simplify the open-loop FLL TF, $\mathrm{H_{FLL,ol}}$ can be recombined into saturation, the SQUID unit, the feedback electronics, and the line delay, where

$$\mathrm{H_{FLL,ol}} = \mathrm{H_{Saturation}} \cdot \mathrm{H_{SQ}} \cdot \mathrm{H_{Electronics}} \cdot \mathrm{H_{Delay}}. \tag{7.2.6}$$

The SQUID unit consists of the SQUID magnetometer and the feedback coil, $\mathrm{H}_{SQ} = \mathrm{H_{Squid}} \cdot \mathrm{H_{fbCoil}}$, with the coil having a mutual feedback inductance, M_f, and a feedback resistor, R_f. The TF for the SQUID unit is

$$\mathrm{H}_{SQ}(i2\pi f) = \mathrm{G}_{SQ} = V_\Phi \frac{M_\mathrm{f}}{R_\mathrm{f}}, \tag{7.2.7}$$

where G_{SQ} is the open-loop gain of the SQUID, V_Φ the voltage sensitivity at W, and $i = \sqrt{-1}$. The SQUID and the feedback coil are considered to be independent of frequency. The preamplifier and the integrator are collectively taken as the feedback electronics, $\mathrm{H_{Electronics}} = \mathrm{H_{Preamp}} \cdot \mathrm{H_{Int}}$, with the TF

$$\mathrm{H_{Electronics}}(i2\pi f) = \frac{A}{i2\pi f}, \tag{7.2.8}$$

where A is the open-loop gain.

The desired unity-gain frequency must be chosen for the open-loop system, which is at the integrator's characteristic unity-gain frequency:

$$f_1 = \frac{1}{2\pi R_\mathrm{int} C_\mathrm{int}}, \tag{7.2.9}$$

where R_int is the input resistor and Cint is the feedback capacitor of the integrator. The open-loop system must have a unity gain at f_1, where

$$|\mathrm{H_{FLL,ol}}(i2\pi f_1)| = \quad 1 \quad = \mathrm{G}_{SQ} A \left| \frac{1}{i2\pi f_1} \right| \tag{7.2.10}$$

$$\Rightarrow A \quad = \quad \frac{2\pi f_1}{\mathrm{G}_{SQ}}, \tag{7.2.11}$$

with the gain of the time delay $|\mathrm{G_{Delay}}| = 1$, and for small input signals the saturation will have a gain of $|\mathrm{G_{Saturation}}| \approx 1$. The feedback electronics (preamplifier plus integrator) must have a gain-bandwidth (GBW) of

$$\mathrm{GBW_{electronics}} = |\mathrm{H_{Electronics}}(i2\pi f_1)| \times f_1 = \frac{f_1}{\mathrm{G}_{SQ}}. \tag{7.2.12}$$

The SQUID unit and the feedback electronics combine to form $\mathrm{H_{system}} = \mathrm{H}_{SQ} \cdot \mathrm{H_{Electronics}}$, where

$$\mathrm{H_{system}}(i2\pi f) = \frac{2\pi f_1}{i2\pi f} = \frac{1}{if/f_1}, \tag{7.2.13}$$

which is basically just the integrator. The ultimate simplified open-loop FLL TF in Figure 7.4(b) is

$$\mathrm{H_{FLL,ol}} = \mathrm{H_{Saturation}} \cdot \mathrm{H_{system}} \cdot \mathrm{H_{Delay}}, \tag{7.2.14}$$

which is relatively simple to examine analytically.

The error signal of the FLL, which is the flux directly applied to the SQUID in FLL, is given by

$$\delta\Phi = \Phi_a - \Phi_\mathrm{f}, \tag{7.2.15}$$

where Φ_f is the feedback flux, and Φ_a is the external applied flux. The (tracking) error must remain

within $\delta\Phi \leq \pm\Phi/4\pi$ (7.2.4), or else the SQUID will transition into non-linearity. This non-linearity is represented by saturation with a linear gain of 1 up to the saturation points $\pm\Phi/4\pi$. The input range of the SQUID can be increased by increasing the value of the mutual inductance of the feedback coil, M_{f}, or decreasing the value of the feedback resistor, R_{f}, thus increasing the open-loop gain, G_{ol}.

The voltage output of the integrator is linear to the applied flux, where

$$V_{\mathrm{Int}} = \Phi_f \frac{R_{\mathrm{f}}}{M_{\mathrm{f}}}. \tag{7.2.16}$$

The feedback resistance for the dynamic range of the FLL is

$$R_{\mathrm{f}} = V_{\mathrm{Int,max}} \frac{M_{\mathrm{f}}}{\Phi_{\mathrm{dyn}}}, \tag{7.2.17}$$

where $V_{\mathrm{Int,max}}$ is the maximum integrator output voltage, and Φ_{dyn} is the dynamic flux range of the FLL. For $M_{\mathrm{f}} = 44000\Phi_0$, $V_{\mathrm{Int,max}} = 5V$ and $\Phi_{\mathrm{dyn}} = 100\Phi_0 = \pm 50\Phi_0$ the value for the feedback resistor must be $R_{\mathrm{f}} = 4.4$ [kΩ].

The mutual inductance for two distinct inductors is

$$M = k\sqrt{L_1 L_2}, \tag{7.2.18}$$

where $k = 0.6$ is the generalized coupling coefficient for a SQUID, and L_1 and L_2 are the respective inductances.

The FLL linearizes the input flux while maintaining a specific amount of flux on the dc SQUID. Reducing the apparent flux on the SQUID helps to maintain lower excess noise (Section 5.5.7) and prevent magnetic hysteresis of the junctions.

7.2.4 Line Delay

The line delay is the summation of all the time delays in the FLL dc SQUID system, starting with the signal from the SQUID delayed through the transmission line to the electronics, then the delays in the electronic components, and finally the delay through the transmission line back to the SQUID [19]. The effects of the SQUID and feedback electronics can therefore be considered as instantaneous, with any perceptible delay included as part of the line delay. The time delay is given by

$$\mathrm{H}_{\mathrm{Delay}}(i2\pi f) = e^{i2\pi f t_d}, \tag{7.2.19}$$

where t_d is the time delay in s and f the frequency in Hz. The closed-loop FLL is

$$\mathrm{H}_{\mathrm{FLL,cl}}(i2\pi f) = 1/\left[1 + \frac{if}{f_1} e^{i2\pi f t_d}\right] \tag{7.2.20}$$

The gain of the FLL, with a small-signal input to prevent saturation, is

$$|\mathrm{G}_{\mathrm{FLL,cl}}(i2\pi f)| = 1/\sqrt{1 + \frac{f}{f_1}\left(\frac{f}{f_1} - 2\sin(2\pi f t_d)\right)}, \tag{7.2.21}$$

where t_d is set by the system and f_1 can be varied, as shown in Figure 7.5.

The danger with a line delay is that it can lead to system instabilities, since it does not change the magnitude of the system but will change the phase. It is thus impossible to stabilize the system for unity-gain frequencies greater than $f = 5/2\pi t_d$, and will still be difficult for frequencies greater than $f \cong 3/2\pi t_d$ [52]. For a frequency of $f_{1,\mathrm{max}} = 1/4\pi t_d$ the magnitude of the frequency response is flat

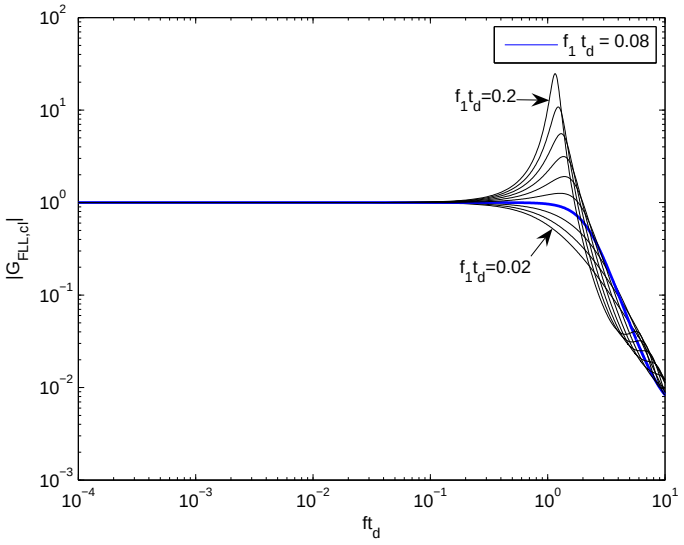

Figure 7.5: Gain $|G_{FLL,cl}(f)|$ of the closed-loop FLL. The response is in terms of frequency and time delay, ft_d, showing behaviour of systems with delays from $f_1 t_d = 0.02$ to $f_1 t_d = 0.2$ in steps of 0.02. The maximum permissible delay for a given frequency is indicated by the blue line with $f_1 t_d = 0.08$.

over the largest frequency range without a peak at the end [19]. The bandwidth for a system with this frequency will be

$$f_{3\text{dB,max}} = 2.25 f_{1,\text{max}} = 0.18/t_d, \tag{7.2.22}$$

which is still below $f \cong 3/2\pi t_d$ and results in a first-order low-pass response [19]. Line delay can reduce the bandwidth of a high-T_c dc SQUID with room temperature electronics, so the limiting factor defining the system's bandwidth will not only be the feedback electronics. Shortening the cables and using the correct read-out scheme can help to improve the system bandwidth.

7.2.5 Flux-locked Loop Noise In Room-temperature Electronics

The flux noise spectral density of the FLL is

$$S_{\Phi,\text{FLL}} = \frac{S_v + S_{v,\text{amp}}}{V_\Phi^2} \tag{7.2.23}$$

$$= S_\Phi + \frac{S_{v,\text{amp}}}{V_\Phi^2}, \tag{7.2.24}$$

where S_v is the SQUID voltage noise spectral density, S_Φ is the SQUID flux noise spectral density, $S_{v,\text{amp}}$ is the sum of the preamplifier and integrator voltage noise spectral density, and V_Φ is the voltage sensitivity [19]. The conversion of the amplifier noise $S_{\Phi,\text{amp}}^{1/2} = S_{v,\text{amp}}^{1/2}/V_\Phi$ can severely degrade the flux noise spectral density of the amplifier, possibly resulting in higher noise levels than exhibited in the SQUID itself. It is important to choose a preamplifier and integrator with a low noise spectral density. Using the correct read-out scheme will improve the noise, either by using flux modulation, additional positive feedback (APF), or a step-up transformer. APF increases the voltage sensitivity V_Φ, reducing the FFL flux noise but raising the slew rate.

The rms value of the noise (5.3.1) is

$$\Phi_{\text{n,FLL,rms}} = \frac{\sqrt{S_v + S_{v,\text{amp}}}}{V_\Phi} \sqrt{\frac{\pi}{2} f_{3\text{dB}}}, \tag{7.2.25}$$

where $BW_{\text{FLL}} = \frac{\pi}{2} f_{3\text{dB}}$ is the bandwidth for the FL, when $ft_d = 0.08$ for a first-order low-pass response

in (7.2.22). For a Gaussian distribution the peak value of the noise is about 4 times the rms value [19], resulting in

$$\Phi_{\mathrm{n,FLL,pp}} = 8\sqrt{\frac{\pi}{2}}\frac{\sqrt{(S_v + S_{v,\mathrm{amp}})f_{\mathrm{3dB}}}}{V_\Phi}. \tag{7.2.26}$$

Combining (7.2.26) with (7.2.2) the noise flux coupling back into the SQUID through the coil is

$$\frac{\Phi_{\mathrm{n,FLL,pp}}}{\Phi_{\mathrm{lin}}} = 10\sqrt{\frac{\pi}{2}}\frac{\sqrt{(S_v + S_{v,\mathrm{amp}})f_{\mathrm{3dB}}}}{V_{\mathrm{pp}}}. \tag{7.2.27}$$

It is important to choose the FLL bandwidth so that $\Phi_{\mathrm{n,FLL,pp}}/\Phi_{\mathrm{lin}} \leq 1$ to ensure the system remains stable, ensuring that the noise fed back to the SQUID does not exceed the linear response.

If the preamplifier has an offset current noise spectral density of $S_{\mathrm{I,amp}}$ for a SQUID with a current sensitivity of M_{dyn} (7.5.3), then the flux noise spectral density of the FLL is

$$S_{\Phi,\mathrm{FLL}} = \frac{S_v + S_{v,\mathrm{amp}}}{V_\Phi^2} + S_{I,\mathrm{amp}}M_{\mathrm{dyn}}^2. \tag{7.2.28}$$

Table 7.1 presents a list of operational amplifiers with their voltage noise and current noise.

7.2.6 Slew Rate

The slew rate for a flux-locked loop system is defined as

$$\dot{\Phi}_f \equiv \left|\frac{\delta\Phi_f}{\delta t}\right|, \tag{7.2.29}$$

where Φ_f is the feedback flux [19]. The maximum slew rate occurs below the frequency where the system becomes saturated or unstable. Practically the maximum slew rate will occur at the unity-gain frequency, $f_{1,\max} = 1/4\pi t_d$, for the maximum linear output, $\Phi_{\mathrm{lin,pp}} \leq \frac{\Phi_0}{\pi}$. The maximum slew-rate becomes:

$$\dot{\Phi}_{f,\max} \leq \pi\Phi_{\mathrm{lin,pp}}f_{1,\max} = \frac{\Phi_0}{4\pi t_d}, \tag{7.2.30}$$

with typical slew rates between $1\Phi_o/\mu s$ and $10\Phi_o/\mu s$ [19].

High slew rate and high bandwidth are very important for unshielded dc SQUID magnetometers, even when operating at low frequencies. When any unwanted high-frequency signal imposes itself onto the system, then the feedback system must accurately track the signal and compensate using the feedback coil. The low-frequency signals can be processed from the output of the system by using a low-pass filter outside the FLL. If the high-frequency signals are not tracked accurately, then they can down-mix and cause unwanted low-frequency signals to appear due to non-linear distortions, and they can cause the flux to jump by multiple of integers. When measuring small low-frequency signals, the environmental interference signals tend to be magnitudes larger than the measured signal.

Using APF to increasing the characteristic voltage, V_Φ, of the SQUID will result in an even maximum higher slew rate. For direct readout electronics the addition of an APF to reduce noise will increase the slew rate of the system and cause the system to become saturated or unstable. Table 7.1 presents a list of operational amplifiers with their voltage slew rates for a certain step-response and gain.

7.3 Digital Flux-locked Loop

With the massive power of the new Atmel Atmega and Microchip dsPIC Digital Signal Processors (DSP) the option of using a digital controller for the SQUID electronics has become a simple reality. The

Model	Supply Voltage [V]	GBW -3dB [GHz]	Slew-Rate [V/μs]	Feed-back Type	Input Offset Voltage [μV] (max)	Input Bias Current [μA] (max)	Voltage Noise S_v [$\frac{nV}{\sqrt{\text{Hz}}}$]	Current Noise S_I [$\frac{pA}{\sqrt{\text{Hz}}}$]
AD8003	± 5	1.65	3800 (G=2) 2V Step	CF	9300	50	1.8	36
AD8009	± 5	1	5500 (G=2) 4V Step	CF	2000	50	1.9	46
EL5166, EL5167	± 5	1.4	6000 (G=2) 5V Step	CF	5000	25	1.7	50
EL5367	± 6	1	6000 (G=2)	CF	5000	25	1.7	50
MAX4223-MAX4228	± 5.5	1	1700 (G=1) 4V Step	CF	5000	25	2	20
THS3201	± 7.5	1.8	10500 (G=2) 10V Step	CF	4000	85	1.65	20
THS3202	± 7.5	1.8	5100 (G=-1) 5V Step	CF	4000	85	1.65	20
THS4303 Fixed 10x	± 2.5	18	5500 (G=10) 2V Step	CF	5250	15	2.5	
AD8351	+ 5.5	2.2	13000 (10dB) 2V Step	VF		15		
OPA355	± 2.5	0.45	360 (G=2) 4V Step	VF CMOS	9000	50×10^{-6}	5.8	50×10^{-3}
OPA637	± 18	0.08	135 (G=-4) 10V Step	VF FET	250	10×10^{-6}	5.6	2.5×10^{-3}
OPA656	± 5	0.5	290 (G=2) 1V Step	VF FET	1800	20×10^{-6}	7	1.3×10^{-3}
OPA657	± 5	1.6	700 (G=10) 1V Step	VF FET	1800	20×10^{-6}	4.8	1.3×10^{-3}
OPA846	± 5	1.75	625 (G=10) 2V Step	VF	600	20	1.3	3.5
OPA847	± 5	3.9	950 (G=20) 2V Step	VF	500	42	0.92	3.5
OPA2846	± 5	1.65	600 (G=10) 2V Step	VF	650	20	1.3	3.5
THS4513	± 2.5	2.8	5100 (G=1) 2V Step	VF	5000	18.5	2.2	1.7

Table 7.1: Properties of Various Operational Amplifiers

preamplifier is used to match the SQUID output to an analog-to-digital converter (ADC) which then sends the digitized output to the DSP. Using a digital-to-analog converter (DAC) the output from the DSP can be fed into the feedback coil. APF can still be performed with an analog circuit in the cooled section.

The preamplifier is used to amplify the SQUID output to voltage levels compatible with the DSP, V_{op}, with the current generation operating between +5V and +3.3V. If the preamplifier transmits the output to a single ADC, then the preamplifier must have an output of $V_{\text{op}}/2$ at the working point, allowing for both rising and falling magnetic fields. If the preamplifier sends the amplified signal to one ADC and an inverted amplified signal to another ADC, then the preamplifier must have an output of zero at the working point, effectively increasing the ADC by one bit and allowing for both rising and falling magnetic fields. The anti-aliasing theory states that for a DSP the sample frequency must be twice the highest measured frequency. For a dsPIC with a 12-bit ADC, which has a maximum sampling rate of 200ks/s, the maximum input frequency is 100kHz [53].

The feedback coil is connected with a feedback resistor to two separate DACs. While one DAC acts as a current sources for the feedback coil the other DAC acts as a current sink. Alternating the output of each DAC allows for dynamic reversal of the feedback current.

Inside the DSP the output from the SQUID is analyzed and digitally integrated. The product of the integration is returned to the feedback coil, resulting in a FLL. The major advantage of this type of system is that the feedback coil can be set to a maximum of $\pm 1\Phi_0$. Whenever the feedback reaches the maximum output, a counter inside the DSP is increased or decreased accordingly and the integrator is reset, allowing the expelled flux to penetrate the SQUID. Unlike the analog FLL, this technique allows all but a small fraction of the applied field to pass through the SQUID, enabling the counting of thousands of fluxons. The DSP has a magnetic field resolution of

$$B_{N,pp} \cdot \mathrm{B} = \frac{\Phi_{\text{in,pp}}}{2^n}, \tag{7.3.1}$$

where n is the amount of bits for the ADC or DAC, $B_{N,pp} = 6B_N$, and B is the bandwidth of the system [19]. Similarly, the amount of bits required can be calculated as

$$n = \frac{\log\left(\Phi_{\text{in,pp}} / \left(B_{N,pp} \cdot \mathrm{B}\right)\right)}{\log 2}. \tag{7.3.2}$$

For a $n = 12$-bit DAC with $\Phi_{\text{in,pp}} = 1\Phi_0$ the noise can be $B_{N,pp} \cdot \mathrm{B} > 244\ \mu\Phi_0/\sqrt{\mathrm{Hz}}$ for the least significant bit (LSB) to be smaller than the noise. This is equivalent to a dc SQUID with a bandwidth of B = 1kHz having a magnetic field resolution of $1.285\ \mu\Phi_0/\sqrt{\mathrm{Hz}}$. The FLL linearizes only a small part if input flux while the bulk of the flux is applied to the dc SQUID. A large amount of apparent flux on the SQUID will increase the excess noise (Section 5.5.7) and could also lead to magnetic hysteresis of the junctions.

Hybrid FLLs can be also be created by combining analog circuitry with a DSP. The DSP can reset the integrator by switching on a transistor that will discharges the integrator's capacitor. The transistor must have a small t_{on} and t_{off} for use in high speed application.

Another potential advantage of the digital FLL is that the thermal noise and EMI generated by the cryocooler can be filtered by the DSP. The filtered output is separate from the FLL feedback, which must still track the EMI, allowing for a more accurate V-Φ measurements for applied signals.

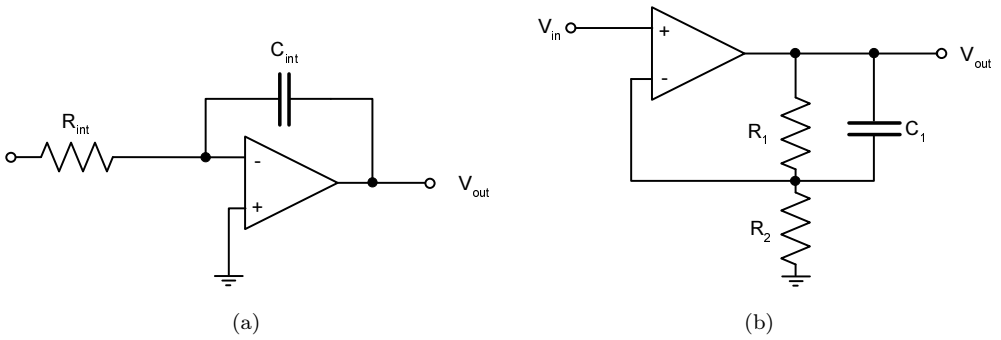

Figure 7.6: Layout of the integrator (a) and the lag compensator (b).

7.4 Integrator

The integrator must have the desired slew rate and gain-bandwidth (GBW) for the FLL. For the maximum slew rate (7.2.30) must be satisfied, while the unity-gain frequency $f_{1,\max}$ specifies the unity GBW of the integrator [54, 55]:

$$\mathrm{GBW_{Int}} = f_1. \tag{7.4.1}$$

The practical one-pole integrator shown in Figure 7.6(a) has the normalized transfer function

$$\mathrm{H_{Int}}(i2\pi f) = \frac{2\pi f_1}{i2\pi f} = \frac{1}{if/f_1}, \tag{7.4.2}$$

resulting in unity-gain at $f_1 = 1/(2\pi R_{\mathrm{int}} C_{\mathrm{int}})$, (7.2.9), and a unity GBW of f_1 [19]. The one-pole integrator gain has a -20dB/decade slope and a constant $-90°$ phase over the entire frequency range, resulting in a low-pass response with no overshoot. The magnitude and phase response for a one-pole integrator with $f_1 = 500$ MHz is shown in Figure 7.7(a). The integrator must have a high enough slew rate to provide good high-frequency performance, but it will also tend to produce low-frequency harmonics. These harmonics are fine for high-frequency measurements, but will result in the deterioration of low-frequency signals. The maximum frequency of a signal due to the effect of the slew-rate is

$$f_{\max,\mathrm{SR}} = \frac{\mathrm{SR}}{2\pi V_{\mathrm{out,peak}}}, \tag{7.4.3}$$

where SR is the slew-rate, and $V_{\mathrm{out,peak}}$ is the peak of the output signal.

A lag compensator, as shown in Figure 7.6(b), can be added to improve low-frequency measurements by increasing the low-frequency gain and slew rate [19, 52]. The transfer function for a lag compensator is

$$\mathrm{H_{lag}}(i2\pi f) = \frac{i2\pi f + \frac{R_1+R_2}{C_1R_1R_2}}{i2\pi f + \frac{R_2}{C_1R_1R_2}} = \frac{if + f_2}{if + f_2'}, \tag{7.4.4}$$

where the frequency of the zero is smaller than the characteristic frequency of the integrator, $f_2 < f_1$, and the pole is significantly smaller than the zero, $f_2' << f_2$. The zero is at

$$f_2 \leq \frac{f_1}{4} = \frac{R_1 + R_2}{2\pi C_1 R_1 R_2}, \tag{7.4.5}$$

and the pole is at

$$f_2' = \frac{f_2}{400} = \frac{R_2}{2\pi C_1 R_1 R_2}. \tag{7.4.6}$$

The magnitude and phase response for a lag compensator with $f_2 = 500/4$ MHz and $f_2' = 500/1600$ MHz

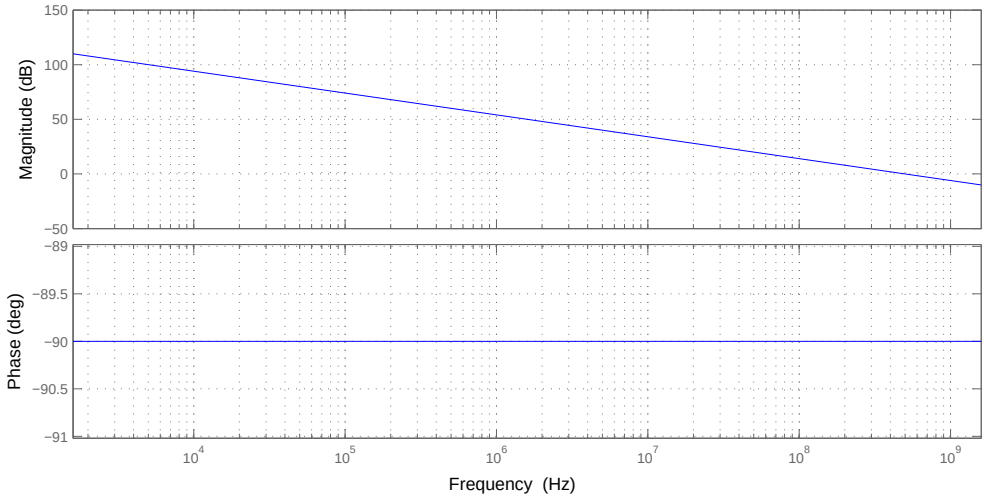

(a)

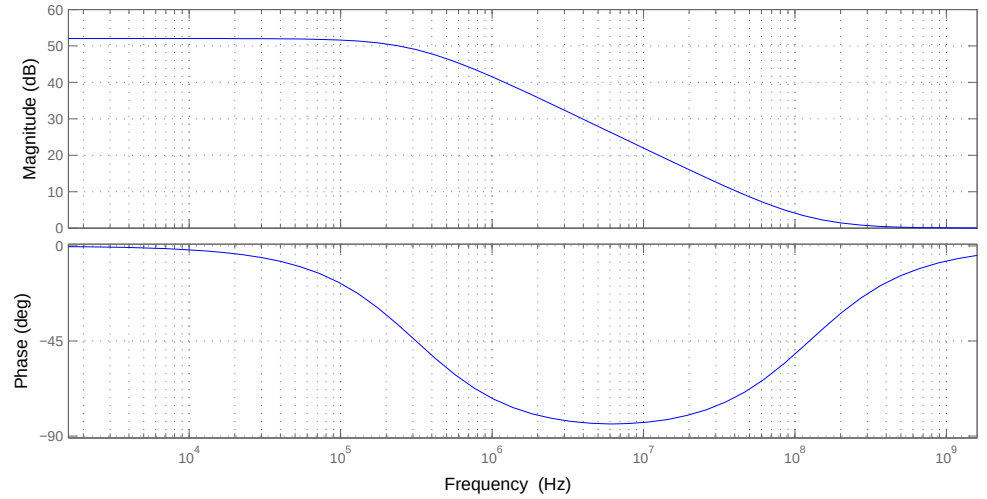

(b)

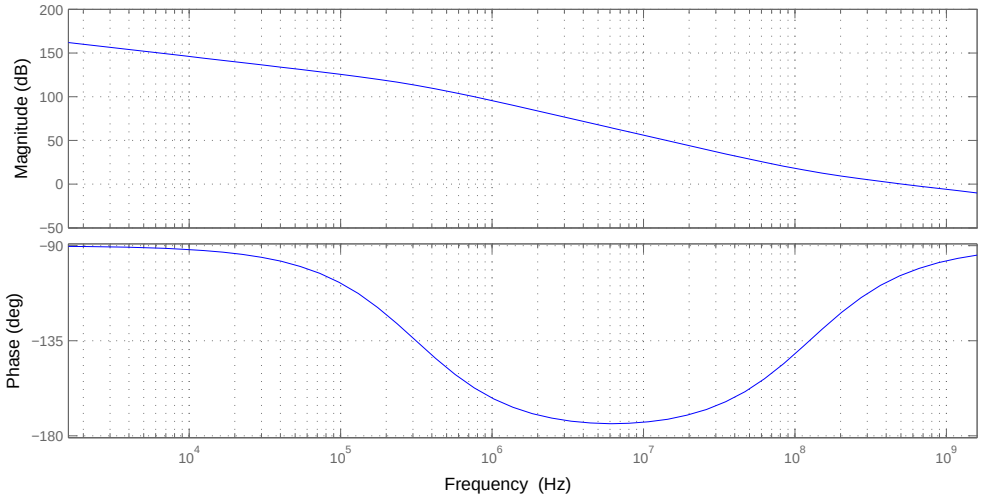

(c)

Figure 7.7: Bode diagrams showing the magnitude and phase response for (a) the integrator with $f_1 = 500$MHz, (b) the lag compensator with $f_2 = f_1/4$ and $f_2^{'} = f_2/400$, and (c) the integrator with lag compensation.

is shown in Figure 7.7(b).

For frequencies lower than $f < f_2^{'}$ the phase of the compensated integrator will remain at $-90°$, while the gain and slew rate will be improve by $|\mathrm{G_{lag}}| = f_2/f_2^{'}$ with a -20dB/decade slope, as shown in Figure 7.7(c). For frequencies between $f_2 >> f >> f_2^{'}$ the phase will reduce down to $-180°$, while the gain and slew rate of the integrator will be improved by $|\mathrm{G_{lag}}| = f_2/f$, resulting in a -40dB/decade slope. For frequencies higher than $f >> f_2$ the phase will remain at $-90°$ and the gain of the lag compensator will remain at unity, $|\mathrm{G_{lag}}| = 1$, resulting in a one-pole integrator response for the compensated integrator. It is important to design the integrator and the lag compensator so that with time delay the magnitude of the system has a flat frequency response over the largest possible range without a peak at the end, preventing the system from becoming unstable (Section 7.2.4).

The lag compensator will increase the low-frequency open-loop gain of the integrator, improving the slew rate and reducing low-frequency harmonics. For high-frequency measurements the lag compensator will result in reduced performance, and is only useful for measuring low-frequency signals.

7.5 Preamplifier

One of the main concerns when interfacing with a SQUID is that the preamplifier should not load the SQUID with a low input resistance or have an excessive offset current to significantly alter the biasing current. The preamplifier must have a high slew rate to accurately track the output and a high GBW to satisfy (7.2.12) [19]. Without the integrator the gain of the preamplifier is

$$A_{\mathrm{Preamp}} = \frac{1}{\mathrm{G}_{SQ}}, \tag{7.5.1}$$

and a $GBW = f_1/\mathrm{G}_{SQ}$ [54]. The maximum frequency of a signal due to the effect of the slew-rate is $f_{\mathrm{max,SR}} = \mathrm{SR}/2\pi V_{\mathrm{out,peak}}$ from (7.4.3), where SR is the slew-rate and $V_{\mathrm{out,peak}}$ is the peak of the output signal.

The small-signal voltage sensitivity of the SQUID (3.2.42) is adapted to include current fluctuation from the bias current leads,

$$\delta V = V_\Phi \left(\delta\Phi_a + M_{\mathrm{dyn}}\delta I\right), \tag{7.5.2}$$

where δV is a small change in voltage, $\delta\Phi_a$ is a small change in the applied flux, and δI a small change in the biasing current for a dc SQUID biased at the working point W. If there are no fluctuation in the biasing current then the voltage sensitivity will remain $\delta V/\delta\Phi_a = V_\Phi$ for small changes in the apparent flux. If there are no fluctuation in the biasing voltage then small changes in the apparent flux will result in the current sensitivity

$$M_{\mathrm{dyn}} = -\frac{\delta\Phi_a}{\delta I}, \tag{7.5.3}$$

where $M_{\mathrm{dyn}} \approx 2L_{SQ}$ and L_{SQ} is the SQUID loop inductance. The dynamic resistance of the SQUID is

$$R_{\mathrm{dyn}} = M_{\mathrm{dyn}} V_\Phi. \tag{7.5.4}$$

The preamplifier also contributes significantly toward noise (7.2.24), so it is important to choose an appropriate design to minimize noise. Another commonly used term for the preamplifier is a low-noise amplifier. There are three basic preamplifier designs to read out the flux applied to the dc SQUID. All three preamplifier are designed to operate at room temperature, with only the step-up transformer and series resistor requiring cryogenic cooling.

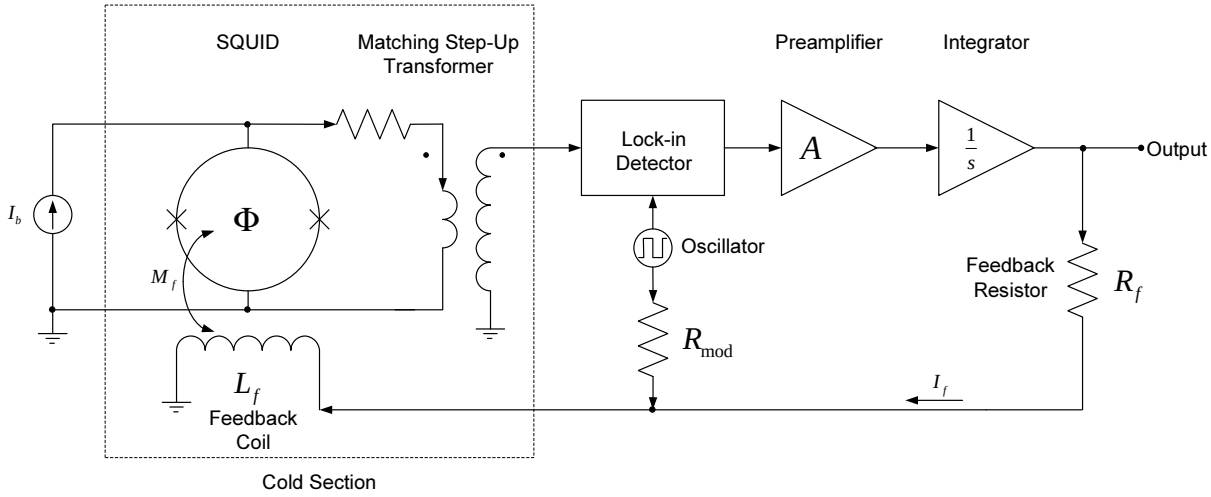

Figure 7.8: Current biased flux-locked loop with a step-up matching transformer. Flux modulation is controlled by the oscillator, lock-in detector and modulation resistor R_{mod}. The components located in the cold section are surrounded by the dashed line.

7.5.1 Preamplifier with Step-Up Transformer and Flux Modulation

The SQUID operates as a flux-to-voltage converter and is biased at the working point, W, by using a constant biasing current I_b. The preamplifier uses a step-up transformer or LC resonant circuit to increase the modulated voltage output of the SQUID and match the SQUID to the high-impedance input of the preamplifier [1, 19]. The turn ratio is chosen to match the SQUID to the preamplifier. A series resistor is usually added to restrict the maximum current through the inductor and prevent short circuiting. Both the transformer and resistor are located inside the cryogenic container and operate at cryogenic temperatures. The voltage sensitivity of the SQUID is given as $\delta V/\delta\Phi_a = V_\Phi$ by (3.2.42) since there is no bias current fluctuation, $\delta I = 0$. The step-up transformer will not change the linear flux range, Φ_{lin}, but will increase the slew rate of the FLL shown in Figure 7.8.

Flux modulation is used to decrease or suppress the preamplifier noise. A square wave modulation flux, Φ_{mod}, is applied to the SQUID at a frequency well above the $1/f$ corner frequency, usually around $f_{\mathrm{mod}} = 100\mathrm{kHz}$. This causes the working point to alternate between two points on opposing slopes on a single wavelength, W_1 and W_2, and any hysteresis in the SQUID's V-Φ response will cause the working points to differ significantly enough to distort the output. The working points are chosen to have the highest voltage sensitivity of V_Φ with no externally applied flux.

When the applied modulation flux is at a minimum, then the slope at W_1 in Figure 7.9 is positive and the output from the SQUID is conveyed directly to the integrator. When the applied modulation flux is at a maximum, then the slope at W_2 is negative and the output from the SQUID is inverted and conveyed to the integrator. This inversion is done by a lock-in detector and causes the V-Φ output of the SQUID to seem continuous, resulting in a linearized SQUID response. A multiplier, FET switch or mixer can be used in the lock-in detector to invert the signal. The output from the integrator is fed back into the SQUID through the feedback resistor, R_f, and coil, M_f, to complete the FLL. The FLL linearizes the input flux while maintains a specific amount of flux on the dc SQUID.

Reducing the apparent flux on the SQUID helps to maintain lower excess noise (Section 5.5.7) and prevent magnetic hysteresis of the junctions. Excess noise is further reduced by flux modulation, with the effect of in-phase noise (5.6.3) offset by the alternating working point. The bandwidth of a flux-modulated FLL is also reduced by the maximum frequency of the step-up transformer.

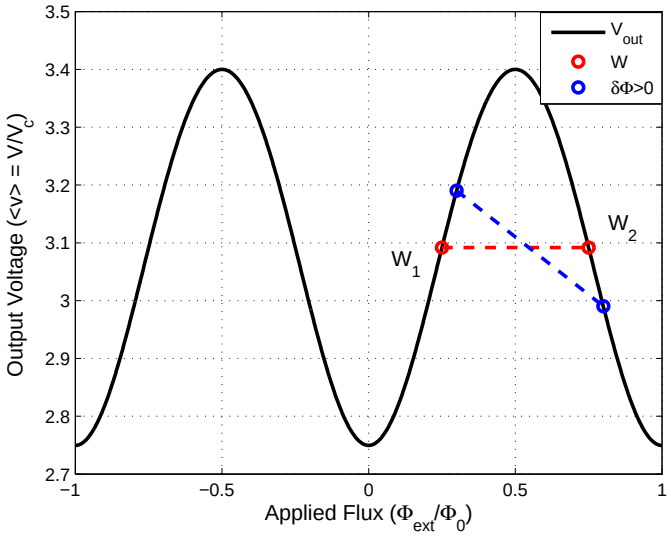

Figure 7.9: Flux modulation scheme. The flux modulator switches the SQUID between the working points W_1 and W_2. The effect of flux switching for a small signal error $\delta\Phi > 0$ is also shown.

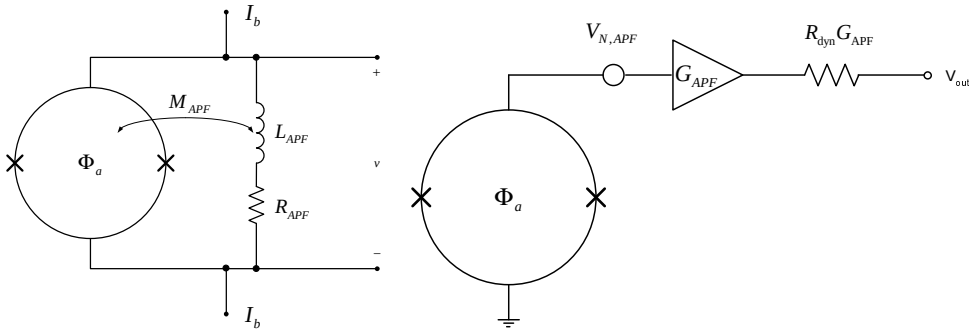

(a) (b)

Figure 7.10: Schematic for (a) the additional positive feedback (APF), and (b) the equivalent APF circuit.

7.5.2 Direct-Readout Preamplifier with Additional Positive Feedback

The SQUID operates as a flux-to-voltage converter and is biased at working point, W, by using a constant biasing current I_b. The preamplifier is directly connected to the SQUID and measures the voltage output from the SQUID, and is known as a direct-readout (DRO) preamplifier [56, 57]. DRO electronics are simpler and less complex to design, especially for very wide bandwidth applications. The voltage sensitivity of the SQUID is given as $\delta V/\delta\Phi_a = V_\Phi$ by (3.2.42) since there is no bias current fluctuation, $\delta I = 0$.

To increase the steepness voltage sensitivity and improve the matching between the SQUID's output and the high-impedance input of the preamplifier additional positive feedback (APF) is added [58, 19, 20, 59, 57]. The APF circuit in Figure 7.10(a) consists of a feedback coil, $L_{\rm APF}$ with mutual inductance $M_{\rm APF}$, in series with the feedback resistor, $R_{\rm APF}$, and is connected in parallel with the SQUID. When the SQUID is biased at working point W, then a small increase in the applied flux will cause the output voltage of the SQUID to increase. This increase in voltage across $R_{\rm APF}$ will cause more current to flow through $L_{\rm APF}$ and produce additional positive flux through the SQUID, further increasing the output voltage. The SQUID will have a far steeper V-Φ slope at W, and the small signal response will be asymmetrical (not sinusoidal). The addition of a shunt resistor $R_{\rm APF}$ will slightly reduce the voltage sensitivity (3.2.42) as some of the biasing current will flow through the resistor when the applied flux

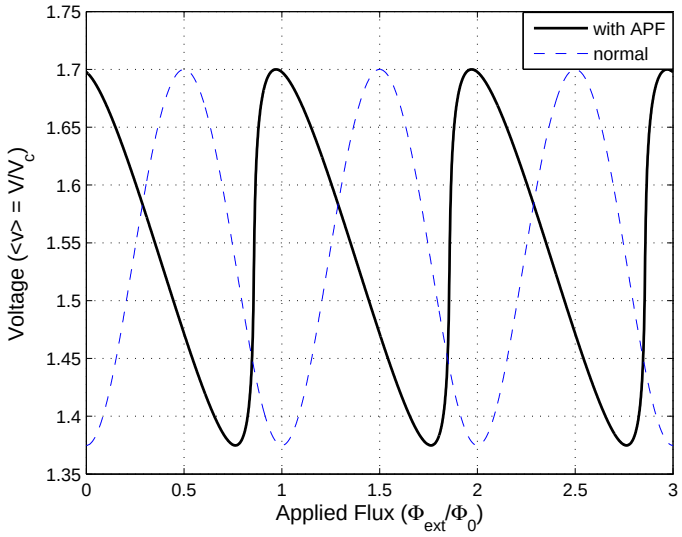

Figure 7.11: The simulated output of a dc SQUID with additional positive feedback (APF). β_{APF} is set to 0.9 for a gain of $G_{\mathrm{APF}} = 10$.

changes. To reduce the effect of R_{APF} on the voltage sensitivity, $R_{\mathrm{APF}} >> R_{SQ}/2$, where R_{SQ} is the shunt resistance of the SQUID junction.

The gain due to the APF [56] is

$$G_{\mathrm{APF}} = \frac{1}{1-\beta_{\mathrm{APF}}}, \tag{7.5.5}$$

where

$$\beta_{\mathrm{APF}} = \frac{V_\Phi}{R_{\mathrm{APF}}}\left(M_{\mathrm{APF}} - M_{\mathrm{dyn}}\right) \leq 1. \tag{7.5.6}$$

$M_{\mathrm{APF}} - M_{\mathrm{dyn}}$ represents the positive flux fed back from the APF less the reduction in bias current through the SQUID (7.5.3), and V_Φ is the voltage sensitivity of the SQUID without the APF. The gain becomes infinite as β_{APF} approaches 1, with values of $\beta_{\mathrm{APF}} > 1$ resulting in hysteresis and an unstable system. The FLL with APF can be modeled as a SQUID with an additional amplifier gain G_{APF} increasing the voltage sensitivity to

$$V_\Phi^* = V_\Phi G_{\mathrm{APF}}, \tag{7.5.7}$$

with a series resistance

$$R_{\mathrm{APF,series}} = R_{\mathrm{dyn}} G_{\mathrm{APF}}. \tag{7.5.8}$$

The series resistance increases the output resistance of the SQUID for better impedance matching with the DRO preamplifier, resulting in less signal reflection at high frequencies. The equivalent APF can be seen in Figure 7.10(b). It must be noted here that using a series resistor to match the DRO preamplifier with the SQUID is inadvisable, with the exception of the equivalent $R_{\mathrm{APF,series}}$ produced by the APF. The series resistor will act as both a thermal noise source (5.5.3) and as a voltage divider for the low output impedance of the SQUID, yet will provide no real benefit. The actual bandwidth of the APF [19] is

$$BW_{\mathrm{APF}} = \frac{f_{\mathrm{APF}}}{G_{\mathrm{APF}}} = \frac{R_{\mathrm{APF}}}{2\pi L_{\mathrm{APF}} G_{\mathrm{APF}}}. \tag{7.5.9}$$

For an increase of $V_\Phi^* = 10V_\Phi$ the usable voltage swing is diminished by about 20% due to the APF resistance R_{APF} [20]. The voltage response of a SQUID with APF is shown in Figure 7.11, with $\beta_{\mathrm{APF}} = 0.9$ and $G_{\mathrm{APF}} = 10$.

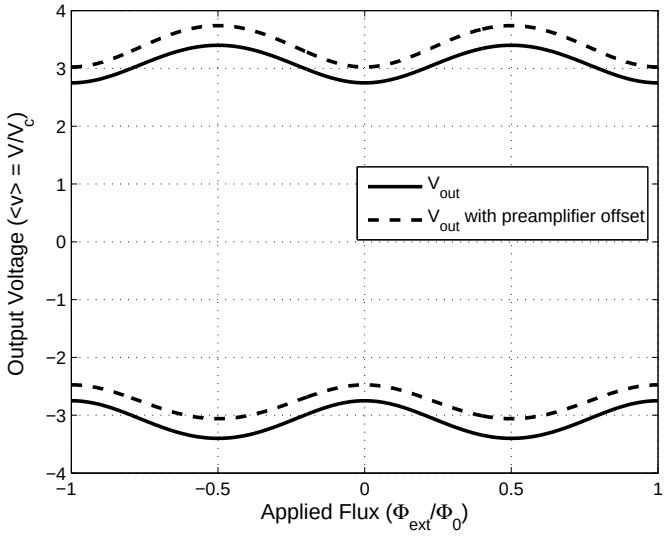

Figure 7.12: Effect of preamplifier voltage fluctuations.

The APF creates an additional noise voltage spectral density

$$S_{v,\mathrm{APF}} = 4k_B T R_{\mathrm{APF}} \beta_{\mathrm{APF}}^2 \approx 8k_B T R_{SQ}, \tag{7.5.10}$$

included ahead of the APF amplifier, where k_B is Boltzmann's constant, and T is the absolute temperature. To reduce the APF noise R_{APF} should be as small as possible, with a typical APF circuit designed to have a voltage noise similar to the SQUID's voltage noise. APF increases the voltage slew rate of the SQUID output and reduces the DRO preamplifier voltage noise, so the preamplifier and the integrator must be able to handle the enhanced slew rate.

The current noise spectral density caused by the preamplifier can also be reduced by including a bias current feedback (BCF) coil [58, 19]. This coil is coupled in series with the current biasing cables and must have a mutual inductance $M_{\mathrm{BCF}} = M_{\mathrm{dyn}}$ for optimal performance. A small change in the SQUID's biasing current, δI, will cause the output voltage to change, but the current change will also cause the flux from the BCF coil to change and reverse the effect of δI. BCF will cause $M_{\mathrm{dyn}} = 0$ and $R_{\mathrm{dyn}} = 0$ (3.2.39), so the preamplifier's current noise will have no effect on the FLL noise.

APF together with BCF allows the use of room-temperature electronics for low-T_c magnetometers without using modulation techniques. Bias reversal schemes are needed for high-T_c magnetometers to suppress the $1/f$ noise caused by critical current fluctuations described in Section 5.6.2, and preamplifier voltage noise in Figure 7.12.

7.5.3 Voltage Bias Preamplifier

In Figure 7.13(b) the SQUID operates as a flux-to-current converter and is biased at working point, W, by using a constant biasing voltage V_b. Unlike the current biased SQUID in Figure 7.13(a), the current through the SQUID is detected and converted by the transimpedance preamplifier into an output voltage [19, 57]. The current sensitivity of the SQUID is given by $\delta\Phi_a/\delta I = -1/M_{\mathrm{dyn}}$.

Broadband noise from the preamplifier is unfortunately fed directly back into the SQUID. Since noise is dependent on the bandwidth of the system, achieving a similar noise performance to current biasing when using voltage biasing will result in a lower system bandwidth.

The APF described in Section 7.5.2 can also be used with a voltage biased SQUID. The current sensitivity remains unchanged and the voltage sensitivity is given by (7.5.7). $\Phi_{\mathrm{lin,pp}}$ also remains unchanged

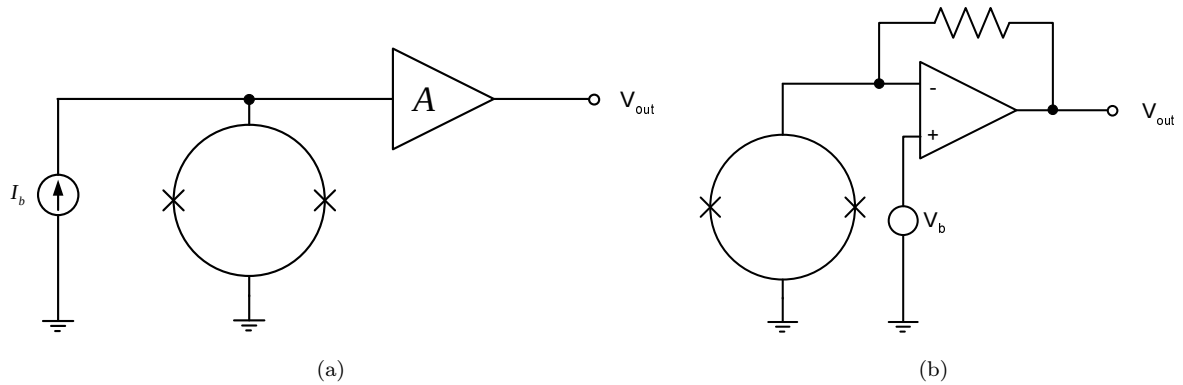

Figure 7.13: Schematic for (a) the current biased, and (b) the voltage biased dc SQUID with a preamplifier.

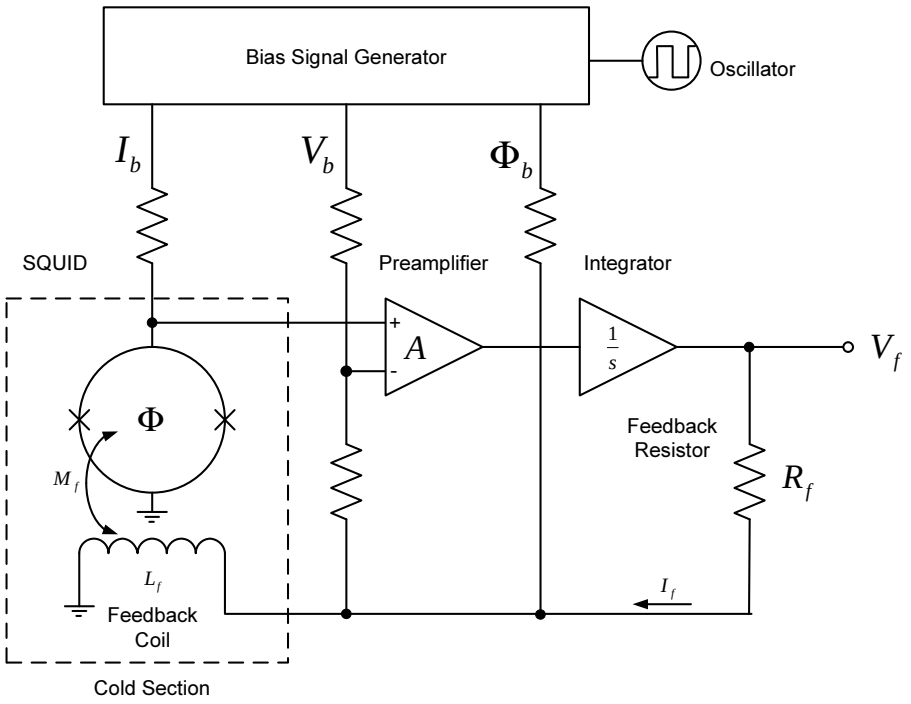

Figure 7.14: Current biased flux-locked loop using a current bias reversal scheme. The bias current I_b, the bias voltage V_b, and the bias flux Φ_b are controlled by the bias signal generator. The components located in the cold section are surrounded by the dashed line.

for voltage biasing and $\beta_{\mathrm{APF}} > 1$ will not result in system instability. This will cause the voltage biased FLL to have a higher slew rate than the current biased FLL.

7.6 Current Bias Reversal

In Section 5.6.2 the effects of critical current fluctuations are described. The in-phase noise offset (5.6.3) will cause the output voltage to shift, increasing or decreasing the offset of the V-Φ output for the working point W. Flux modulation will reduce the in-phase noise offset but will not reduce the out-of-phase noise offset [58]. The out-of-phase noise offset (5.6.4) will cause a shift in the apparent flux, increasing or decreasing the working point along the V-Φ slope.

To reduce the effect of critical current fluctuations a bias current reversal scheme shown in Figure 7.14 can be used. The phase noise offsets tend to be expressed in one direction over a given time period. A good example is when the in-phase noise offset increases the V-Φ output by V_x and the out-of-phase

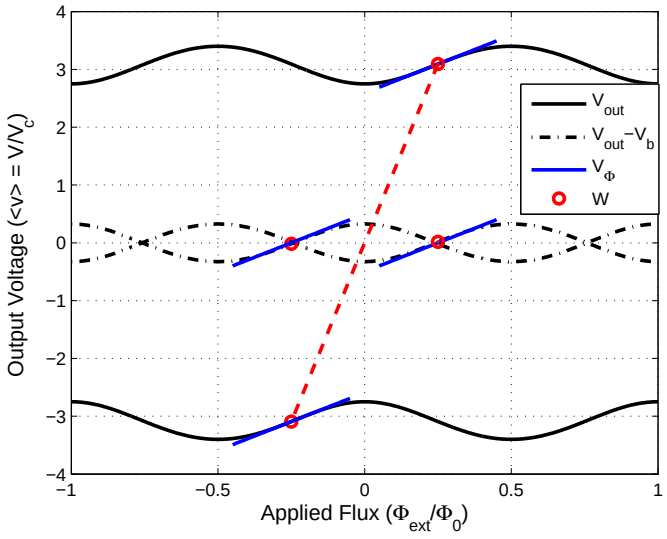

(a)

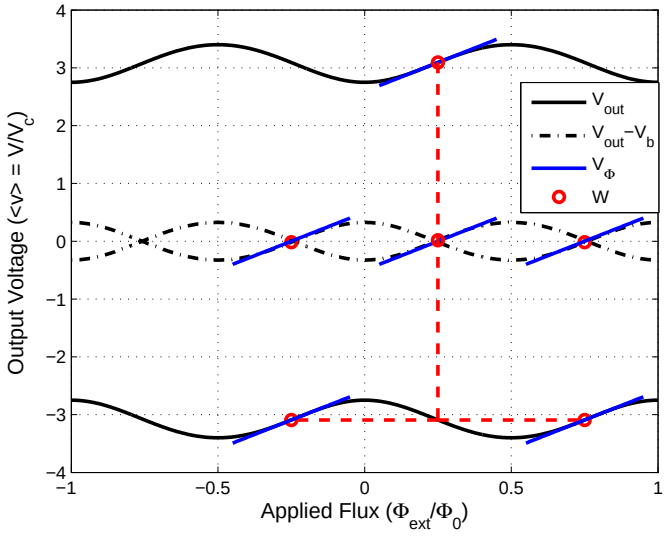

(b)

Figure 7.15: Current bias modulation scheme. The bias current I_b in (a) is reversed synchronously with the bias flux Φ_b, resulting in a linear output and definite working points W. The bias current I_b in (b) is reversed without reversing the bias flux Φ_b, causing the integrator to compensate and lock onto a working point offset by $\Phi_0/4$ on either side.

noise offset adds Φ_n flux to the apparent flux. For a positive current bias the output from the SQUID will have a voltage offset $(V_b + V_x)$ and an apparent flux $(\Phi_a + \Phi_n)$, whereas for a negative current bias the output will have a voltage offset $(-V_b + V_x)$ and an apparent flux $(\Phi_a - \Phi_n)$. For one bias reversal period the net effect of the noise offset will be reduced to zero, negating the noise. A reduction of about 100 times was achieved by [40] by using bias reversal.

The additional bias flux Φ_b in Figure 7.14 is required when using a current bias reversal scheme, whereas for a dc current bias scheme the bias flux is not required. This is done to ensure that the correct amount of biasing flux is provided for the working point (I_b=$\Phi_0/4$) without the integrator having to compensate. Figure 7.15(a) provides a graphical analysis of what happens when the bias current is reversed synchronously with the bias flux. Without the additional biasing flux the integrator will try to generate flux to return the SQUID to a working point, causing it to skip $\Phi_0/2$ for every switch. This

can result in the integrator slowly running away in one direction until its output is saturated. Figure 7.15(b) provides a graphical analysis of what happens when the bias current is reversed without reversing the bias flux. If the bias current, I_b, the working point voltage, V_b, and the bias flux, Φ_b, are reversed synchronously, then the integrator will perceive a continuous non-inverting input. The FLL will have a linear V-Φ response. Noise fluctuation of the various shunt resistances, such as R_n and R_{APF}, will also be reduced by the bias reversal scheme. The frequency of bias reversal should be significantly higher than the $1/f$ noise corner frequency f_c, with $f_c = 10$ kHz typical for DRO preamplifier [19]. The APF circuit must be designed to operate with the bias reversal scheme, since there might be overshoot or a long settling time for the step-response of each bias polarity reversal. If the APF is designed to have a voltage noise similar to the SQUID's voltage noise then the settling time will be insignificant.

7.7 Shielding

It is important to properly shield the electronics and the cables, preventing them from receiving external interference or creating interference with the SQUID. Failing to properly shield the electronics can lead to self-field generation in the SQUID or loosing the lock in a FLL. A portion of the EMI is absorbed by the shield due to the skin effect, where the signal attenuates by

$$A = e^{-d/\delta}. \tag{7.7.1}$$

The distance of the wave traveled into the shield is d, and the penetration depth of the material is δ [19]. Increasing the thickness of the material or using a material with a lower penetration depth will improve the shielding. Penetration depth is a function of frequency

$$\delta = \sqrt{\frac{1}{\pi \mu_0 \mu_r \sigma f}}, \tag{7.7.2}$$

where $\mu_0 = 4\pi \times 10^{-7}\mathrm{Hm}^{-1}$ is the permeability of free space, μ_r is the material's relative permeability, and f is the frequency of the wave in Hz. The frequency dependence indicates that the shield is more effective at higher frequencies and has almost no effect on dc signals. Since most of the noise associated with interference occurs due to rf interference, preventing the FLL from locking and the output to drift, using only rf shielding should suffice.

7.7.1 SQUID Shielding

The magnetometer is supposed to measure magnetic fields emanating from room temperature sources. To improve the noise performance and reduce eddy currents, all magnetic materials in the vicinity of the magnetometer and cryostat must be removed. The magnetometer is said to work in an unshielded environment. Addition of low-frequency (lf) of radio-frequency (rf) shielding to the magnetometer will cause sites for eddy currents to form. The SQUID must be able to operate in the earth's magnetic field and movement of the shielding in a magnetic field will cause eddy current formation. Only the use of composite materials and crystals close to the magnetometer will result in lower noise, and the environmental noise can be filtered afterward.

By using electronic or digital filtering the effect of common environmental noise can be removed. For lf measurements a low-pass filter can be used when viewing the output, and for hf measurements a high-pass filter can be used. If a wider bandwidth is to be analyzed, a notch filter can be used to filter out the respective noise frequencies. Common sources of noise are 50 Hz for the power grid, and 60 Hz to 120 Hz for various CRT monitors. A more efficient and accurate method to filter out environmental

noise is to create a baseline measurement before and after the DUT has been tested [60]. The baseline is compared to the measured signal and the noise can then be removed digitally.

If the SQUID needs to be tested under conditions with almost no EMI or external flux, then a shield made from high-quality bulk superconductor can be used. The shield must have a higher critical temperature than the SQUID and can be surrounded by mu-metal to further attenuate EMI. The mu-metal will reduce the flux penetrating the shield when it becomes superconductive and expels the remaining penetrating flux.

7.7.2 Shielding the Feedback Electronics

The feedback electronics are prone to the effects of external interference. They also tend to produce their own EMI that cause self-fields to form in the SQUID and degrade the performance. Placing the electronics inside a shielded enclosure will attenuate the external noise and reduce the radiated noise from the electronics. Aluminium of sufficient thickness will absorb a significant portion of the noise and can be used to construct the enclosure. If the lf noise from the environment becomes a problem, using mu-metal inside the aluminium enclosure will reduce the noise.

The aluminium shielding must have a good seal along the seams to prevent EMI from penetrating through a slot in the material. The various cables should pass through the shield using the smallest diameter hole possible, and each twisted pair must use a separate hole.

7.7.3 Cable Shielding

To prevent the current flowing through the cabling from generating a magnetic field, the cables can be twisted and covered by a layer of aluminium. Using Stoke's theorem (2.9.1), twisting the cables reduces the loop area and reduces the magnetic field generated by the electronics. Another advantage of using twisted cables is that external magnetic fields coupling into the wire are simultaneously reduced. This reduces the differential-mode current noise in the wire, but does not decrease the common-mode current noise. The preamplifier is designed to have a large common-mode rejection ratio, reducing the effect of common-mode current noise. Differential mode signals are amplified by the preamplifier and the differential-mode noise can not be reduced electronically.

To further reduce EMI, especially those generated by the power lines, a mu-metal or ferrite cylinder can be be used to surround both ends of the cable. They must be positioned far enough from the SQUID so that their generated eddy currents will not interfere with the SQUID's operation. Differential signal communication used in USB devices require these mu-metal cylinders for improved data rates and lower noise. Keeping the cables as short as possible increases the potential bandwidth of the FLL and reduces the effect of EMI.

Using CAT-5 network cabling is a good choice for connecting the feedback electronics to the SQUID. This type of cabling has been extensively tested and uses four pairs of twisted wires for communication at frequencies higher than 1 GHz. The cabling is usually shielded by an aluminium layer and the wires are high quality single-stranded copper.

7.8 Conclusion

With a properly designed dc SQUID magnetometer the performance of the SQUID microscope rests on the controlling electronics. The noise present in a SQUID microscope can usually be attributed to incorrectly designed electronics.

A flux-locked loop is used to linearize the V-Φ response of the SQUID, increasing the linear input signal range from a fraction of a fluxon to hundreds of fluxons. Maintaining a persistent amount of flux

across the SQUID prevents excess $1/f$ noise from forming by preventing additional flux from forming vortices in the pinning sites.

A bias current and a bias flux set the working point of the SQUID to an optimal position. The signal from the SQUID is read by a matched low noise preamplifier, with a large effort placed on reducing the additional noise generated by the preamplifier. The direct-readout preamplifier has the widest output bandwidth of all the preamplifiers and the addition of additional positive feedback improves the matching with the SQUID.

The integrator maintains the output of the feedback coil and causes the apparent flux to remain at the bias point. The gain-bandwidth of the feedback electronics set the maximum bandwidth of the SQUID system.

The use of bias reversal will reduce the effect of fluctuations in the critical current due to the current noise in the junctions.

When using room temperature electronics the bandwidth of the flux-locked loop is dominated by the line delay.

Chapter 8

Simulations

8.1 Introduction

Simulations are used to verify the theory describing the behaviour of the Josephson junctions and the SQUID magnetometers. They also provide a convenient and simple way to test the feedback system for the flux-locked loop (FLL) before building and testing a complete system.

The different types of Josephson junctions, the basic SQUID and then a simple FLL are simulated using the WRSpice® simulation software [61]. A more complete analysis of the FLL is then performed using the MATLAB® Simulink® software [62].

8.2 WRSpice Simulations

8.2.1 Introduction

WRSpice [61] is a very fast simulation package specially designed for simulating Josephson junctions and other high-speed superconducting electronics. The software uses a text-based input and has the option of storing the simulation output as a data file. The simulation data file is imported into MATLAB to normalize and display the various figures. WRSpice features a built-in Gaussian random number generator that can be used to simulate noise. This simplifies the analysis of the effect of noise.

The Josephson junctions are based on the dynamic junction equations for the superconducting channel, the capacitive channel and the shunt resistance. A dc SQUID is simulated using these dynamic junctions. The dc SQUID with no hysteresis, with an inductance $L_{SQ} = \Phi_0/\pi I_c$ from (3.2.24), and a dc SQUID with slight hysteresis but at the optimal screening parameter $\beta_L = 1$ (3.2.40), with an inductance $L_{SQ} = \Phi_0/2I_c$, are compared. For the dc SQUID with optimal screening both the effect of additional positive feedback (APF) and the flux-locked loop (FLL) are simulated.

White Gaussian current noise is also added to the junction to analyze the effect of thermal noise due to the normal shunt resistance R_n.

8.2.2 Noise Simulations

In Sections 5.3 and 5.5.2 the theory of thermal noise and its effect on the Josephson junction are discussed. The thermal noise source for the junction has a current noise spectral density $S_I = 4k_BT/R_n$ in (5.5.4), where $k_B = 1.38 \times 10^{-23}$(J/K) is Boltzmann's constant, T is the absolute temperature, and R_n is the normal shunt resistance of the junction. The theoretical rms noise current is $i_{\text{rms}} = \sqrt{4k_BT/R_n} \cdot \sqrt{B}$ (5.3.1), and the peak value is approximately $i_{\text{peak}} = 3\sqrt{4k_BT/R_n}\sqrt{B}$ (5.3.2). Thermal noise is considered to be white noise and will be simulated by using a Gaussian random current source parallel to R_n. The source code for the simulation is given in Appendix B.1.

Bandwidth [MHz]	R_n [Ω]	Temperature [K]	$\sqrt{S_i}$ [pA/Hz$^{1/2}$]	i_{rms} [nA]	I_{peak}=3i_{rms} [μA]	I_{peak}=4i_{rms} [μA]
500000	10	77	6.21759	14581.5	43.7446	58.3262
500	10	77	6.21759	461.109	1.38333	1.84444
1	10	77	6.21759	20.6214	0.0618642	0.0824857

Table 8.1: Theoretical current noise for a 10 Ω resistor at 77 K at 500 GHz, 500 MHz and 1 MHz.

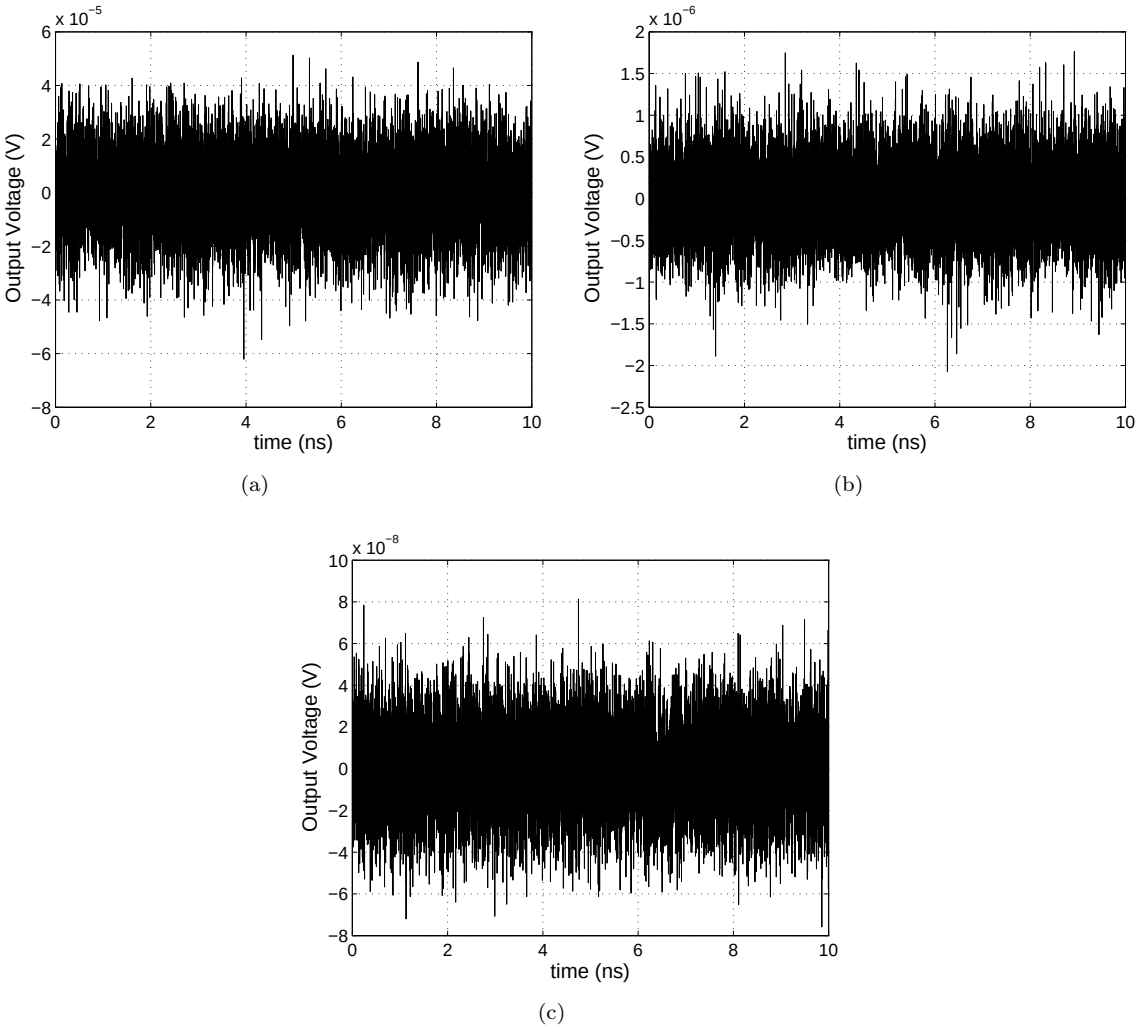

Figure 8.1: Simulated noise using WRSpice's built-in Gaussian random generator for (a) a 500 GHz bandwidth, (b) a 500 MHz bandwidth, and (c) a 1 MHz bandwidth.

The critical current, $I_c = 10$ μA, and the shunt resistance, $R_n = 10$ Ω, are the typical values for the M1000 HTS magnetometer in Table A.3 on p. 140 and the M2700 HTS magnetometer in Table A.4 on p. 141 provided by STAR Cryoelectronics [4]. The liquid nitrogen used to cool the magnetometer has an operating temperature of about $T = 77$ K.

Table 8.1 presents the theoretical noise values for three different bandwidths. Figure 8.1(a), Figure 8.1(b) and Figure 8.1(c) show the simulated noise levels at 500 GHz, 500 MHz and 1 MHz, respectively. The 500 GHz noise is for comparison only. The approximation made by Clarke *et al* [19] in (7.2.26) that $i_{\text{peak}} \approx 4i_{\text{rms}}$ seems to correlate better with the peaks observed in the simulated noise in Figure 8.1 than the approximation $i_{\text{peak}} \approx 3i_{\text{rms}}$ made in (5.3.1).

8.2.3 Basic Josephson Junction Simulations

The Josephson junctions are based on the dynamic junction equations (2.8.8) and (2.8.9) for the superconducting channel, (2.8.22) for the capacitive channel, and (2.8.19) for the shunt resistance. Figure 2.7 on p.16 provides a graphical representation of the simulated circuit. Appendix B.2 contains the relevant source code for the simulations.

The Josephson junction's voltage-current characteristic is time-averaged to eliminate the Josephson oscillation described in Section 2.8.3. The frequency of the voltage oscillation in (2.8.34) is dependent on the input current, but has a constant peak-to-peak amplitude of $2V_c$. To see if the simulation also predicts this oscillation the input current is set to a constant $I = 3I_c = 30\ \mu$A, $I = 6I_c = 60\ \mu$A, and $I = 9I_c = 90\ \mu$A. This provides a uniform basis to compare the theoretical results in Figure 2.10 on p. 19 to the simulation results in Figure 8.2(a), which are basically the same.

Figure 8.2(b) shows the normalized voltage-current characteristic of an unfiltered RSJ junction, with the input current swept between $-3I_c$ and $3I_c$. A high-frequency voltage oscillation with an amplitude of $2V_c$ is superimposed onto the time averaged voltage-current in Figure 8.2(c), making it difficult to predict the behaviour of the junction. The output is filtered with a simple 500 MHz low-pass RC filter buffered by an ideal voltage-controlled voltage source (VCVS). The VCVS does not load the junction, which would change its characteristics. Choosing a larger sampling time for the simulation will not get rid of the oscillations. In practical systems the electronics are bandwidth limited, filtering the output without the need for the low-pass RC filter.

Figure 8.2(c) shows the time-averaged voltage-current response of the simulated RSJ junction, which is identical to the voltage-current response of the theoretical RSJ junction in Figure 2.9 on p. 19. The RSJ junction is used throughout this thesis as the basis for the SQUID, since YBCO grain-boundary junctions have negligible capacitance and exhibit an overdamped response.

For verification purposes the time-averaged voltage-current response of the strongly underdamped junctions and the general damped junction are also simulated. In Figure 8.3(a) the normalized simulation output of the strongly underdamped junction, with $\beta_c >> 1$, is shown. With no initial voltage across the junction, the output voltage rises sharply from zero to V_c as the applied current exceeds I_c. When a finite voltage is already present across the junction, the voltage-current response has a linear slope of 1 as defined by the shunt resistance, R_n. The return current is near 0 μA, so when the current through the junction drops below the return current it causes the voltage across the junction to dissipate and return to zero. This is similar to the theoretical response in Figure 2.11 on p. 20.

The general damped junction with a damping constant $\beta_c = 100$ is used to clearly show the return current of the RCSJ junction displayed. The time-averaged voltage-current response displayed in Figure 8.3(b), with the return current at $i = 0.34I_c$. The general response in Figure 8.3(b) is generally the same as the theoretical value in Figure 2.12 on p. 21.

8.2.4 Josephson Junction Noise Simulations

Gaussian white noise is added to the Josephson junction to simulate the effect of thermal noise occurring due to the shunt resistance R_n. Appendix B.2 contains the relevant source code for the simulations. As in Section 8.2.2, the critical current is $I_c = 10\ \mu$A, the shunt resistance is $R_n = 10\ \Omega$, and the operating temperature is at $T = 77$ K.

Figure 8.4(a) shows the effect of noise for a system with a 1 MHz bandwidth. The effect of noise is too small to notice over such a long current sweep, so in Figure 8.4(b) the section from $i = -1.05I_c$ to $i = -0.98I_c$ is enlarged. A system with a small bandwidth should have relatively little noise. For a 1 MHz bandwidth, the noise should be approximately 824.857 nV_{peak}, or 8.24857 $\text{m}V/V_{\text{c,peak}}$ normalized. This value for the voltage noise is obtained by multiplying the 1 MHz peak current noise in Table 8.1

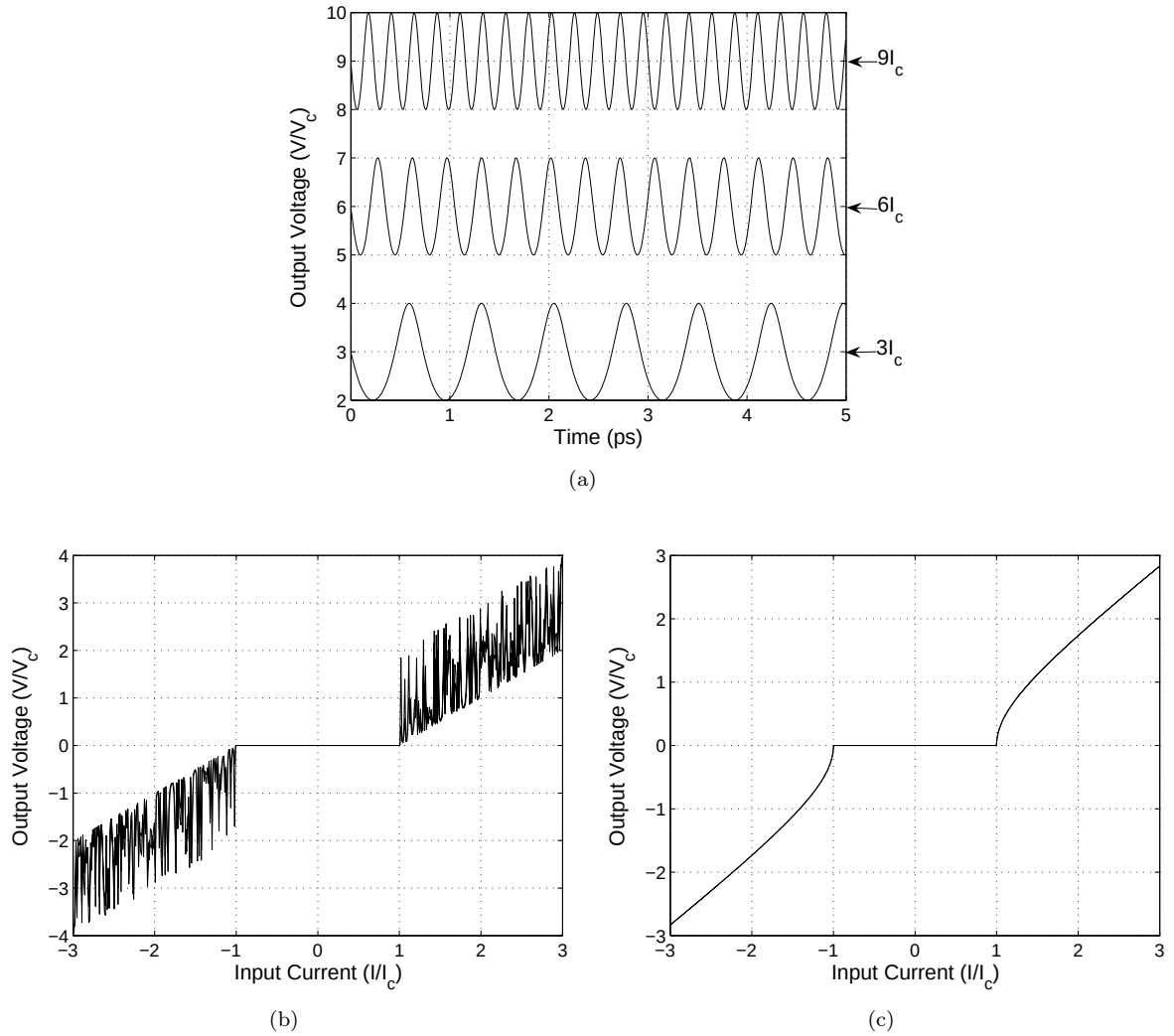

(a) (b) (c)

Figure 8.2: Simulated overdamped Josephson junctions using WRSpice: (a) The normalized oscillation of the junction for a constant input current of $3I_c$, $6I_c$ and $9I_c$. (b) The normalized dynamic, unfiltered voltage-current response. (c) The normalized time-averaged voltage-current response.

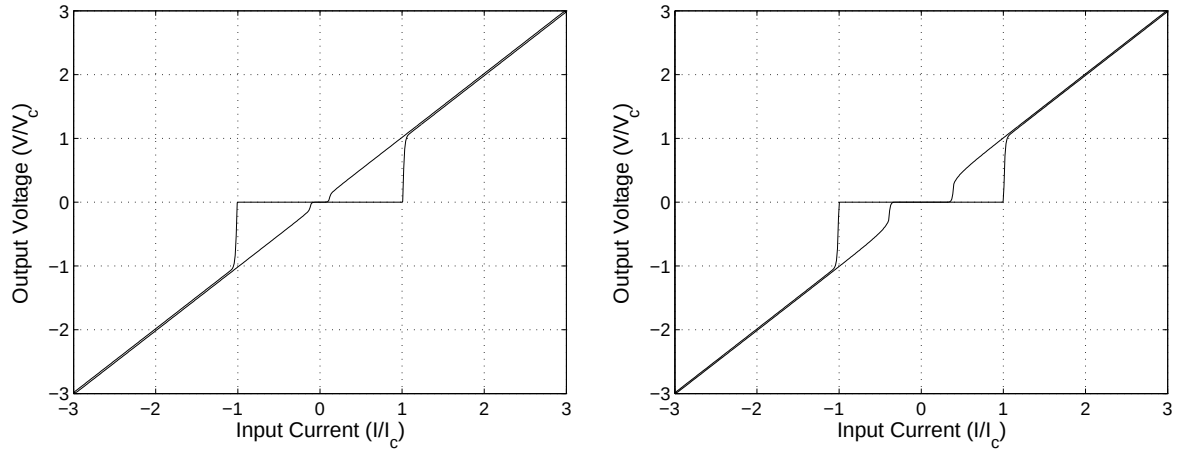

(a) (b)

Figure 8.3: Simulated Josephson junctions using WRSpice: The normalized time-averaged voltage-current response for (a) the underdamped junction and (b) a general damped junction.

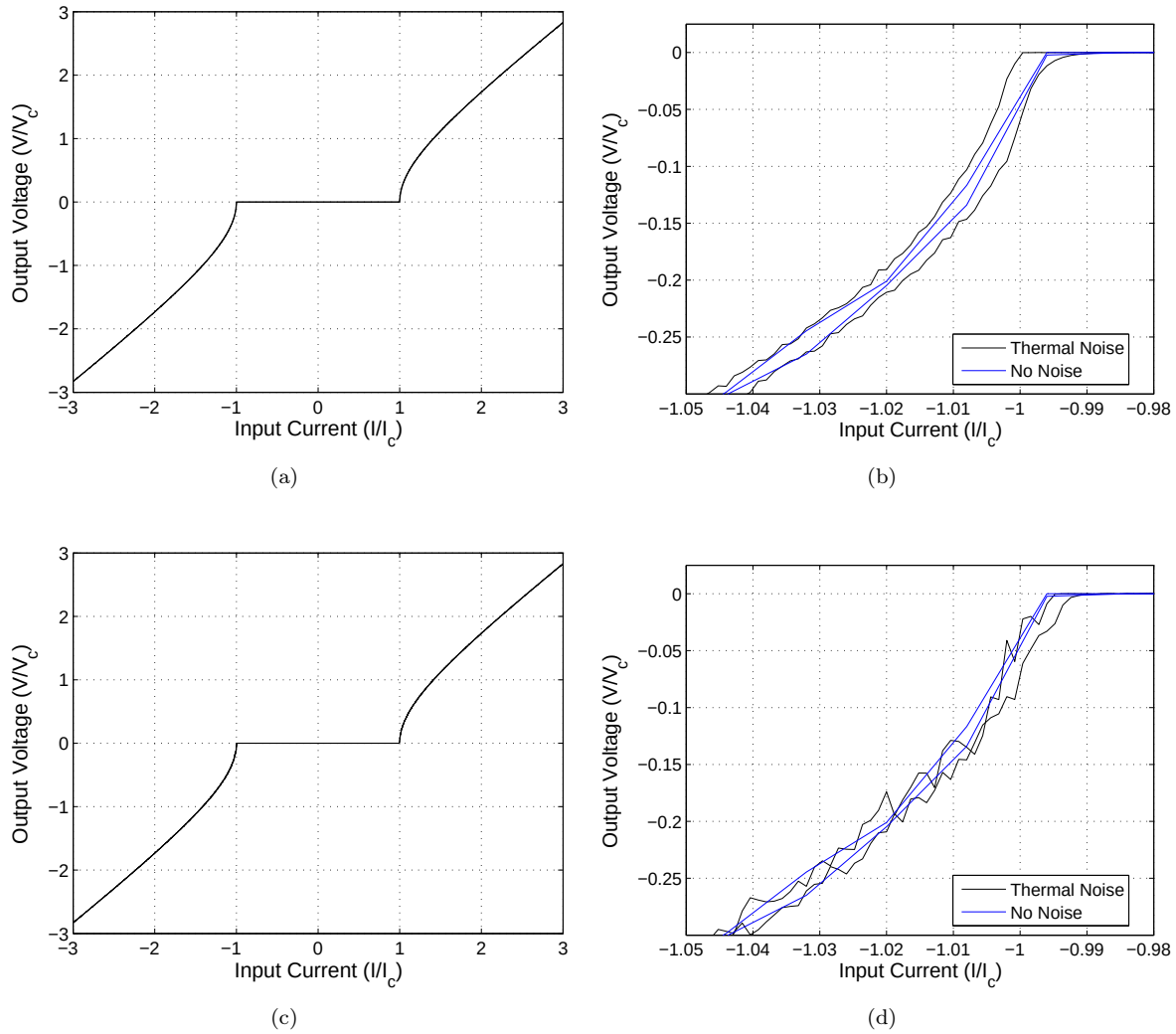

Figure 8.4: Simulated overdamped Josephson junctions with current noise using WRSpice: (a) The normalized voltage-current response for a junction with thermal noise for a 1 MHz bandwidth, and (b) the enlarged section displaying the effect of the noise. (c) The normalized voltage-current response for a junction with thermal noise for a 500 MHz bandwidth, and (d) the enlarged section displaying the effect of the noise. The current is swept from -3I/I_c to 3I/I_c and back to -3I/I_c.

with the normal resistance R_n. Noise will only become a problem if the input current signal is not larger than the noise current. It is important to ensure that the input current must always be large enough not to produce a output voltage swing near to or smaller than the voltage produced by the thermal noise, or the signal will be unrecoverable. For large input signals noise should not pose a problem. At low bias currents, near the transition point at I_c, the voltage-current response is rounded due to the thermal noise, as predicted in Section 5.5.2.

Figure 8.4(c) shows the effect of noise for a system with a 500 MHz bandwidth. The effect of noise is still too small to notice over the long current sweep, so in Figure 8.4(d) the section from $i = -1.05I_c$ to $i = -0.98I_c$ is again enlarged. A system with a large bandwidth will have significantly more noise than a system with a relatively small 1 MHz bandwidth. For a 500 MHz bandwidth the noise should be approximately 18.4444 μV_{peak}, or 184.444 m$V/V_{c,\text{peak}}$ normalized, which is 22.4 times higher than the noise of a 1 MHz system. In Figure 8.4(d) the effect of thermal noise is more substantial than in Figure 8.4(b), so minimum input current signal's amplitude must be much larger to produce a voltage output larger than the thermal noise. At low bias currents the voltage-current response is rounded due to the thermal noise.

β_L	β_c	L_{SQ} [pH]	L_i [pH]	k	M [Φ_0/A]	$1/M$ [μA/Φ_0]
1	0	103.4	80	1	43984	22.735
$2/\pi$	0	65.82	80	1	35092	28.497

Table 8.2: Simulation parameters for the dc SQUIDs.

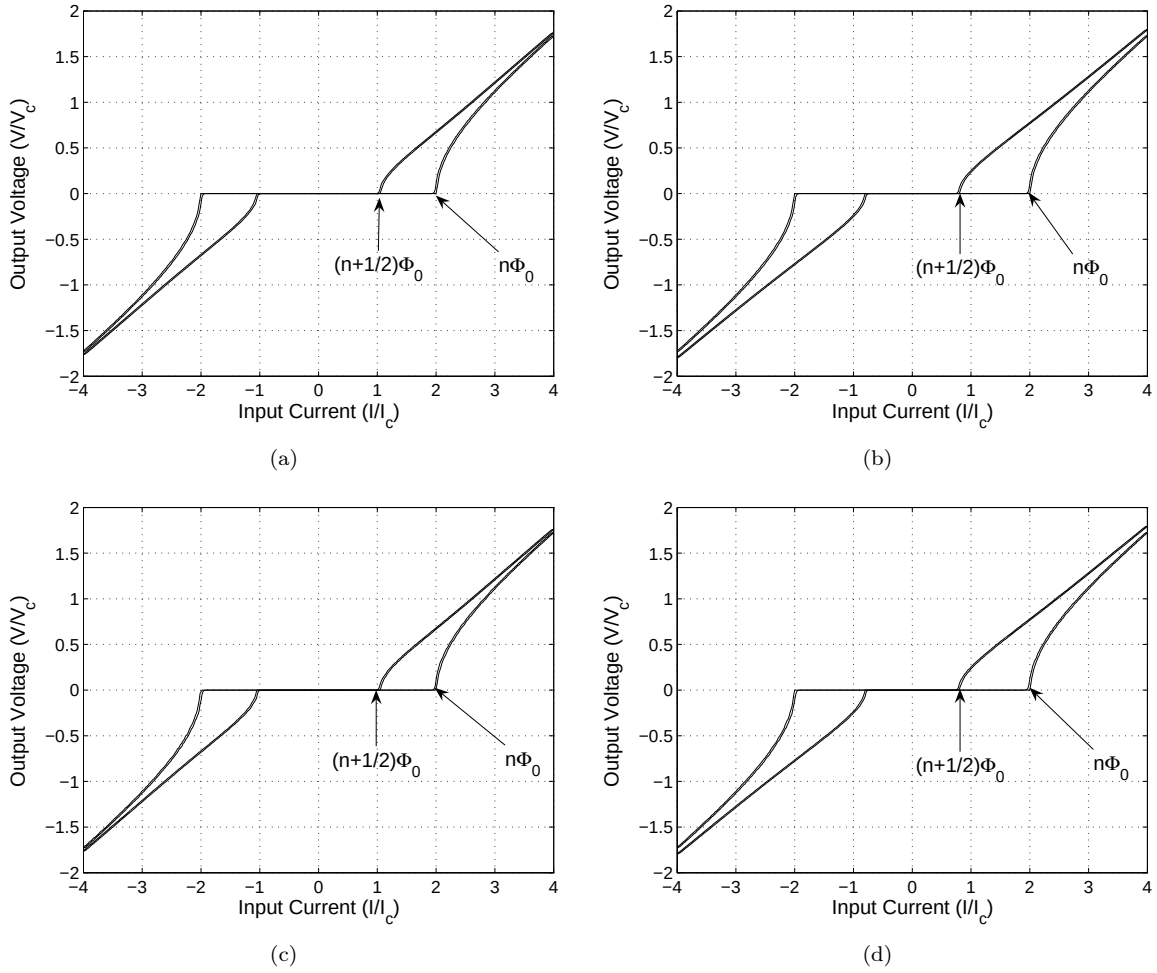

Figure 8.5: dc SQUID simulation using WRSpice: The voltage-current response for a basic dc SQUID with (a) $L_{SQ} = \Phi_0/2I_c$, and (b) $L_{SQ} = \Phi_0/\pi I_c$. The voltage-current response with thermal noise for a dc SQUID with (c) $L_{SQ} = \Phi_0/2I_c$, and (d) $L_{SQ} = \Phi_0/\pi I_c$.

8.2.5 DC SQUID Voltage-Current Response

There are two distinct types of dc SQUIDs that have been simulated. Appendix B.3 contains the relevant source code for the simulations. In Section 3.2.3 the hysteretic effect of the SQUID's loop inductance is discussed, and in Figure 3.4 the effect of a large inductance is shown. For the SQUID simulation the non-hysteretic SQUID has a loop inductance $L_{SQ} = \Phi_0/\pi I_c$ with the screening parameter $\beta_L = 2/\pi$, while the SQUID with slight hysteresis has a loop inductance $L_{SQ} = \Phi_0/2I_c$ for an optimal screening parameter $\beta_L = 1$. As in Section 8.2.2, the critical current for the RSJ junction is $I_c = 10$ μA, the shunt resistance is $R_n = 10$ Ω, and the operating temperature is at $T = 77$ K.

A SQUID with $\beta_L = 1$ has a loop inductance $L_{SQ} = \Phi_0/2I_c = 103.4$ pH, split into two separate inductors $L_2 = L_3 = 51.7$ pH. The external flux source is generated by two inductors, $L_2 = L_3 = 40$ pH for a total input inductance $L_i = 80$ pH, each coupled to one of the SQUID's separated loop inductors. Using (7.2.18) with a unity coupling factor $k = 1$, the mutual inductance between the SQUID and the flux source is $M = k\sqrt{L_{SQ}L_i} = 90.951\text{x}10^{-12}$ A^{-1}, which normalizes into $M = 43984$ Φ_0/A and

$1/M = 22.735\ \mu\text{A}/\Phi_0$. For each 22.736 μA flowing through the 80 pH input inductance one fluxon is applied through the SQUID's pickup loop.

A SQUID with $\beta_L = 2/\pi$ has a loop inductance $L_{SQ} = \Phi_0/2I_c = 65.82$ pH, split into two separate inductors $L_2 = L_3 = 32.91$ pH. The external flux source is generated by two inductors, $L_2 = L_3 = 40$ pH for a total input inductance $L_i = 80$ pH, each coupled to one of the SQUID's separated loop inductors. With a unity coupling factor of $k = 1$ the mutual inductance between the SQUID and the flux source is $M = 72.565\text{x}10^{-12}\ \text{A}^{-1}$, which normalizes into $M = 35092\ \Phi_0/\text{A}$ and $1/M = 28.497\ \mu\text{A}/\Phi_0$. For each 28.497 μA flowing through the 80 pH input inductance one fluxon is applied through the SQUID's pickup loop.

The simulation parameters are summed up in Table 8.2. The simulated voltage-current response for a noiseless dc SQUID with $\beta_L = 1$ is shown normalized in Figure 8.5(a). The flux applied to the SQUID is $n\Phi_0$ for the outer line and $(n + 1/2)\Phi_0$ for the inner line. The simulated response is identical to the theoretical response in Figure 3.5, with the maximum critical biasing current at $(n + 1/2)\Phi_0$ half the critical biasing current at $n\Phi_0$. The same simulation with added noise for a system with 500 MHz bandwidth is shown in Figure 8.5(c). Noise is imperceptible for a large current sweep, but will become more obvious with the analysis of a small input signal.

The simulated voltage-current response for a noiseless dc SQUID with $\beta_L = 2/\pi$ is shown normalized in Figure 8.5(b). The main difference to the dc SQUID with $\beta_L = 1$ is that the maximum critical biasing current at $(n+1/2)\Phi_0$ less than half the critical biasing current at $n\Phi_0$. The SQUID is also less sensitive to external flux due to the smaller loop inductance L_{SQ}, requiring a 25.34% increase in current from the external flux source for each measured fluxon (Φ_0). The same simulation with added noise for a system with 500 MHz bandwidth is shown in Figure 8.5(c). Noise is also imperceptible for a large current sweep, but will become more obvious with the analysis of a small input signal.

Due to the lower maximum critical biasing current at $(n + 1/2)\Phi_0$ in Figure 8.5(b), the dc SQUID with $\beta_L = 2/\pi$ has a larger operating range at $3.4I_c$, resulting in a larger output signal.

8.2.6 DC SQUID Large Flux Response

The simulation parameters in Table 8.2 are used for the simulation of the large-flux dc SQUID response. Appendix B.3 contains the relevant source code for the simulations. The two dc SQUIDs with $\beta_L = 1$ and $\beta_L = 2/\pi$ are biased using a constant biasing current $I_b = 3.4I_c$ for the optimum working point W, as discussed in Section 3.2.6. The bias currents between $3.3 \leq I_b/I_c \leq 3.5$ were simulated as the best fit for the voltage sensitivity $V_\Phi \approx R_n/L_{SQ}$ in (3.2.44). In a practical SQUID system the optimal working point is usually determined by trial and error. The external flux is swept from $-3\Phi_0$ to $3\Phi_0$, and then the output is normalized.

Figure 8.6(a) shows the response of a noiseless dc SQUID with $\beta_L = 1$, while Figure 8.6(c) shows the response with added noise. Figure 8.6(b) shows the response of a noiseless dc SQUID with $\beta_L = 2/\pi$, while Figure 8.6(d) shows the response with added noise. Both SQUIDs have the expected periodic output, with each period corresponding to one applied fluxon. The slight shift of $0.05\Phi_0$ to the right is due to the 500 MHz low-pass filter shifting the signal.

For the noiseless simulation, the SQUID with $\beta_L = 1$ has a peak-to-peak voltage response of 60 mV_c (6 μV) and $V_\Phi = 200\ \text{m}V_c/\Phi_0$. The SQUID with $\beta_L = 2/\pi$ has a peak-to-peak voltage response of 103 mV_c (10.3 μV), which is almost twice as large, and $V_\Phi = 320\ \text{m}V_c/\Phi_0$. With thermal noise the SQUID with $\beta_L = 1$ has a peak-to-peak voltage response of 50 mV_c (5 μV), while the SQUID with $\beta_L = 2/\pi$ has a peak-to-peak voltage response of 85 mV_c (8.5 μV). Thermal noise has reduced the sensitivity of the SQUID, and in Figure 8.6(c) the output has been roughened when compared to the

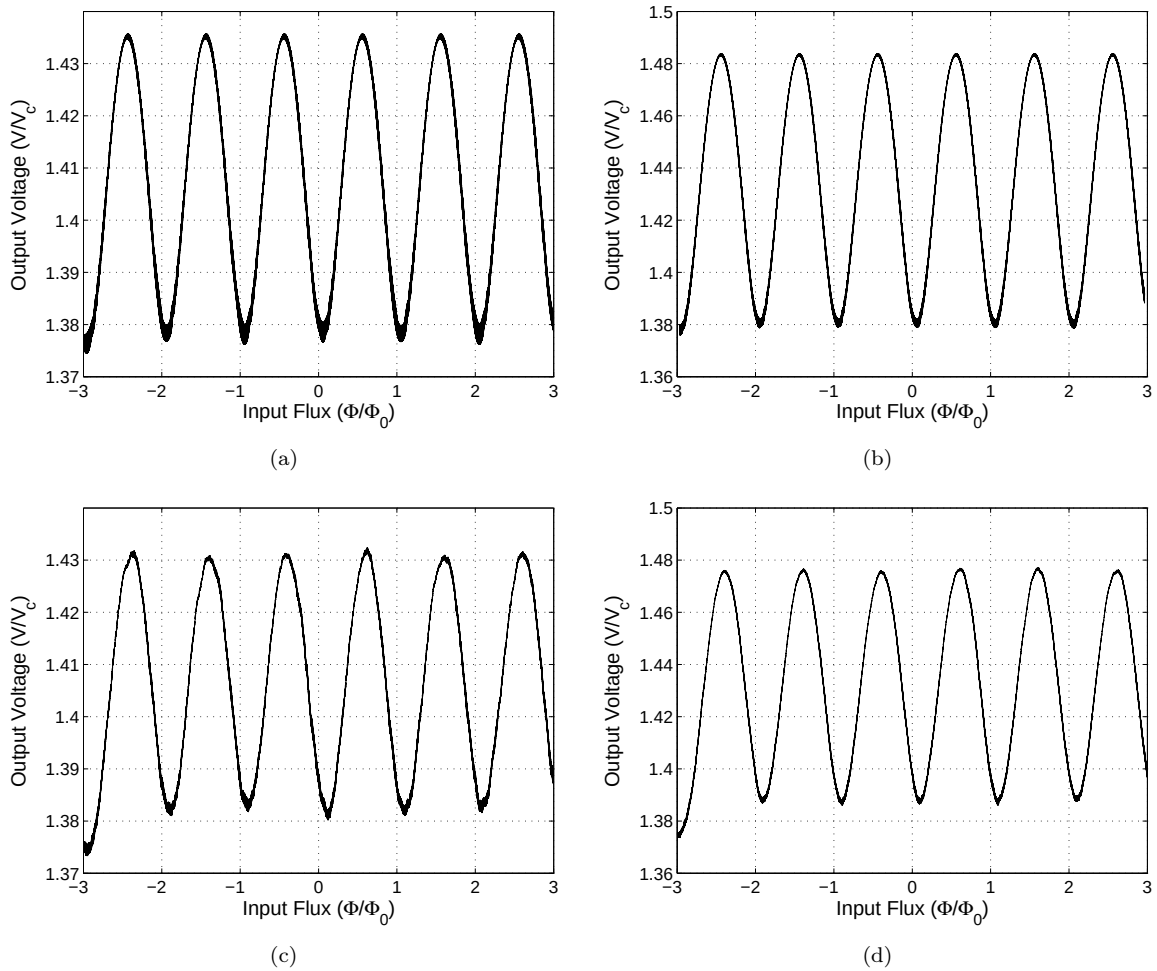

Figure 8.6: dc SQUID simulation using WRSpice: The voltage-flux response for a basic dc SQUID with (a) $L_{SQ} = \Phi_0/2I_c$, and (b) $L_{SQ} = \Phi_0/\pi I_c$. The voltage-flux response with thermal noise for a dc SQUID with (c) $L_{SQ} = \Phi_0/2I_c$, and (d) $L_{SQ} = \Phi_0/\pi I_c$.

β_L	BW [MHz]	I_c [μA]	R_n [Ω]	I_b [μA]	f_{signal} [MHz]	T [K]
1	500	10	10	34	40	77
$2/pi$	500	10	10	34	40	77
β_c	$I_{\text{noise,peak}}$ [μA]	L_{SQ} [pH]	L_i [pH]	k	$1/M$ [μA/Φ_0]	$\Phi_{\text{app,peak}}$
0	1.84444	103.4	80	1	22.735	$\Phi_0/4\pi$
0	1.84444	65.82	80	1	28.497	$\Phi_0/4\pi$

Table 8.3: Simulation parameters used for the dc SQUID small signal response.

smoother noiseless output in Figure 8.6(a). To best observe the effect of noise, simply look at the peaks of the sinusoidal output for deflections in the output.

8.2.7 DC SQUID Small Signal Response

The simulation parameters in Table 8.3 are used for the small signal response of dc SQUID. Appendix B.3 contains the relevant source code for the simulations. The 40 MHz sinusoidal input signal has a maximum amplitude of $\Phi_{\text{app,peak}} = \Phi_0/4\pi$ for the small signal response, described in Section 7.2.1 and shown in Figure 7.1 on p. 73. This sweeps the entire range for the minimized non-linear error in (7.2.4), which results in a very linear voltage-flux response and minimizes the production of harmonic frequencies. By using a constant biasing current $I_b = 3.4I_c$ and a biasing flux $\Phi_b = \Phi_0/4$, as shown in Section 3.2.6,

the dc SQUIDs with $\beta_L = 1$ and $\beta_L = 2/\pi$ are biased at the optimum working point W.

Figure 8.7(a) shows the output of a dc SQUID with $\beta_L = 1$ operating in the linear region at the working point W. For a 40 MHz input signal a 40 MHz output signal is expected with the possibility of a slight phase shift. The flux-to-voltage transfer is $V_\Phi = V_{\text{out}}/\Phi_{\text{in}} = 172.788$ mV_c/Φ_0. This is about 9% of the theoretical maximum value $V_\Phi = 2V_c/\Phi_0$ in (3.2.43). The effect of the slight hysteresis due to the loop inductance is noticeable at the peaks as a thickening of the line. The output has a voltage offset of 1.41 V_c, and without thermal noise the output has a smooth sinusoidal shape. There is also a slight phase shift due to the 500 MHz low-pass filter, but no harmonics due to non-linearity are evident.

In Figure 8.7(c) the small signal response of a dc SQUID with $\beta_L = 1$ with added thermal noise is shown. The effect of noise is clearly visible as the line is not as smooth as it is in Figure 8.7(a). Noise adds measurement uncertainty and limits the minimum resolution for small input signals. To simulate the effect of additional noise, the output of a dc SQUID with $S_I^* = 4S_I$ is shown in Figure 8.7(e), which simply translates into twice the noise of the previous example. The effect of noise becomes even more visible, with a coarser output due to large noise peaks. As the noise floor rises the sinusoidal output signal will to deteriorate until it will become hidden. The additional noise creates a larger measurement uncertainty and further limits the minimum resolution for small input signals.

For the SQUID with $\beta_L = 2/\pi$ Figure 8.7(b) shows the sinusoidal output for a sinusoidal input, operating in the linear region at the working point W. For a 40 MHz input signal a 40 MHz output signal is expected with the possibility of a slight phase shift. The flux-to-voltage transfer is $V_\Phi = V_{\text{out}}/\Phi_{\text{in}} = 295.310$ mV_c/Φ_0. This s about 15% of the theoretical maximum value $V_\Phi = 2V_c/\Phi_0$ in (3.2.43). Hysteresis due to the loop inductance does not occur in this example. The output has a voltage offset of about 1.438 V_c, and without thermal noise the output also has a smooth sinusoidal shape. There is a slight phase shift due to the 500 MHz low-pass filter, but no harmonics due to non-linearity are evident.

In Figure 8.7(d) the small signal response of a dc SQUID with $\beta_L = 2/\pi$ with added thermal noise is shown. The effect of noise is clearly visible as the line is not as smooth as it is in Figure 8.7(b). Noise adds measurement uncertainty and limits the minimum resolution for small input signals, but for an equal amount of applied flux this type of SQUID has a lower noise floor. To simulate the effect of additional noise, the output of a dc SQUID with $S_I^* = 4S_I$ is shown in Figure 8.7(f), which simply translates into twice the noise of the previous example. The effect of noise becomes even more visible, with a coarser output due to large noise peaks. As the noise floor rises the sinusoidal output signal will to deteriorate until it will become hidden. The additional noise creates a larger measurement uncertainty and further limits the minimum resolution for small input signals.

In both types of SQUIDs the small signal response has a very linear voltage-flux conversion. This supports the theory in Section 7.2.1 For the flux-locked loop (FLL) to have a linear behaviour, the error flux $\delta\Phi$ must stay within $\Phi_0/4\pi$ of the working point.

8.2.8 Additional Positive Feedback

The parameters for the dc SQUID with $\beta_L = 1$ in Table 8.3 are used for the APF simulations, with the schematic for the APF circuit shown in Figure 7.10. Appendices B.3 and B.4 contain the relevant source code for the simulations. The gain of the APF is chosen as $G_{\text{APF}} = 10$, so by using (7.5.5) we have $\beta_{\text{APF}} = 0.9$. A feedback resistance $R_{\text{APF}} = 1000\ \Omega$ is chosen to ensure $R_{\text{APF}} >> R_n$ to reduce the effect of R_{APF} on the voltage sensitivity. From (7.5.6) the mutual inductance of the SQUID and the APF coil is $M_{\text{APF}} = (\beta_{\text{APF}} \times L_{SQ} \times R_{\text{APF}})/R_n + 2L_{SQ}$, resulting in a mutual inductance $M_{\text{APF}} = 9.5128\text{x}10^{-9}$ A^{-1}. From (7.2.18) the inductance for the APF coil is $L_{\text{APF}} = (M_{\text{APF}}/k)^2/L_{SQ} = 871.792$ nH. L_{APF} is split into two separate inductors, $L_6 = L_7 = 435.896$ nH, and each is coupled to one of the sep-

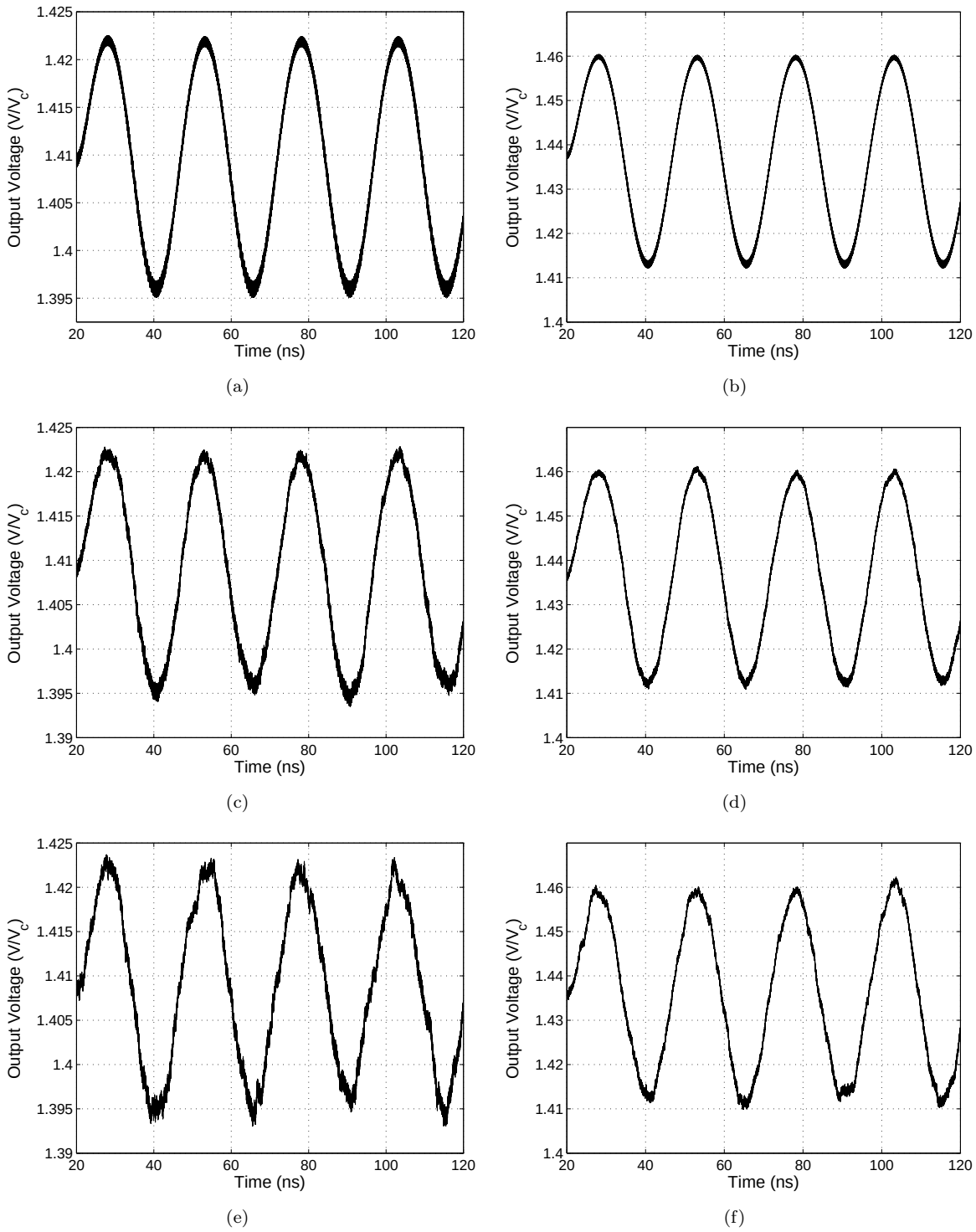

Figure 8.7: dc SQUID simulation using WRSpice: The small signal flux response for a basic dc SQUID with (a) $L_{SQ} = \Phi_0/2I_c$, and (b) $L_{SQ} = \Phi_0/\pi I_c$. The small signal flux response with thermal noise for a dc SQUID with (c) $L_{SQ} = \Phi_0/2I_c$, and (d) $L_{SQ} = \Phi_0/\pi I_c$. The small signal flux response with excessive thermal noise for a dc SQUID with (e) $L_{SQ} = \Phi_0/2I_c$, and (f) $L_{SQ} = \Phi_0/\pi I_c$.

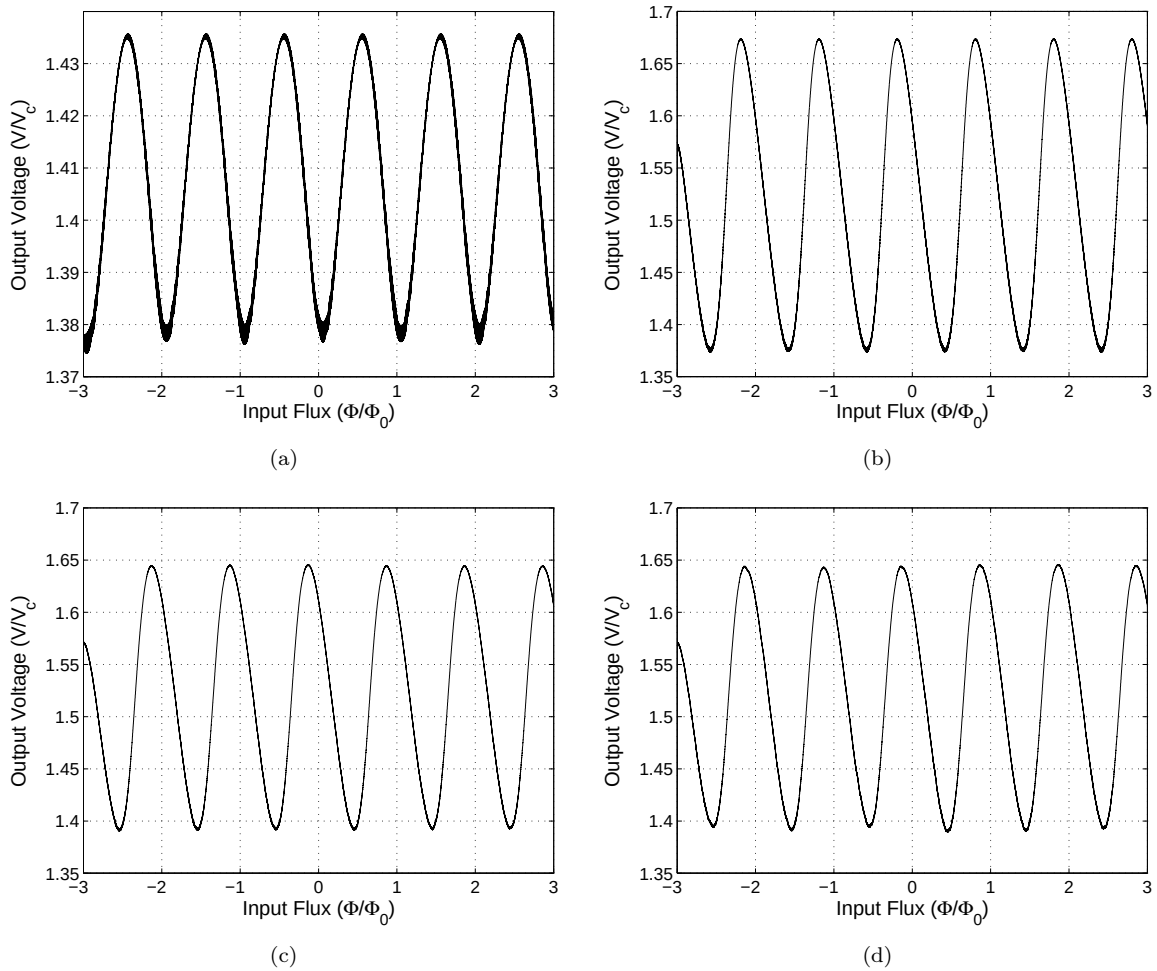

Figure 8.8: dc SQUID simulation for $L_{SQ} = \Phi_0/2I_c$ with APF using WRSpice: The noiseless voltage-flux response (a) without APF, and (b) with APF. The voltage-flux response for the APF (c) with thermal noise, and (d) with excessive thermal noise.

arated SQUID loop inductances with a unity coupling factor $k = 1$.

The APF has a corner frequency $f_{\rm APF} = R_{\rm APF}/(2\pi L_{\rm APF}) = 182.56$ MHz, but the bandwidth of the APF system in (7.5.9) is reduced to $BW_{\rm APF} = 18.256$ MHz for large signals. For a 500MHz bandwidth system without FLL the bandwidth of the APF needs to be increased, but the mutual inductance and the feedback resistance $R_{\rm APF} >> R_n$ severely limit the possible bandwidth for high gains. For low-frequency small input signals with the effect of $BW_{\rm APF}$ is small. For an increase of $V_\Phi^* = 10V_\Phi$ the usable voltage swing is diminished by about 20% due to the APF resistance $R_{\rm APF}$ [20].

Figure 8.8(a) shows the response of the normal, noiseless SQUID without APF, which is compared to the same SQUID with APF in Figure 8.8(b). The input flux swept from $-3\Phi_0$ to $3\Phi_0$. The addition of APF causes the rising slope of the SQUID to become steeper, as predicted in Section 7.5.2. The theoretical rise in the voltage sensitivity is $V_\Phi^* = 10V_\Phi$ using (7.5.7), so the slope at the working point should be 10 times steeper,. The APF only increasing output swing by a factor of about five, from $60{\rm m}V_{c,\rm pp}$ to $300V_{c,\rm pp}$. With added thermal noise in Figure 8.8(c) and excessive thermal noise in Figure 8.8(d), the SQUID with APF reduces the effect of the noise. The only apparent effect is that thermal noise reduces the output swing to $270V_{c,\rm pp}$ in Figure 8.8(c), and to $270V_{c,\rm pp}$ with twice the noise in Figure 8.8(d). At the steepest section around the working point W in Figure 8.8(b), the slope is increased by an APF gain of $G_{\rm APF} = 6.65$ to $V_\Phi^* = 1.333V_c/\Phi_0$.

By using a constant biasing current $I_b = 3.4I_c$ and a biasing flux $\Phi_b = \Phi_0/4$, as shown in Section

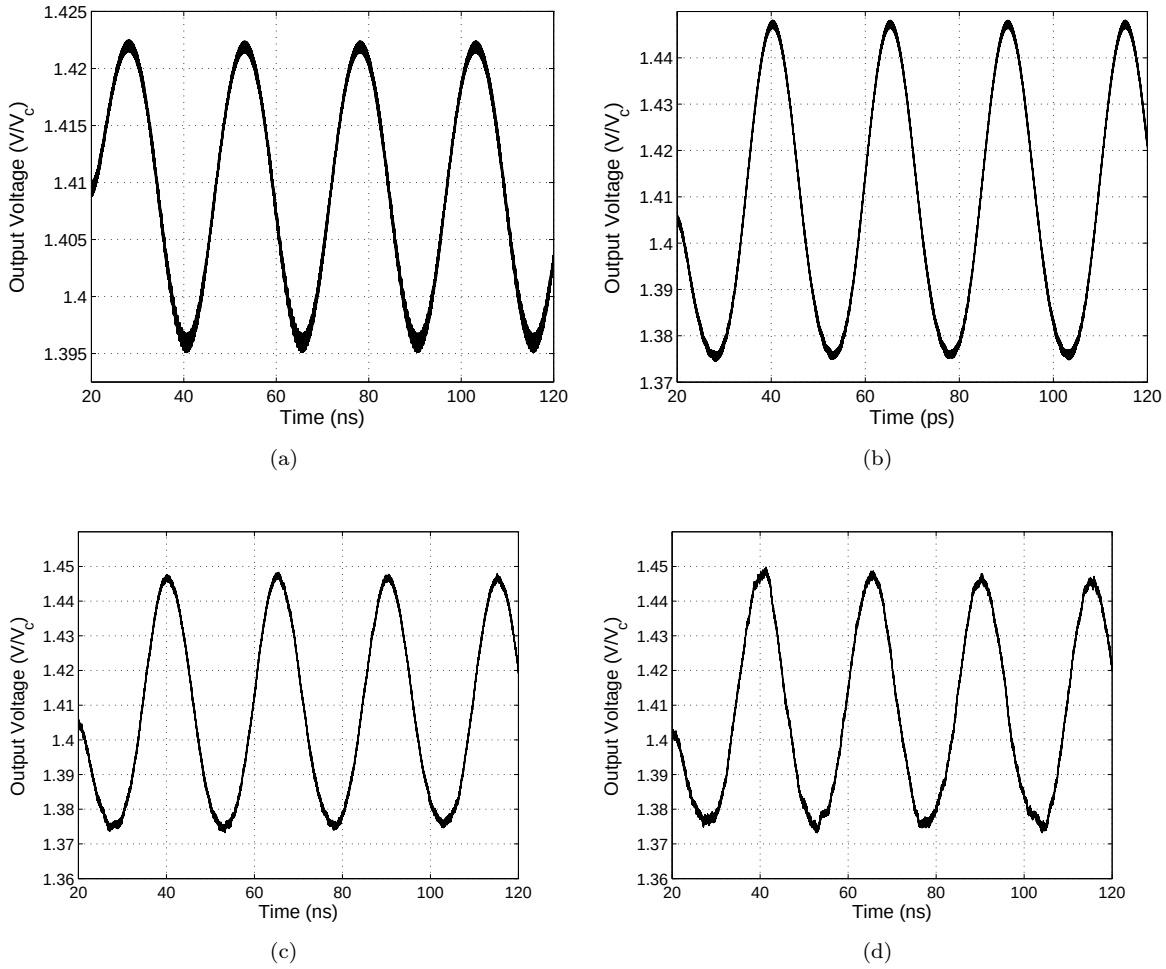

Figure 8.9: dc SQUID simulation for $L_{SQ} = \Phi_0/2I_c$ with APF using WRSpice: The noiseless small-signal flux response (a) without APF with $2\Phi_m athrmapp$, and (b) with APF. The small-signal flux response for the APF (c) with thermal noise, and (d) with excessive thermal noise.

3.2.6, the dc SQUID is biased at the optimum working point W. The 40 MHz sinusoidal input signal has a maximum amplitude of $\Phi_{\text{app,peak}} = \Phi_0/4\pi$ for the small signal response, described in Section 7.2.1 and shown in Figure 7.1 on p. 73. Since the SQUID is biased in the linear region around the working point W, the dc SQUID with APF will have linear response to the small signals with a maximum amplitude of $\Phi_{\text{app,peak}} = \Phi_0/8\pi$, which is half the maximum linear of the normal. If the input flux signal with $\Phi_{\text{app,peak}} = \Phi_0/4\pi$ is used then the output will cause the signal to operate in the non-linear region.

Figure 8.9(a) shows the small signal output of the noiseless SQUID without APF, which is compared to the same SQUID with APF in Figure 8.9(b). The flux-to-voltage transfer with APF is $V_\Phi = 942.47\ \mu V_c/\Phi_0$. This translates into a realistic APF linear gain of $V_\Phi^* = 5.46 V\Phi$. The APF gain is reduced due to $BW_{\text{APF}} = 18.256$ MHz filtering the 40 MHz signal.

8.2.9 Flux-locked Loop

The simulated flux-locked loop (FLL) uses the direct-readout (DRO) method without line (time) delay, as shown in Figure 7.3. The effect of line delay will be discussed in Section 8.3. Parameters for the dc SQUID with $\beta_L = 1$ used for the FLL simulations are presented in Table 8.3. Appendices B.3 and B.5 contain the relevant source code for the simulations.

Please refer to Section 7.2.3 for the design theory of the FLL used in this section. By using a constant biasing current $I_b = 3.4I_c$ and a biasing flux $\Phi_b = \Phi_0/4$, as shown in Section 3.2.6, the dc SQUIDs is

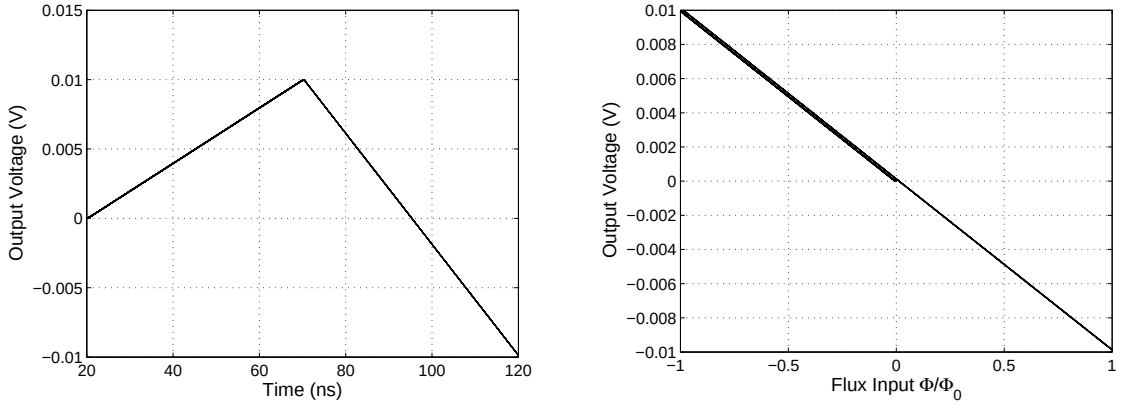

(a) (b)

Figure 8.10: FLL simulation using WRSpice: (a) The output voltage of the FLL for an input flux decreasing from $0\Phi_0$ to $-\Phi_0$ and then increasing to Φ_0. (b) The linear FLL voltage-flux response.

biased at the optimum working point W. Biasing the SQUID causes it to operate at an offset voltage of $V_{\text{off}} = 154.15$ V, which must be removed by the biasing voltage source V_b for the integrator to operate properly. If there is a large enough offset voltage present, then the integrator will increase its output to add flux to the SQUID in an effort to return the integrator's input to zero, causing it to run away and preventing the FLL from locking. If there is a small offset voltage present, then the integrator will create an additional bias flux to return its input to zero, thereby changing the working point and possibly causing the SQUID to operate in a non-linear region.

The FLL is designed for an input range of $\Phi = 1000\Phi_0$, which translates into a dynamic flux range of $\Phi_{\text{dyn}} = \pm 500\Phi_0$, for an integrator with a maximum output voltage $V_{\text{Int,max}} = \pm 5$ V. From (7.2.17) the gain of the feedback circuitry, the feedback coil and resistor, is $M_f/R_f = \Phi_{\text{dyn}}/V_{\text{Int,max}} = 100\Phi_0$.

The gain of the SQUID in (7.2.7) operating with the optimal voltage sensitivity $V_\Phi = 2V_c/\Phi_0$ in (3.2.44) results in a gain of $\text{G}_{SQ} = V_\Phi M_f/R_f = 200V_c = 20\text{x}10^{-3}$ V, so the preamplifier gain in (7.5.1) should be $A_{\text{Preamp}} = 1/\text{G}_{SQ} = 50$. In the simulated SQUID in Section 8.2.6 the slope at the working point W results in an actual voltage sensitivity $V_\Phi = 200$ mV_c/Φ_0, so the preamplifier gain is adjusted accordingly to $A_{\text{Preamp}} = 500$.

The integrator is designed for a unity gain at $f_1 = 1/2\pi R_{\text{int}} C_{\text{int}} = 80$ MHz, and has a unity gain-bandwidth (GBW) of $\text{GBW}_{\text{int}} = 80$ MHz. Choosing the integrator resistor as $R_{\text{int}} = 100\ \Omega$ will require the integrator capacitor to be $C_{\text{int}} = 20$ pF. The minimum slew-rate for a 80 MHz signal using the full 5V peak output in (7.4.3) is 2.5133 kV/μs.

The feedback inductance $L_f = 36\ \mu$H is taken from the M1000 HTS magnetometer in Table A.3, split into two distinct inductors $L_{f1} = L_{f2} = 18\ \mu$H, with a unity coupling factor $k = 1$. Using (7.2.18) the mutual inductance between the SQUID and the feedback coil is $M_f = 29.505\text{x}10^6\ \Phi_0$/A, which results in $1/M_f = 33.893$ nA/Φ_0. The feedback resistor is $R_f = 294.47$ kΩ.

To show the linearity of the FLL, the input flux is swept from 0 to $-1\Phi_0$ over 50 ns, and then to $1\Phi_0$ over the same time interval. The rising flux produces a linear output of $V_{\text{FLL}} = -0.01$ V/Φ_0 with a slew-rate of SR=200 mV/μs, and the falling flux also produces a linear output of $V_{\text{FLL}} = -0.01$ V/Φ_0 with a slew-rate of SR=400 mV/μs, as shown in Figure 8.10(a). This is the linear response predicted for the FLL in Section 7.2, with the integrator creating a negative feedback flux to cancel out the applied flux. The voltage sensitivity is at the designed $V_\Phi = -10$ mV/Φ_0 for the dynamic range $\Phi_{\text{dyn}} = \pm 500\Phi_0$. In Figure 8.10(b) the voltage response is plotted against the input flux, showing the linear slope of $V_\Phi = -10$ mV/Φ_0.

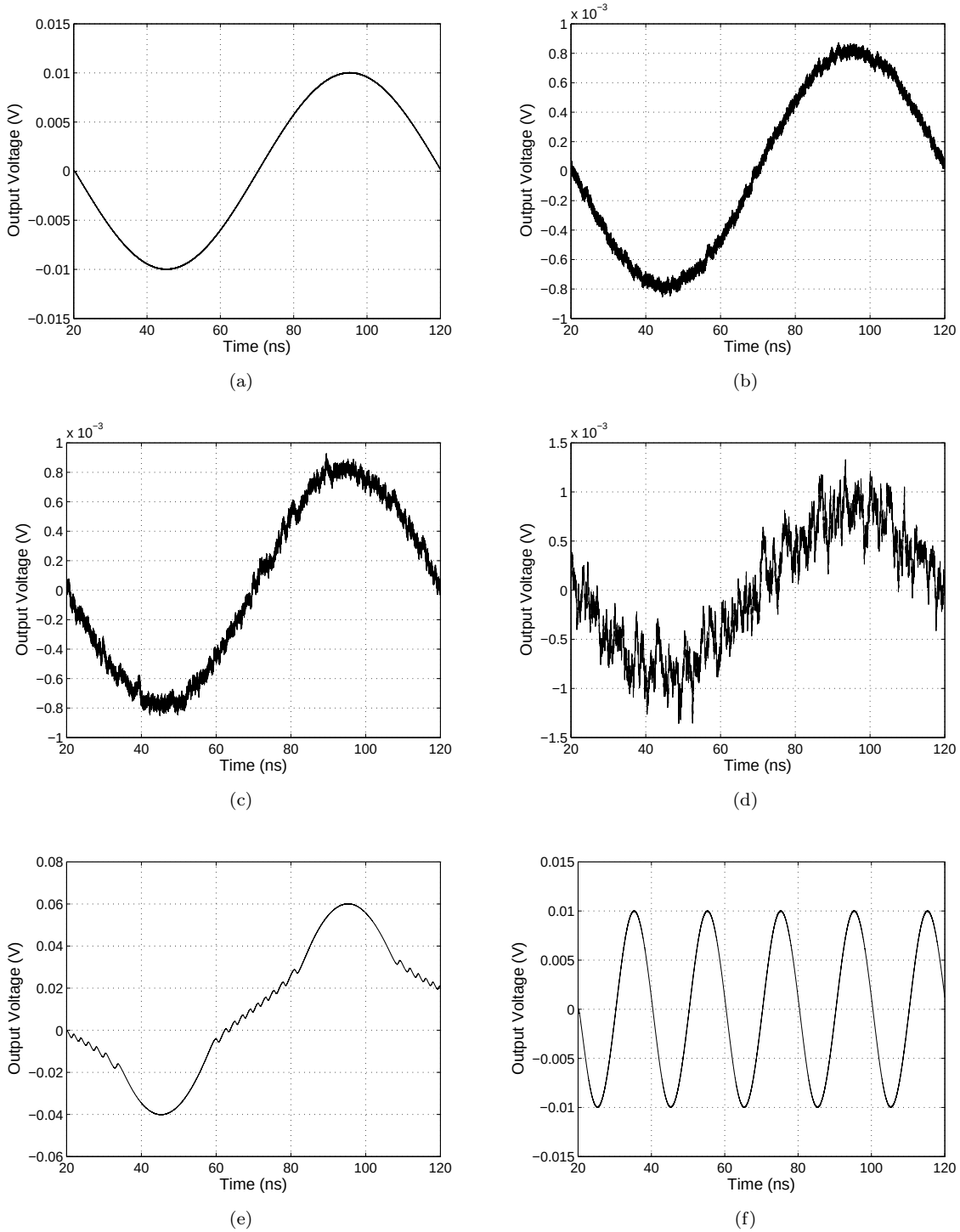

Figure 8.11: FLL simulation using WRSpice: The voltage output of a 10 MHz input signal with an amplitude of $1\Phi_0$ in (a) a noiseless FLL, (b) a FLL with thermal noise only from the SQUID, (c) with additional thermal noise, and (d) with excessive thermal noise. The voltage output of a 10 MHz input signal with (e) an amplitude of $10\Phi_0$ in a noiseless FLL. The voltage output of (f) a 50 MHz input signal with an amplitude of $1\Phi_0$ in a noiseless FLL.

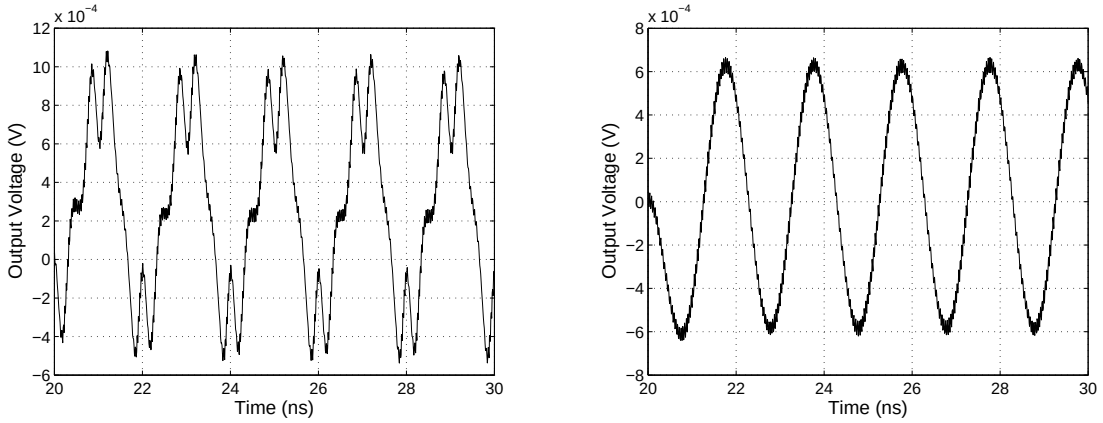

(a) (b)

Figure 8.12: FLL simulation using WRSpice: The voltage output of a 500 MHz input signal with (a) an amplitude of $1\Phi_0$, and (b) an amplitude of $\Phi_0/4\pi$ in a noiseless FLL.

A 10 MHz input signal with an amplitude of one fluxon ($\Phi_{\text{app,peak}} = 1\Phi_0$) is applied to the FLL, which is the input signal $\Phi_{\text{app}} = \Phi_0 \sin(2\pi 10^7 t)$. The output of the FLL without noise is shown in Figure 8.11(a). The output signal has a period of 100 ns (10 MHz), an amplitude of $V_{\text{out,max}}$, resulting in $V_{\text{out,max}} = 0.01 \sin(2\pi 10^7 t)$ V with no phase shift. The FLL acts as a linear flux-to-voltage converter, and does not exhibit the periodic output had it been applied to only the SQUID. By using a FLL, the flux applied to the SQUID is maintained at $\Phi_b = \Phi_0/4$ with only a small error $\delta\Phi_{\text{pp}} = \Phi_0/2\pi$ in (7.2.4). Thermal noise is added in Figure 8.11(c), indicating the minimum expected noise from the FLL. This is because only the SQUID current noise has been added and the rest of the components are considered noiseless. Figure 8.11(b) doubles the noise current, 2xi_{rms}, and Figure 8.11(d) increases the noise twelve fold, 12xi_{rms}. This gives a more accurate representation of the output one can expect from a FLL with noise generated by the SQUID, the amplifiers, and the various other constituents. The theoretical noise of the FLL is given by (7.2.25) and is highly dependent on the noise of the amplifier.

In Figure 8.11(e) the input signal's amplitude has been increased to $\Phi_{\text{app}} = 10\Phi_0 \sin(2\pi 10^7 t)$ for a noiseless FLL and SQUID. The slew-rate is so great that the integrator can not keep up with the actual change in flux, allowing some of the external flux to penetrate the SQUID and increase the error flux $\delta\Phi$. There is a small sinusoidal signal evident between 20 ns and 35 ns, between 60 ns and 80 ns, and between 85 ns and 120n s. This is because the flux penetrating the SQUID increases the offset from the working point faster than the integrator can recover, causing SQUID to diverge so far from the working point that it spills over onto the negative slope and breaks the lock. Rather than reduce the external flux, the integrator will then add to the applied flux in an attempt to find the next working point, causing the asymmetry visible in the small sinusoidal signal.

In Figure 8.11(f) the input signal's frequency has been increased to 50 MHz for the noiseless FLL. The FLL behaves similar to the FLL in Figure 8.11(e) with a period of 20 ns. A slight shift in phase can be observed, due to the integrator behaving as a one-pole integrator as predicted by (7.4.2).

A 500 MHz signal with an amplitude of one fluxon ($\Phi_{\text{app,peak}} = 1\Phi_0$) is applied to the noiseless FLL. The response of the FLL is shown in Figure 8.12(a), with the FLL unable to lock properly with the high-frequency signal. A high-frequency large signal has a high slew-rate, and the integrator is unable to counter the applied flux fast enough, causing it to either enter the non-linear region, or diverge far enough from the working point that it spills over onto the negative slope and breaks the lock. This will cause the severe distortions evident in the output. If the amplitude of the input signal is reduced to $\Phi_{\text{app,peak}} = \Phi_0/4\pi$, then the input can be tracked by the FLL. The small signal response is shown in

Figure 8.12(b), with an output of $V_{\text{out,500MHz}} = 7.5$ mV/Φ_0.

High-frequency signals can be measured with a FLL as long as their slew-rate is low enough and attenuation of the signal poses no problem. This is a boon for the unshielded SQUID, since the FLL will track most of the incoming signals from low to high frequencies and keep the SQUID locked at the working point, as long as the slew rate does not exceed the integrator's response. The output can then be filtered for the desired frequency range, either digitally or with analog circuitry.

8.3 Simulink Simulations

MATLAB's Simulink simulation software allows for faster simulation of the FLL's low-frequency response. Appendix C contains the relevant schematics for the simulations. Parameters for the dc SQUID with $\beta_L = 1$ used for the FLL simulations are presented in Table 8.3, and (3.2.37) is used for the transfer box y=fcn(u), with the output of y in [v] and the input u in [Φ_0]. By using a constant biasing current $I_b = 3.4I_c$ and a biasing flux $\Phi_b = \Phi_0/4$, as shown in Section 3.2.6, the dc SQUIDs with $\beta_L = 1$ and $\beta_L = 2/\pi$ are biased at the optimum working point W. The voltage offset generated by the SQUID with a static biased current $3.4I_b$ and only the biasing flux $\Phi_0/4$ is removed by the voltage offset compensation.

Since the ideal SQUID given by (3.2.37) is used for the simulations, the voltage sensitivity at the working point W is given by (3.2.44) as $V_\Phi \approx \frac{2V_c}{\Phi_0}$, resulting in a SQUID gain of $G_{SQ} = 20\text{x}10^{-3}$ V. The preamplifier is used to return the gain of the SQUID to unity in (7.2.11), so in (7.5.1) the gain of the preamplifier is $A_{\text{Preamp}} = 1/G_{SQ} = 50$.

A dynamic range of $\Phi_{\text{dyn}} = \pm 500\Phi_0$ for an integrator with a maximum output voltage $V_{\text{Int,max}} = \pm 5$ V is chosen. From (7.2.17) the gain of the feedback circuitry, the feedback coil and resistor, is $M_f/R_f = 100\Phi_0$ or simply a feedback gain of $G_f = 100$. The integrator is designed for a unity gain at $f_1 = 80$ MHz, and has a unity gain-bandwidth (GBW) of $\text{GBW}_{\text{int}} = 80$ MHz. At 1 Hz the theoretical open-loop gain of the integrator is $80\text{x}10^6$, but the closed loop will ensure that the integrator will not run away at low frequencies.

The time delay is set as needed, with $f_1 t_d = 0$ meaning that there is no time delay, $f_1 t_d = 0.08$ indicating the maximum allowed bandwidth without causing positive feedback, as described in Section 7.2.4.

The input to the system is either a linear source, a single sinusoidal source, or multiple sinusoidal sources with different frequencies. When multiple signals are applied to the SQUID, the low-pass and high-pass Butterworth filters are used to filter out the undesired frequencies from the desired 1 kHz input signal. As a comparison the output from the bare squid can also be shown.

The system is considered to be free from thermal noise.

8.3.1 Linear Input FLL Response

The schematic for the FLL with a linear input is shown in Appendix C.1, with no time delay included. The input flux is swept from $0\Phi_0$ to $10\Phi_0$, and the linear voltage-flux relation of the FLL is shown in Figure 8.13(a). As predicted the output has a linear gain of $V_\Phi = 0.01V/\Phi_0$

To clearly show the effect of the closed, locked flux-locked loop, in Figure 8.13(b) the output of a bare dc SQUID without the FLL or a biasing flux is shown. The signal shows the periodic signal predicted in Section 3.2.4, and it is impossible to estimate the input signal from the output of the SQUID.

8.3.2 FLL With Time Delay

The effect of time delay on the FLL system is discussed in Section 7.2.4. A perfect SQUID with an ideal set of electronics will have no noticeable line delay, and the response for such a system is shown in Figure

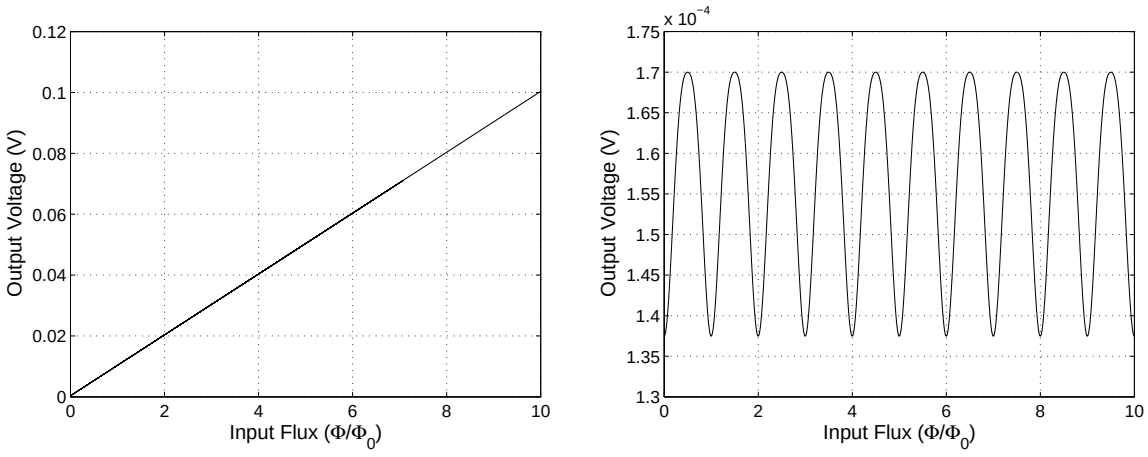

(a) (b)

Figure 8.13: FLL simulation using Simulink: (a) The output voltage of the FLL for an input flux increasing from $0\Phi_0$ to $10\Phi_0$, and (b) the output of the bare SQUID without the FLL showing its periodic voltage-flux relation for a biased SQUID.

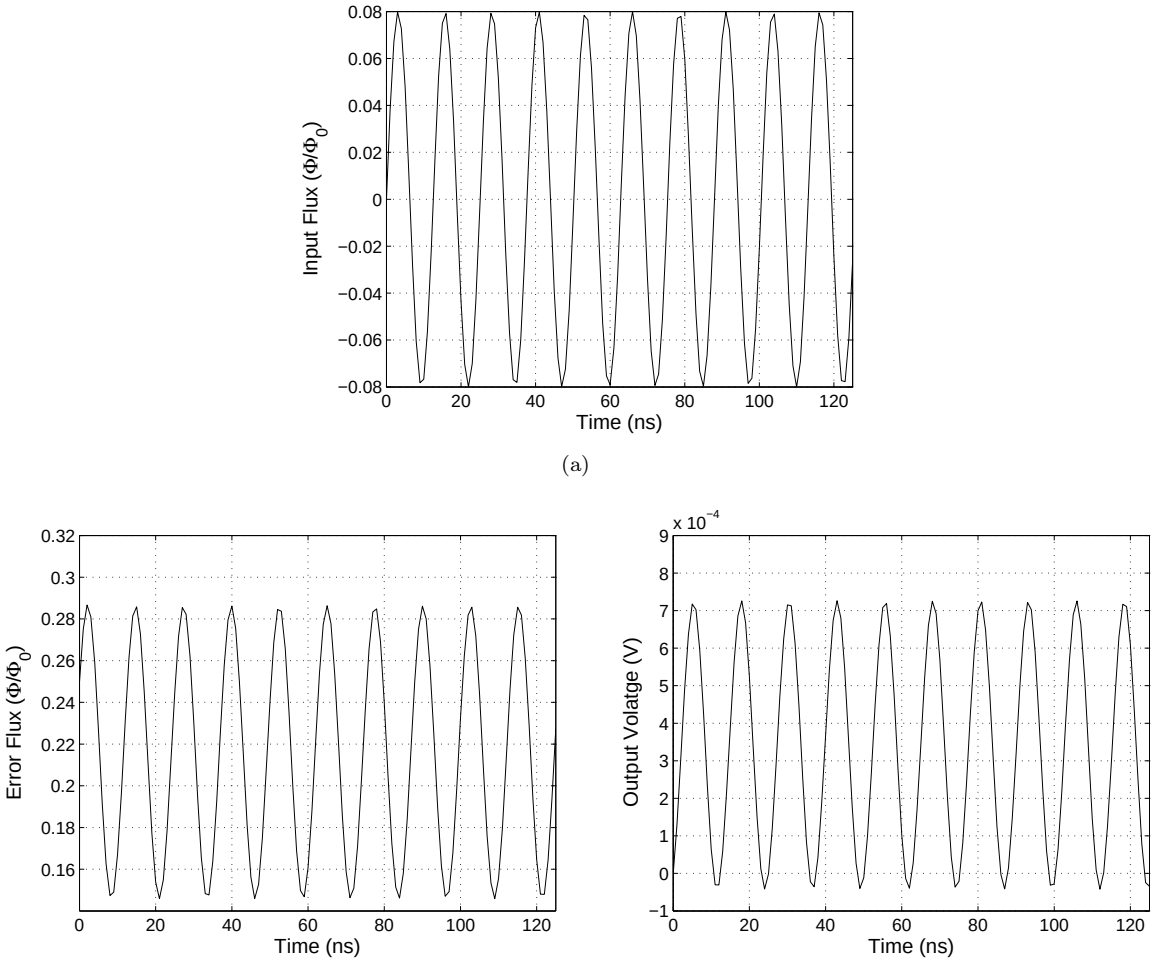

(a)

(b) (c)

Figure 8.14: FLL simulation with no time delay, $ft_d = 0$, using Simulink: (a) The small input flux signal at the integrator's characteristic 80 MHz, (b) the error flux applied to the SQUID with feedback, and (c) the output of the integrator.

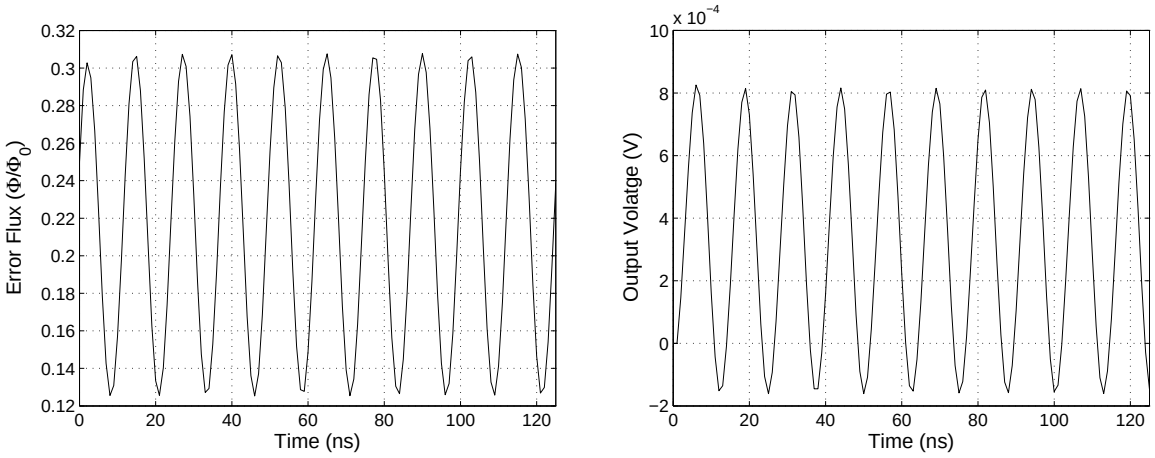

(a) (b)

Figure 8.15: FLL simulation with maximum time delay, $ft_d = 0.08$, using Simulink: (a) the error flux applied to the SQUID with feedback, and (b) the output of the integrator.

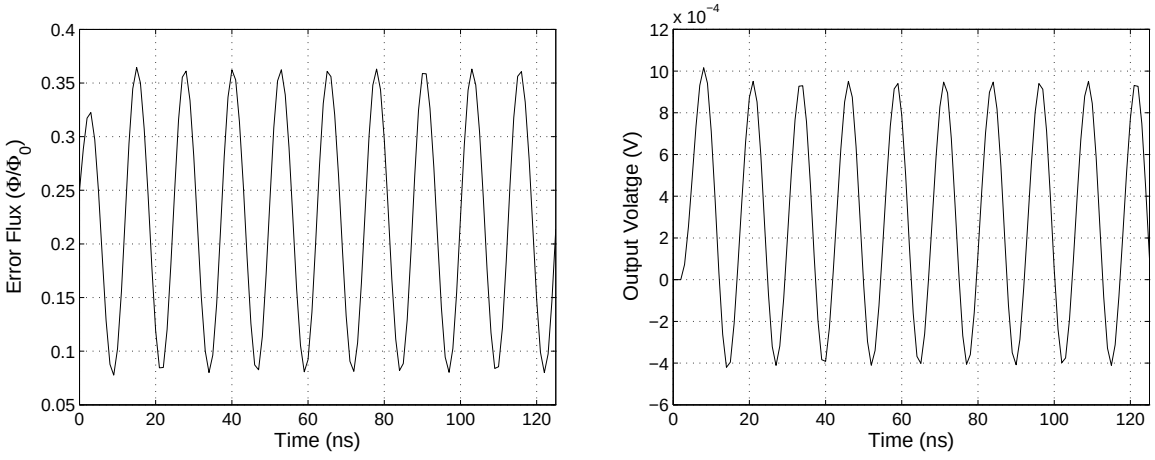

(a) (b)

Figure 8.16: FLL simulation with excessive time delay, $ft_d = 0.2$, using Simulink: (a) the error flux applied to the SQUID with feedback, and (b) the output of the integrator.

8.14 at the integrator's characteristic frequency. The input flux constrained to the linear region of the SQUID, $\Phi_{\text{app}} = \Phi_0/4\pi$, for a linear output, and is shown in Figure 8.14(a). If the amplitude of signal is increased above this value, the error flux will operate outside the linear range when $f_1 t_d = 0.08$.

The error flux for the system with no time delay is shown in Figure 8.14(b), with the error signal at the working point with an offset of about $0.25\Phi_0$. The amplitude of the error flux is $\Phi_{\text{error}} = 0.07\Phi_0$, which is within the linear range of the SQUID's working point, W. The integrator's output is shown in Figure 8.14(c), with a slight phase shift occurring due to the integrator, and an output amplitude of 0.375 mV. An attenuation of the output is expected, with the gain of the FLL in Figure 7.5 on p. 78 indicating that the output will decrease when $f_1 t_d < 0.08$. As the time delay increases, the amplitude at f_1 will also increase.

With the time delay increases to the maximum value of $f_1 t_d = 0.08$, the error flux in Figure 8.15(a) increases to $\Phi_{\text{error}} = 0.09\Phi_0$. This error flux is just outside the linear region described in Section 7.2.1, but will still result in a minimal error for the FLL. The output is increased to 0.5 mV in Figure 8.15(b)

With the time delay increases above the maximum value to $f_1 t_d = 0.2$, the error flux in Figure 8.16(a)

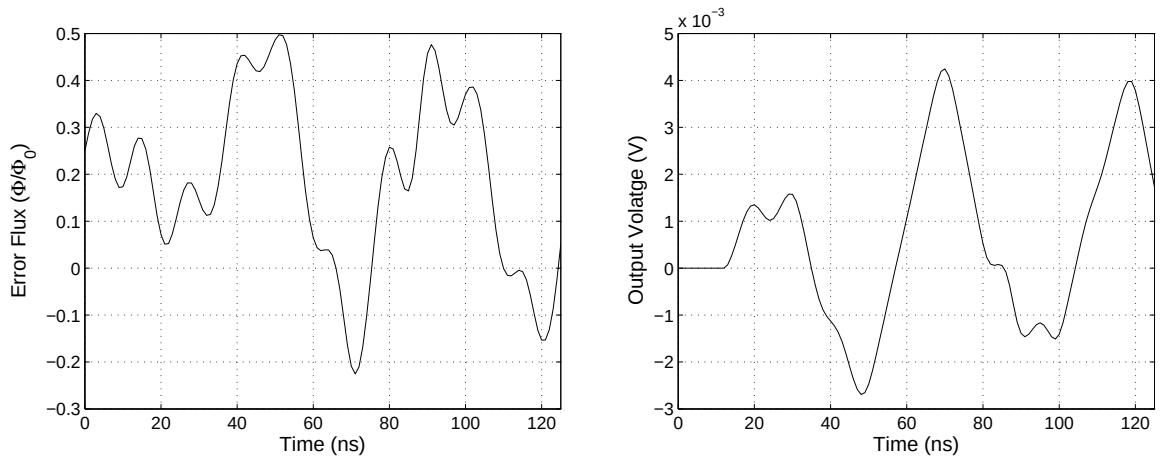

(a) (b)

Figure 8.17: FLL simulation with excessive time delay, $ft_d = 1$, using Simulink: (a) the error flux applied to the SQUID with feedback, and (b) the output of the integrator.

increases to $\Phi_{\text{error}} = 0.15\Phi_0$. This error flux is outside the linear region, resulting in a potential distortion of the signal and an additional output gain. The output is increased to 0.675 mV in Figure 8.16(b).

With the time delay increases even further to $f_1 t_d = 1$, the error flux in Figure 8.17(a) has become nonsensical. This error flux is outside the linear region, resulting in a FLL that will not lock onto the signal. The output in Figure 8.17(b) is also nonsensical, showing that the system has become unstable. As was indicated in Section 7.2.4, a system with a delay greater than $f_1 t_d > 5/2\pi$ is impossible to stabilize.

8.3.3 Mixed Input FLL Response

To get an idea of the measurement output to expect in a laboratory environment, the FLL is excited with a variety of frequencies. The 2.4 GHz signal represents a weak Wi-Fi signal, with an amplitude of $0.01\Phi_0$. The 1.8 GHz signal represents a cellular carrier signal, which is usually more prominent, with an amplitude of $0.03\Phi_0$. A more common and more powerful signal originates in switching power supplies and CRT monitors at 100 Hz, with an amplitude of $40\Phi_0$. By far the largest source of noise in any environment stems from the power grid at 60 Hz, with an amplitude of $100\Phi_0$. The signal to be measured is at 1 kHz with an amplitude of $2\Phi_0$.

Figure 8.18(a) shows the 1 kHz input signal, and Figure 8.18(b) shows the summation of all the input signals applied to the SQUID. To have an idea of what to expect on the output of the SQUID, the noisy signal is filtered and the output is shown in Figure 8.18(c). The 100 Hz signal has a settling time from 0 to 4ms, but after 5ms the 1 kHz input signal is visible.

The output from the FLL's integrator is shown in Figure 8.18(e). A large portion of the output signal are due the 100 Hz and 60 Hz signals applied. The FLL's output is filtered and shown in Figure 8.18(f). After the 100 Hz has had time to settle, the 1 kHz signal is clearly visible.

The error flux $\delta\Phi$, the external flux applied to the SQUID, is shown in Figure 8.18(d). The 2.4 GHz and 1.8 GHz signals are not blocked by the FLL, and are the cause for the widening of the error flux. Bias flux causes the offset on the error flux of $0.25\Phi_0$, indicating that the SQUID is operating at the correct bias point. As long as the error flux remains within $\Phi_0/2\pi$ the SQUID is operating inside the linear region.

In an effort to see what happens if the FLL is overpowered by the noise, the noise signals are increased and the input signal is decreased. The 2.4 GHz signal has an amplitude of $50\Phi_0$, the 1.8 GHz signal has an

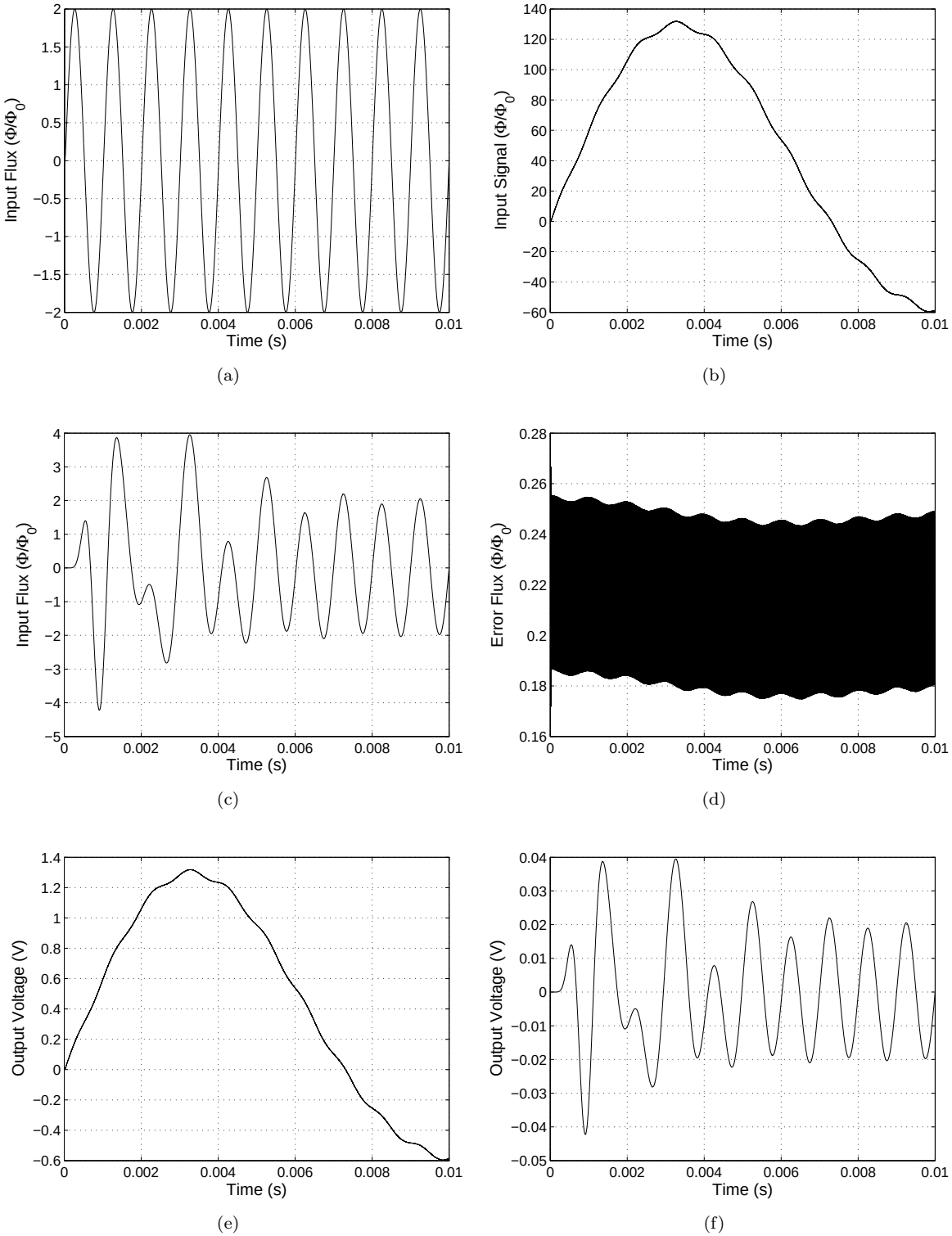

Figure 8.18: FLL simulation using Simulink: (a) The 1 kHz input signal, (b) the mixed input signals with added noise, (c) the filtered mixed input signal, (d) the error flux applied to the SQUID, (e) the output of the FLL, and (f) the filtered output of the FLL.

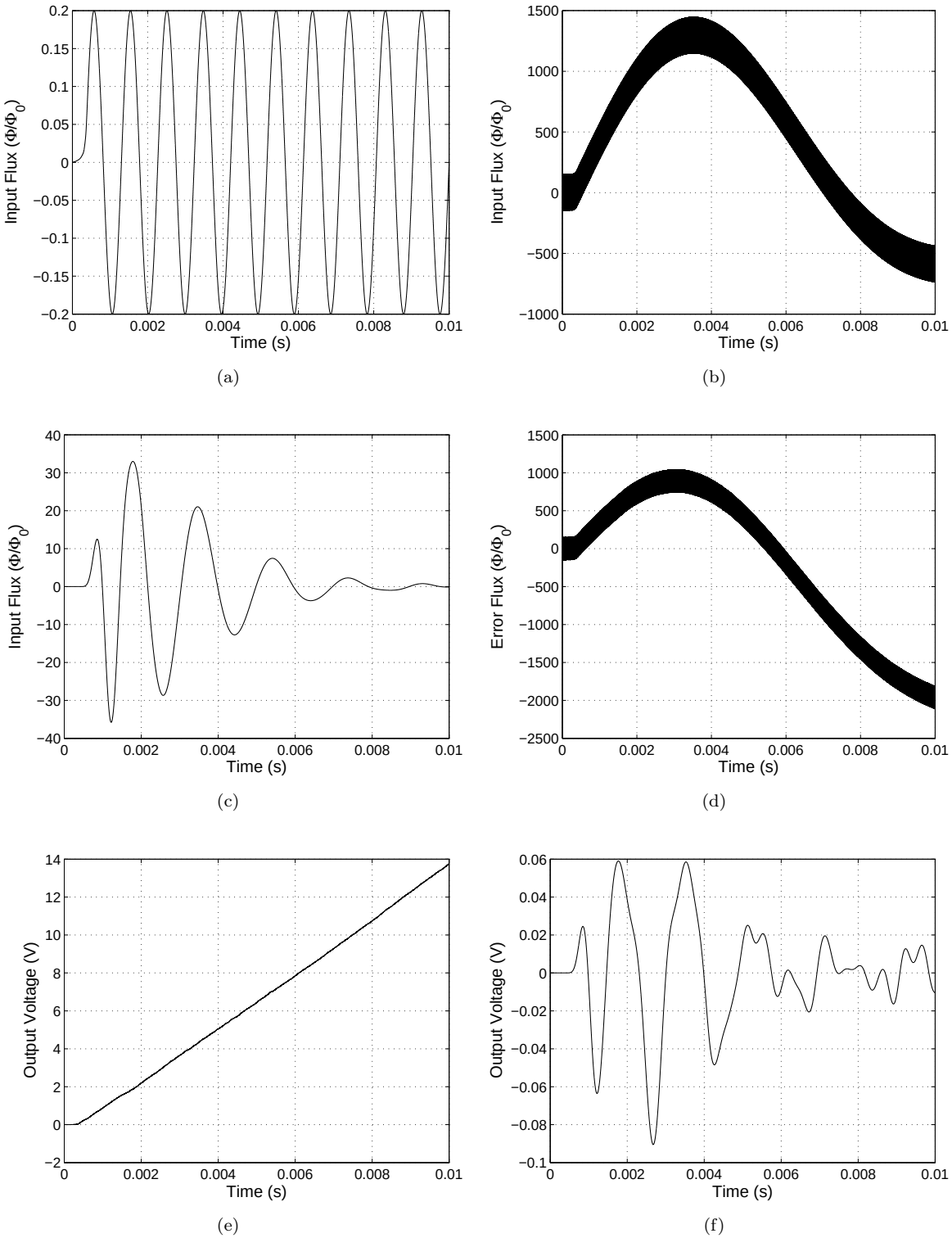

Figure 8.19: FLL simulation using Simulink: (a) The small 1 kHz input signal, (b) the mixed input signals with added noise, (c) the filtered mixed input signal, (d) the error flux applied to the SQUID, (e) the output of the FLL, and (f) the filtered output of the FLL.

amplitude of $100\Phi_0$, the 100 Hz signal has an amplitude of $400\Phi_0$, and the 60 Hz signal has an amplitude of $1000\Phi_0$. The 1 kHz input signal has also been reduced to $0.22\Phi_0$.

Figure 8.19(a) shows the 1 kHz input signal, and Figure 8.19(b) shows the summation of all the input signals applied to the SQUID. The noisy input is filtered and the output is shown in Figure 8.18(c).

The error flux $\delta\Phi$ is shown in Figure 8.19(d). The 2.4 GHz and 1.8 GHz signals are not blocked by the FLL, and are the cause for the widening of the error flux and cause the FLL to immediately operate outside the linear range $\Phi_0/2\pi$. The SQUID is unable to track all the sigals ant the lock is lost.

The output from the FLL's integrator is shown in Figure 8.19(e). Since the FLL is unable to maintain the lock, the integrator starts to run away and exceeds the maximum desired output voltage of $V_{\text{Int,max}} = 5$ V after 5 ms. The FLL's output is filtered and shown in Figure 8.18(f), and is of no real use since the FLL is unable to function properly.

Large high-frequency input signals and high slew-rates have the ability to cause the FLL to lose its lock, allowing flux to penetrate the SQUID. This causes an incorrect translation of the input signal, and could also cause the signal to be lost in the noise. Increasing the flux through the SQUID will also increase the $1/f$ noise described in Section 5.6.1, resulting in lower noise performance.

8.4 Conclusion

In this chapter the dc SQUID is simulated and compared the theoretical models. The simulations include the behaviour of a single Josephson junction all the way to the flux-locked loop.

The voltage-current response of all three types of Josephson junction are examined with and without thermal noise, agreeing with the theoretical response in Section 2.8. The SQUID is then simulated, first for the voltage-current response and then for the voltage-flux response. When the simulations are compared to theoretical models in Section 3.2, the voltage-flux response has a lower voltage sensitivity V_Φ at the working point W. The APF also produces a lower gain than the theory would indicate, which is due to the dynamic interaction between the SQUID and the APF. The relatively small bandwidth of the APF also poses a problem, causing it to only be effective when low-frequency signals are measured.

Finally the flux-locked loop (FLL) is implemented, linearizing the periodic output of the SQUID. The FLL only works as long as the SQUID is operated in the linear region. Large signals with high slew-rates and high-frequency signals can distort the output signal or cause the FLL to lose its lock. Small high-frequency signals do not pose this problem and can be tracked by the FLL.

Chapter 9

Measurements

9.1 Introduction

The electronics for the FLL in Section 7.2.3 are designed using the room-temperature direct-readout (DRO) scheme in Section 7.4 with the integrator in Section 7.5.2.

The DRO is relatively simple to manufacture and is a far more versatile design than the preamplifier with a step-up converter, especially if the device under test has unknown characteristics. It allows for the measurement of both a SQUID and a single Josephson junction, making it a more versatile tool for characterizing superconductors.

The integrator design uses the one-pole integrator described in Section 7.4. The output is then fed back to the SQUID using a feedback resistor and a feedback coil, locking the error flux at the working point W.

For this design the dc SQUID is biased using a current source. The simplest current source is created by simply applying a voltage to a series resistor, but for safety reasons a bipolar current source is created and used. A bipolar current source can generate a positive or negative constant biasing current, or can be excited by a signal generator to produce a sinusoidal or triangular current output of varying amplitudes.

After the SQUID or the Josephson junction is cooled using either the cryocooler or a cryostat, the device is attached to the electronics and characterized. IF the SQUID shows the characteristic voltage-flux response, then the FLL circuit can be closed and the output of the SQUID will be linearized.

9.2 Four-Point Measurement Setup

To measure the resistance of a device, a current is passed from a current source through the DUT by means of a single pair of wires. The current flowing through the device creating a potential across the device linear to the applied current, which can then be measured all the way back through the wires at

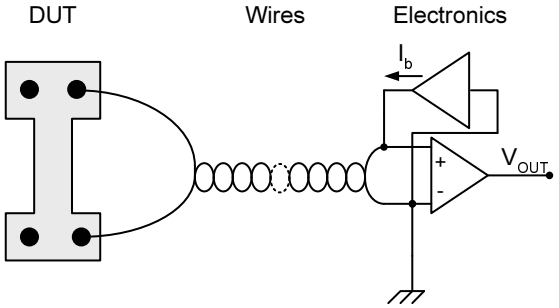

Figure 9.1: Schematic for the two-point measurement setup.

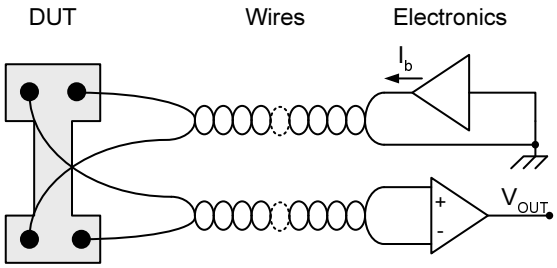

Figure 9.2: Schematic for the four-point measurement setup.

the output of the current source. This type of measurement is known as a two-point probe measurement, shown in Figure 9.1.

By using a single set of wires for the measurement, the current will be forced to pass through the same wires used for the voltage measurements. Since any wire not made out of superconducting material cooled to cryogenic temperatures will show a dc resistance, the potential is increased due to the finite resistance in the wires. For devices with large resistance this will not pose a problem, since the increase in the potential is only a small fraction of the total potential. A $R_{\mathrm{DUT}} = 1$ kΩ resistor measured through a $R_{\mathrm{wire}} = 0.1$ Ω wire using a $I_b = 100$ μA current source will develop a total measured potential of $V_{\mathrm{measured}} = 100.01$ mV. The resistor will develop a potential of $V_{\mathrm{measured}} = 100$ mV, while the wire will only develope a potential of $V_{\mathrm{measured}} = 10$ μV, giving the measurement an error of error=10^{-6}%.

When devices with smaller resistances are measured, then the impedance of the wires will have a far greater effect. A $R_{\mathrm{DUT}} = 1$ Ω resistor measured through a $R_{\mathrm{wire}} = 0.1$ Ω wire using a $I_b = 100$ μA current source will develop a total measured potential of $V_{\mathrm{measured}} = 110$ μV. The resistor will develop a potential of $V_{\mathrm{measured}} = 100$ μV, while the wire will develop a potential of $V_{\mathrm{measured}} = 10$ μV, giving the measurement an error of error=10%. If, on the other hand, the measured resistance is $R_{\mathrm{DUT}} = 0$ Ω for a junction in the superconductive region, the output will only show the $V_{\mathrm{measured}} = 10$ μV potential developing across the wire.

By using two separate sets of wires, one set for the current source and one set for the voltage measurement, the problem of the additional voltage generated by the wires will be minimized. It is important to have both the ground wires and the signal wires separated, and the voltage must be measured by a high-impedance instrumentation amplifier that will not cause a significant flow of current back through the wires used for the voltage measurement. This is known as a four-point probe measurement, shown in Figure 9.2.

When devices with small resistances are measured, then the impedance of the wires will have a very little effect. A $R_{\mathrm{DUT}} = 1$ Ω resistor measured through a $R_{\mathrm{wire}} = 0.1$ Ω wire will develop a potential of $V_{\mathrm{measured}} = 100$ μV across the DUT. The amplifier will cause a $I_{\mathrm{offset}} = 50$ pA current to flow through the measuring wires with a $R_{\mathrm{wire}} = 0.1$ Ω impedance, causing a voltage increase of $V_{\mathrm{offset}} = 50$ pV. This is an measurement an error of error=50x10^{-6}%, far smaller than with the use of only one set of wires. If the measured resistance is $R_{\mathrm{DUT}} = 0$ Ω for a junction in the superconductive region, the output will show only a $V_{\mathrm{measured}} = 50$ pV potential developing across the wire.

The effect of the four-point probe measurements is so significant, that when the junction or the SQUID is wire-bonded onto a single pad at each side of the superconducting film, using only a 5 mm length of gold wire, the output of the electronics will show that there is a small resistance present. The junction will appear to never reach 0 Ω.

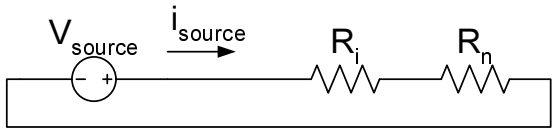

Figure 9.3: Schematic of the simple current source using a series resistor.

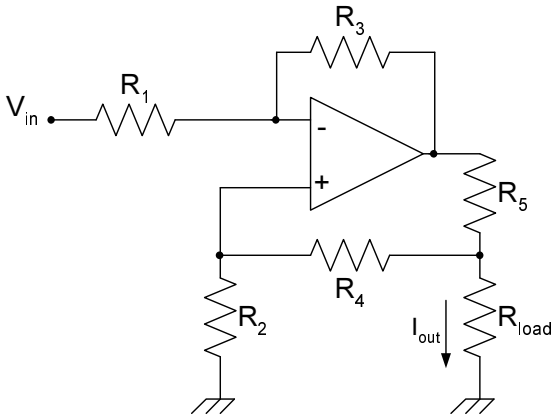

Figure 9.4: Schematic of the bipolar current source.

9.3 Current Source

For a simple current source the simplest design would be to use a series resistor and a voltage source, as shown in Figure 9.3. The Josephson junction or the SQUID has a theoretical normal resistance of $R_n = 10\ \Omega$ with a critical current $I_c = 10\ \mu$A. If a 1 V input equates to the critical current, I_c, the a series resistance of $R_i = 99.99 \approx 100\ \text{k}\Omega$. When the normal resistance is unknown, then the resistor will result in an unknown current. Another problem with using a series resistor is if the signal source experiences an error, then the device under test (DUT) could be biased with large currents. Star Cryoelectronics' sensor handling procedures manual [63] states that the maximum current that should be applied to the SQUID to test the normal resistance at room temperature is $50\mu A$ If, for example, a $V_{\text{error}} = 15$ V error signal is applied to the current source, it will result in an applied current of $I_{\text{source}} = 150\ \mu$A, which is capable of damaging the device.

For a device specific electronic control system where the values of the SQUID are clearly defined, operating with batteries providing a stable and reliable voltage supply, the simple resistive current source provides a current source with the lowest possible noise. For an unknown device, a more reliable and dynamic current source is required.

The bipolar current source provides a stable platform and functions as a voltage-controlled current-source (VCCS) [64]. The output current of the VCCS is

$$I_{\text{out}} = V_{\text{in}} \frac{R_3}{R_1 \cdot R_f}, \tag{9.3.1}$$

where

$$R_3 = R_4 + R5 \tag{9.3.2}$$

$$R_1 = R_2, \tag{9.3.3}$$

where R_x is the relevant resistance in Figure 9.4. For an input voltage $V_{\text{in}} = 5$ V and an output current of $I_{\text{out}} = 400\ \mu$A, the resistance values are: $R_1 = R_2 = 100\ \text{k}\Omega$, $R_3 = 12\ \text{k}\Omega$, $R_4 = 10.5\ \text{k}\Omega$, and

$R_5 = 1.5$ kΩ. For an input voltage $V_{\text{in}} = 5$ V and an output current of $I_{\text{out}} = 2$ mA, the resistance values are: $R_1 = R_2 = 100$ kΩ, $R_3 = 20$ kΩ, $R_4 = 19.5$ kΩ, and $R_5 = 500$ Ω.

The VCVS is a very wide-band current source, and can produce significant thermal current noise. Adding a shunt resistance to R_3 will reduce the bandwidth of the current source, reducing the current noise. In a complete SQUID feedback system using a battery power supply, the VCVS is an unnecessary source of noise and a series resistor current source is preferable.

An input buffer precedes the current generator. The buffer ensures that a varying input load can not excessively load the input of the current generator. A voltage divider at the buffer's input can be used to attenuate any incoming signal, or set the bias current at a fixed value. The current source is designed to operate at a fixed bias point by shorting the input of the voltage divider to the positive or negative rail. A secondary input is also provided for, and can either be set at different bias current or provide a secondary signal if required. The complete schematic for the VCCS is shown in Figure D.2 on p.151, and the populated boards for both a 1-channel and a 2-channel VCCS are shown in Figure E.1 on p.154.

9.4 Preamplifier

Three different types of direct-readout (DRO) electronics were tested. The operational amplifier specifications are summed up in Table 7.1 on p.80.

The first preamplifier built and tested is a simple current-feedback (CF) operational amplifier [65, 66]. CF amplifiers are known for their high gain-bandwidths (GBW), with the THS4303 having a GBW of 18 GHz. The one problem with the CF amplifier is the large input bias current, with the THS3201 having a maximum biasing current of 85 μA. This is over eight times the critical current of the junction with $I_c = 10$ μA, and over four times the the critical current of the SQUID using the same junction. Even for a junction with a critical current of $I_c = 100$ μA there will be an 80% uncertainty. Adding a series resistance to the input of the amplifier will improve the matching, but will attenuate the output of the SQUID. The second problem experienced with the CF amplifier is that the gain and GBW can not be dynamically chosen, and the feedback resistances from the specification (data) sheets must be taken. There are no formulas for the CF amplifier's feedback resistances or bandwidths, with the manufacturers having to test the operational amplifiers and provide a table of resistances for various gains.

The CF amplifier is built using 0.1% tolerances on the resistors, and follows the design guidelines provided in [2], with the recommended schematic shown in Figure 9.5. Only surface-mounted components are used, providing for a solid ground plane used by high-frequency electronics. The amplifier proved to be unstable, oscillating with low-impedance inputs. The output of the current-feedback amplifier with a grounded input is shown in Figure 9.6(a) for the low-frequency noise, and in Figure 9.6(b) for high-frequency measurements.

The second type of amplifier built is the voltage-feedback (VF) operational amplifier based on bipolar-junction transistor (BJT) inputs. BJT VF amplifiers tend to have a large input bias current, ranging from 15 μA to 42 μA as shown in Table 7.1. This input bias current still causes a large uncertainty, and for a SQUID or a junction with $I_c = 10$ μA there will be a unknown bias current of up four times the critical current. For the inverting amplifier in Figure 9.7(a) the gain is

$$V_{\text{out}} = -V\text{in}\frac{R_{\text{f}}}{R_{\text{in}}}, \tag{9.4.1}$$

where V_{in} is the input voltage, and V_{out} is the output voltage. Similarly, the non-inverting amplifier in Figure 9.7(b) has a gain of

$$V_{\text{out}} = V_{\text{in}}\frac{R_1 + R_2}{R_1}. \tag{9.4.2}$$

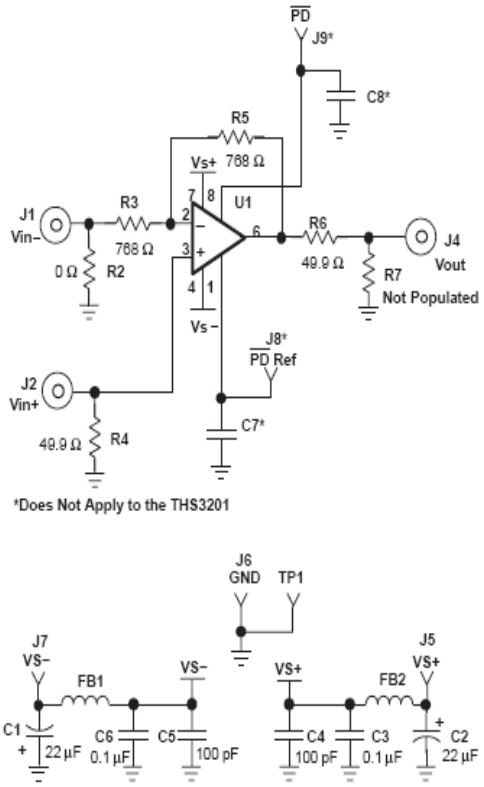

Figure 9.5: Schematic for the design of a CF amplifier [2].

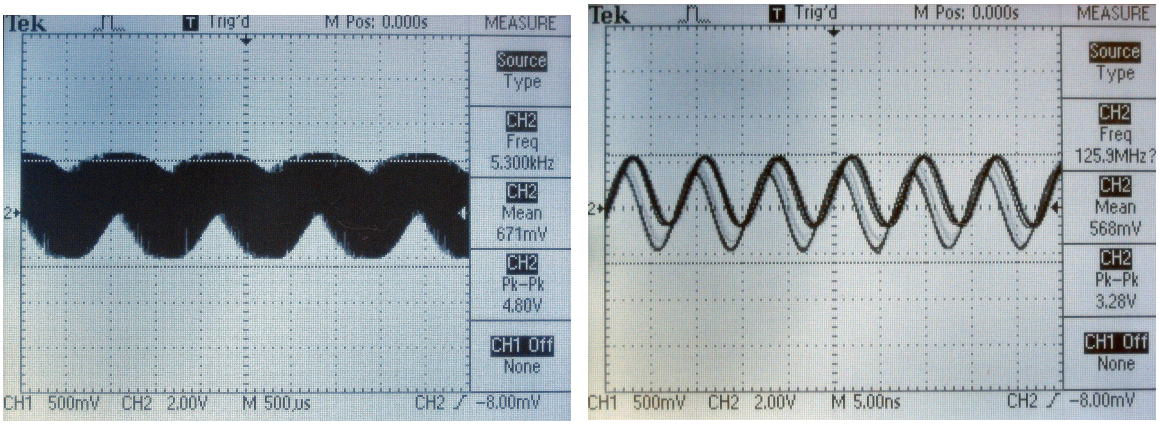

(a) (b)

Figure 9.6: Screen capture of a current-feedback amplifier showing (a) the low frequency oscillations and (b) the high frequency oscillations.

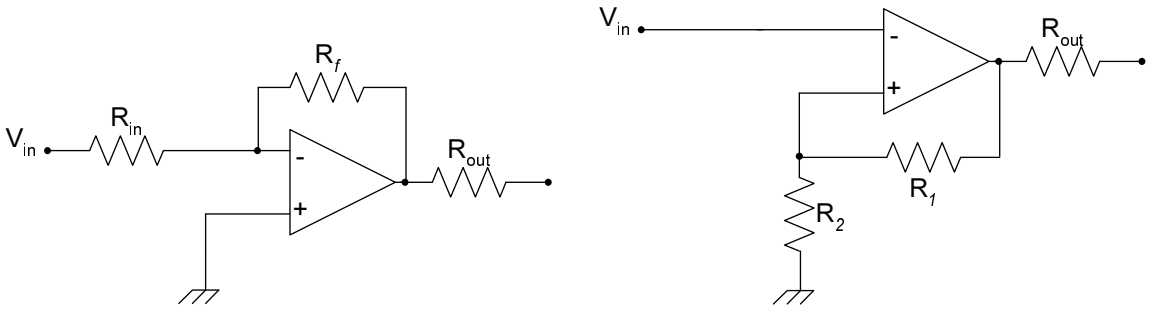

Figure 9.7: Schematic for the design of a basic (a) inverting VF amplifier and (b) non-inverting VF amplifier.

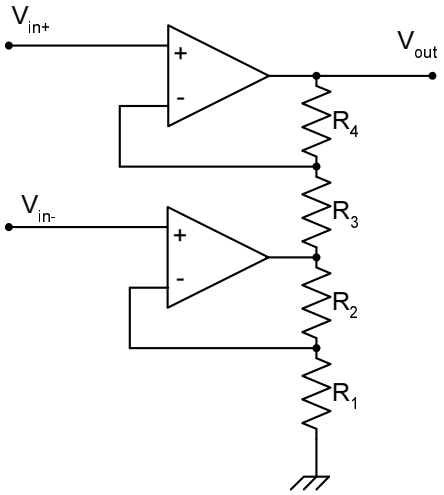

Figure 9.8: Schematic for the high-impedance instrumentation amplifier.

For an inverting amplifier with a gain of $A = -10$ the feedback resistance is $R_f = 10$ kΩ and the input resistance is $R_{\text{in}} = 1$ kΩ. For an inverting amplifier with a gain of $A = -1000$ the feedback resistance is $R_f = 1000$ kΩ and the input resistance is $R_{\text{in}} = 1$ kΩ.

The third type of amplifier built is the voltage-feedback (VF) operational amplifier based on the complementary metal oxide semiconductor (CMOS) or field effect transistor (FET) inputs. These VF amplifiers tend to have a small input bias current, ranging from 10 pA to 50 pA as shown in Table 7.1. The input bias current causes a negligible small uncertainty, for a SQUID or a junction with $I_c = 10$ μA the effect of this current will be unnoticeable.

To further improve the preamplifier for DRO, the four-point measurement setup in Section 9.2 is used. A high-impedance instrumentation amplifier, shown in Figure 9.8, is the only viable option for measuring the output in a four-point measurement setup [64, 55]. The gain of the high-impedance instrumentation amplifier is

$$\frac{V_{\text{out}}}{V_{\text{in}+} - V_{\text{in}-}} = 1 + \frac{R_1}{R_2}, \tag{9.4.3}$$

where

$$R_1 = R_4 \tag{9.4.4}$$

$$R_2 = R_3. \tag{9.4.5}$$

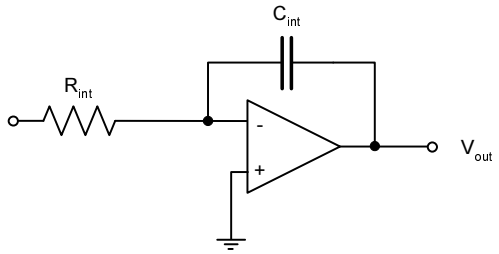

Figure 9.9: Layout of the integrator.

The DUT is connected with the ground reference point to the negative input, $V_{\text{in}-}$, and the output is connected to the positive input, $V_{\text{in}+}$. To invert the output, simply reverse the input connections, resulting in an inverting amplifier.

The gain of the preamplifier is chosen as $A_{\text{preamp}} = 10$. With standard resistor values of R_1=R_4=91 kΩ and $R_2 = R_3 = 91$ kΩ, the gain of the preamplifier is $V_{\text{out}}/(V_{\text{in}+} - V_{\text{in}-}) = 10.1$. Both the OPA656 and OPA657 operational amplifiers in Table 7.1 have very low current noise ($S_I = 1.3\ fA/\sqrt{\text{Hz}}$), very low voltage noise ($S_v \leq 7$ nV/$\sqrt{\text{Hz}}$), and extremely low input bias currents ($I_B = 20\ pA$), and are thus ideal for the high-impedance preamplifier. Due to the OPA657 operational amplifier having a higher gain-bandwidth at GBW=1.6 GHz and a higher slew-rate at SR=700 V/μs, the OPA657 operational amplifier was chosen to construct the preamplifier rather than the OPA656 operational amplifier.

The complete schematics for the various amplifiers are presented in Appendix D on p.150, while the populated boards are shown in Appendix E.1 on p.154. The preamplifier used for the measurements is the high-impedance instrumentation amplifier with a gain of $A_{\text{preamp}} = 10$.

9.5 Integrator

A design for the integrator is discussed in Section 7.4, and the schematic for the integrator is shown in Figure 9.9. The integrator has an output voltage of

$$V_{\text{out}} = -\frac{1}{R_{\text{int}}C_{\text{int}}}\int_{t_2}^{t_1} V_{\text{in}}dt, \tag{9.5.1}$$

where

$$f_1 = \frac{1}{2\pi R_{\text{int}}C_{\text{int}}}. \tag{9.5.2}$$

For an integrator with $f_1 = 1$ MHz the resistance is $R_{\text{int}} = 1$ kΩ and the capacitance is $C_{\text{int}} = 159$ pF. For an integrator with $f_1 = 1$ GHz the resistance is $R_{\text{int}} = 100$ Ω and the capacitance is $C_{\text{int}} = 1.59$ pF. The OPA657 operational amplifier is ideal for the integrator due to its low noise, low bias current and low input offset voltage.

The complete schematic for the integrator is shown in Figure D.3 on p.152, and the populated boards are shown in Figure E.4 on p.155.

9.6 Load Reference Measurement

The current source and preamplifier are tested using the four-point measurement configuration described in Section 9.2. A short circuit will indicate if there is any mutual series resistance between the current

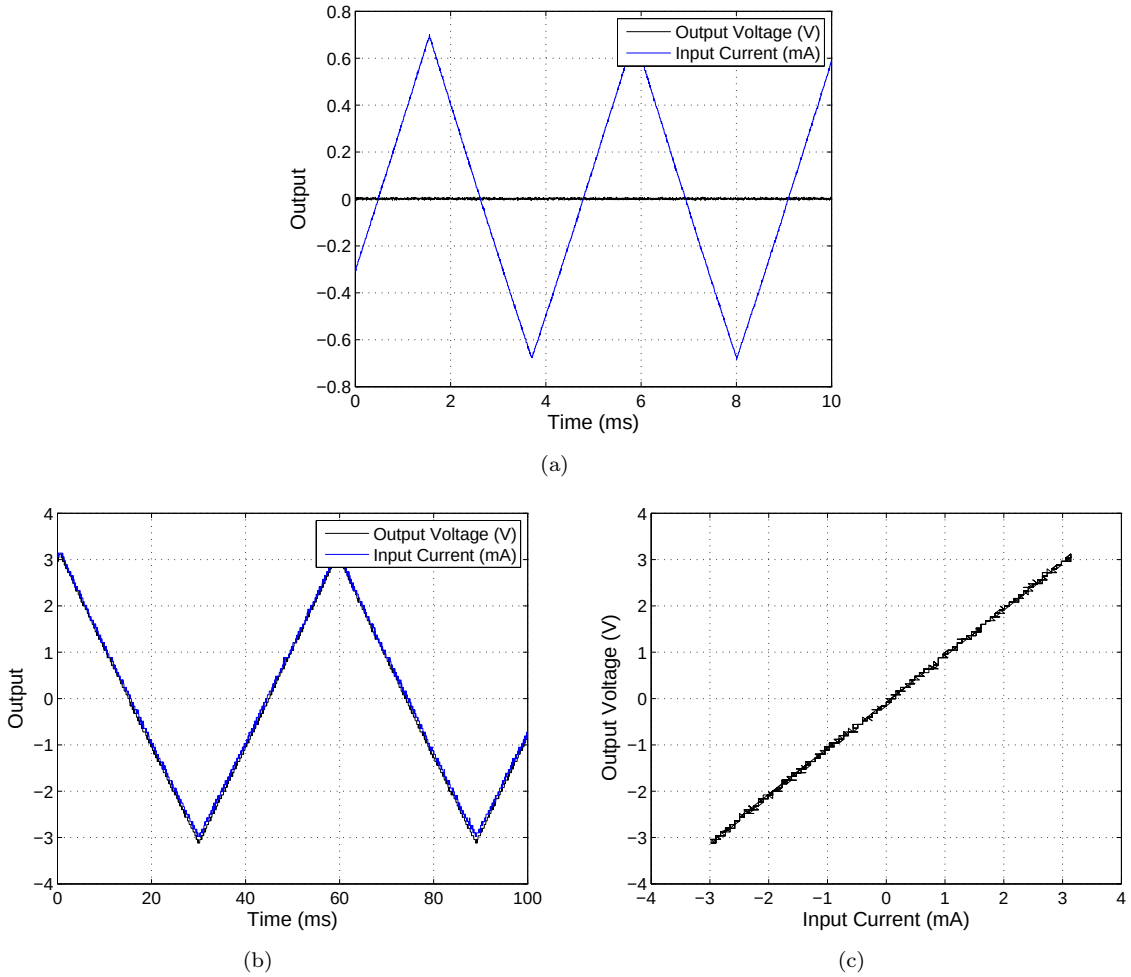

Figure 9.10: Four-point measurements using (a) a short circuit, and (b) and (c) a 10 Ω resistor.

source and the preamplifier, while a known load resistance is used to verify that the electronics function as desired.

In Figure 9.10(a) the input current is swept linearly between $I_{\text{peak}} = \pm 700$ μA at 232 Hz for a short-circuit load. Any mutual series resistance present between the current source and the preamplifier should clearly show up, yet only noise is measured at the preamplifier's output. This validates the four-point measurement theory in Section 9.2, ensuring that only the resistance of the DUT is tested, and not that of the connecting cables. When the probe is short-circuited, the noise figure remains unchanged. The noise measured in Figure 9.10(a) is due to noise intrinsic to the oscilloscope and 10x probes used, indicating the maximum resolution possible with the measurement setup.

In Figure 9.10(b) the input current is swept linearly between $I_{\text{peak}} = \pm 3$ mA at 17 Hz for a 10 Ω load. This results in a $V_{\text{DUT,peak}} = 30$ mV potential developing across the DUT. The preamplifier was initially designed to amplify the potential developed across the DUT by a factor of $G_{\text{preamp}} = 100$, resulting in an output of $V_{\text{out,peak}} = 3$ V. The linear voltage-current relation for the 10 Ω load is shown in Figure 9.10(c), with the oscilloscope's analog-to-digital converter's (ADC's) maximum bit resolution visible as steps in the output.

9.7 Josephson Junction Measurement

Basic Josephson junctions were produced locally at the University of Stellenbosch's Engineering department, produced by U. Büttner and postgraduate students. Two examples are shown in Figures E.5 and

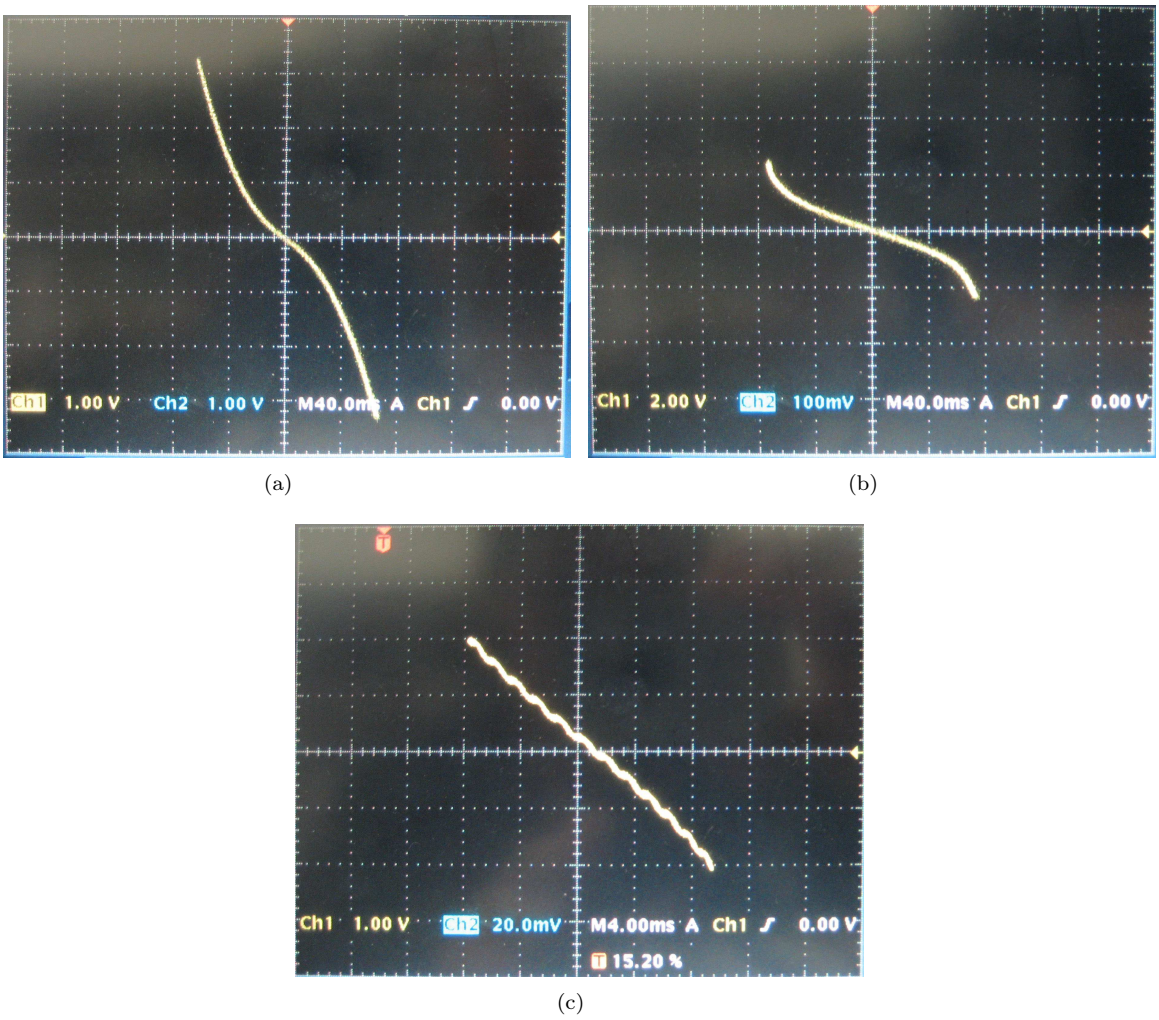

(a) (b)

(c)

Figure 9.11: Screen capture of a measured Josephson junction for (a) a large input current sweep, (b) a smaller input current sweep slightly higher than the critical current, and (c) a high-frequency magnetic field resulting in Shapiro steps.

E.6 on p. 156. The substrate used is a purchased wafer of magnesium-oxide (MgO) described in Section 4.4, onto which a layer of YBCO is deposited using the magnetron sputtering technique discussed in Section 4.5.2. The YBCO layer was then patterned into thin strips by using photolithography and an Argon-ion mill to remove the excess YBCO. These strips were then cut using a high-powered laser to form constriction junctions. For more information on the production of Josephson junctions, please refer to [18, 67, 68].

The Josephson junction is cooled down to 60 K using a Gifford-McMahon (GM) cryocooler (Section 6.4.4). This temperature is lower the critical temperature for YBCO and the material turns superconductive. Due to the gold wire-bonds used to connect the sample holder to the YBCO layer, the sample must be cooled slowly. If the sample is slowly submerged into liquid nitrogen, then the wire-bonds break and must be reapplied. To be able to use liquid nitrogen as a coolant, the sample must be sealed inside a thermal epoxy bubble, but this protective layer will prevent the substrate from being reused for additional samples [69]. Appendix E.4 on p.158 provides additional information on the GM cryocooler used.

The current source and only the preamplifier with a basic gain of $G = 10$ are initially used to help verify the design of the electronics.

A large input current sweep is applied to the junction in Figure 9.11(a), and the junction shows the voltage-current characteristic of an overdamped junction described in Section 2.8.3 with an additional

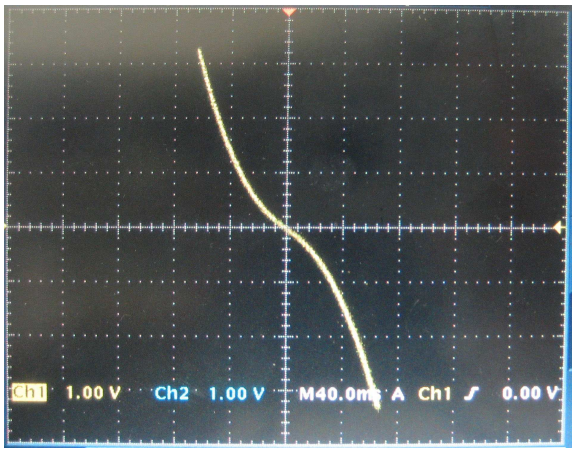

Figure 9.12: Screen capture of a measured Josephson junction using the Mr. SQUID's reference electronics.

resistive element in series. The junction was wire-bonded onto the sample holder using a single ground connection and a single copper strip, to which the current source and preamplifier were connected. There is about 3 cm of copper and 0.5 cm of gold wire-bonding shared by the current source and the preamplifier. This mutual resistance causes the slope visible in the measurements, when the junction should be superconductive and produce no measurable resistance.

In Figure 9.11(b) the input current sweep is reduced to just above the critical current, and the characteristic transition of the junction from superconductivity into the shunt resistance is clearly visible. The additional series resistance due to the shared copper conductor/wire-bonding is visible as a slope about the origin. The junction has a critical current of $I_c \approx 290$ μA, and the rounding of the voltage-current curve is due to thermal noise, as predicted in Section 5.5.2. If a powerful magnet is placed near the junction, then the critical current is reduced due to the magnetic field effect (Section 2.8.7).

When a high-frequency signal is applied to the junction, then the Shapiro steps predicted in Section 2.8.6 appear, as shown in Figure 9.11(c). This test is used to verify that the DUT is in fact a Josephson junction and not an unwanted artifact, since the Shapiro steps will only appear across junctions.

The Mr. SQUID's reference electronics were used to test the junction, and the results compare favourably to the output to the designed electronics. The voltage-current relation is shown in Figure 9.12 for the Mr. SQUID reference electronics. An additional series resistance in the junction is still visible as a slope about the origin, and the measured output signal is noisier compared to the measurements using the designed electronics.

To test the effect of temperature on the critical current, the cryocooler was switched off. This resulted in a static discharge that irreparably destroyed the junction, and was the first indicator that something is wrong with the cryocooling unit. In a subsequent experiment, when a researcher soldered a wire inside the cryocooler after allowing it to heat up to room temperature after use, the unit caused a visible discharge. It is important to always heat the sample above the critical temperature before switching off the cryocooler to reduce the chance of damaging any superconductor under test. The cryostat measurement system shown in Figure E.11(b) can be used to both measure the temperature of the the head of the cold section, and to increase the temperature of the cold section by using a built-in electric heater.

9.8 Manufactured Directly-Coupled DC SQUID Measurement

Directly-coupled dc SQUIDs were produced locally at the University of Stellenbosch's Engineering department, and is based on the design by F. W. Graser [18]. The samples were produced by U. Büttner and postgraduate students. The substrate used is a purchased wafer of magnesium-oxide (MgO) described in

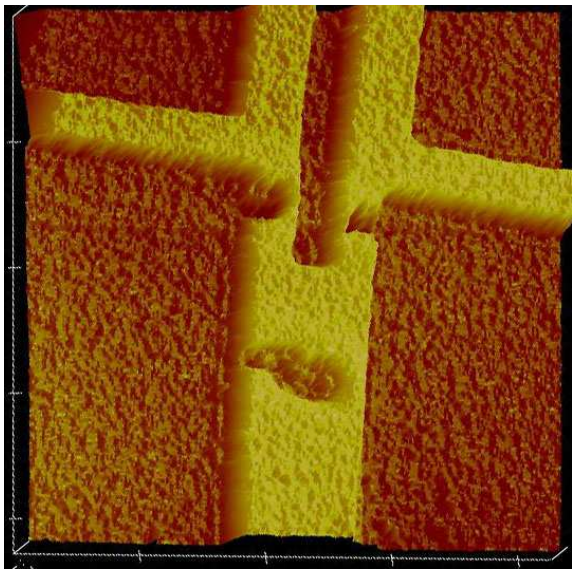

Figure 9.13: Scan of the SQUID loop and Josephson junctions for the directly-coupled dc SQUID.

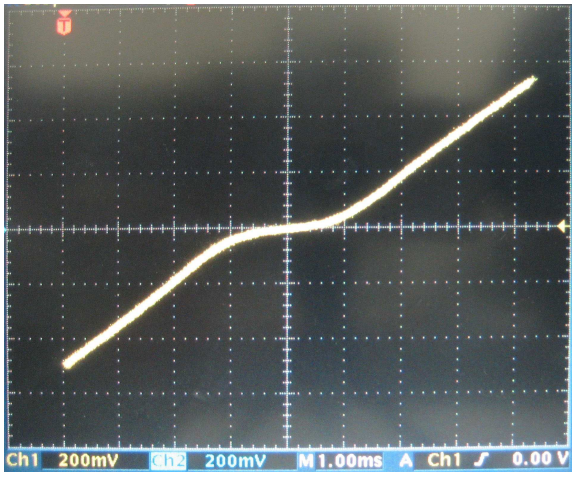

Figure 9.14: Screen capture of the directly-coupled dc SQUID.

Section 4.4, onto which a layer of YBCO is deposited using the magnetron sputtering technique discussed in Section 4.5.2. The YBCO layer was then patterned by using photolithography and an Argon-ion mill to remove the excess YBCO. These junctions were then cut using a high-powered laser to form constriction junctions. For more information on the production of a magnetometer and Josephson junctions, please refer to [18, 67, 68].

A scan of the manufactured device is shown in Figure 9.13. The lower half of the SQUID pickup loop is shown, with the pickup loop attached to either side of the SQUID loop. The junctions are clearly visible on either side of the lower part of the SQUID pickup loop, forming constriction junctions. Unfortunately the YBCO strip used for the return current, below the junctions, was also damaged during the manufacturing process. If the critical current of the damaged section is lower than that of the constriction junctions, then the SQUID will not behave as a magnetometer but as a simple Josephson junction.

The preamplifier with a gain of $G = 10$ is connected to an additional amplifier for a total gain of $G = 100$ to simplify the measurement and reduce the noise created by the oscilloscope. The secondary amplifier can also be used to compensate for any offset voltage by adjusting a variable resistor.

In Figure 9.14 the voltage-current characteristics of the magnetometer is shown. The curve is what is expected of a simple Josephson junction. With all the magnetic field noise permeating the laboratory,

Normal Resistance ($R_n/2$) @ 295K [Ω]	300 - 400
Normal Resistance ($R_n/2$) @ 77K [Ω]	0.2 - 0.5
Critical Current ($2I_c$) @ 77K [μA]	5

Table 9.1: Mr. SQUID HTS magnetometer basic specifications [3]

generated by the cryocooler's compressor, the cold section, the vacuum pump and all the surrounding electronic noise sources, the output should have a significant amount of noise as it nears the critical current. An output similar to the predicted output in Figure 3.5 on p.33 should be seen, with a half-fluxon ($\Phi_0/2$) of applied magnetic field significantly reducing the critical current of the magnetometer. For a magnetometer with an optimal screening parameter, $\beta_L = 1$, the critical current with $n\Phi_0 + \Phi_0/2$ applied should be half the critical current with $n\Phi_0$ applied. The critical current should vary from I_c to $2I_c$ during measurements. The damage to the lower section of the magnetometer most probably causes the device to act a single Josephson junction.

When a strong magnet is brought near to the magnetometer, the critical current is reduced, as is expected with a normal junction. Unfortunately the magnetometer was destroyed when the coil used for magnetic stimulation was attached to a signal generator. The signal generator was powered off at the time of the incident, but was plugged into an outlet. The cryocooler probably discharged into the coil, damaging the magnetometer beyond repair.

Due to the gold wire-bonds used the sample must be cooled slowly. If the sample is slowly submerged into liquid nitrogen, then the wire-bonds break and must be reapplied. The cryocooler must therefore be used to test the basic functionality of the magnetometer before applying thermal epoxy to harden the sensor to thermal cycling.

There were no other directly-coupled dc SQUID successfully manufactured.

9.9 Mr SQUID Magnetometer Measurement

The critical parameters for the Mr. SQUID magnetometer are given in Table 9.1. Bicrystal grain boundary junctions described in Section 4.8 are used to manufacture the magnetometer. The SQUID pickup loop is based on the large-area washer dc SQUID configuration described in Section 3.3, and an external mu-metal shield is used to attenuate the environmental magnetic fields. Figure E.7(a) on p.157 shows the complete Mr. SQUID unit mounted on a printed circuit board (PCB). The actual sensor is enlarged in Figure E.7(c), and the dimensions for the sensor are given in Figure E.7(d). Figure E.7(b) shows the mu-metal shield used during the testing.

Initially room temperature measurements of the magnetometer are taken to verify the device, with the current applied to the DUT and the amplified output shown in Figure 9.15. The input current is swept linearly between $I_{\text{peak}} = \pm 120$ μA at 17 Hz. From Table A 300 Ω series resistance is expected at room temperature, but the actual measurement only results in a 1 Ω resistance for the magnetometer. There is a high probability that the magnetometer has been damaged, either due to age degradation, repeated thermal cycling, or due to improper handling.

The magnetometer is eased into a cryostat filled with liquid Nitrogen, allowing it to cool down to about 77 K. The cryostat used is shown in Figure E.8 on p.158. The gain of the preamplifier had to be increased to a total of $G_{\text{preamp}} = 10000$ in order to measure the output of the magnetometer. A high preamplifier gain is required to significantly raise the output signal above the oscilloscope's intrinsic noise. The low output of the magnetometer is due to the low I_cR_n product.

With the input current swept linearly between $I_{\text{peak}} = \pm 125$ μA at 11 Hz in Figure 9.16(a), the output in Figure 9.16(b) is expected to look similar to the voltage-current relation predicted in in Figure 3.5 in Section 3.2.4 on p.33. The critical current of the magnetometer is specified as $I_c = 5$ μA in Table 9.1,

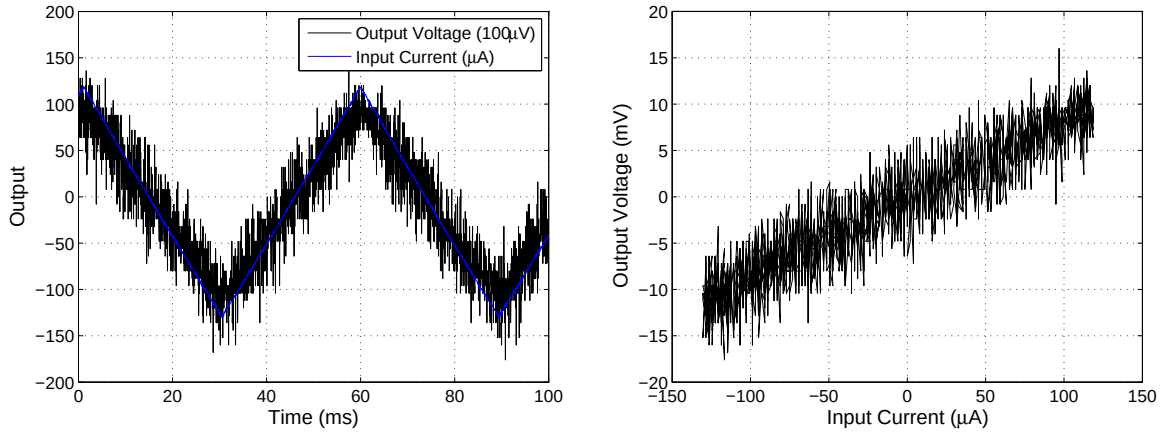

(a) (b)

Figure 9.15: Measurements of the Mr SQUID sensor probe at room temperature for (a) the input current and output voltage for a 17 Hz sweep frequency, and (b) the current-voltage response.

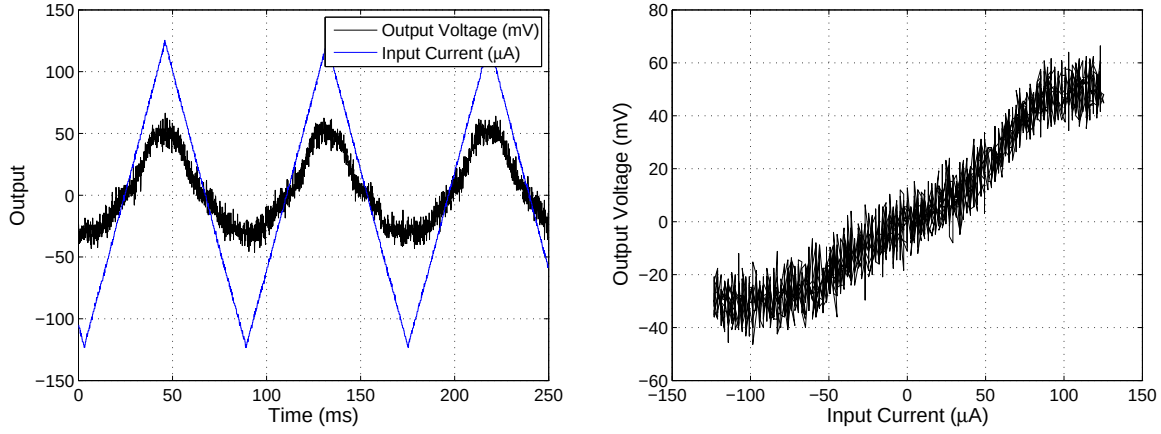

(a) (b)

Figure 9.16: Measurements of the Mr. SQUID sensor probe in liquid nitrogen at 77 K for (a) an 11 Hz input current and output voltage, and (b) the current-voltage response.

so there should be a clearly visible transition when the supercurrent saturates at 5 μA and the normal current becomes dominant.

This transition does not appear, and could be either due to excessive magnetic flux causing the junctions to saturate, or could be due to damage to the magnetometer. When tested at room temperature the measured resistance of the DUT is far lower than specified by the manufacturer, and damage to the device could explain the lack of the transition current. The superconducting laboratory is situated two floors above a heavy-current machine laboratory, and is also surrounded on all sides by offices containing running personal computers. These devices can create large magnetic fields that could interfere with the magnetometer. The mu-metal shield surrounding the magnetometer could be insufficient to attenuate these fields, causing both an increase in the 1/f noise and saturating the sensor.

In Figure 9.17 the apparent noise appearing in Figure 9.16(b) is measured. The measured noise is a nearly sinusoidal signal with a 52 kHz fundamental harmonic. This signal is most probably due to large applied magnetic fields causing the SQUID to switch, even through the mu-metal shield. Unfortunately there is no available area where noise-free measurements can be taken. Since a Faraday cage does reduce magnetic noise but only external electromagnetic radiation, using a cage did not significantly improve subsequent measurements

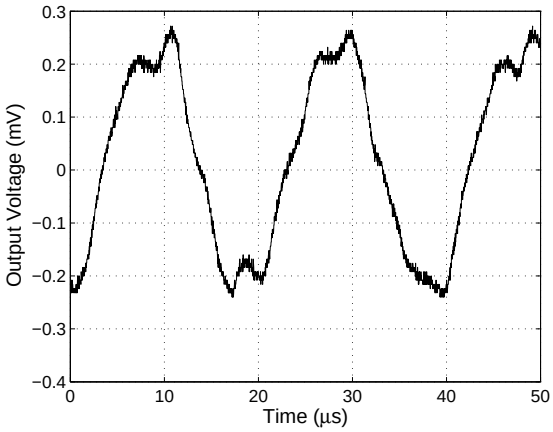

Figure 9.17: Measurements of the amplified noise for the Mr. SQUID sensor probe in liquid nitrogen at 77 K.

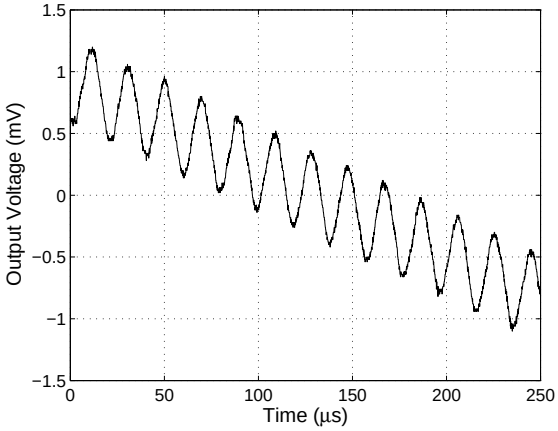

Figure 9.18: Measurements of the amplified noise for the Mr. SQUID sensor probe in liquid nitrogen at 77 K for a 0 A current source.

To further examine the workings of the magnetometer, in Figure 9.18 the input current is reduced to 0 A. Theoretically the output of the magnetometer should be zero as the supercurrent should not be saturated, unless the external magnetic field causes the SQUID to switch. The 52 kHz sinusoidal signal is still present, and is probably due to external magnetic fields.

When the magnetometer is removed from the liquid nitrogen and allowed to warm in the atmosphere for a few seconds, all the effects measured in Figures 9.16(a) to 9.18 disappear and the SQUID becomes a purely resistive system. The YBCO layer transitions from a superconductor at 77 K into a normal conductor above 90 K when it is heated. This thermal transition indicates that all of the measured signals occur due to superconducting material in the sensor, and thus the sensor must be at least minimally functional.

Stimulating the magnetometer with an additional magnetic field generated by a coil, applied to the sensor inside the mu-shield, has no measurable effect. The integrator was added to the system in an effort to create a flux-locked loop (FLL), and the output fed back to the SQUID with first an external coil and then using the feedback loop patterned onto the sensor. The flux-locked loop refuses to lock on and the integrator runs away.

The reference electronics supplied with the Mr. SQUID magnetometer were unable to produce any better results.

9.10 Conclusion

The electronics with which to interface with superconductors and linearize them were built and tested on actual superconductors. Four-point measurements are made using high-impedance, low-noise operational amplifiers in a high-impedance operational amplifier configuration to reduce unwanted interference with or unnecessary loading of the device under test. The current source can be either used to sweep over a specified current range, or provide a fixed current irrespective of the load attached.

The measurement of basic constriction Josephson junctions proved to be quite successful. Most of the effects predicted by the theory and simulations have been observed when measuring the junctions. The voltage-current relation, the effect of large magnetic fields on the critical current, and the Shapiro steps due to high-frequency signals were observed.

Since the wire-bonds used to connect the superconductors to the electronics could not sustain immersion into liquid nitrogen, a cryocooler is required to test the devices. Unfortunately, since the cryocooler has a high probability of damaging any devices tested due to electrostatic discharge, a complete set of measurements on a manufactured dc SQUID magnetometer was not possible. The magnetometer expired before the effects of magnetic stimuli could be tested, so it remains unknown if it would have functioned as predicted.

The Mr. SQUID magnetometer also failed to measure properly, with initial room-temperature measurements of the SQUID's resistance placing doubt on the integrity of the device. A flux-locked loop could not be created.

Chapter 10

Results

10.1 Introduction

The important results from Chapters 8 and 9 are summarized and briefly discussed in this chapter. These discussion are there to determine if the progression from a purely theoretical model, in Chapters 2 to 7, into a practical application was successful.

10.2 Results of the Simulations

10.2.1 Result of the Josephson Junction Simulations

A simulation model was created to model the Josephson junction using the ideal Josephson junction with an additional shunt resistance and junction capacitance. The three types of Josephson junction, namely the overdamped junction, the underdamped junction and the general damped junction, were simulated and compared to the theoretical model in the preceding chapters. The simulations behaved as was predicted by the theoretical models. Both the oscillations in the critical current for an applied potential and the oscillation in the potential for an applied current were simulated. The overdamped Josephson junction has a non-hysteretic voltage-current behaviour, while the general damped and overdamped junctions both exhibited significant hysteresis.

When thermal noise was added to the simulation of a overdamped junction, a slight rounding of the voltage-current at the critical current, the point where the junction transitions from a purely superconductive element with no resistivity into a shunt resistance, could be observed. This is also predicted by the noise model used to describe the effect of thermal noise due to the shunt resistance.

The simulation model behave acceptably and could be used for further simulations.

10.2.2 Result of the DC SQUID Simulations

The overdamped Josephson junction model was expanded into a directly-coupled (dc) SQUID model. Analysis of the voltage-current curve for the dc SQUID both without any applied magnetic field and with a half-fluxon ($\Phi_0/2$) applied magnetic field were run to compare to the theoretical model. Two distinct SQUIDs were simulated. The first type of SQUID has an optimal screening parameter, $\beta_L = 1$, with a loop inductance of $L_{SQ} = \Phi_0/2I_c$. In theory this type of SQUID has half the critical current when a magnetic field of $n\Phi_0 + \Phi_0/2$ is applied than when a magnetic field of $n\Phi_0$ is applied. The second a loop inductance of $L_{SQ} = \Phi_0/\pi I_c$ and exhibits a non-hysteretic behaviour for applied magnetic fields. In theory this type of SQUID has a critical current of less than half when a magnetic field of $n\Phi_0 + \Phi_0/2$ is applied. The simulations support the predicted effect of a magnetic field on the critical currents for the relevant SQUID types.

In following simulations the dc SQUIDs were biased at an optimal working point by using a constant current source. A large magnetic field, ranging from $-3\Phi_0$ to $3\Phi_0$, was was used in a linearly magnetic sweep of the SQUIDs. The voltage-flux response behaves as predicted, resulting in the sinusoidal voltage-flux conversion predicted by the theoretical models.

The input was then replaced by a small-signal sinusoidal input, which is used to observe the linearity of the SQUID for small input signals. When the SQUID is biased at the optimal working point and a small input flux signal is applied, then the SQUID produces a sinusoidal output at an offset voltage. The output is linear to the input, but at an offset voltage due to the working point being at an offset voltage. The SQUID transforms a magnetic signal into a measurable electric signal, becoming a flux-to-voltage converter. Noise is added to the SQUID to observe its effect on the flux-to-voltage conversion for small-signal inputs. When the thermal noise becomes sufficiently large enough, a noticeable distortion appears on the output. It becomes apparent that the thermal noise and 1/f noise should be kept as low as possible for a highly linear flux-to-voltage conversion.

Additional positive feedback (APF) can be used to increase the slope of the flux-to-voltage converter. When noise is added to the SQUID using APF, the effect of the noise is attenuated. Even with a significantly large amount of thermal noise added to the SQUID, the APF manages to reduce the effect to imperceptibly levels.

The simulated SQUIDs are nearly indistinguishable from the theoretical model. The advantage of adding simulations to the analysis of the SQUID, rather than only using theoretical models, is that they can predict the effect of noise in a system.

10.2.3 Result of the Flux-Locked Loop Simulations

A flux-locked loop (FLL) is used to keep the SQUID operating near the optimal working point. As a result the SQUID becomes a linearized device, with the output of the FLL becoming a linear function of the applied flux. The error signal, the actual flux applied to the SQUID, must remain within the linear region for the small-signal response. Using a FLL successfully converts the periodic flux-to-voltage conversion into a linear flux-to-voltage conversion, as predicted by the theoretical model. The effect of noise is also investigated, with even a small amount of thermal noise having a noticeable effect on the output of the SQUID. In practical magnetometers the effect of noise is one of the main design concerns, with a respectable amount of research conducted into reduction of noise.

Time delay in a FLL, which is a result of signals traveling through wires and electronics, severely reduces the bandwidth of a SQUID system. The FLL is basically a feedback system, and with large time delays the SQUID will not operate within the linear region. Large time delays will either in result a distortion of the output signal, or will cause the FLL to lose its lock on the working point. It is thus important to choose an appropriate bandwidth for the system, which is set by the integrator, and to reduce the line delay between the SQUID and the electronics. The simulated effect of the line delay was also predicted by the theoretical model of the FLL.

10.3 Results of the Measurements

10.3.1 Result of the Josephson Junction Measurements

Overdamped Josephson junctions manufactured at the University of Stellenbosch were measured using the four-point measurement setup designed for the dc SQUID magnetometer. The junctions have a high critical current and exhibit the characteristic voltage-current curve expected, and applying a high-frequency signal also resulted in the formation of Shapiro steps. Thermal noise is evident in the junction as a rounding of the voltage-current when the applied current exceeds the critical current. With no

thermal noise the transition should result in a sharp changeover. The measurements compare favourably to both the theoretical and simulated models. The constriction junctions are also shown to behave as overdamped junctions exhibiting no hysteresis.

A four-point measurement scheme was implemented in order to improve the quality of the measurement and remove unwanted loading of the superconductor. The measurement setup is sensitive enough to even measure the short communal connecting wires preceding the junction, which caused the resistive slope to form about the origin. The electronics designed for the SQUID are ideal for testing junctions, and the operational amplifiers employed were chosen to produce very little noise.

Gold wire-bonds are used to connect the sample holder to the junction, but these wires do not survive submersion into liquid nitrogen. Therefore the junctions had to be measured using a GM cryocooler. Unfortunately the cryocooler has a tendency to create an electrostatic discharge that damages the junctions.

Measurements of the junctions were successful except for the damage caused by the cryocooler. A recently acquired oscilloscope, capable of storing the measurements for further analysis, will help to improve the quality of future measurements.

10.3.2 Result of the Directly-Coupled DC SQUID Measurements

A directly-coupled dc SQUID manufactured at the University of Stellenbosch was measured using the four-point measurement setup. The SQUID exhibited the voltage-current curve expected from a single junction and not the behaviour expected from a SQUID. Before any further measurements could be made to validate the SQUID, the cryocooler destroyed the sample.

Gold wire-bonds are also used to connect the sample holder to the dc SQUID, and these wires do not survive submersion into liquid nitrogen. The SQUID had to be measured using a GM cryocooler. Unfortunately the cryocooler has a tendency to create an electrostatic discharge that damages the junctions, and when a signal generator was connected to the excitation coil, a discharge occurred.

No manufactured SQUIDs proved viable, so the testing of a locally manufactured SQUID was unsuccessful. The electronics for a FLL could also not be tested with the manufactured devices.

10.3.3 Result of the Mr. SQUID Measurements

The Mr. SQUID magnetometer was tested using the electronics designed for a unit with a higher I_cR_n product. The initial measurement of the SQUID at room temperature showed that the normal resistance was far below the manufacturer's specification, indicating a possible problem with the unit. Using a cryostat filled with liquid nitrogen was possible as the unit is sealed with thermal epoxy to resist damage from repeated thermal cycling.

The SQUID did not behave as predicted, either due to damage to the magnetometer or due to excessive environmental magnetic noise. The voltage-flux curve did not behave as predicted by the theory or simulations, and the unit even produced a sinusoidal output when the biasing current was reduced to zero. The FLL was unable to lock onto the signal.

Measurements of a closed FLL proved unsuccessful, and no magnetometer was operated as a linear unit.

10.4 Recommendations

Production of high-quality YBCO films deposited onto MgO substrates has been greatly improved at the University of Stellenbosch in recent years. As the production of high-quality, reliable Josephson junctions also improves, it becomes possible to produce application specific SQUIDs for use in a SQUID microscope.

The current generation of magnetometers available for purchase is prohibitively expensive. In 2006 the price for the M1000 magnetometer [70] produced by Star Cryoelectronis was in the order of $5000 per device, and a single discharge from the cryocooler would have destroyed the device. SQUIDs are very sensitive to mishandling, and even the smallest mistake during measurement could result in the device becoming inoperable. A reliable production of SQUIDs will reduce the cost of designing and testing of superconductors.

The superconducting laboratory is also not situated in an ideal area, as it is surrounded by devices that create significant magnetic fields. In some universities the research laboratories are situated in shielded chambers in basements to reduce electromagnetic noise. Another alternative is to replace the SQUID design with a design for superconducting gradiometers, which are more resistant to environmental magnetic noise.

The cryocooler poses the largest hazard when working with superconductors. An electrostatic discharge can destroy valuable equipment or cause hours of work to become lost in an instant. With ongoing research into producing low-cost and highly reliable cryocoolers, it would be advisable to upgrade the unit when they become available. A pulse tube cryocooler is currently the optimal closed-cycle cryocooling solution for testing SQUIDs.

Chapter 11

Conclusion

In Chapter 1 this thesis begins by providing the motivation for the analysis and design of a SQUID microscope and superconductors in general. An additional brief history of superconductors is provided for background information.

In Chapter 2 the theory behind basic superconductivity is explained. Initially the classic electromechanical models are used to describe the effects of superconductivity, such as a material having no DC resistance and the Meissner effect. The macroscopic quantum model (MQM) creates a whole new model based on the microscopic quantum model. The classic electromechanical model can be inferred from the MQM, but the new mode can also explain the Josephson effect observed in certain superconductive materials. Using the MQM model, a theoretical model describing the workings of the various types of Josephson junction is created. The overdamped junction, the underdamped junction and the general damped junction each exhibit different behaviors, and the merit of each is discussed. For a SQUID the overdamped junction is ideal as it does not exhibit hysteresis. Additional effects such as the magnetic field effect and the response of a junction to a varying input signal are explained.

Chapter 3 creates a theoretical model of a dc SQUID. Initially a very basic model created in an effort to best explain how a SQUID would function as a flux-to-voltage converter. In practical SQUIDs there are additional parameters that must be included, such as a finite inductance in the pickup loop. The basic SQUID model is expanded to include these effects to create The effect of the loop inductance is investigated, and it is shown that a large loop inductance can result in a SQUID with a hysteretic flux-to-voltage conversion, thus limiting the sensitivity of a practical SQUID. Two additional SQUID variants that can be manufactured as a single layer device are examined, as these devices could be produced at the University of Stellenbosch. The large-area washer and the directly-coupled dc SQUID increase the effective area, and thus the sensitivity, of the dc SQUID without increasing the SQUID loop inductance.

In Chapter 4 the practical aspect of high-temperature superconducting materials is discussed. It is important to understand how the superconducting material, of which the SQUID is composed, functions. In the first half of the chapter emphasis is placed on the effect on anisotropy in a superconductor and how this effect can be used to either create a junction at a specific point, or how to prevent unwanted junctions from occurring. Deposition of the superconducting material onto a substrate is critical to the performance of a SQUID, as any defects in the material will increase the 1/f noise.

In the second half of the chapter various types of practical junction are compared. Each type of junction has advantages and disadvantages, from the difficulty to manufacture and accurately reproduce a junction to what type of junction will be created. Most of the junctions described are intrinsically overdamped, but under certain circumstances some will behave as underdamped junctions. When man-

ufacturing or purchasing a SQUID, it is important to understand the type of junction used in the design and how it will perform.

Chapter 5 introduces noise. Various types of noise and their origins are discussed. Thermal noise can result in a Josephson junction with a low energy gap to malfunction, and can also create sufficient noise in a SQUID to hide any input signals. At higher frequencies thermal noise is the dominant an is attributed to the shunt resistance in the Josephson junction. Noise also restricts the maximum size of the SQUID's pickup loop, since the thermal energy can cause the SQUID's quantum interference to become unobservable.

At low frequencies the 1/f noise becomes dominant and restricts the measurement of low-frequency signals. 1/f noise is due to thermal motion of vortices, which is strongly dependent on the quality and layout of the superconducting film, and fluctuations in the critical current of the Josephson junctions.

Superconductors work at very low temperatures, and cooling is an important part for the design of a SQUID microscope as the SQUID is highly sensitive to thermal change, mechanical vibrations and magnetic noise. In Chapter 6 a quick overview of thermodynamics is given. The two kinds of cooling, the open cycle and closed cycle systems, are discussed in depth.

Open cycle cryogenic systems cool down by converting a loss of mass into cooling power. Typically a liquid is allowed to turn into gas, or pressurized gas are allowed to expand, resulting in cooling power. The excess gas is vented into the atmosphere, or must be stowed for recycling. Open cycle systems have the advantage of producing stable temperatures and little or no mechanical and magnetic noise, but the coolant needs to be replenished regularly. The complexity to manufacture the coolant is usually ignored by the user.

Closed cycle systems convert electric power into heat and cooling power. Thermal energy is extracted from the cold section of the cryocooler, and the heat is dumped into the environment through passive or active cooling. Closed cycle cryocoolers usually produce unstable temperatures and significant mechanical and magnetic noise, but operates off the energy grid. This makes the cryocooler easier to operate, but it is susceptible to power outages. When using a SQUID magnetometer inside closed cycle cryocooler, the temperature needs to be stabilized and the mechanical and magnetic noise needs to be damped or removed altogether for stable operation.

Construction material for building a cryostat or cryocooler are also discussed. Strong, non-magnetic materials that can operate at cryogenic temperature and resisting a vacuum are ideal materials. For certain sections the material must be thermally insulating, while in other sections the material must be as conductive as possible.

Chapter 7 describes the theory behind the electronics used to interface with the SQUID. The SQUID can be used in what is known as a flux-locked loop (FLL), effectively linearizing the non-linear flux-to-voltage conversion. The design of the FLL is discussed in length, along with all the shortcomings and limitations placed on a practical system. The components that make up the FLL are analyzed separately, with an emphasis placed on optimizing them for use with a practical SQUID. Electronic and mechanical techniques to reduce noise are looked at. Current bias reversal reducing fluctuations in the critical current. Proper shielding of the electronics and cabling will reduce noise created and received by the electronics.

In Chapter 8 the Josephson junctions, the dc SQUID and the FLL are simulated. Simulations are comparable to the theoretical models describing the behaviour of Josephson junctions and SQUIDs, and can more accurately predict the effects of noise in a practical system. Simulations provide a way to observe how additional positive feedback (APF) can be used for the reduction of noise. Practical dc

SQUIDs will operate with thermal noise, and can be exposed to significant environmental noise when used in the unshielded configuration. Only by using simulations can a prediction be made on how well the FLL would work in such an environment.

In Chapter 9 the electronics used to interface with the SQUID are designed and tested. Testing basic Josephson junctions proved to be relatively simple, but equipment malfunction caused damage to some of the devices. The overdamped junctions behaved as predicted, exhibiting the characteristic voltage-current curve. Even Shapiro steps were produced when a high frequency signal was applied to the junction.

The testing of the locally manufactured directly-coupled dc SQUID and the Mr. SQUID magnetometer were unsuccessful. The manufactured SQUID expired due to equipment malfunction before an exhaustive set of tests could be performed, and no other manufactured device proved viable. Initial tests on the Mr. SQUID magnetometer were discouraging as the resistance at room temperature was far lower than expected. The characteristic voltage-current curve expected of a magnetometer did not show up, and the device behaved strangely when no current was applied to the device.

Chapter 10 summarizes the most important results and includes a brief discussion with each result.

This thesis aims to provide an in-depth analysis for the design and operation of dc SQUIDs and a SQUID microscope. The techniques used to interface and control a dc SQUID magnetometer can easily be adapted for accurate testing of general superconductors. Theoretical models and simulations of Josephson junctions and dc SQUIDs looked promising for the design of practical electronics. Actual testing of basic Josephson junctions was successful, but the dc SQUIDs did not behave as predicted and a full systems test was unsuccessful. This thesis will hopefully help simplify future research into SQUID microscopes and electronics at the University of Stellenbosch.

Appendices

Appendix A

Tables

A.1 STAR Cryoelectronics Magnetometer Specifications

A.2 Material Properties

Parameter	M2700	M1000
Pickup Loop Outer Dimensions [mm]	2.7×2.7	9.3×8.5
Feedback Coupling Current Lock [μA/Φ_0]	45	7
Field Sensitivity $B\Phi$ [nT/Φ_0]	25	10
Field Noise $S_B^{1/2}$, f>10 Hz [fT/Hz$^{1/2}$]	<300	<100

Table A.1: HTS Magnetometer Specifications [4]

Parameter	M050	M200	M600	M800
Pickup Loop Outer Dimensions [mm]	0.55	1.8×2.35	5.75	7.75
Screened SQUID Inductance. L_{dc} [pH]	87	63	103	103
Feedback Coupling Current Lock [μA/Φ_0]	7	3	50	50
Field Sensitivity $B\Phi$ [nT/Φ_0]	43	7	1.2	0.83
Field Noise $S_B^{1/2}$, f>10 Hz [fT/Hz$^{1/2}$]	130	21	4	2.5
Energy Resolution ϵ_c [$\times 10^{31}$ J/Hz]	0.5	1.1	1	1.6

Table A.2: LTS Magnetometer Specifications [4]

Parameter	Value		
Pickup Loop Size [mm]	9.3×8.5 Outer Dimension 3.8×3.0 Inner Dimension		
Feedback Coil Inductance L_f [μH]	36 (wire-wound copper coil)		
Operating Temperature [K]	76 to 78 (77 typical)		
	Minimum	Typical	Maximum
SQUID Critical Current $2I_c$ [μA]	10	20	100
SQUID Resistance $R/2$ [Ω]	1	5	10
Feedback Mutual Inductance $1/M_f$ [μA/Φ_0]	4	7	10
Voltage Swing ΔV [μV]	20	30	-
Field Calibration [nT/Φ_0]	7	10	13
Field Noise $S_B^{1/2}(f)$, f>10 Hz [fT/Hz$^{1/2}$]	-	-	100
Temperature Coefficient at 77K [nT/K]	-	1	-
Heater Power (Ω at 77K) [W]	-	-	2
Heat Time to Normalize [s]	-	-	5
Storage Temperature (dry) [°C]	0	20	40

Table A.3: M1000 HTS Magnetometer Specifications [5]

Parameter	Value		
Pickup Loop Size [mm]	2.7×2.7 Outer Dimension 0.9×0.9 Inner Dimension		
Feedback Coil Inductance L_f [nH]	1.5 (integral thin-film coil)		
Operating Temperature [K]	76 to 78 (77 typical)		
	Minimum	Typical	Maximum
SQUID Critical Current $2I_c$ [μA]	10	20	100
SQUID Resistance $R/2$ [Ω]	1	5	10
Feedback Mutual Inductance $1/M_f$ [μA/Φ_0]	40	45	50
Voltage Swing ΔV [μV]	20	30	-
Field Calibration [nT/Φ_0]	20	25	30
Field Noise $S_B^{1/2}(f)$, f>10 Hz [fT/Hz$^{1/2}$]	-	-	300
Temperature Coefficient at 77K [nT/K]	-	2.5	-
Heater Power (Ω at 77K) [W]	-	-	2
Heat Time to Normalize [s]	-	-	5
Storage Temperature (dry) [°C]	0	20	40

Table A.4: M2700 HTS Magnetometer Specifications [5]

Material	T [K]	Thermal Expansion Coefficient [$\times 10^6$/K]	Thermal Conductivity [W/(m·K)]	Specific Heat [J/(K·kg]	Dielectric Constant	Electric Resistivity [Ω·m]	Young's Modulus [GPa]
Aluminium	293 80	24	237 415	913 340		$26.50\text{x}10^{-9}$ $2.52\text{x}10^{-9}$	70 77
Copper	293 80	17	401 571	385 200		$16.78\text{x}10^{-9}$ $2.16\text{x}10^{-9}$	130 140
Diamond	293	1	895	525		10^{10}-10^{12}	1166
Fiberglass	293 80	10.3	0.035	1400			38 41
Glass, Ordinary	293	9	1.1-1.2	670	5-10		71
Iron	293	12	80.2	106		$100\text{x}10^{-9}$	206
Mylar	293		0.0001				
Neoprene	293		0.15-0.45				
Polystyrene Foam	293	70	0.03-0.05	1300	2.55		3.1
Polyurethane Foam	293		0.02-0.03				
Pyrex	293 80	4		732 220			63
Quartz, Fused	293	0.59	1.46	670	3.8	10^{16}	72-74
Sapphire	293 91	5.8	46.06 800	761 105	9.39	10^{14}	345
Silicon	293	3					
Stainless Steel	293 80	17.3	14 8	378 179		$724.7\text{x}10^{-9}$ $552.5\text{x}10^{-9}$	194 208
Steel	293	13	45-65	420		$150\text{x}10^{-9}$	210
Silica Aerogel	293		0.026				
Vacuum			0				

Table A.5: Properties of Materials

Appendix B

WRSpice Simulations Files

B.1 Noise Source Code

```
* * * * Noise For A Bandwidth Of 500GHz, 500MHz, 1MHz
.tran 1ps 100ns 0ns 500fs UIC

* * * Noise
* CurrentName PosNode NegNode gauss(sqrt(4*boltz*Temp*Bw/(Rn)),0,SampleTime,1)
* Current Passes Through A 1 Ohm Resistive Load, T=77K *500GHz 1p Sample
I1 1 0 gauss(sqrt(4*boltz*77*500e+9/10),0,1p,1)
Rn1 1 0 1

*500MHz 1p SampleTime
I2 2 0 gauss(sqrt(4*boltz*77*500e+6/10),0,1p,1)
Rn2 2 0 1

*1 MHz 1p SampleTime
I3 3 0 gauss(sqrt(4*boltz*77*1e+6/10),0,1p,1)
Rn3 3 0 1

.save all
```

B.2 Josephson Junctions Simulation Source Code

```
* * * * Josephson Junction RCSJ Model * * * *
* Ic = 10 uA Critical Current
* Rn = 10 Ohm Normal Shunt Resistance
* T = 77 K(elvin) Operating Temperature
* * * *

* * * Simulation Time Parameters
* 10ns Sample Time, 10us Run Time, 0ns Start Time, 500fs Step Time, Use Initial Conditions (UIC)
.tran 10ns 10us 0ns 500fs UIC

* * * Josephson Junction
* * Superconducting Channel
```

```
F0 1 0 function(sin(i(L0))*10e-6)
E0 2 0 1 0 1
L0 2 0 3.291061e-16
* * Normal Shunt Resistance And Capacitive Channel
R0 1 0 10
C0 1 0 3.291061e-9
* Remove The Capacitance By Adding "*" For An RSJ Model
* * Noise
* 500MHz Bandwidth, 1p Sample Rate
I1 1 0 gauss(sqrt(4*boltz*77*1e+6/10),0,1p,1)

* * * Input Signal
* V0 Used For Current Measurements And To Display Figures
V0 3 1 0
* For A Current Source Swinging -3Ic To 3Ic Use The Following Line
I0 0 3 pwl 0ns 0 2.5us 30u 7.5us -30u 10us 0u
* For A Constant Current Source xIc Use The Following Line
I0 0 3 pwl 0ns 0 2.5us 30u 7.5us -30u 10us 0u

* * * 500MHz Filter Removes The Josephson Noise
C1 5 0 1e-9
E1 4 0 3 0 1
R1 4 5 0.31831

* Save All Points
.save all
```

B.3 DC SQUID Source Code

```
* * * * SQUID Simulation
* Ic = 10 uA Critical Current
* Rn = 10 Ohm Normal Shunt Resistance
* T = 77 K(elvin) Operating Temperature
* * * *

* * * Simulation Time Parameters
* 0.01ns Sample Time, 120us Run Time, 20ns Start Time, 500fs Step Time, Use Initial Conditions (UIC)
.tran 0.01ns 120ns 20ns 500fs UIC

* * * Josephson Junction 1
* Rn=10 Ic=10u
E0 2 0 1 0 1
L0 2 0 3.291061e-16
F0 1 0 function(sin(i(L0))*10e-6)
R0 1 0 10

* * * Josephson Junction 2
```

```
* Rn=10 Ic=10u
E1 4 0 3 0 1
L1 4 0 3.291061e-16
F1 3 0 function(sin(i(L1))*10e-6)
R1 3 0 10

* * * SQUID Induction Loop
* Lsq = 103.4 pH, For Lsq = Phi0 / (2 Ic) * Lsq = 65.82 pH, For Lsq = Phi0 / (pi Ic) * Separate Into Two Distinct Inductors
L2 3 5 51.7p
L3 5 1 51.7p

* * * SQUID Biasing
* * For A Constant Bias Current Use Following Line
I0 0 6 34u
* * For A Varying Bias Current Use Following Line
I0 0 6 pwl 0us 0 0.5us 0 0.75us 40u 1.25us -40u 1.5us 0 2us 0 2.25us 40u 2.75us -40u 3us 0
* V0 Used For Current Measurements And To Display Figures
V0 6 5 0

* * * External Flux Source
* L1 Is The Feedback Coil Set At 80 pH; k Is The Coupling Factor; m Is The Mutual Inductance
* m=k * sqrt(L1 * L2); 1/M = phi0/A
* For Lsq = Phi0 / (2 Ic): 22.7798uA = One Fluxon
* For Lsq = Phi0 / (2 Ic): 28.49652uA = One Fluxon
* small signal Is When 22.79/4pi
L4 7 8 40p
L5 8 0 40p
K1 L5 L2 1
K2 L4 L3 1
* * For A Linear Varying External Flux Use Following Line
Is1 0 7 pwl 0us 0 0.5us 0 0.75us 40u 1.25us -40u 1.5us 0 2us 0 2.25us 40u 2.75us -40u 3us 0
* * For A Sinusoidally Varying External Flux Use Following Line
Is1 0 7 1.812759u * sin(6.283 * (pwl 20ns 0 120n 4))
* * For An Additional Bias Flux Of Phi0/4 Use Following Line
Is2 0 7 5.69495u

* * * Noise
* 500MHz Bandwidth, 1p Sample Rate
In1 1 0 gauss(sqrt(4*boltz*77*500e+6/10),0,1p,1)
In2 3 0 gauss(sqrt(4*boltz*77*500e+6/10),0,1p,1)

* * * 500MHz Filter Removes The Josephson Noise
Ef 9 0 8 0 1
Cf 10 0 1e-9
Rf 0 10 0.31831

* Save All Points
.save all
```

B.4 DC SQUID APF Code

```
* * * APF
* Mapf = (Bapf * Lsq * Rapf / Rn) + 2 * Lsq
* Lapf = (Mapf / k)^2 / Lsq
* k=1; Bapf=0.9; Rn=1000
Rapf 5 20 1000
L6 20 21 435.896n
L7 21 0 435.896n
K3 L6 L2 1
K4 L7 L3 1
```

B.5 DC SQUID FLL Code

```
* * * 80MHz FLL integrator
Vb 5 29 154.15u
Efll1 30 0 29 0 500
Rint 30 31 100
Cint 31 32 20p
Eint 32 0 31 0 1E40
Lf1 33 34 18u
Lf2 34 0 18u
Rf 32 33 294.47E3
Kf1 Lf1 L2 1
Kf2 Lf2 L3 1
```

Appendix C

Simulink Simulations Layouts

C.1 SQUID FLL Linear Response Schematic

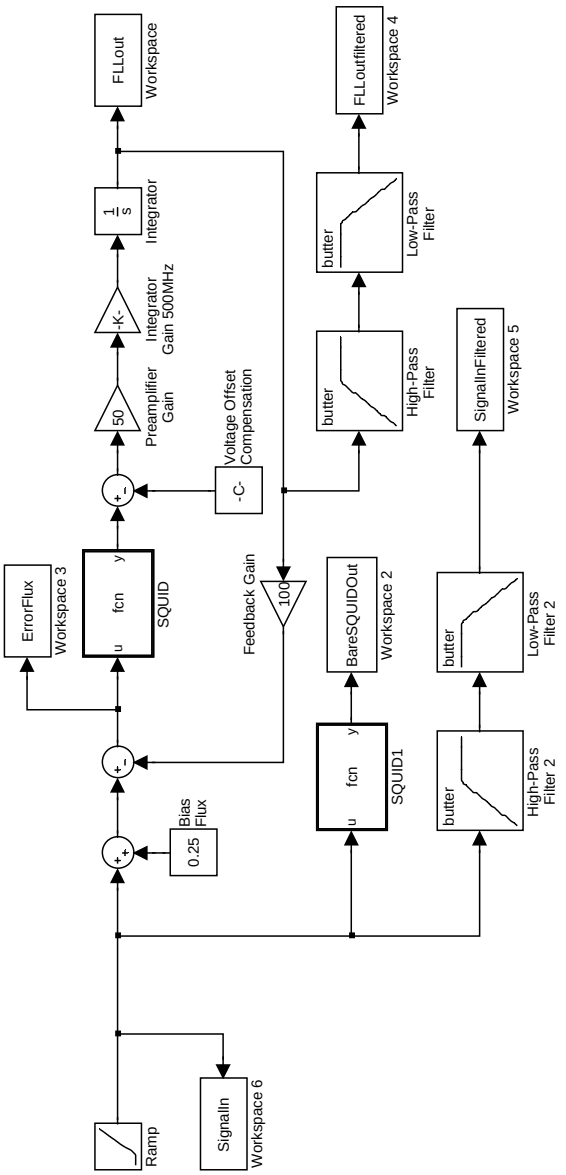

Figure C.1: Simulink Simulation Schematic: The dc SQUID FLL with a linear input.

C.2 SQUID FLL Linear Response Schematic

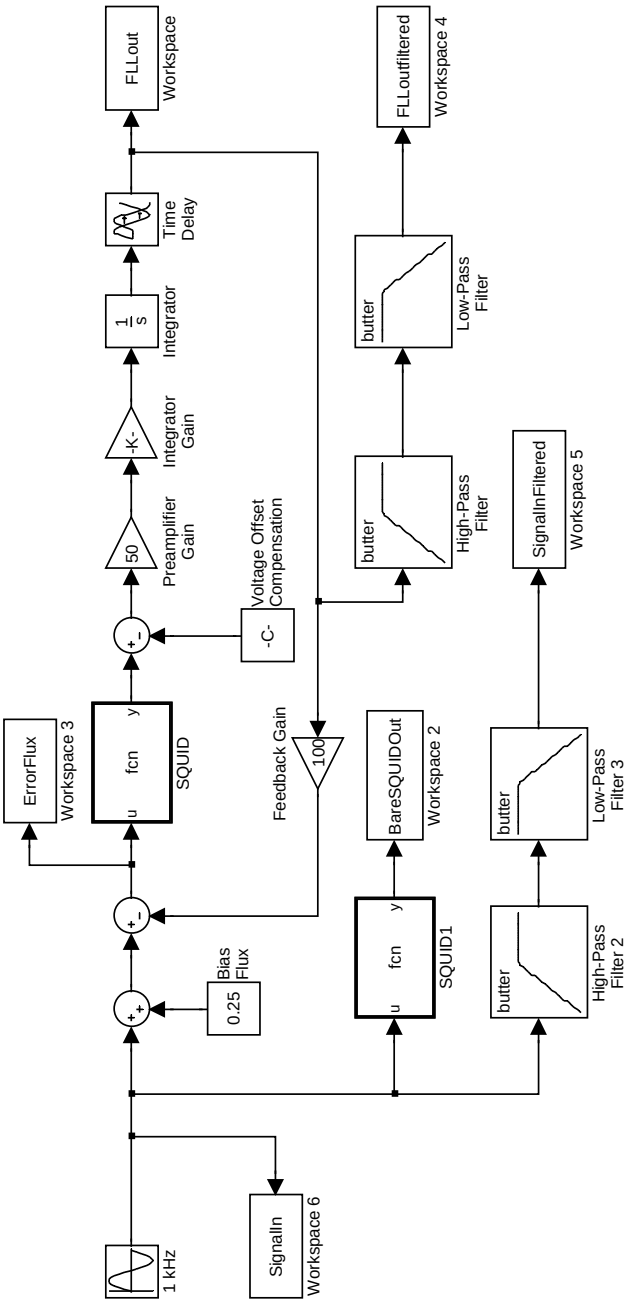

Figure C.2: Simulink Simulation Schematic: The dc SQUID FLL with a single input.

C.3 SQUID FLL Linear Response Schematic

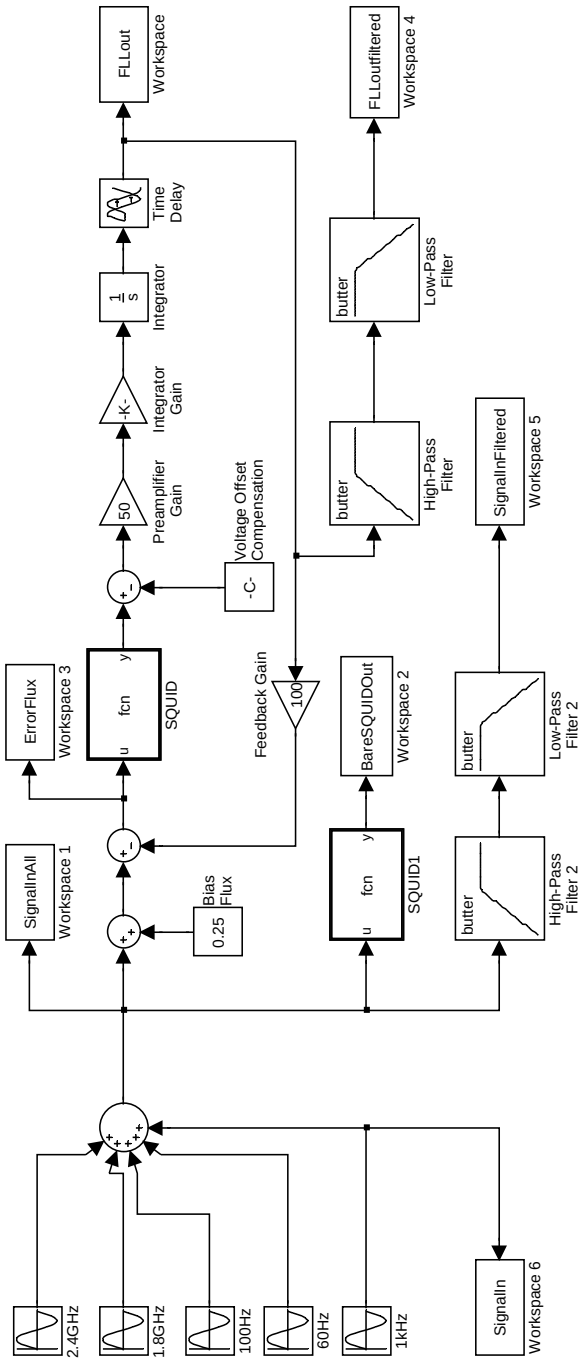

Figure C.3: Simulink Simulation Schematic: The dc SQUID FLL with multiple inputs.

Appendix D

Schematics

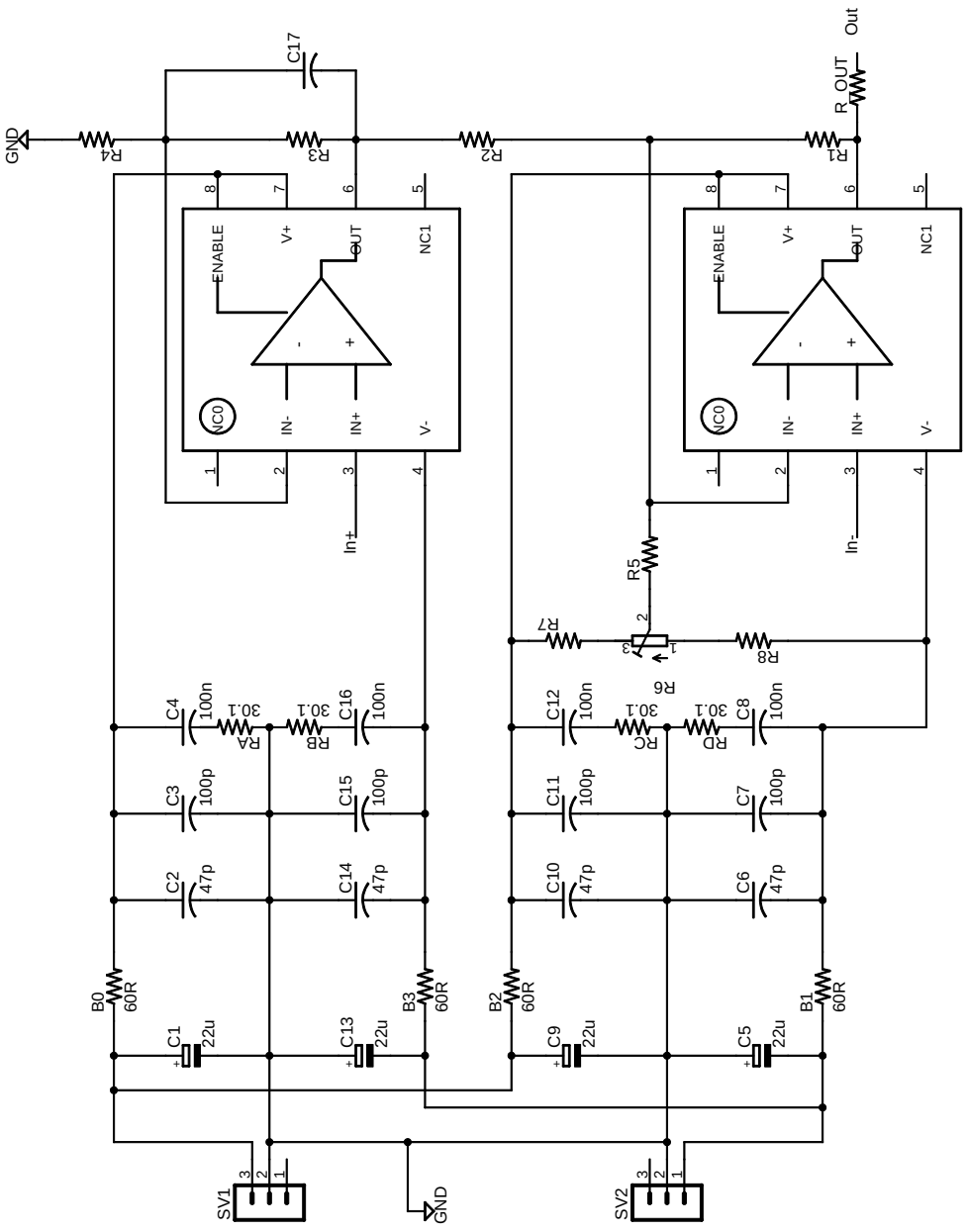

Figure D.1: Schematic of the high-impedance instrumentation amplifier.

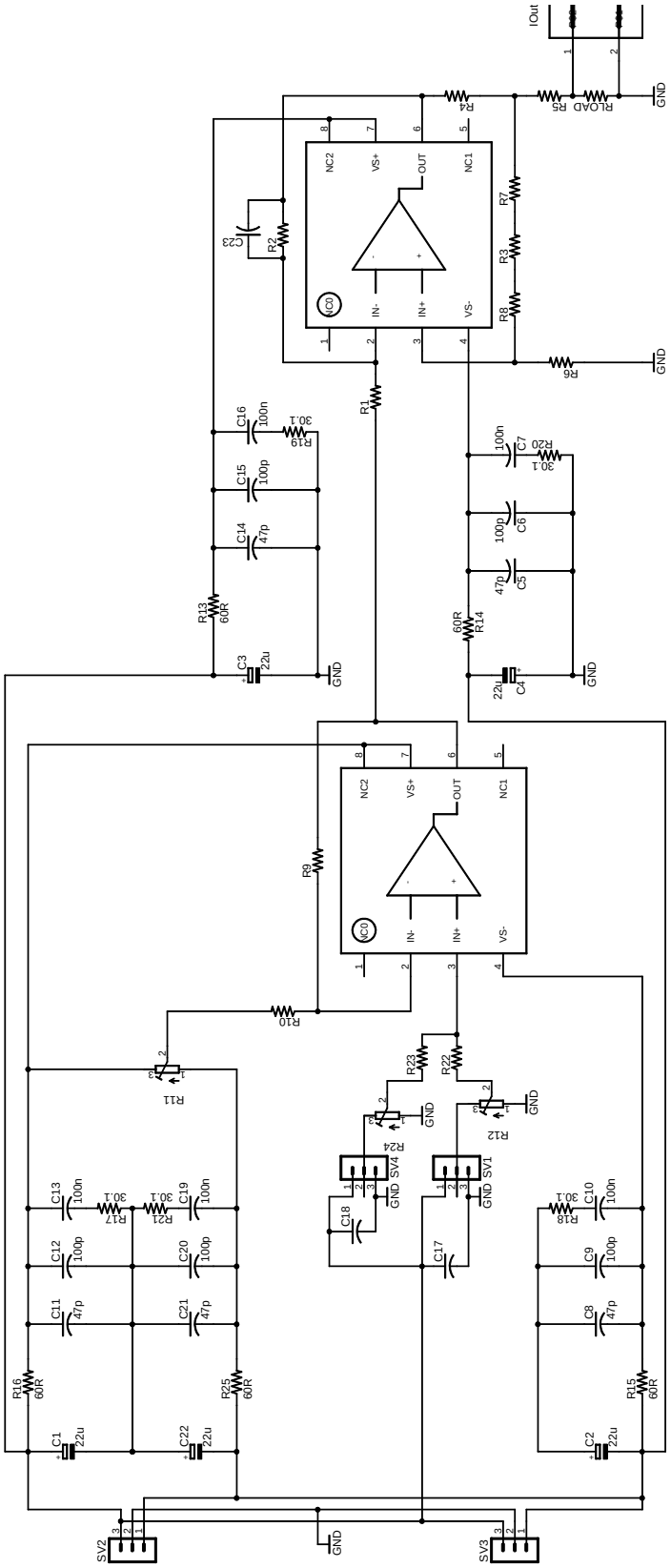

Figure D.2: Schematic of a 2-channel voltage-controlled current-source.

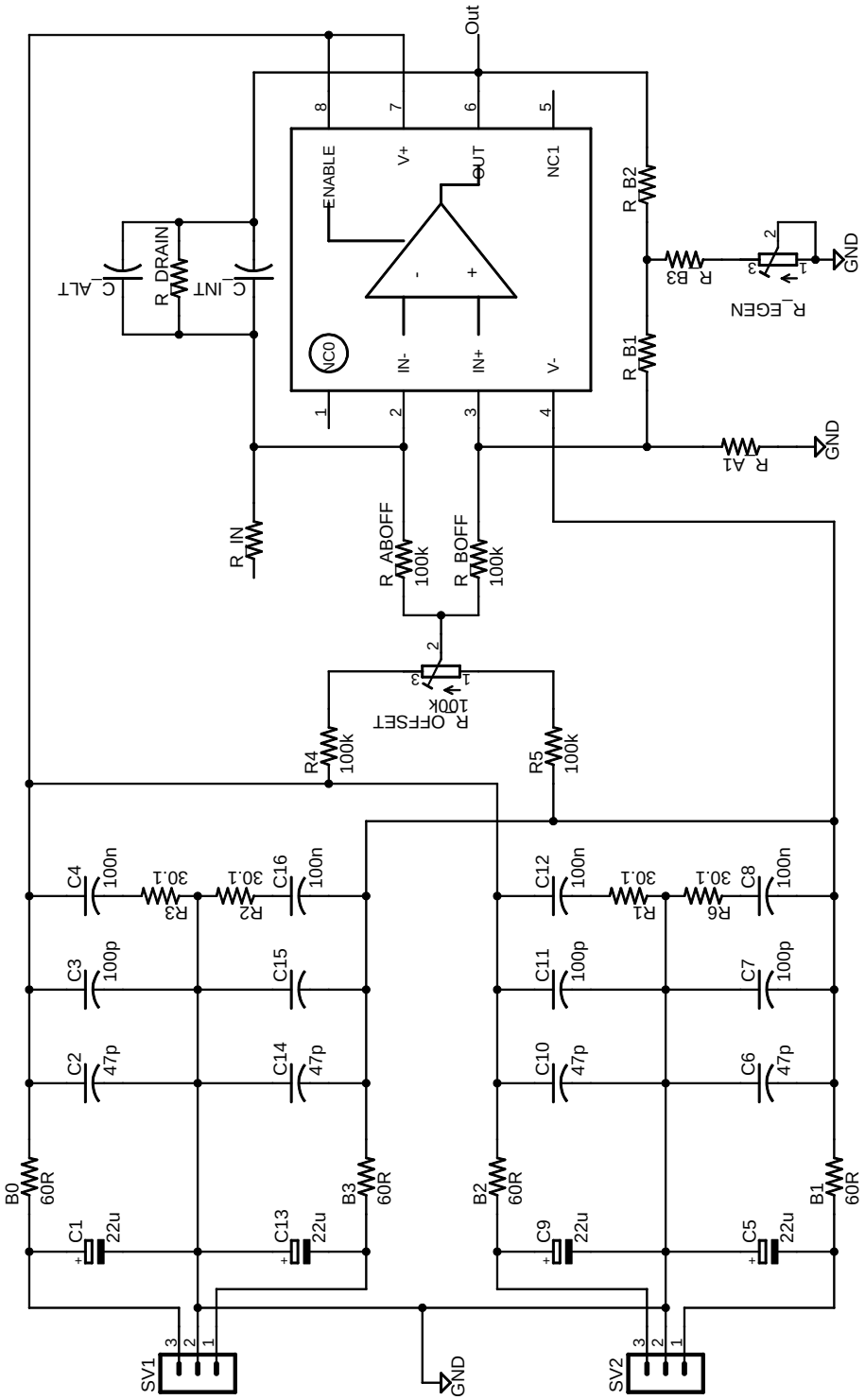

Figure D.3: Schematic of both the integrator and the inverting amplifier.

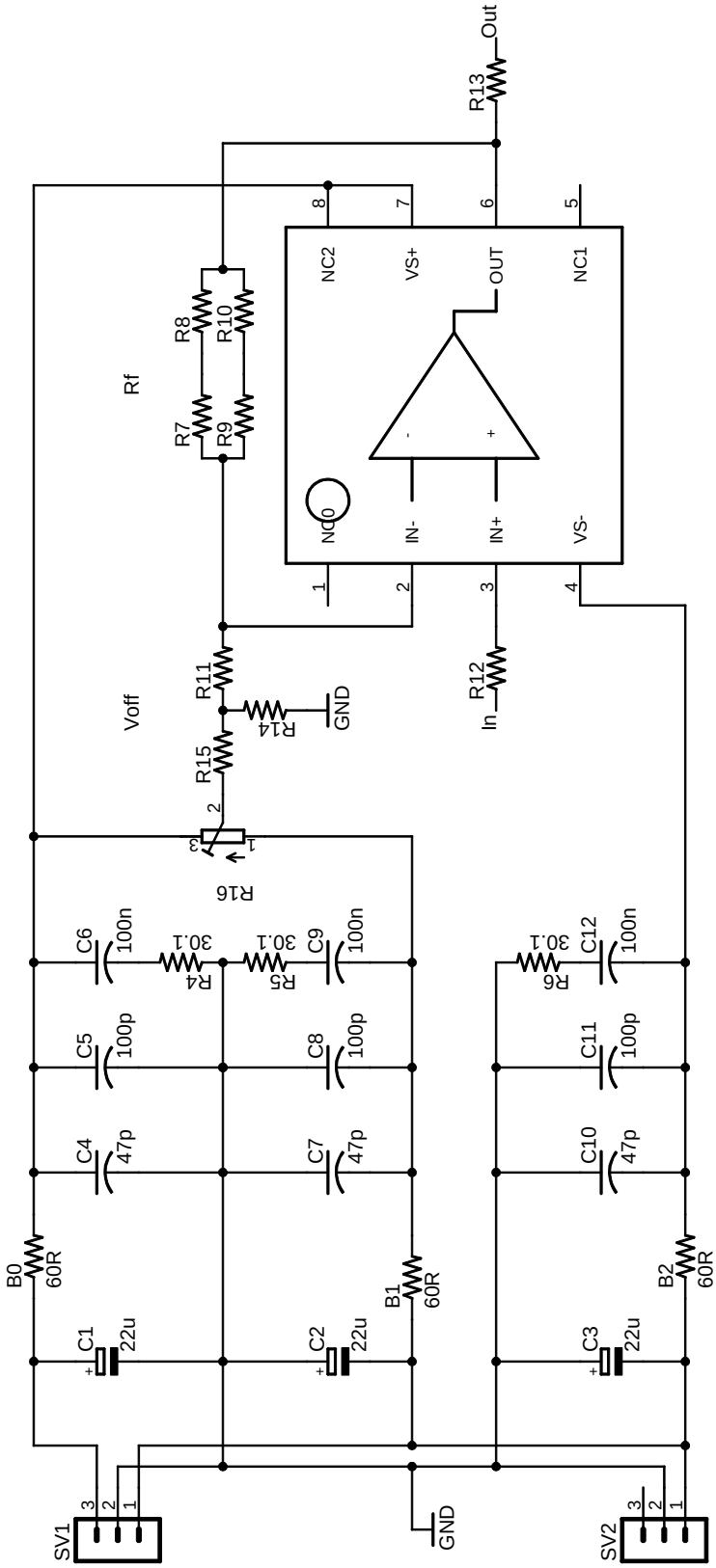

Figure D.4: Schematic of the non-inverting amplifier.

Appendix E

Measurements

E.1 Measurement Electronics Circuit Boards

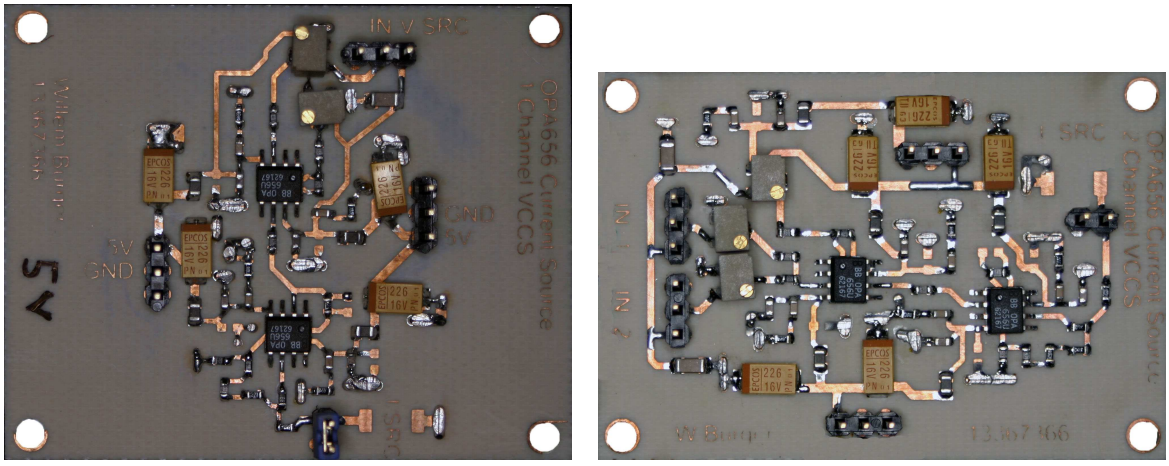

(a) (b)

Figure E.1: Populated circuit board of a voltage-controlled current-source with (a) a 1-channel and (b) a 2-channel input.

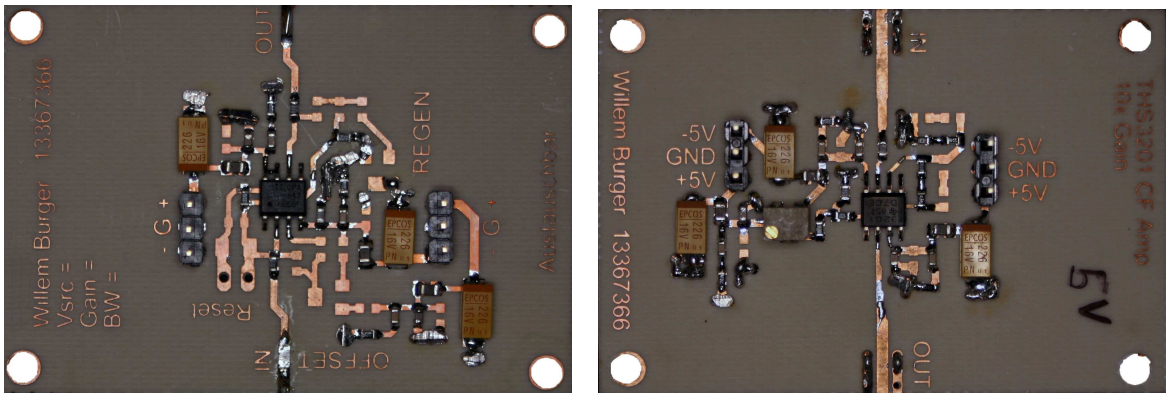

(a) (b)

Figure E.2: Populated circuit board of (a) an inverting voltage-feedback amplifier and (b) an inverting current-feedback amplifier.

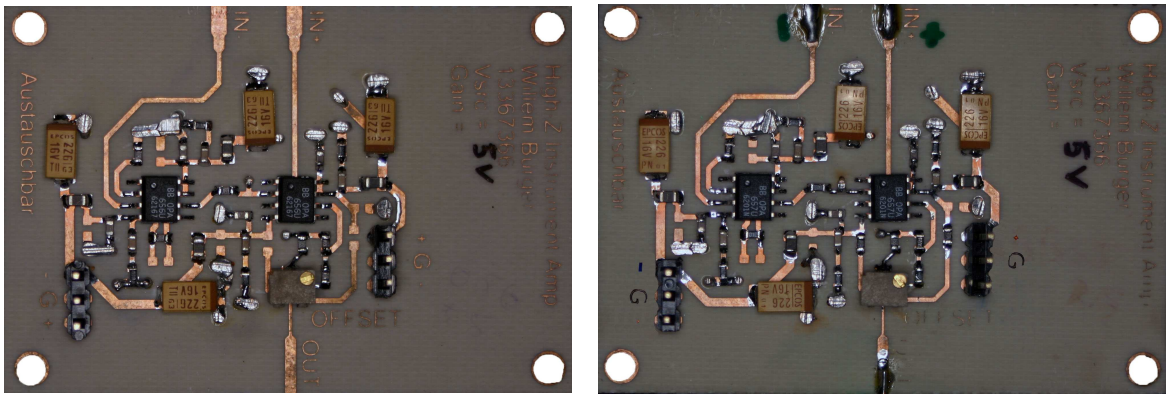

(a) (b)

Figure E.3: Populated circuit board of a high-impedance instrumentation amplifier using (a) the OPA656 operational amplifier and (b) the OPA657 operational amplifier.

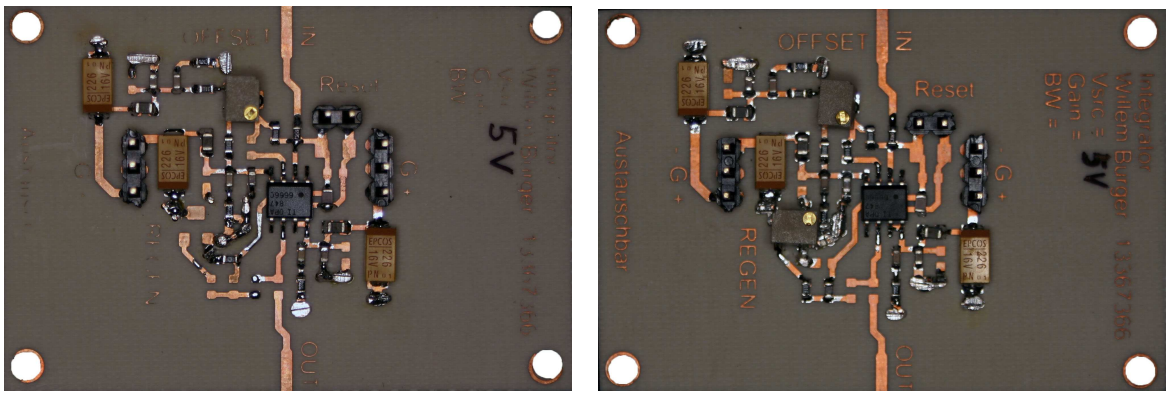

(a) (b)

Figure E.4: Populated circuit board of the integrator (a) without offset compensation and (b) with offset compensation.

E.2 Josephson Junction Samples

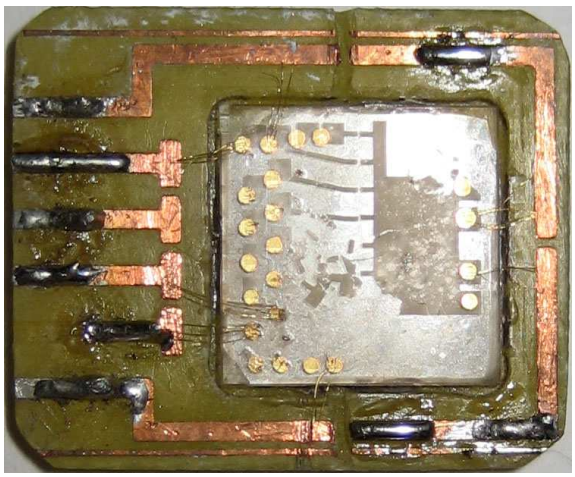

Figure E.5: Josephson junctions mounted onto a sample holder with the wire-bonding visible. The YBCO film has become semitransparent and partially dislodged due to environmental damage.

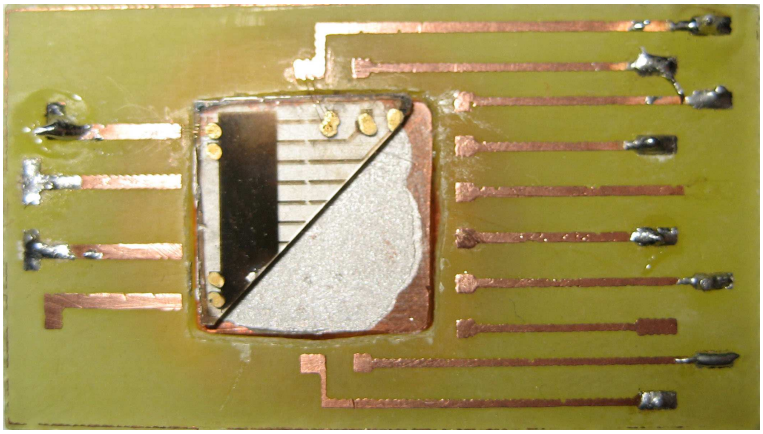

Figure E.6: Josephson junctions mounted onto a sample holder. The YBCO film is visible as a dark patch with lines crossing the substrate. The copper thermal capacitor is shown. The junctions are formed at the constrictions points in the lines.

E.3 Mr SQUID Sensor

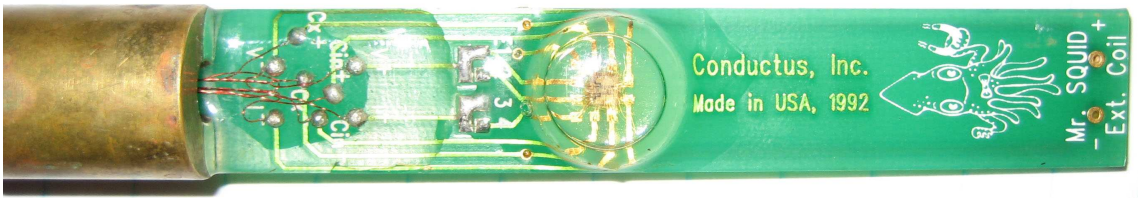

(a)

(b)

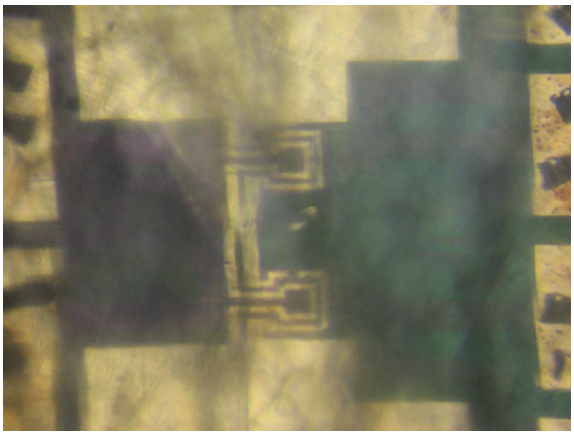

(c)

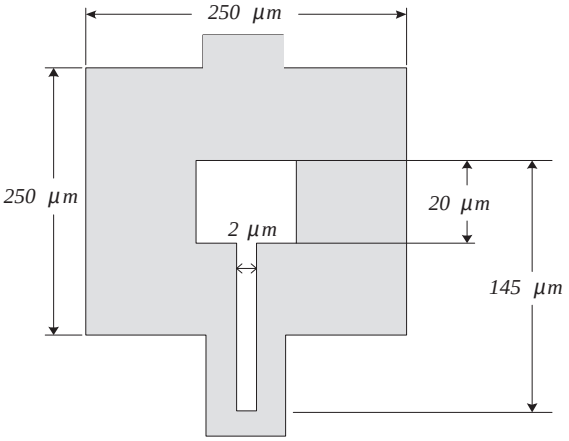

(d)

Figure E.7: Mr SQUID magnetometer. (a) The complete unit mounted on a printed circuit board. (b) The mu-metal shield used to attenuate magnetic fields and noise. (c) The large-area washer dc SQUID enlarged, with the feedback coils clearly visible. (d) The dimensions of the large-area washer dc SQUID.

E.4 Cryogenic Equipment

Figure E.8: Cryostat used to contain the liquid nitrogen coolant.

Figure E.8 shows the cryostat used to cool the Mr. SQUID sensor.

Figure E.9 shows the main compressor of the Gifford-McMahon (GM) cryocooler. The cold section is shown in Figure E.10, with the displacer motor visible in Figure E.10(a) for the fully assembled cold section. With the cold section opened in Figure E.10(b), the various transmission wires used to interface with the electronics can be seen. A typical sample holder is connected to the head of the cold section in Figure E.10(c). The vacuum pump in Figure E.11(a) is used to maintain a vacuum inside the assembled cold section, thereby thermally insulating the cold section from the environment. The cryostat measurement system shown in Figure E.11(b) can be used to both measure the temperature of the the head of the cold section, and to increase the temperature of the cold section by using a built-in electric heater.

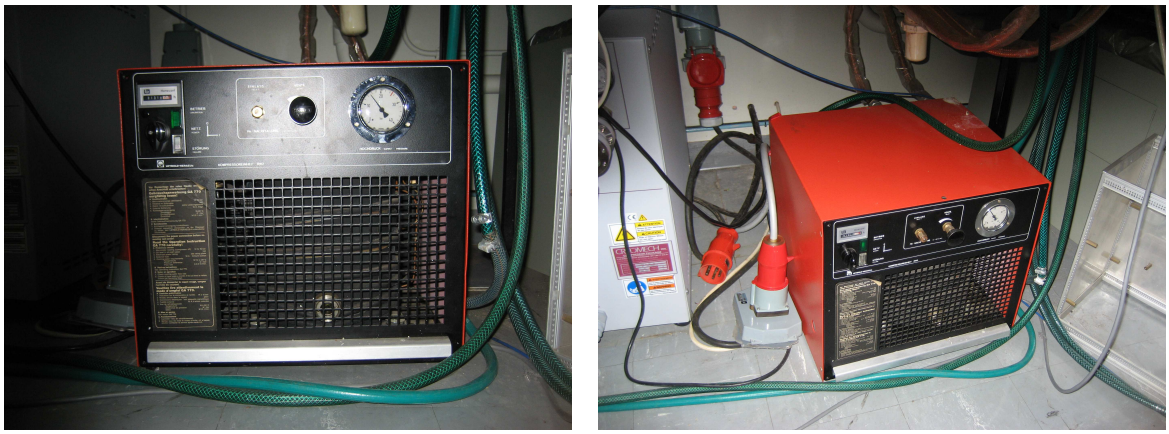

(a) (b)

Figure E.9: Compressor for the Gifford-McMahon Cryocooler.

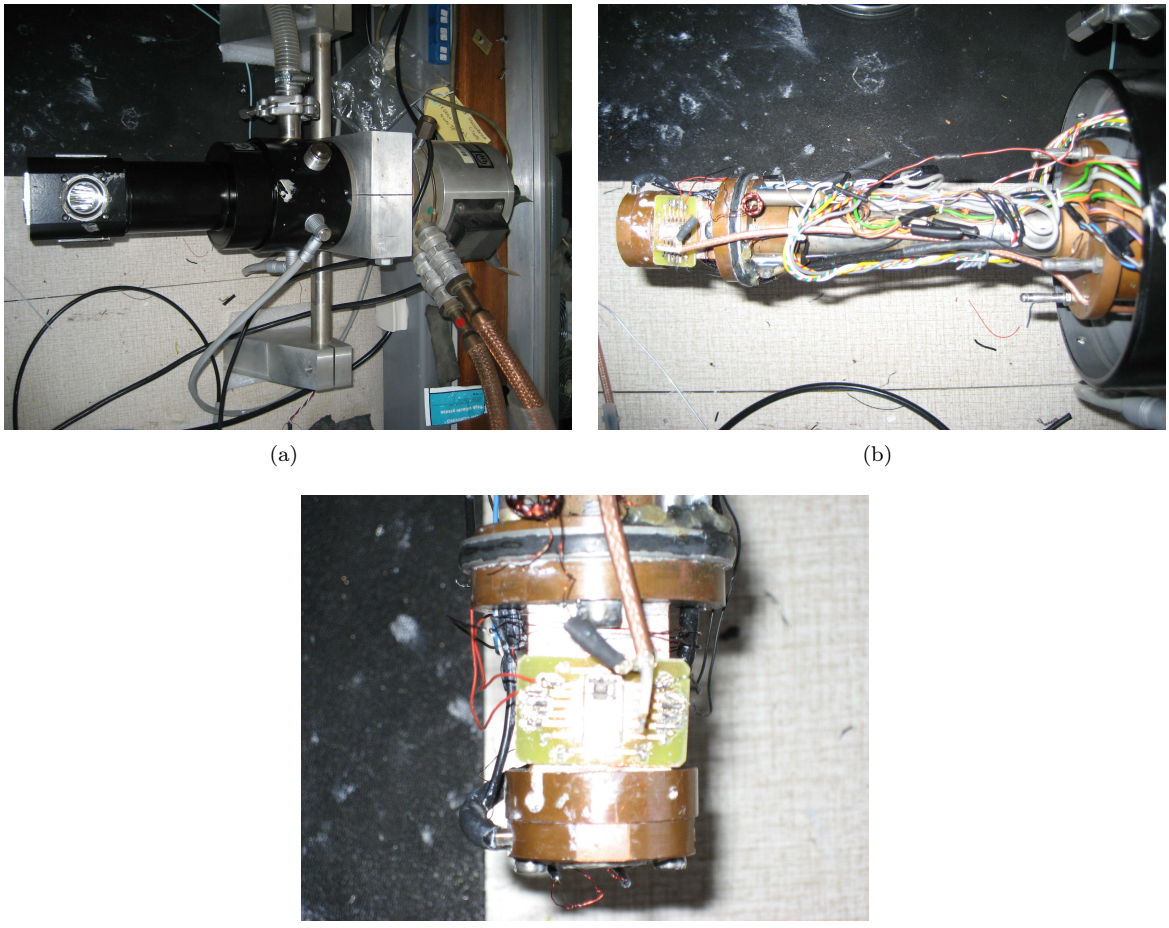

(a) (b)

(c)

Figure E.10: Cold section of the Gifford-McMahon Cryocooler. (a) The closed unit with the displacer visible at the back. (b) The inside of the cold section with various transmission wires visible. (c) The head of the cold section with a sample holder mounted.

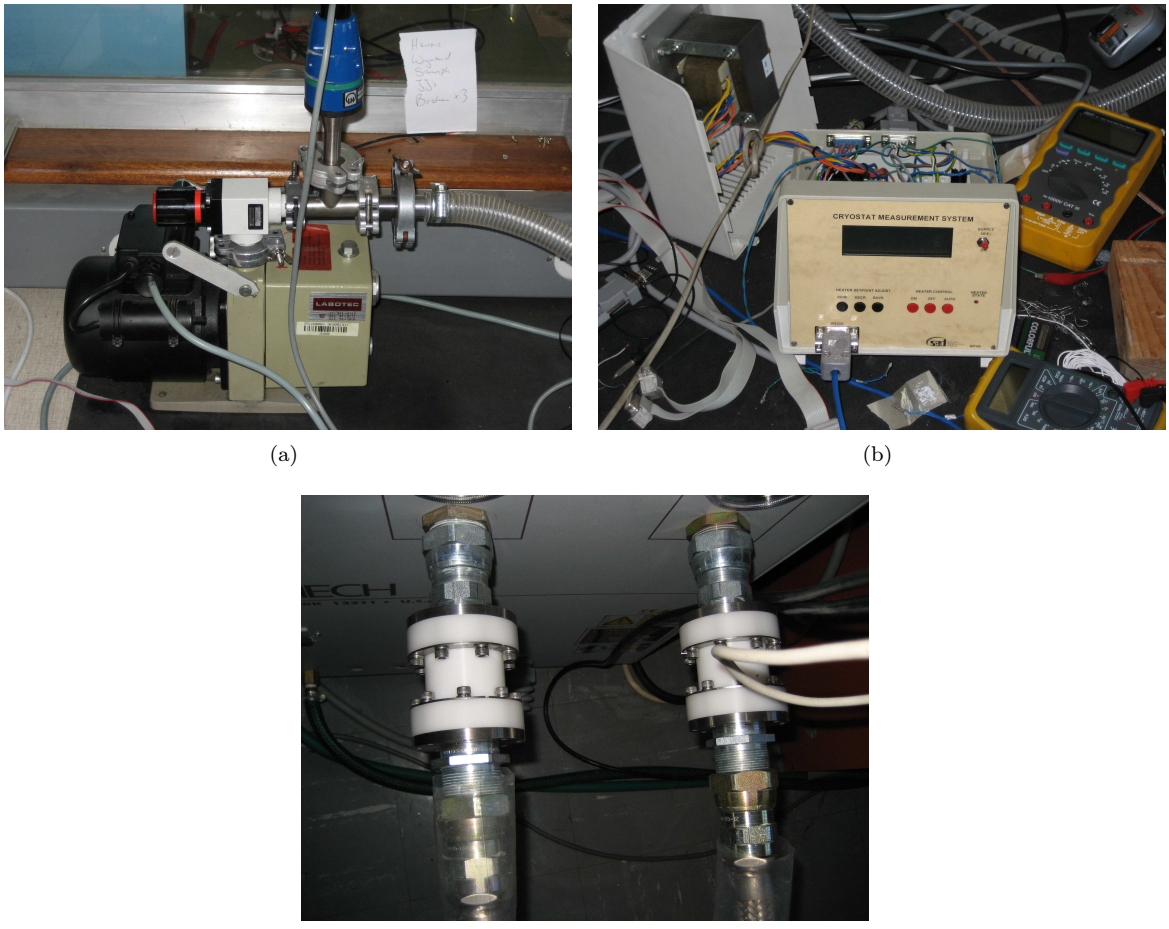

(a) (b)

(c)

Figure E.11: Equipment used to control the Gifford-McMahon Cryocooler including (a) the vacuum pump to thermally insulate the cold section, and (b) the cryostat measurement system to measure and control the temperature. (c) An example of the isolation plugs that can be used to remove the grounding loop to the compressor and reduce noise.

List of References

[1] Neeraj Khare, *Handbook of High-Temperature Superconductor Electronics*, Marcel Dekker, Inc., 2003. (Cited on pages ix, 9, 12, 32, 34, 35, 36, 37, 39, 40, 42, 43, 46, 48, 49, 50, 52, 53, 54, 62, 63, 64, 65, 66, 72, 73, and 85.)

[2] Texas Instruments Incorporated, Post Office Box 655303, Dallas, Texas 75265, *1.8-GHz, Low Distrotion, Current Feedback Amplifier*, 2007. (Cited on pages xi, 119, and 120.)

[3] Conductus Inc. / STAR Cryoelectronics, 25-A Brisbane Court, Santa Fe, NM 87508, *Mr. SQUID User's Guide*, April 1992. (Cited on pages xiii and 127.)

[4] STAR Cryoelectronics, 25-A Brisbane Court, Santa Fe, NM 87508, *SQUID Sensors*, September 2004. (Cited on pages xiii, 95, and 139.)

[5] STAR Cryoelectronics, 25-A Brisbane Court, Santa Fe, NM 87508, *HTS Magnetometer M2700*, April 2002. (Cited on pages xiii, 140, and 141.)

[6] Jeremy Webb, "Safer and cheaper MRI scanners," *Scientific American*, p. 27, November 2007. (Cited on page 1.)

[7] The Nobel Foundation, *Nobel Lectures*, Physics 1901-1921, Elsevier Publishing Company, Amsterdam, 1967. (Cited on page 2.)

[8] J. D. van der Waals, *On the Continuity of the Gaseous and Liquid States*, Dover Publications, 1988. (Cited on page 2.)

[9] Heike Kamerlingh Onnes, "On the cryogenic laboratory at leyden and on the production of very low temperature," *Comm. Leiden*, vol. 120b, 1894. (Cited on page 2.)

[10] Heike Kamerlingh Onnes, "The resistance of pure mercury at helium temperatures," *Comm. Leiden*, vol. 120b, 28 April 1911. (Cited on page 2.)

[11] Heike Kamerlingh Onnes, "The disappearance of the resistivity of mercury," *Comm. Leiden*, vol. 122b, 27 May 1911. (Cited on page 2.)

[12] J. Bardeen, L. N. Cooper, and J. R. Schrieffer, "Theory of superconductivity," *Phys. Rev.*, vol. 108, 1957. (Cited on pages 2 and 9.)

[13] Terry P. Orlando and Kevin A. Delin, *Foundations of Applied Superconductivity*, Addison-Wesley Publishing Company, 1982. (Cited on pages 3, 4, 7, 9, 22, 23, 24, 28, 29, 32, 35, and 50.)

[14] G. Ghigo, A. Chiodoni, R. Gerbaldo, L. Gozzelino, B. Minetti, E. Mezzetti cnd C. Camerlingo, C. Giannini, L. Tapfer, and S. Martelli, "Correlation between structure and magnetic transport mechanism in YBCO films," *International Journal of Modern Physics B*, vol. 14, no. 25–27, pp. 2773–2778, 2000. (Cited on pages 9 and 24.)

[15] Roger Penrose, *The Road to Reality*, Jonathan Cape, London, 2004. (Cited on page 10.)

[16] V. Foglietti, W. J. Gallagher, M. B. Ketchen, A. W. Kleinsasser, and R. H. Koch, "Performance of a dc SQUID with resistively shunted inductance," *Appl. Phys. Lett.*, vol. 55, no. 14, October 1989. (Cited on pages 17, 34, and 50.)

[17] P. A. Nisson, Z. G. Ivanov, H. K. Olsson, T. Claeson, E. A. Stepantsov, and A. Ya. Tzalenchuk, "Bicrystal junctions and superconducting quantum interference devices in $YBa_2Cu_3O_7$ thin films," *Journal of Applied Physics*, vol. 75, no. 12, June 1994. (Cited on pages 23, 24, and 44.)

[18] F. W. Graser, "A reproducible design and manufacturing process for SQUID magnetometers," M.S. thesis, Department of Electrical and Electronic Engineering, University of Stellenbosch, 2005. (Cited on pages 31, 37, 42, 124, 125, and 126.)

[19] John Clarke and Alex I. Braginski, Eds., *The SQUID Handbook*, vol. Vol. I Fundamentals and Technology of SQUIDs and SQUID systems, WILEY-VCH verlag GmbH and Co. KGaA, 2004. (Cited on pages 32, 35, 50, 51, 52, 53, 54, 69, 72, 73, 75, 77, 78, 79, 81, 82, 84, 85, 86, 87, 88, 91, and 95.)

[20] D. Drung, F. Ludwig, W. Mueller, U. Steinhoff, L. Trahms, H. Koch, Y. Q. Shen, M. B. Jensen, P. Vase, T. Host, T. Freltoft, and G. Curio, "Integrated $YBa_2Cu_3O_{7-x}$ magnetometer for biomagnetic measurements," *Appl. Phys. Lett.*, vol. 68, no. 10, March 1996. (Cited on pages 34, 86, 87, and 104.)

[21] J. Beyer, D. Drung, F. Ludwig, T. Minotani, and K. Enpuku, "Low-noise $YBa_2Cu_3O_{7-x}$ single layer dc superconducting quantum interference device (SQUID) magnetometer based on bicrystal junctions with $30_\circ$ misorientation angle," *Appl. Phys. Lett.*, vol. 72, no. 2, January 1995. (Cited on pages 34 and 40.)

[22] Direk Grundler, Bernd David, and Olaf Doessel, "Experimental investigation of the kinetic inductance in $YBa_2Cu_3O_7$ square washer superconducting quantum interference devices," *Journal of Applied Physics*, vol. 77, no. 10, May 1995. (Cited on page 36.)

[23] D. Koelle, A. H. Miklich, E. Dantsker, F. Ludwig, D. T. Nemeth, John Clarke, W. Ruby, and K. Char, "High performance dc squid magnetometers with single layer $YBa_2Cu_3O_{7-x}$ flux transformers," *Appl. Phys. Lett.*, vol. 63, no. 26, December 1993. (Cited on page 37.)

[24] D. Koelle, A. H. Miklich, F. Ludwig, E. Dantsker, D. T. Nemeth, and J. Clarke, "dc SQUID magnetometers from single layers of $YBa_2Cu_3O_{7-\delta}$," *Applied Physics Letters*, vol. 63, no. 16, pp. 2271–2273, October 1993. (Cited on page 38.)

[25] L. E. Fong, J. R. Holzer, K. K. McBride, E. A. Lima, F. Baudenbaucher, and M. Radparvar, "High-resolution room-temperature sample scanning superconducting quantum interference device microscope configurable for geological and biomagnetic applications," *Review of Scientific Instruments*, vol. 76, January 2005. (Cited on pages 38, 50, and 71.)

[26] R. C. Black, A. Mathai, F. C. Wellstood, E. Dantsker, A. H. Miklich, D. T. Nemeth, J. J. Kingston, and J. Clarke, "Magnetic microscopy using a liquid nitrogen cooled $YBa_2Cu_3O_7$ superconducting quantum interference device," *Appl. Phys. Lett.*, vol. 62, no. 17, April 1993. (Cited on pages 38 and 71.)

[27] D. Dimos, P. Chaudhari, and J. Mannhart, "Superconducting transport properties of grain boundaries in $YBa_2Cu_3O_7$ bicrystals," *Physical Review B*, vol. 41, no. 7, March 1990. (Cited on pages 40, 41, 43, 44, and 45.)

[28] Julia M. Phillips, "Substrate selection for high-temperature superconducting thin films," *Journal of Applied Physics*, vol. 79, no. 4, February 1996. (Cited on page 41.)

[29] Temel H. Büyüklimanli anf Joseph H. Simmons, "Surface degradation of $YBa_2Cu_3O_{7-x}$ superconductors on exposure to air and humidity," *Physical Review B*, vol. 44, no. 2, July 1991. (Cited on page 41.)

[30] H. S. Kwok, H. S. Kim, S. Witanachchi, E. Petrou, J. P. Zheng, S. Patel, E. Narumi, and D. T. Shaw, "Plasma-assisted laser deposition of $YBa_2Cu_3O_{7-x}$," *Applied Physics Letters*, vol. 59, no. 27, December 1991. (Cited on page 42.)

[31] Philippe V. Komissinski, Bjoern Hoegberg, Alexander Ya. Tzalenchuk, and Zdravko Ivanov, "Submicron $YBa_2Cu_3O_x$ ramp josephson junctions," *Applied Physics Letters*, 2001. (Cited on page 43.)

[32] B. H. Moeckly and K. Char, "Properties of interface-engineered high T_c josephson junctions," *Applied Physics Letters*, vol. 71, no. 17, October 1997. (Cited on page 43.)

[33] K. Char, M. S. Colclough, S. M. Garrison, N. Newman, and G. Zaharchuk, "Bi-epitaxial grain boundary junctions in $YBa_2Cu_3O_7$," *Applied Physics Letters*, vol. 59, no. 6, August 1991. (Cited on page 44.)

[34] R. Gross, P. Chaudhari, M. Kawasaki, and A. Gupta, "Scaling behaviour in electrical transport across grain boundaries in $YBa_2Cu_3O_{7-\delta}$ superconductors," *Physical Review B*, vol. 42, no. 16, December 1990. (Cited on page 46.)

[35] J. Luine, J. Bulman, J. Burch, K. Daly, A. Lee, C. Pettiette-Hall, S. Schwarzbek, and D. Miller, "Characteristics of high performance $YBa_2Cu_3O_7$ step-edge junctions," *Applied Physics Letters*, vol. 61, no. 9, August 1992. (Cited on page 46.)

[36] David M. Pozar, *Microwave engineering*, John Wiley & Sons Inc., 3 edition, 2005. (Cited on pages 49 and 50.)

[37] K. Enpuku, Y. Shimomure, and T. Kisu, "Effect of thermal noise on the characteristics of a high T_c superconducting quantum interference device," *Journal of Applied Physics*, vol. 73, no. 11, June 1993. (Cited on page 49.)

[38] R. Gross, P. Chaudhari, D. Dimos, A. Gupta, and G. Koren, "Thermally activated phase slippage in high-T_c grain-boundary josephson junctions," *Physical Review Letters*, vol. 64, no. 2, January 1990. (Cited on page 50.)

[39] Y. Huang, K. L. Merkle, L. P. Lee, M. Teepe, and K. Char, "Microstructural origin of $1/f$ noise in high T_c bicrystal squid magnetometers," *Appl. Phys. Lett.*, vol. 71, no. 25, December 1997. (Cited on pages 51, 53, and 54.)

[40] R. H. Koch, W. Eidelloth, B. Oh, R. P. Robertazzi, S. A. Andrek, and W. J. Gallagher, "Identifying the source of $1/f$ noise in SQUIDs made from high-temperature superconductors," *Appl. Phys. Lett.*, vol. 60, no. 4, January 1992. (Cited on pages 51, 53, 54, and 90.)

[41] F. Ludwig and D. Drung, "Low-frequency noise of improved direct-coupled high-T_c superconducting quantum interference device magnetometers in ac and dc magnetic fields," *Appl. Phys. Lett.*, vol. 75, no. 18, November 1999. (Cited on pages 53 and 54.)

[42] H Yamada, H Yamasaki, K Develos-Bagarinao, Y Nakagawa, YMawatari, J C Nie, H Obara, and S Kosaka, "Flux pinning centres correlated along the c-axis in PLD-YBCO films," *Supercond. Sci. Technol.*, vol. 17, pp. 58–64, 2004. (Cited on page 53.)

[43] A. H. Miklich, D. Koelle, T. J. Shaw, F. Ludwig, D. T. Nemeth, E. Dantsker, John Clarke, Neil McN. Alford, W. Button, and M. S. Colclough, "Low-frequency excess noise in $YBa_2Cu_3O_{7-x}$ dc superconducting quantum interference devices cooled in static magnetic fields," *Appl. Phys. Lett.*, vol. 64, no. 25, June 1994. (Cited on page 53.)

[44] K. Enpuku, D. Kuroda, D. Tokimizu, and T. Q. Yang, "Suppression of thermally activated flux entry through a flux dam in high T_c superconducting quantum interference device magnetometer," *Journal of Applied Physics*, vol. 92, no. 8, October 2002. (Cited on page 54.)

[45] A. Marx, U. Fath, L. Alff, and R. Gross, "Correlation of critical current and resistance fluctuations in bicrystal grain boundary josephson junctions," *Applied Physics Letters*, vol. 67, no. 13, September 1995. (Cited on page 54.)

[46] H. J. M. ter Brake, W. A. M. Aaenink, P. J. van den Bosch, J. W. M. Hilgenkamp, J. Flokstra, and H. Rogalla, "Temperature dependence of the effective sensing area of high-T_c dc squids," *Supercond. Sci. Technol.*, vol. 10, pp. 512–515, January 1997. (Cited on page 54.)

[47] Lei Zhouh, J. S. Kapat, L. C. Chow, and S. Y. Lei, "Design of a high performance cryocooler for propellant liquefaction and storage on mars," *2000 Proceedings of IMECE : International Mechanical Engineering Congress & Exposition*, 5 November 2000. (Cited on pages 58, 59, 62, 64, and 65.)

[48] Ray Radebaugh, "Pulse tube cryocoolers for cooling infrared sensors," *Proceedings of SPIE, The International Society for Optical Engineering, Infrared Technology and Applications XXVI*, vol. 4130, pp. 363–379, 2000. (Cited on pages 58, 62, 63, 64, 65, 66, and 67.)

[49] Philip Yam, "Into thin air," *Scientific American*, p. 8, October 2007. (Cited on page 60.)

[50] S. J. Nieczkoski and R. A. Mohling, "Development of a novel brayton-cycle cryocooler and key component technologies," Paper, Technology Applications, Inc., 2003. (Cited on page 63.)

[51] E. Kuffel, W. S. Zaengl, and J. Kuffel, *High Voltage Engineering: Fundamentals*, Newness, 2 edition, 2000. (Cited on page 69.)

[52] Gene F. Franklin, J. David Powell, and Abbas Emami-Naeini, *Feedback Control of Dynamic Systems*, Prentice Hall, 4 edition, 2002. (Cited on pages 76, 77, and 82.)

[53] Microchip Technology Inc., *dsPIC30F Family Reference Manual*, 2005. (Cited on page 81.)

[54] Donald A. Neaman, *Electronic Circuit Analysis and Design*, McGraw-Hill Higher Education, London, 2 edition, 2004. (Cited on pages 82 and 84.)

[55] Texas Instruments Incorporated, Post Office Box 655303, Dallas, Texas 75265, *Handbook of Operational Amplifier Applications*, 2001. (Cited on pages 82 and 121.)

[56] T. Ryhaenen, R. Cantor, D. Drung, and H. Koch, "Practical low-noise integrated dc superconducting quantum interference device magnetometers with additional positive feedback," *Appl. Phys. Lett.*, vol. 59, no. 2, July 1991. (Cited on pages 86 and 87.)

[57] Mikko Kiviranta and Heikki Seppä, "Comparison of dc SQUID readout methods based on positive feedback," Tech. Rep., VTT Automation, Measurement Technology, 1999. (Cited on pages 86 and 88.)

[58] Dietmar Drung, "Low-frequency noise in low-T_c multiloop magnetometers with additional positive feedback," *Appl. Phys. Lett.*, vol. 67, no. 14, September 1995. (Cited on pages 86, 88, and 89.)

[59] D. Drung, R. Cantor, M. Peters, H. J. Scheer, and H. Koch, "Low-noise high-speed dc superconducting quantum interference device magnetometer with simplified feedback electronics," *Journal of Applied Physics*, vol. 57, no. 4, July 1990. (Cited on page 86.)

[60] D. F. He and M. Yoshizawa, "A method of background noise cancellation for SQUID applications," *Supercond. Sci. Technol.*, vol. 16, pp. 1422–1425, 2003. (Cited on page 92.)

[61] Sunnyvale USA Whitley Research Inc., "WRSpice®," . (Cited on page 94.)

[62] The MathWorks Inc., "MATLAB®," Copyright 1984 – 2006. (Cited on page 94.)

[63] STAR Cryoelectronics, 25-A Brisbane Court, Santa Fe, NM 87508, *Sensor Handling Procedures*, January 1999. (Cited on page 118.)

[64] National Semiconductor, Application Notes 31, 1111 West Bardin Road, Arlington, TX 76017, *Op-Amp Circuit Collection*, 1978. (Cited on pages 118 and 121.)

[65] Erik Barnes, "Ask the applications engineer, current feedback amplifiers," . (Cited on page 119.)

[66] Ron Mancini, "Current-feedback op amp analysis," . (Cited on page 119.)

[67] H. A. C. De Villiers, "A process for the manufacture of high temperature bi-epitaxial josephson junctions," M.S. thesis, Department of Electrical and Electronic Engineering, University of Stellenbosch, 2006. (Cited on pages 124 and 126.)

[68] Wynand Fourie van Staden, "The fabrication of pbco buffered step-edge josephson junctions," M.S. thesis, Department of Electrical and Electronic Engineering, University of Stellenbosch, 2006. (Cited on pages 124 and 126.)

[69] Jun Kawai, Yushi Sakamoto, Miki Kawabata, Tatsuyuki Shimozu, Gen Uehara, and Hisanao Ogata, "A reliable molding technique by using epoxy-based resin for thin-film superconducting quantum interference devices," *IEEE Transaction on applied superconductivity*, vol. 15, pp. 3901–3905, 2005. (Cited on page 124.)

[70] STAR Cryoelectronics, 25-A Brisbane Court, Santa Fe, NM 87508, *HTS Magnetometer M1000*, April 2002. (Cited on page 134.)